Combating antimicrobial resistance through underexplored drug targets and drug-delivery systems

Dissertation

zur Erlangung des akademischen Grades

des Doktors der Naturwissenschaften

der Naturwissenschaftlich-Technischen Fakultät

der Universität des Saarlandes

von

Justine Bassil

Saarbrücken

2025

Tag des Kolloquiums: 15.09.2025

Dekan: Prof. Dr.-lng. Dirk Bähre

Berichterstatter: Prof. Dr. Anna K. H. Hirsch

Prof. Dr. Claus-Michael Lehr Prof. Dr.-Ing. Markus Gallei

Akad. Mitglied: Dr. Daniel Krug

Vorsitz: Prof. Dr. Christine Beemelmanns

Die vorliegende Arbeit wurde von August 2021 bis Januar 2025 unter Anleitung von Frau Prof. Dr. Anna K. H. Hirsch und Prof. Dr. Claus-Micheal Lehr in der Fachrichtung Pharmazie der Naturwissenschaftlich-Technischen Fakultät der Universität des Saarlandes sowie am Helmholtz-Institut für Pharmazeutische Forschung Saarland (HIPS) – Abteilung Wirkstoffdesign und Optimierung (DDOP) und Wirkstofftransport über biologische Barrieren (DDEL) – angefertigt.

"It always seems impossible until it's done"

Nelson Mandela

Acknowledgments

This PhD journey has been a life-changing experience, filled with challenges, learning, and growth, and I am grateful to everyone who has supported me along the way.

I would like to sincerely thank my advisors, Prof. Dr. Anna K. H. Hirsch and Prof. Dr. Claus-Michael Lehr, for providing me with the opportunity to join HIPS and their research groups. Being the first joint PhD student between both departments has been an exciting and rewarding experience. Your guidance, support, and encouragement have been invaluable in my growth as a research scientist, and I truly appreciate both of your mentorships. I am also grateful to Prof. Dr. Anna K. H. Hirsch for her expert advice regarding my career path.

I would like to express my gratitude to my thesis committee members, Prof. Markus Gallei, Dr. Brigitta Loretz, Dr. Mostafa Hamed, and Jun. Prof. Sangeun Lee, for their valuable insights and support during our meetings. I would also like to thank everyone involved in the Biodynamers and ECF transporters projects for their outstanding collaboration and dedication.

I am deeply grateful to Jun. Prof. Sangeun Lee and Dr. Mostafa Hamed for their supervision and continuous scientific advice throughout my journey. Their knowledge and experience made a huge difference in my work and inspired me to think outside the box. The projects would not have been possible without your guidance and recommendations.

I am extremely thankful to all my colleagues from the DDOP, DDEL, and Lee groups for their scientific and emotional support, and for the wonderful working environment. I especially appreciate those with whom I shared moments of stress but also moments of excitement, particularly Mohamed Kamal, Lena Zeroug, and Ioulia Exapicheidou. A warm thank you to my colleagues who became great friends Atanaz, Ahmed, Roya, Yingwen, Mostafa, Alaa, Lena and Angeliki, and made this experience more enjoyable with our small talks and best coffee breaks.

I am forever grateful to all my friends and family in Lebanon and Germany. A special thanks to Lea for listening to all my complaints and keeping me sane during this

period. To Lara and Sari thank you for your support in so many ways and for being there for me nearly every day, as well as for your little Laure's smile and energy that always brightened my mood. To my parents and siblings, your unconditional love, support, and belief in me have meant everything. Despite the distance, your encouragement kept me going. I would not be where I am today without you.

The last words go to my partner Jack. Thank you so much for being by my side throughout this journey. Your unwavering patience, support, and motivation kept me moving forward, especially in the final months. I could not have done this without you.

Table of Contents

Ackr	nowled	lgmentsIV
Sum	mary .	IX
Zusa	mmer	nfassungX
1 lı	ntrodu	ıction 1
1.1	Antin	nicrobial resistance1
	1.1.1	Mechanisms of AMR2
	1.1.2	Strategies proposed to overcome AMR
1.2	ECF	transporters8
	1.2.1	ATP Binding cassette (ABC) transporter family
	1.2.2	Discovery of ECF transporters9
	1.2.3	Structure of ECF transporters
	1.2.4	Transport mechanism of ECF transporters
	1.2.5	ECF transporter inhibitors14
1.3	Мусс	bacterium tuberculosis17
	1.3.1	Origin and evolution
	1.3.2	Progression of TB: from inhalation to active disease
	1.3.3	Challenges in tuberculosis treatment: drug resistance
1.4	Biody	ynamers21
	1.4.1	Definition and background21
	1.4.2	Types of biodynamers and their structural properties22
	1.4.3	Biodynamers pharmaceutical application25
1.5	Aims	of the thesis
1.6	Refe	rences28
2 R	esults	s & Discussion39
2.1	Chap	oter A: Discovery of Picolinic Acid Derivatives as a New Class of Energy-Coupling
Fac	tor Tra	ansporters (ECF-T) Inhibitors

2.1.1 Supplementary information	59
2.2 Chapter B: Discovery of a New Oxadiazole Derivative as Antitubercular Ag	gents:
Structure—Activity Relationship and Mode-of-Action Studies	119
2.2.1 Supplementary information	131
2.3 Chapter C: Direct Monitoring of Intracellular Polymer Degradation via BC	DIPY
Dynamic Dequenching	165
2.3.1 Supplementary information	206
3 Conclusions & Future Perspectives	217
4 Appendix	219
Abbreviations	219
Publications included in this thesis and contribution declaration	221
Publications not included in this thesis and contribution declaration	222

Summary

Finding new ways to fight infections is more important than ever, particularly due to the global threat of antimicrobial resistance, which has rendered many current treatments ineffective, leading to prolonged hospital stays and increasing healthcare costs. This thesis tackles this challenge by investigating underexplored drug targets, discovering new antitubercular agents, and improving antibiotic efficacy through advanced drug-delivery systems.

First, we focus on an underexplored drug target, energy-coupling factor transporters, which are crucial for nutrient uptake in Gram-positive bacteria but are absent in humans, making them an ideal target for selective inhibition. In parallel, we explore the development of new antitubercular agents targeting *Mycobacterium tuberculosis*. Both projects involve compound library screening, hit identification, and lead optimization to discover new inhibitors that serve as potent anti-infective agents against these pathogens.

Second, we explore biodynamers, dynamic biopolymers with pH-responsive reversible covalent bonds, for the delivery and controlled release of potent drugs. These biocompatible and biodegradable materials offer unique drug-delivery advantages such as infection and endo/lysosome-responsive behavior. This research focuses on designing a novel fluorescent biodynamer to study polymer behavior and fate *in situ* after cellular uptake, with the potential to answer unresolved questions and advance drug-delivery applications.

Zusammenfassung

Die Entwicklung neuer Strategien zur Bekämpfung von Infektionen ist angesichts der weltweiten Bedrohung durch antimikrobielle Resistenzen, die viele aktuelle Behandlungen unwirksam gemacht haben, dringender denn je. Diese Doktorarbeit befasst sich mit diesem Problem, indem sie wenig erforschte Zielproteine untersucht, neue antituberkulöse Wirkstoffe entdeckt und die Wirksamkeit von Antibiotika durch fortschrittliche Wirkstofftransportsysteme verbessert.

Im ersten Teil konzentrieren wir uns auf den Energy Coupling Factor (ECF)-Transporter, der für die Nährstoffaufnahme Gram-positiver Bakterien unerlässlich ist, beim Menschen jedoch nicht vorkommt und daher ein ideales Ziel für selektive Hemmstoffe darstellt. Parallel dazu erforschen wir die Entwicklung neuer Wirkstoffe gegen *Mycobacterium tuberculosis*. Beide Projekte umfassen das Screening von Substanzbibliotheken, die Identifizierung von hits und die Optimierung von Leitstrukturen, um neue potente Hemmstoffe zu entdecken.

Im zweiten Teil werden Biodynamere, dynamische und pH-sensitive Biopolymere mit reversiblen kovalenten Bindungen, für die Abgabe und kontrollierte Freisetzung wirksamer Arzneimittel untersucht. Diese biokompatiblen und biodegradierbaren Materialien zeichnen sich durch ein infektions sowie endo-/lysosomenresponsives Verhalten aus. Ein neuartiges fluoreszierendes Biodynamer wurde entwickelt, um das intrazelluläre Verhalten des Polymers und den Verbleib *in situ* nach der zellulären Aufnahme zu untersuchen, um die Anwendung der Arzneimitteltransport voranzutreiben.

1 Introduction

1.1 Antimicrobial resistance

Antimicrobial resistance (AMR) poses a serious global health challenge, defined by the ability of microorganisms—such as bacteria, viruses, fungi, and parasites—to develop mechanisms that render antimicrobial drugs ineffective.[1] This growing phenomenon, particularly bacterial resistance, has become one of the leading causes of morbidity and mortality worldwide. The introduction of antibiotics in the 20th century has initially brought hope that bacterial infectious diseases could be eradicated.[2] However, factors such as the overuse and misuse of antibiotics in human health care (e.g., for non-bacterial diseases and poor patient compliance)[3,4], in agriculture practice^[5] and in animal husbandry and healthcare^[6] have contributed to the emergence of resistant strains against nearly every antibiotic developed so far. The history of AMR dates back to the early days of antibiotic use, beginning with Alexander Fleming's discovery of penicillin in 1928. [7] Following its widespread use, resistance emerged almost immediately, with the first case of penicillinresistant Staphylococcus aureus reported in early 1940s[8] and tetracycline resistance in 1953.[9] The overuse of antibiotics during the 1950s–60s in agriculture and healthcare further accelerated resistance, leading to the emergence of multidrug resistance (MDR) against multiple antibiotic classes.[10,11] By the 1980s, MDR tuberculosis became a global issue,[12] and gram-negative bacteria (GNB) like Klebsiella pneumoniae and Escherichia coli developed extended-spectrum βlactamase resistance.[13] As a result, we now face a post-antibiotic era, where common infections and injuries could once again become life-threatening.[1,14] In response to this urgent crisis, the World Health Organization (WHO) launched the 'Global Action Plan' in 2015 to combat AMR and ensure effective treatment. [15] This plan categorizes priority pathogens into critical, high, and medium groups to guide research and development efforts. Despite the development of nine new antibiotics over the past seven years, resistant strains have surfaced for many of them, highlighting the dynamic nature of AMR and the critical need for ongoing efforts to address this pressing issue.[16] Therefore, understanding the molecular mechanisms

underlying AMR is important for developing novel therapeutic strategies and improving existing treatments to effectively combat these resistant pathogens.^[17]

1.1.1 Mechanisms of AMR

Antimicrobials and bacteria coexist in the same environment, prompting bacteria to develop defenses against the harmful effects of antibiotics. To address this problem of resistance, we first need to understand how antimicrobial agents work, the types of bacterial resistance, and their mechanisms.^[17,18]

Antimicrobial agents usually target essential bacterial functions such as the cell envelope, protein and nucleic acid synthesis. They can be classified based on their molecular structure, activity, mode of action, and their effects on bacteria by either killing them or inhibiting their growth. [19,20] Bacterial resistance is categorized into two distinct forms: intrinsic and acquired resistance. Intrinsic resistance refers to the natural ability of certain bacterial species to resist specific antibiotics due to its preexisting structural or functional characteristics, independent of therapy. [21,22] For instance, the impermeable cell wall in GNB often prevents antibiotic access. In contrast, acquired resistance arises through bacteria genetic changes, such as mutations, transformation, transposition, or conjugation, usually occurring during therapy and often leading to treatment failure. [23,24] The primary mechanisms by which microorganisms develop resistance fall into four main categories: limiting drug uptake, modifying the drug target, inactivating the drug, and actively expelling the drug via efflux pumps. Additionally, microorganisms can form biofilms, a surfacebound community that further restrict antibiotic penetration.^[2,17,18] These resistance mechanisms are illustrated in Figure 1 and are discussed briefly in the following paragraph.

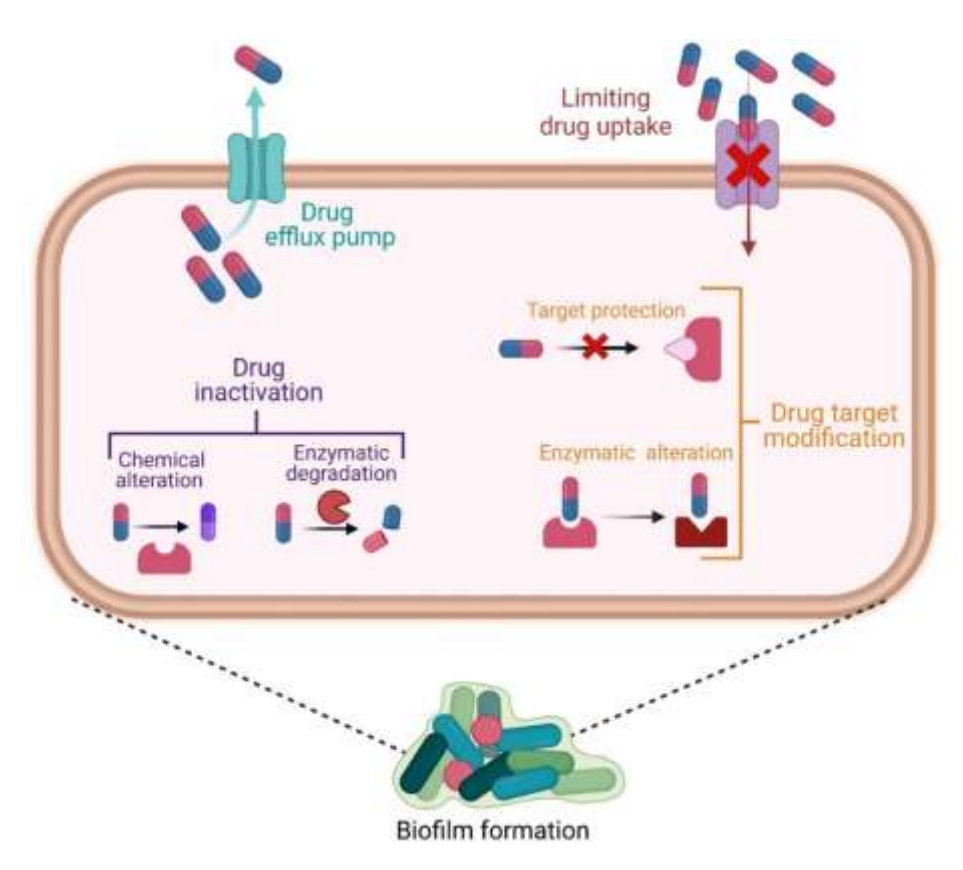


Figure 1. Illustration of the possible mechanisms of antimicrobial resistance in bacteria. Figure created using BioRender.

Limiting drug uptake is mostly observed in GNB due to the presence of a doublemembrane structure, known as the lipopolysaccharide (LPS) outer membrane, which acts as a protective permeability barrier against many antibiotics. [25] For antibiotics to exert their effects, they first must penetrate the bacterial cell envelope to reach their targets. Generally, hydrophilic antibiotics, such as β-lactams and fluoroquinolones, rely on porin channels to penetrate membrane barriers. However, acquired resistance can occur through reduced porin expression or mutations that alter porin selectivity.[26,27] For example, Enterobacteriaceae reduces porin numbers to resist carbapenems, [28,29] while Neisseria gonorrhoeae mutations impair the entry of βlactams and tetracyclines.[30] Similarly, mycobacteria, with their lipid-rich outer membranes, restrict the uptake of hydrophilic drugs while allowing easier access for hydrophobic agents like rifampicin (RIF).[31] Beyond membrane barriers, biofilm formation adds another layer of resistance. By producing a protective exopolysaccharide layer, these microbial communities obstruct drug diffusion and prevent the accumulation of bactericidal drugs concentration, thereby enhancing bacterial survival.[32,33]

Most antibiotics are highly selective for specific bacterial cellular targets, where they bind and disrupt cellular functions. ^[34] In response, bacteria modify and protect these binding targets, thereby reducing or blocking the drug-binding affinity. These changes can occur through genetic mutations or enzymatic modification. ^[17,34] For instance, fluoroquinolone resistance in either GNB or Gram-positive bacteria (GPB) is due to mutations in the quinolone-resistance-determining region of deoxyribonucleic acid (DNA) gyrase and topoisomerase enzymes. ^[35] Another modification method is methylation, where ribosomal methyltransferases, such as erm methylases, methylate ribosomal ribonucleic acid targets to prevent the binding of macrolides, lincosamides, and streptogramins antibiotics. ^[36]

Unlike drug-target modification, drug inactivation does not affect any core bacterial components but instead alters the drug structure. This mechanism typically involves enzymes and follows two pathways: degradation or chemical transfer of groups to the drug. [37] For example, the amide-bond of the β -lactam ring is hydrolyzed by β -lactamases enzymes in penicillin and cephalosporins. [38] Tetracycline is another drug that can be inactivated through oxidation, mediated by the tetX gene. [39] Additionally, aminoglycosides are modified by various transferases (acetylation, phosphorylation, adenylation), which modify their hydroxyl or amino groups, significantly reducing their effectiveness. [40]

The final mechanism by which bacteria can achieve intrinsic or acquired self-resistance is through efflux pumps, located on the cytoplasmic membrane. These membrane-proteins actively expel antimicrobial compounds from the cells, thereby reducing their intracellular concentration and preventing them from reaching their targets. ^[41] In the early 1980s, the first plasmid-encoded efflux pump was identified in *E. coli*, which exported tetracyclines from the cell. ^[42] Since then, various efflux mechanisms have been discovered in both GPB and GNB, contributing to the evolution of AMR. Efflux pumps are classified into several families based on their unique structures and energy sources: the multidrug and toxic compound extrusion family, the adenosine 5'-triphosphate (ATP) binding cassette (ABC) family, the small multidrug resistance family, the resistance-nodulation-cell division family, and the major facilitator superfamily. ^[24]

1.1.2 Strategies proposed to overcome AMR

As previously discussed, the emergence of AMR is a natural evolutionary process that resulted in life-threatening infections. According to WHO's priority pathogen list^[16], fifteen bacterial species show resistance to currently available antibiotic treatments (Table 1). The real challenge here lies in developing innovative strategies to stay ahead of this growing threat. These strategies include, but are not limited to: i) discovering, developing, and optimizing new antibiotics; ii) enhancing the efficacy of existing antibiotics through combination and conjugation therapy e.g., antibiotic adjuvants or nanotechnology.

Table 1. WHO priority pathogens list 2024

First Priority: Critical group

Enterobacterales, carbapenem-resistant

Enterobacterales, third-generation cephalosporin-resistant

Acinetobacter baumannii carbapenem-resistant

Mycobacterium tuberculosis, rifampicin-resistant

Second Priority: High group

Salmonella typhi, fluoroquinolone-resistant

Shigella spp., fluoroquinolone-resistant

Enterococcus faecium, vancomycin-resistant

Pseudomonas aeruginosa, carbapenem-resistant

Non-typhoidal Salmonella, fluoroquinolone-resistant

Neisseria gonorrhoeae, third-generation cephalosporin, and fluoroquinolone-resistant

Staphylococcus aureus, methicillin-resistant

Third Priority: Medium group

Group A Streptococci, macrolide-resistant

Streptococcus pneumoniae, macrolide-resistant

Haemophilus influenzae, ampicillin-resistant

Group B Streptococci, penicillin-resistant

Modern drug discovery is undergoing a revolutionary transformation, employing cutting-edge technologies in nearly every phase of the process. The use of artificial intelligence and advanced computational methods such as high-throughput virtual screening, structure-based bioinformatics, molecular docking, and *de novo* drug design, significantly accelerate identification, optimization and preclinical development of a new drug, while reducing development timelines and costs.^[43-45] The phases of drug discovery and optimization are illustrated in Figure 2. The process

begins with target identification and validation, where potential biological targets and their role in disease are thoroughly studied. Next, a library of compounds is selected and screened against a specific bacterial target to identify compound known as "hit" capable of modulating the desired activity. Alternatively, fragment-based drug discovery using endogenous ligands, kinetic target profiling, or dynamic covalent chemistry can also be employed. Further optimization of the hit is carried out through structure—activity relationship (SAR) analysis, which involves in-depth investigation of the core structure of the compound. This analysis aims to generate more selective and potent lead compounds, ultimately yielding better candidates for preclinical development. [46,47] Despite these advancements in drug discovery, the development of new classes of antibiotics remains time- and cost-intensive, often accompanied by commercial risks. [48] Thus, alternative strategies have also been implemented to enhance conventional antibiotics and combat AMR.



Figure 2. Overview of the drug discovery and development process (around 4–7 years).

One approach involves the use of adjuvants, also known as antibiotic potentiators, which are chemical entities that enhance the efficacy of antibiotics by restoring their susceptibility against resistant pathogens. Adjuvants typically exhibit little to no antimicrobial activity on their own but work synergistically with conventional antibiotics by inhibiting bacterial resistance mechanisms, such as improving antibiotic penetration into cells, inhibiting efflux pumps, or disrupting biofilms formation.^[49,50]

Another approach involves nanoantibiotics, which combine existing antimicrobial agents with nanotechnologies, like nanoparticles.^[51,52] These nanoparticles not only serve as carriers to deliver antimicrobials to target sites but can also exhibit intrinsic antimicrobial or adjuvant properties. Due to their small size and high surface area-to-volume ratio, nanoantibiotics offer advantages in membrane penetration,

pharmacokinetics and therapeutic potential compared to their conventional forms.^[53] Existing antibiotics can be conjugated to nanoparticles or encapsulated within the nanoscale structure. Ultimately, co-delivery of multiple therapeutic agents through simultaneous conjugation or encapsulation within a single nanoparticle is possible, potentially enhancing treatment efficacy through synergistic effects. Other advantages of this approach include the potential to bypass bacterial resistance mechanisms, protect drugs from degradation, improve solubility, enable targeted delivery, increase drug accumulation at infection sites, and minimize toxicity. Consequently, nanoparticles and antibiotic potentiators offer promising treatment strategies to prolong the life and efficacy of existing drugs and counteract the development of AMR.^[50,53-55]

In the following sections, the role of ABC efflux pump transporters, with a specific focus on the energy-coupling factor (ECF) transporter family in GPB pathogens like *Streptococcus pneumoniae*, and *Enterococcus faecalis*, and their implications for antimicrobial resistance, will be addressed. Additionally, the challenges posed by *Mycobacterium tuberculosis (Mtb)*, a WHO-critical pathogen, will be highlighted. Finally, the exploration of biodynamers, dynamic polymers with potential adjuvant and delivery properties, will be discussed as strategy to enhance the efficacy of antimicrobial agents.

1.2 ECF transporters

1.2.1 ATP Binding cassette (ABC) transporter family

Any substrate, whether it's a nutrient, virus, ion or waste, must pass through specific membrane proteins to enter, move within or exit a cell.^[56] The ATP-binding cassette (ABC) transporters are one of the largest and most ancient groups of membrane proteins, found in all living organisms, from bacteria to humans.^[57] These transporters harness the energy derived from ATP-hydrolysis to adenosine 5'-diphosphate (ADP) to translocate a wide variety of substrates including lipids, amino acids, sugars, vitamins, and antibiotics across biological membranes, often against their concentration gradients.^[58]

ABC transporters have two main functions: importers, primarily present in prokaryotes, facilitate uptake of nutrients into cells; or exporters, found in both prokaryotes and eukaryotes, pump out drugs and toxins out of cells. [59,60] Moreover, ABC transporters are involved in various cellular processes such as ion flux, protein secretion, pathogenesis, and translation of DNA and mRNA. Dysfunctions in these processes can lead to diseases, such as cystic fibrosis and Tangier disease. These transporters have also been implicated in multidrug resistance in both GNB and GPB, as well as in the progression of human cancer. [56,61]

Despite the fact that each ABC transporter has specific functionality, regulation and mechanism, they all share a similar architecture. It consists of two transmembrane domains (TMDs) that span the lipid bilayer and control substrate specificity and pathway (influx or efflux), and two nucleotide-binding domains (NBDs) located in the cytoplasm that facilitate ATP binding and hydrolysing. In prokaryotes, these four domains are typically expressed as four independent polypeptide chains and require a substrate-binding protein (SBP) to transfer the substrate into the TMDs. In contrast, in eukaryotic, the TMDs and NBDs are often fused together forming a "half-transporter" that assembles into functional complexes as homodimer or heterodimer and do not require SBP (Figure 3).^[62–64]

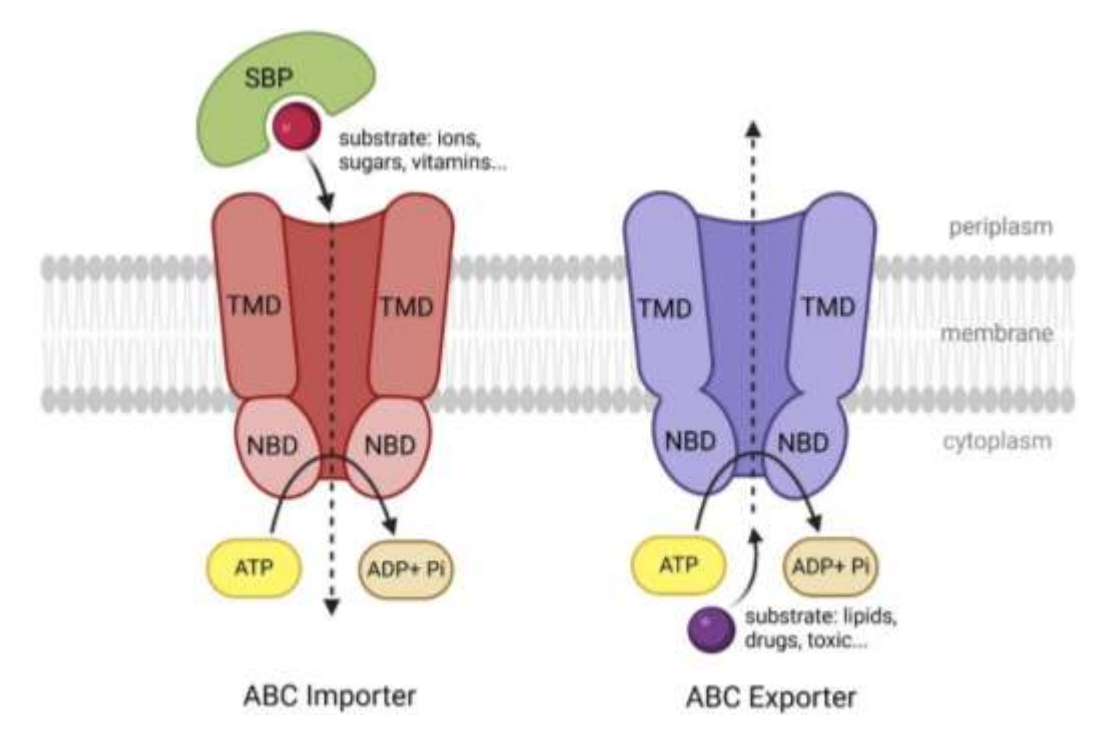


Figure 3. Schematic representation of ATP-binding cassette (ABC) transporters, showing how the hydrolysis of ATP into ADP and phosphate (Pi) provides the energy to transport substrates across the cell membrane. The four structural domains are highlighted: two transmembrane domains (TMDs) and two nucleotide-binding domains (NBDs), along with the substrate binding protein (SBP), which is specific for the ABC importers. Figure created using BioRender.

1.2.2 Discovery of ECF transporters

Energy-coupling factor (ECF) transporters are transmembrane proteins that belong to the superfamily of ABC transporters, and they are exclusively classified as importers in prokaryotes.^[65,66] These transporters mediate the uptake of essential micronutrients such as biotin^[67], cobalamin^[68], folate^[69], riboflavin^[70], pantothenate^[71], and thiamine^[72], as well as metal cations^[73,74] like Ni²⁺ and Co²⁺.

ECF transporters were first identified in the late 1970s by Henderson *et al.* during studies on the uptake of various vitamins (*e.g.*, folate, thiamine, and biotin) in *Lactobacillus casei*. Their work revealed that the transport process depends on a highly hydrophobic, specific integral membrane protein (later termed the S component) and is driven by ATP hydrolysis. Interestingly, it was also observed that thiamine inhibited folate transport without binding to the protein, suggesting the presence of a shared energy component, which was subsequently termed energy-coupling factor.^[75–79]The molecular identities of ECF transporters remained unknown

until the mid- to late 2000s, when Rodionov *et al.* used comparative genomics analysis and experimental approaches to identify them as a distinct subclass of ABC importers.^[65,80–82]

ECF transporters are predominantly found in GPB and are absent in humans, making them crucial transmembrane proteins for the survival of many pathogens. For instance, *Listeria monocytogenes* lacks the biosynthetic pathway for thiamine and relies on an ECF transporter to acquire this essential micronutrient. Similarly, *Mycoplasma genitalium* S. *pneumoniae* and S. *aureus* styles, also rely on genes encoded ECF transporters, likely due to their inability to synthesize folate, biotin, and thiamine, respectively. Therefore, ECF transporters play a critical role in pathogen survival and growth and are promising targets for the development of new antimicrobial drugs.

1.2.3 Structure of ECF transporters

The architecture of ECF transporters consists of four domains: a transmembrane protein (EcfT or T-component), two NBDs also called cytosolic ATPases (EcfA and EcFA'), which together form an energy-coupling module (ECF module), and a specific integral membrane protein known as S-component. While ECF transporters share structural similarity with ABC transporters, with two domains embedded in the lipid bilayer and two NBDs in the cytoplasm, they differ functionally. Instead of using an extracytoplasmic SBP, ECF transporters rely on their S-component to capture the specific substrates and use the ECF module to provide the necessary energy for micronutrient transport. [88,89]

Like all other ABC transporters, each ATPase consists of a RecA-like domain, an α -helical domain, and sometimes a C-terminal extension. [90,91] ATP binding induces a transition from an open to a closed conformation, bringing the RecA-like domain of one subunit in close contact to the α -helical domain of the other subunit. ATP hydrolysis to ADP and phosphate restore the open conformation of the dimer, preparing it for the next cycle. [74,83,92,93]

The transmembrane protein EcfT forms the structural core of ECF transporters complex, connecting the two ATPases with the S-component. EcfT interacts with the

cytoplasmic ATPases through two long α-helices that extend from the membrane and form an X-shaped structure, known as the coupling helices.^[83,94] Unlike other ABC transporters, which typically have only one coupling helix per membrane domain, the EcfT domain uniquely have both helices, allowing simultaneous interaction with the two ATPases.^[95] These coupling helices likely transmit conformational changes caused by ATP binding and hydrolysis in the ATPases to the S-component, potentially leading to its dissociation and reorientation, which facilitates substrate transport.^[66,91,96]

The S-component's structure consists of six hydrophobic α -helices arranged in a cylindrical configuration, with a typical size of 20–25 kDa. The interaction of the S-component with EcfT coupling helices occurs via complementary hydrophobic surfaces, stabilizing the resulting complex. [89]

ECF transporters are divided into two groups (Figure 4): Group I involves a "dedicated" ECF module that exclusively interacts with one "single" S-component, with all subunit genes located within the same operon. In contrast, Group II features a "common" ECF module that interacts with multiple S-components, which compete for binding to the ECF module. In this group, the genes encoding the various S-components are scattered across the chromosome. [89,97]

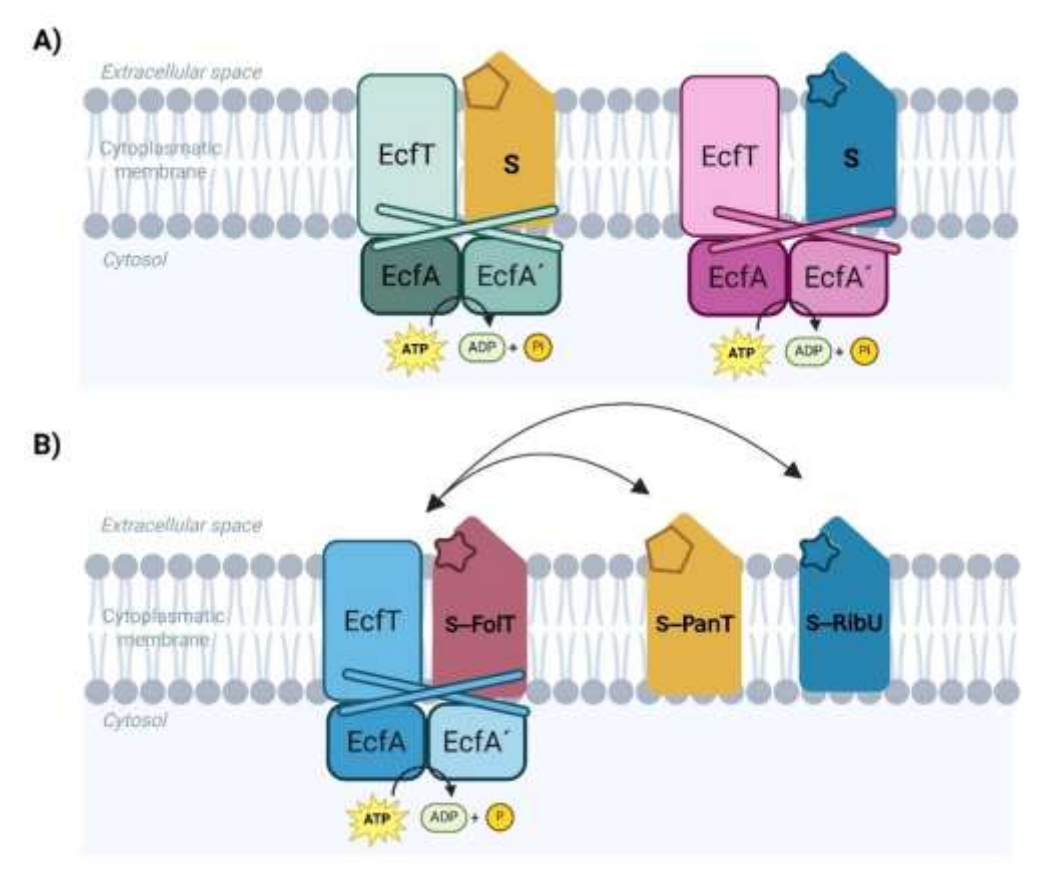


Figure 4. Architecture of energy-coupling factor transporters. A) A special ECF module interacts with dedicated S-components to form group I ECF transporters. B) A shared ECF module interacts with exchangeable S-components (shown in different colors) for specific micronutrient substrates [e.g., riboflavin (RibU), pantothenic acid (PanT), folic acid (FolT)] to form group II ECF transporter. Figure created using BioRender.

1.2.4 Transport mechanism of ECF transporters

The ECF transporters operate through a series of dynamic states to transport substrates across the membrane. Here, we discuss the most recently identified ECF mechanism for group II, shown in Figure 5, and proved by new cryogenic electron microscopy insights.^[98]

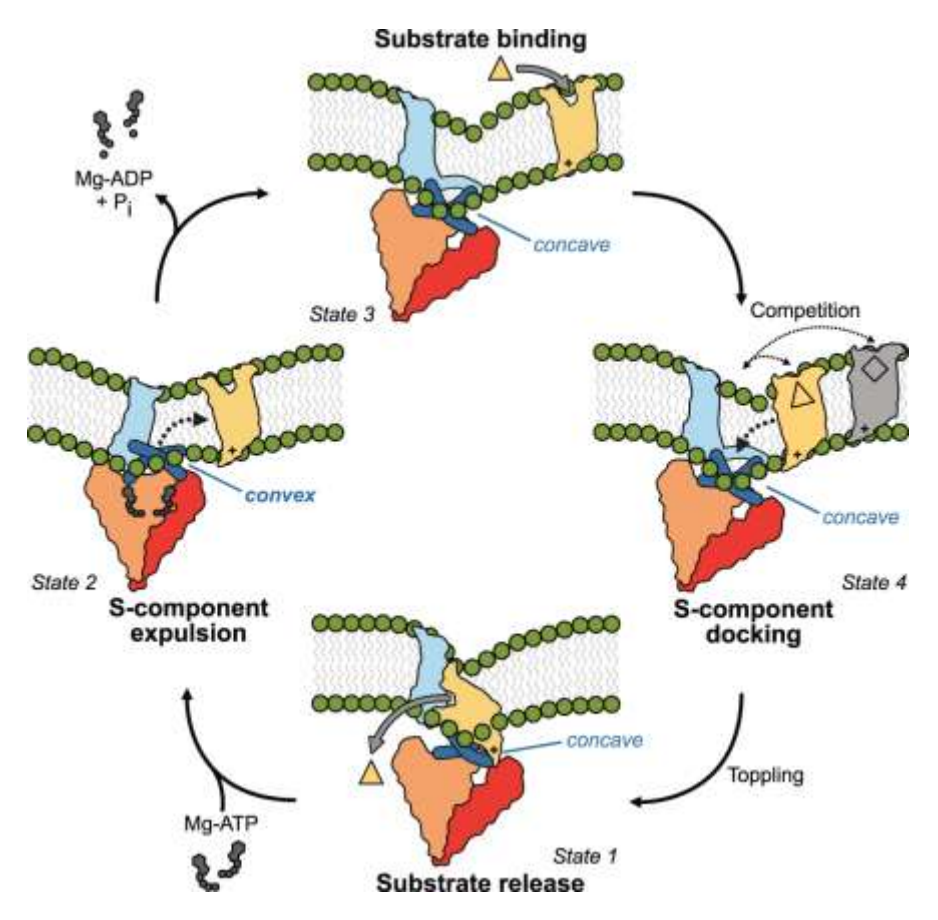


Figure 5. Mechanism illustration of Group II energy-coupling factor transporters. The ATPases (EcfA and EcfA') are shown in orange and red. The transmembrane protein EcfT is shown in turquoise, along with its coupling helices (α -helices) shown in dark blue. The S-components are shown in yellow and grey. The figure design is adapted from Thangaratnarajah C. et. al.^[98]

First, in the inward-facing state, the substrate is released into the cell and the unloaded S-component remains associated with the ECF module. At this stage, the coupling helices of the EcfT subunits adopt a concave shape (state 1). Upon ATP binding, the ATPase domains shift from an open to a closed configuration, triggering the coupling helices to adopt a convex shape. This conformational change reorients the S-component to an outwards-facing state and ejects it into the lipid bilayer (state 2). During ATP hydrolysis, the coupling helices return to their original concave shape, and EcfT moves away from the S-component, resetting the binding site for a new S-component (state 3). Finally, the substrate-loaded S-components compete with each other to interact with the ECF module, which bends the membrane and guides the selected S-component into a 90-degree toppled orientation. This interaction and orientation enable the continuation of the transport cycle.

1.2.5 ECF transporter inhibitors

The crucial role of ECF transporters in many WHO-priority pathogens, including *S. pneumoniae*, *S. aureus* and *E. faecium*, coupled with their absence in humans, makes them highly promising targets for the development of novel drugs to combat the growing challenge of AMR. Our research group focuses on designing and optimizing allosteric inhibitors that target "Group II" ECF transporters by binding to the ECF module, specifically the EcfT domain. This approach effectively blocks the uptake of multiple vitamins with one single inhibitor, thereby impairing bacterial growth and survival.

The biological evaluation of ECF transporter inhibitors is performed using radiolabeled uptake assays to measure their ability to reduce vitamin uptake across the membrane. The *in vitro* transport-activity assay uses two transporters, ECF-FolT2 (folate transporter) and ECF-PanT (pantothenate transporter) from *Lactobacillus delbrueckii*, which are expressed in *E. coli*, purified and reconstituted into proteoliposomes. This method allows testing of the intrinsic property of Group II ECF transporter, specifically the competition between two S-components for the same ECF module, without interference from other cellular components. [99] Alternatively, the recently developed whole-cell based assay for evaluation of folic acid uptake inhibition is conducted in *L. casei*, a nonpathogenic GPB strain known for its ability to transport multiple vitamins from the environment. This bacterial assay offers higher throughput, enabling rapid and convenient identification of ECF transporter inhibitors while allowing the monitoring multiple parameters such as the vitamins uptake, permeability, and activity. [100]

Our research group embarked on the discovery of new ECF inhibitors through structure-based virtual screening (SBVS) campaign, using the crystal structure of the ECF-FolT2 transporter from *L. delbrueckii* (PDB ID: 5JSZ)^[66]. We first identified key druggable pockets with the DoGSiteScorer algorithm^[101], focusing on allosteric inhibitors while avoiding ATP-binding subunits. The P2-pocket, located at the interface between ECF-FolT2 and the coupling helices near the membrane surface, was first predicted as the preferred target site for binding. Then, the Princeton BioMolecular Research library (1.3 million compounds) was screened, and twelve

promising drug-like compounds were selected. These compounds were further tested in the transport-activity assay using purified ECF-FolT2, leading to the identification of the first two ECF transporters inhibitors hit **1** and hit **2** (Figure 6).^[102,103] Both hits were further developed, characterized and validated for their ability and selectivity to inhibit ECF transporters.

Figure 6. Chemical structures of the energy-coupling factor transporters inhibitors. Hit **1** from the salicylic acid class, Hit **2** with its Zwitterionic nature, Hit **3** from the ureidothiophene class.

Hit **1** exhibited a half-maximal inhibitory concentration (IC₅₀) value of $282 \pm 108 \,\mu\text{M}$ in the *in vitro* transport activity assay and showed its ability to effectively reduce the translocation of both folate and pantothenate across the membrane. This strongly indicated that this compound targets the group II ECF transporter. Moreover, hit **1** was evaluated against the ABC transporter OpuA from *Lactobacillus lactis*, which is responsible for glycine betaine uptake, and showed no inhibitory activity, indicating selectivity for the ECF transporter family. Through systematic SAR, derivatives were identified with significantly improved activity against ECF transporters, while showing minimal cytotoxicity across a panel of human cell lines. [102] Furthermore, coarsegrained molecular dynamic simulations were performed on *L. delbrueckii* ECF-FolT2 and ECF-PanT to validate the predicted binding pocket and to profile the binding mode of this series. The simulations suggested that, in addition to the P2-pocket binding site, the interface between the S-component and the ECF module could act as a potential binding site (P9-pocket). [103,104]

Hit **2** initially demonstrated limited potency, with an $IC_{50} > 1.2$ mM in the *in vitro* transport activity assay, compared to hit **1**. Although a more potent derivative was identified through an SAR study, showing an IC_{50} of $204 \pm 22 \,\mu\text{M}$ in the *L. casei* wholecell based assay, its low solubility and unfavorable physicochemical properties hindered further development.^[100]

In 2022, a SBVS of our in-house library of over 2,000 small molecules combined with the whole-cell uptake assay, identified the substituted ureidotheiophene hit $\bf 3$ as a potent ECF inhibitor (Figure 6). Subsequent SAR studies led to the development of two analogues, which exhibited single-digit micromolar inhibition in the $\it L. casei$ cell-based assay (IC50 values of 2.3 μ M and 2.8 μ M). Further profiling revealed strong antibacterial effects against a panel of GPB, particularly penicillin-resistant $\it S. pneumoniae$ (Minimum inhibitory concentration (MIC)= 0.5 μ M), with minimal cytotoxicity observed in human cell lines.[105]

1.3 Mycobacterium tuberculosis

1.3.1 Origin and evolution

Mtb is the bacterium responsible for tuberculosis (TB), a life-threatening infectious disease that primarily affects the lungs but can also spread to other parts of the body. The disease is transmitted through airborne droplets expelled when an infected patient coughs, sneezes, or speaks. [106] Mtb is characterized by its slow growth, ability to evade the host immune system, capacity to enter a dormant state known as latent TB, and complex cell-wall structure. These features make TB one of the deadliest human pathogens worldwide. Following infection with Mtb, several outcomes may occur: in some individuals, the immune system may eliminate the bacteria; others may immediately develop active TB, which is symptomatic and highly contagious; and some may harbor the bacteria in a latent form, remaining asymptomatic with the risk of developing active TB later in life. [107]

TB has a long history, with evidence of its existence in human remains dating back to ancient civilizations, including Egyptian mummies and a Neolithic infant and woman from the Eastern Mediterranean. The understanding of TB as a disease evolved gradually over time. It was described in various cultures under different names, such as "schachepheth" in the Old Testament, "phthisis" by Hippocrates, and "consumption" in many 19th century myths. The term "tuberculosis" was first introduced in 1834 by Johann Lukas Schönlein, who identified the characteristic tubercles present in all forms of the disease. In 1865, Jean-Antoine Villemin demonstrated the infectious nature of TB, and a significant breakthrough followed in 1882 when Robert Koch isolated and identified *Mtb* as the causative agent. [108,109]

This discovery paved the way for improved diagnosis, treatment, and prevention strategies. The introduction of the sanatorium cure in 1854 marked the first successful remedy against TB. [110] Subsequent milestones included the development of the Bacillus Calmette-Guérin vaccine in 1920, the discovery of streptomycin in 1944, and the introduction of isoniazid (INH) in 1952. These advancements, along with improved living conditions and public-health measures, led to a significant decline in TB cases, particularly in industrialized countries by the mid-20th century. [108,109] However, the emergence of drug resistance, observed shortly after the

discovery of streptomycin, when many TB patients initially improved but later relapsed, has hindered efforts to eradicate this disease.^[111] Thus, despite being preventable and treatable with various discovered antibiotics, TB continues to be a major global health challenge, with more than 10 million people develop TB, and over 1.3 million deaths annually.^[112]

1.3.2 Progression of TB: from inhalation to active disease

The progression of TB infection occurs in four stages (Figure 7). Stage 1 begins when Mtb particles are inhaled, traveling through the mouth and nose to reach deep into the lungs. Once there, the bacteria invade alveoli of the host, where they resist destruction by manipulating the host's immune system. Alveolar macrophages and dendritic cells attempt to phagocytize the bacteria by activating T-cells to initiate an immune response. If eradication fails, stage 2 begins, in which Mtb rapidly multiplies within these cells and spreads throughout the lung tissue, triggering an adaptive immune reaction. In stage 3, as an attempt to contain the TB infection, the immune system forms a cluster of immune cells that forms a structure called "granuloma". This granuloma helps isolate and control the infection by confining it to a localized area. Initially, granulomas are well-vascularized, allowing immune cells and drugs to reach the infection site. As they mature however, they develop thick fibrous walls and necrotic cores, forming a protective niche where Mtb can persist in a latent, noncontagious state. The final stage occurs when the immune system weakens, causing the granulomas to break down and release the bacteria within the lungs, leading to active TB. This stage is characterized by rapid bacterial reproduction and systemic symptoms, with the potential for transmission. Approximately 5–10% of individuals with latent TB progress to active TB during their lifetime. In advanced stages, Mtb can spread beyond the lungs to other organs, through the bloodstream, resulting in extrapulmonary TB, which complicates treatment.[113-115]

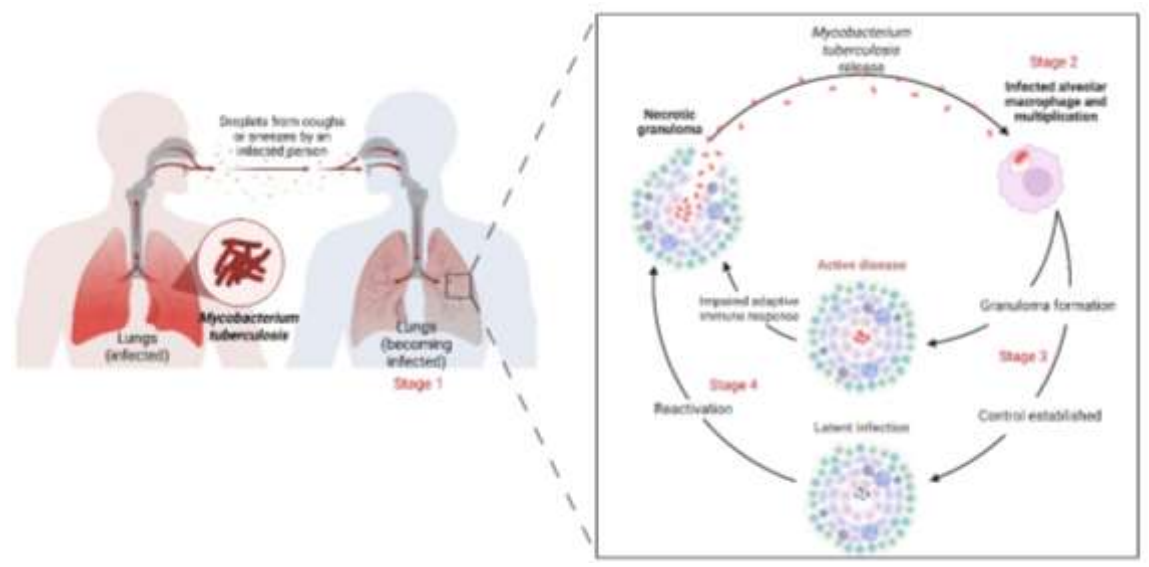


Figure 7. The life cycle of *Mycobacterium tuberculosis* infection: From inhalation to persistence in macrophages, escaping immune system and leading to active disease. Figure created using BioRender.

1.3.3 Challenges in tuberculosis treatment: drug resistance

For over 40 years, TB has been treated with a standard six-month regimen comprising a combination of first-line drugs: INH, RIF, ethambutol, and pyrazinamide. The treatment begins with an intensive two-month phase, during which all four first-line drugs are used, followed by a four-month continuation phase involving only INH and RIF. This regimen typically achieves a success rate of approximately 85%, provided the infecting strain is drug-susceptible and the prescribed regimen is adhered to consistently. In the rise of multidrug-resistant (MDR) and extensively drug-resistant (XDR) TB, however, significantly complicate this treatment. MDR-TB results from *Mtb* strains resistant to INH and RIF, necessitating the use of second-line drugs such as fluoroquinolones, bedaquiline (approved in 2012), linezolid, and pretomanid (approved 2019). In contrast, XDR-TB involves resistance to INH and RIF, in addition to any fluoroquinolone (e.g., moxifloxacin or levofloxacin), and at least one of the key second-line injectable drugs (e.g., amikacin, kanamycin, bedaquiline). Treatment of both resistant forms often requires prolonged regimens lasting up to two years, increased costs, higher side effects, and lower success rates. [116,117]

A major barrier to effective treatment and development of TB drug-resistance is the unique structure of *Mtb* cell wall. Although *Mtb* is classified as GPB, its outer membrane closely resembles that of GNB. The outer layer is rich in long-chain fatty

acids, primarily mycolic acids, and free lipids such as lipoglycans or glycopeptidolipids, creating a highly hydrophobic barrier around the bacilli. Beneath this lipid-rich outer membrane lies a thick layer of peptidoglycan linked to arabinogalactan, which is also covalently linked to mycolic acids, forming a protective complex known as mycolyl-arabinogalactan-peptidoglycan complex. These structural features are crucial for the pathogen's survival and resistance, enabling it to evade host immune systems and withstand antibiotic treatment.[118-120] For instance, the first line-drug INH is a prodrug that targets the Mtb cell wall by inhibiting the biosynthesis of mycolic acid. Upon entering the Mtb cell via passive diffusion, INH is activated by the catalase peroxidedase (KatG) enzyme. Any mutations in the KatG enzyme leads to resistance against INH by preventing its activation. Similarly, resistance to RIF arises from mutations in the rpoB gene, which encodes the RNA polymerase β -subunit, the drug's primary target, thereby impairing the drug's efficacy against actively growing bacteria. [120] A breakthrough in MDR-TB treatment occurred with the discovery of bedaquiline, the first novel MDR-TB drug approved in decades. Bedaquiline targets a unique mechanism by inhibiting Mtb ATP synthase and disrupting energy production crucial for bacterial survival. However, resistance to bedaquiline emerged shortly after its introduction, involving mechanisms such as the upregulation of efflux pumps or mutations in the atpEgene, which encodes the binding site of the drug.[118,121]

Hence, the rapid emergence of drug-resistance, along with the pathogen's persistence in a latent state, showcases the challenges of combating TB. This highlights the urgent need for innovative strategies and the continuous development of new antitubercular drugs to meet the WHO's goal of eliminating TB as a public health threat by 2050.^[122]

1.4 Biodynamers

1.4.1 Definition and background

The concept of biodynamers has evolved since the early 21st century from Constitutional Dynamic Chemistry (CDC). CDC involves a library of molecules capable of constructing/deconstructing and reshuffling their constitution through reversible linkages at both molecular and supramolecular levels, driven by external or internal factors. These linkages include reversible covalent bonds, belonging to dynamic covalent chemistry (DCC), as well as noncovalent interactions referred to as dynamic non-covalent chemistry.[123-125] The implementation of CDC principles in polymer science has revolutionized the field, leading to the rise of constitutionally dynamic polymers known as "dynamers".[126-129] These polymers exhibit adaptability, self-healing, reconfigurability, monomers exchange, and stimuli-responsive behavior through reversible interactions at both molecular and supramolecular levels, allowing them to generate the best dynamer under given condition. Additionally, dynamers that combine both reversible covalent and noncovalent interactions can dynamers, exhibiting give rise to dual properties at both levels simultaneously.[126,130,131]

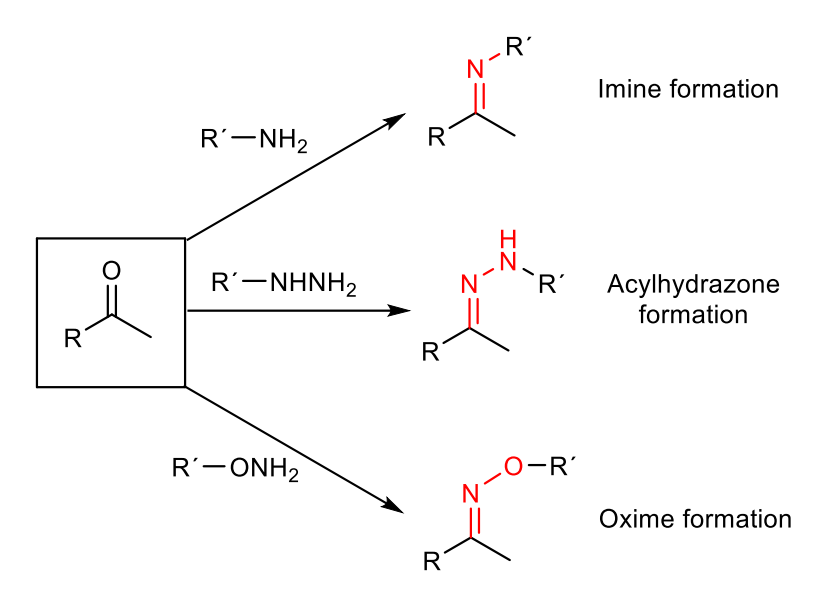
As the study of dynamers at the molecular level expanded into biopolymers, a new class of materials "biodynamers" emerged. [131] Biodynamers combine the adaptive properties of DCC with the biofunctionality of naturally occurring biological molecules, resulting in synergistic effects. These materials are thus capable of undergoing spontaneous physical and chemical modification via reversible dynamic covalent bonds (DCBs) under specific conditions, while also mimicking biological processes like enzyme catalysis, molecular recognition, and cellular interactions. Therefore, biodynamers have gained significant attention as an innovative class of stimuli-responsive polymers. [132] By bridging the gap between natural and synthetic polymers, they hold immense potential for various biomedical applications including drug delivery, drug discovery, treatments, and diagnostics, making them also a promising strategy to tackle AMR challenges. [131,133–135]

In the following section, we will explore the key types of biodynamers, focusing on their structural features and inherent properties of biopolymers.

1.4.2 Types of biodynamers and their structural properties

As described earlier, biodynamers are dynamic polymeric structures based on biorelevant monomers, connected via reversible DCBs. The ability of these materials to self-heal, assemble, disassemble, and adapt to various conditions is due to the dynamic and reversible nature of their covalent bonds.^[132,133]

Polycondensation reactions between amino and carbonyl groups to form C=N bonds represent the most fundamental DCBs used in synthesizing biodynamers. The formation of imine, acylhydrazone, and oxime bonds occurs through the condensation of primary amines, hydrazides, or hydroxylamine with aldehyde or ketone groups, respectively, each exhibiting unique features in DCC (Scheme 1).[136] Imine-bonds are highly reversible, biocompatible, with fast reaction kinetics between formation and hydrolysis. Their behavior is strongly dependent on pH, particularly under mild acidic conditions, making them very dynamic and responsive. Their weak stability in aqueous solutions generally favors reversibility which often limits their applications in biomaterials.[137-139] Acylhydrazone-bonds, on the other hand, are more stable due to the additional nitrogen atom and acyl group, offering chemoselectivity in aqueous media, biocompatibility and tunable reaction kinetics under weak acid catalysis. Their pH-dependent reversibility enables hydrolysis or exchange of monomers, typically accelerated under acidic conditions, with these processes often occurring within one hour. [140,141] Oxime-bonds are the most stable of the three in aqueous solution, characterized by rapid formation and high yields under mildly acidic conditions. They exhibit superior resistance to hydrolysis, owing to their inherent stability derived from the alpha effect of the adjacent oxygen atom. However, this stability is pH- and temperature-dependent, with increased susceptibility to hydrolysis in strongly acidic environments. Their biorthogonality, and potential for nucleophilic catalysis make oxime bonds particularly useful for bioconjugation applications.[142-144] In conclusion, all three bond types offer a spectrum of adaptability, reactivity, stability, and tunability, making them highly valuable for stimuli-responsive dynamic systems, especially in biological environments.



Scheme 1. Polycondensation reactions between amino and carbonyl groups, illustrating the formation of imine, acylhydrazone, and oxime bonds, which are reversible under specific conditions.

Building on the versatility of these C=N bonds, various classes of biodynamers have been developed to mimic biological macromolecules (e.g., polysaccharides, proteins, and nucleic acids) and to modify and enhance their functionality.[131,133] Dynamic analogues of nucleic acids (DyNAs) are one class of biodynamers designed to replicate the structure and function of nucleic acids. These dynamers are synthesized through DNA-templated reversible polymerization via imine or acylhydrazone bonds, allowing sequence-specific and length-controlled properties. DyNAs can dynamically adapt their structure in response to stimuli such as pH changes, electrostatic forces, or target binding. By combining the biomimetic features of nucleic acids with the reversibility of DCBs, DyNAs hold significant promise in biomedical applications, including gene delivery and biosensors.[133,145-147] Another notable class of biodynamers are the glycodynamers, which mimic polysaccharides, abundant biopolymers found in living organisms and are involved in immune responses, cell-cell recognition, and other biological processes. The synthesis of glycodynamers often involves the formation of reversible oxime or acylhydrazone bonds, which can occur in the main chain, side chains of the polymer, or a combination of both. These bonds allow structural and physicochemical modifications, as well as tunable properties, by reorganizing the molecular components in response to various chemical or physical stimuli, such as pH changes or enzymatic activity. Therefore, glycodynamers combine the bioactivity of carbohydrates such as biocompatibility and biodegradability, with the adaptability of DCBs, making them valuable for biomedical applications including drug-delivery systems, self-healing materials, studies for carbohydrate-mediated biological interactions, and biosensing platforms.^[133,148,149]

Lastly, proteoid biodynamers represent a unique class of molecular biodynamers, that mimic proteins and peptides, which have recently been developed and investigated. These dynamers are formed by polymerizing amino acid (e.g., lysine(Lys), histidine (His), and arginine(Arg)) hydrazides with carbazole-dialdehyde hexaethylene glycol (CA-HG) monomers via reversible imine and acylhydrazone bonds (Figure 8).[132,150,151] A key feature of proteoid biodynamers is their amphiphilic nature, derived from the π - π stacking and hydrophobic interactions of carbazoledialdehyde components along with the hydrophilic hexaethylene glycol (HG) shell. This enables them to fold into single-nanorod structures with high stability, high molecular weights (70–130 kDa), and improved biocompatibility. For instance, in the cell viability assay, Lys-biodynamers demonstrated 44 times higher IC₅₀ value compared to conventional poly-L-lysine. They also exhibit dynamic behavior, such as polymerization and depolymerization or changes in molecular weight in response to concentration and pH. For example, when the concentration is reduced tenfold (from 10 to 1 mg/mL), their molecular weight decreases by approximately 50% at pH 5. The nanorod structure, amphiphilic characteristics, biodegradability, and biocompatibility of proteoid biodynamers make them ideal candidates for various biomedical applications, such as drug loading and drug delivery.[152,153]

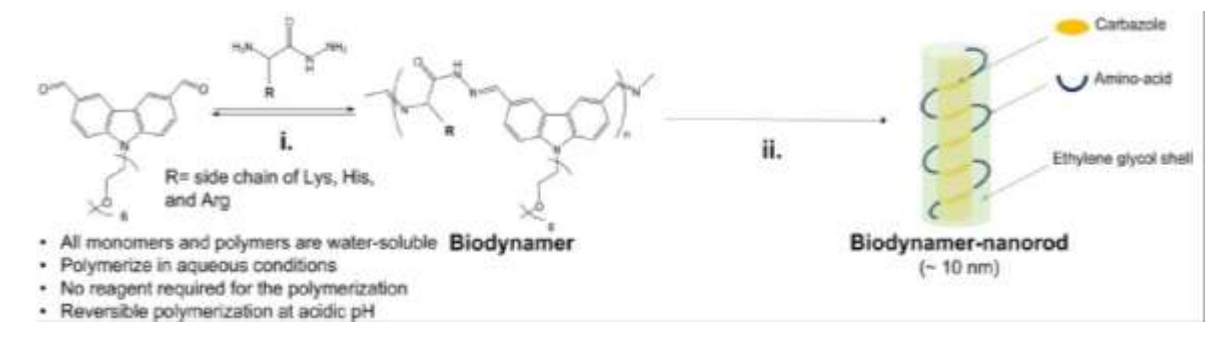


Figure 8. Illustration of biodynamers i) Carbazole-dialdehydes conjugated hexaethylene glycol (CA-HG) and amino acid hydrazides derivatives undergo reversible polymerization in acidic aqueous medium through acylhydrazone and imine bond formation. ii) The biodynamer self-assembles into a nanorod structure, featuring a hydrophobic carbazole core and a hydrophilic outer shell incorporating hexaethylene glycol and amino acid derivatives. This figure was adapted from Lee *et al.*^[153]

1.4.3 Biodynamers pharmaceutical application

Biodynamers have emerged as a promising class of materials in biopharmaceutical applications, with significant advancements made in recent years. Their unique properties, such as pH-responsiveness and biocompatibility, make them ideal candidates for overcoming biological barriers and improving drug-delivery systems leading to advanced strategies to combat AMR.

One of the primary applications of biodynamers in drug-delivery systems lies in gene therapy, where they enhance the delivery of nucleic acids, such as mRNA, through the formation of dynaplexes. Lee et al. showed that positively charged biodynamers, synthesized from Lys, Arg, and His amino acid hydrazides combined with CA moieties, form dynaplexes with negatively charged mRNA. These complexes protect the cargo from degradation, promote efficient cellular uptake and ensure successful delivery to intracellular targets. Within the acidic environment of endosomes, biodynamers undergo conformational changes, enabling them to disrupt endosomal membranes up to 10 times more effectively than conventional vectors. They change their structure, swell, and degrade in endosomes, leading to controlled release of their cargo into the cytoplasm. This method has shown significantly improved transfection efficiency with reduced cytotoxicity compared to traditional agents like polyethyleneimine. Additionally, biodynamer ability to form stable complexes with mRNA positions them as promising carriers for mRNA vaccines, ensuring efficient delivery and antigen expression within target cells. [153] Similarly, Liu et al. reported that biodynamers cross-linked with siRNA form stable nanocomplexes that exhibit pH-dependent size changes, ensuring efficient siRNA release. They serve as potent inducers of apoptosis in carcinoma cells, outperforming lipid-based transfection agents. This underscores the potential of biodynamers in overcoming barriers in gene therapy, particularly for cancer and infectious diseases. [154]

Beyond nucleotide delivery, biodynamers have been explored as innovative nanoparticle carriers in protein and peptide delivery. They can form polymeric nanocomplexes or double emulsion nanoparticles that encapsulate and deliver proteins efficiently. They are capable of delivering both anionic and cationic proteins by adapting the charge properties of their amino-acids derivatives. They exhibited high

encapsulation efficiency and high loading capacity for various proteins like ovalbumin. For instance, these systems have achieved drug loading efficiencies of up to 78% for fluorescent dye-conjugated proteins due to their cylindric shape and their hydrophobic component, significantly outperforming other systems, which typically exhibit loading rates of only 1–5 wt%.^[155,156]

Furthermore, biodynamers have shown promising potential as biosensors, particularly for metal ion detection. For instance, Zeroug *et al.* have identified Hisderived biodynamers as biocompatible and water-soluble Cu(II) sensors. The fluorescent properties of biodynamers, often derived from the CA components, provide a direct indicator of ion binding, enabling their use as effective tools for monitoring cellular processes and advancing disease diagnostics.^[157]

Lastly, biodynamers have been investigated for their potential activity as antibiotic potentiators, enhancing the effectiveness of existing antibiotics against resistant bacterial strains by improving drug interaction with bacterial membranes. *Kamal et al.* found that Arg-biodynamers interact with the lipopolysaccharide (LPS) layer of the outer membrane of Gram-negative bacteria, thereby enhancing antibiotic penetration and efficacy. In experiments with *E. coli*, Arg-biodynamers improved the MIC value of colistin by 32-fold, with similar enhancements observed in *Pseudomonas aeruginosa* strains. This potentiation effect was attributed to the biodynamers' ability to adopt a predominant β-sheet structure in the LPS microenvironment, facilitating stronger interactions with bacterial membranes. Moreover, Arg-biodynamers retain their antibacterial activity while exhibiting significantly reduced cytotoxicity to mammalian cells compared to traditional polymers such as poly-L-arginine. This combination of properties highlights biodynamers as promising adjuvants to existing antibiotics, offering an approach to combating AMR.^[158]

Overall, biodynamers represent a groundbreaking class of dynamic polymers with different approaches in combating the challenge of AMR. They can enhance the efficacy of existing antibiotics, improve drug-delivery to bacterial targets by overcoming biological barriers and might potentially reduce the development of resistance by allowing for lower antibiotic doses using nano-delivery systems.

1.5 Aims of the thesis

The rapid emergence of resistance to commonly used antibiotics is increasingly limiting therapeutic options, even for minor infections. This growing challenge in AMR calls for the identification of novel bacterial targets and effective strategies to combat resistant pathogens. The aim of this PhD thesis is divided into two main parts. Each of these sections offers potential solutions for combating AMR by advancing therapeutic targets and improving treatment efficacy:

Part I of the thesis focuses on the identification and optimization of new anti-infective agents using diverse medicinal-chemistry strategies targeting critical pathogens:

- a. **ECF transporters as drug targets:** These are transmembrane proteins crucial for the survival and growth of GPB, as they facilitate the uptake of essential micronutrients and vitamins. These transporters were identified as potential underexplored drug targets in several pathogenic bacteria linked to serious infections. Herein, we describe the discovery of a novel chemical class of ECF transporter inhibitors. This class consists of picolinic acid derivatives, initially identified through experimental screening of compound libraries using a whole-cell uptake assay. A comprehensive SAR study was conducted to the initial hit by sequentially refining its chemical structure, followed by biological evaluations to assess the antimicrobial efficacy of the frontrunner compounds (**Section 2.1, Chapter A**).
- b. **TB drug discovery:** TB, caused by *Mtb*, remains one of the deadliest diseases worldwide. This project aims to identify new antitubercular agents, through screening of compound libraries. An initial hit was identified, and a systematic SAR study was performed to develop potent frontrunner compounds. Further investigations are ongoing to elucidate the mode of action of these compounds against *Mtb* (Section 2.2, Chapter B).

Part II focuses on the design and optimization of a novel dynamic biodynamer, based on BODIPY-dialdehyde and lysine hydrazide (BDP-Lys), with the aim of enabling real-time monitoring of polymer degradation within biological systems. This approach seeks to address critical questions about the fate of biodegradable polymers and

their interaction *in situ*, ultimately advancing the understanding and development of biodynamers as effective tools for drug delivery applications (**Section 2.3, Chapter C**).

1.6 References

- [1] S. K. Ahmed, S. Hussein, K. Qurbani, R. H. Ibrahim, A. Fareeq, K. A. Mahmood, M. G. Mohamed, *Journal of Medicine, Surgery, and Public Health* **2024**, *2*, 100081.
- [2] M. A. Salam, M. Y. Al-Amin, M. T. Salam, J. S. Pawar, N. Akhter, A. A. Rabaan, M. A. A. Alqumber, *Healthcare (Basel, Switzerland)* 2023, 11.
- [3] P. R. Lee, C. Lin, *The Antibiotic Paradox: How the Misuse of Antibiotics Destroys Their Curative Powers (review)* **2003**.
- [4] C. Llor, L. Bjerrum, Therapeutic advances in drug safety 2014, 5, 229.
- [5] W. Witte, Science (New York, N.Y.) 1998, 279, 996.
- [6] W. Vanderhaeghen, J. Dewulf, The Lancet. Planetary health 2017, 1, e307-e308.
- [7] A. Fleming, Clinical Infectious Diseases 1980, 2, 129.
- [8] C. H. Rammelkamp, T. Maxon, Experimental Biology and Medicine 1942, 51, 386.
- [9] V. KNIGHT, A. R. HOLZER, The Journal of clinical investigation 1954, 33, 1190.
- [10] M. T. PARKER, M. P. JEVONS, *Postgraduate medical journal* **1964**, *40*, SUPPL:170-8.
- [11] M. P. JEVONS, M. P. JEVONS, *BMJ* **1961**, *1*, 124.
- [12] P. Steiner, M. Rao, M. Mitchell, M. Steiner, *American journal of diseases of children (1960)* **1985**, *139*, 780.
- [13] G. A. Jacoby, P. Han, Journal of clinical microbiology 1996, 34, 908.
- [14] A. J. Alanis, Archives of medical research 2005, 36, 697.
- [15] WHO, Global action plan on antimicrobial resistance **2015**, https://www.who.int/publications/i/item/9789241509763.
- [16] WHO, bacterial priority pathogens list, 2024: bacterial pathogens of public health importance to guide research, development and strategies, https://www.who.int/publications/i/item/9789240093461.
- [17] E. M. Darby, E. Trampari, P. Siasat, M. S. Gaya, I. Alav, M. A. Webber, J. M. A. Blair, Nature reviews. Microbiology 2023, 21, 280.

- [18] W. C. Reygaert, AIMS microbiology 2018, 4, 482.
- [19] E. Etebu, I. Arikekpar, Int. J. Appl. Microbiol. Biotechnol. Res. 2016.
- [20] J. F. Prescott, *Veterinary microbiology* **2014**, *171*, 273.
- [21] J. L. Martinez, Drug discovery today. Technologies 2014, 11, 33.
- [22] G. Cox, G. D. Wright, *International journal of medical microbiology IJMM* **2013**, 303, 287.
- [23] A. H. Holmes, L. S. P. Moore, A. Sundsfjord, M. Steinbakk, S. Regmi, A. Karkey, P. J. Guerin, L. J. V. Piddock, *Lancet (London, England)* 2016, 387, 176.
- [24] J. M. Munita, C. A. Arias, Microbiology spectrum 2016, 4.
- [25] J. M. A. Blair, G. E. Richmond, L. J. V. Piddock, Future microbiology **2014**, 9, 1165.
- [26] I. Ghai, S. Ghai, Infection and drug resistance 2018, 11, 523.
- [27] U. Choi, C.-R. Lee, Frontiers in microbiology **2019**, 10, 953.
- [28] J. W. Chow, D. M. Shlaes, *The Journal of antimicrobial chemotherapy* **1991**, *28*, 499.
- [29] G. Cornaglia, A. Mazzariol, R. Fontana, G. Satta, *Microbial drug resistance* (Larchmont, N.Y.) **1996**, *2*, 273.
- [30] M. J. Gill, S. Simjee, K. Al-Hattawi, B. D. Robertson, C. S. Easmon, C. A. Ison, Antimicrobial agents and chemotherapy **1998**, *42*, 2799.
- [31] P. A. Lambert, Journal of Applied Microbiology 2002, 92, 46S-54S.
- [32] T.-F. Mah, Future microbiology **2012**, 7, 1061.
- [33] H. van Acker, P. van Dijck, T. Coenye, Trends in microbiology 2014, 22, 326.
- [34] F. Baquero, B. R. Levin, Nature reviews. Microbiology 2021, 19, 123.
- [35] R. E. Ashley, A. Dittmore, S. A. McPherson, C. L. Turnbough, K. C. Neuman, N. Osheroff, *Nucleic acids research* **2017**, *45*, 9611.
- [36] R. Bhujbalrao, R. Anand, *Journal of the American Chemical Society* **2019**, *141*, 1425.
- [37] A. J. Schaenzer, G. D. Wright, Trends in molecular medicine 2020, 26, 768.
- [38] C. L. Tooke, P. Hinchliffe, E. C. Bragginton, C. K. Colenso, V. H. A. Hirvonen, Y. Takebayashi, J. Spencer, *Journal of molecular biology* **2019**, *431*, 3472.
- [39] J. M. A. Blair, M. A. Webber, A. J. Baylay, D. O. Ogbolu, L. J. V. Piddock, *Nature reviews*. *Microbiology* **2015**, *13*, 42.

- [40] M. S. Ramirez, M. E. Tolmasky, *Drug resistance updates reviews and commentaries in antimicrobial and anticancer chemotherapy* **2010**, *13*, 151.
- [41] K. Nishino, S. Yamasaki, R. Nakashima, M. Zwama, M. Hayashi-Nishino, *Frontiers in microbiology* **2021**, *12*, 737288.
- [42] L. McMurry, R. E. Petrucci, S. B. Levy, *Proceedings of the National Academy of Sciences of the United States of America* **1980**, *77*, 3974.
- [43] G. Muteeb, M. T. Rehman, B. Pani, R. H. Khan, *Frontiers in molecular biosciences* **2023**, *10*, 1342702.
- [44] V. Hemamalini, A. K. Tyagi, V. Vennila, S. Kumari, *Revolutionizing drug Discovery*With Cutting-Edge Technologies **2024**.
- [45] I. Doytchinova, Molecules (Basel, Switzerland) 2022, 27.
- [46] J. P. Hughes, S. Rees, S. B. Kalindjian, K. L. Philpott, *British journal of pharmacology* **2011**, *162*, 1239.
- [47] A. I. Visan, I. Negut, *Life (Basel, Switzerland)* **2024**, *14*.
- [48] N. Singh, P. Vayer, S. Tanwar, J.-L. Poyet, K. Tsaioun, B. O. Villoutreix, *Front. Drug Discov.* **2023**, 3.
- [49] B. Das, D. Mahajan, J. Rakonjac, Frontiers in microbiology 2023, 14, 1173906.
- [50] V. Kumar, N. Yasmeen, A. Pandey, A. Ahmad Chaudhary, A. S. Alawam, H. Ahmad Rudayni, A. Islam, S. S. Lakhawat, P. K. Sharma, M. Shahid, Frontiers in cellular and infection microbiology 2023, 13, 1293633.
- [51] R. Jijie, A. Barras, F. Teodorescu, R. Boukherroub, S. Szunerits, *Mol. Syst. Des. Eng.* **2017**, *2*, 349.
- [52] M. M. Mamun, A. J. Sorinolu, M. Munir, E. P. Vejerano, *Frontiers in chemistry* **2021**, 9, 687660.
- [53] M. A. Adefisoye, A. O. Olaniran, JAC-antimicrobial resistance 2023, 5, dlad127.
- [54] M. Thambirajoo, M. Maarof, Y. Lokanathan, H. Katas, N. F. Ghazalli, Y. Tabata, M. B. Fauzi, Antibiotics (Basel, Switzerland) 2021, 10.
- [55] S. K. Mondal, S. Chakraborty, S. Manna, S. M. Mandal, RSC Pharm. 2024, 1, 388.
- [56] D. C. Rees, E. Johnson, O. Lewinson, *Nature reviews. Molecular cell biology* **2009**, *10*, 218.

- [57] F. Leisico, L. M. Godinho, I. C. Gonçalves, S. P. Silva, B. Carneiro, M. J. Romão, T. Santos-Silva, I. de Sá-Nogueira, Scientific reports 2020, 10, 19564.
- [58] A. A. Akhtar, D. P. Turner, *Microbial pathogenesis* **2022**, *171*, 105734.
- [59] C. F. Higgins, Annual review of cell biology 1992, 8, 67.
- [60] C. C. Choi, R. C. Ford, *Biological reviews of the Cambridge Philosophical Society* **2021**, 96, 1318.
- [61] V. Kos, R. C. Ford, Cellular and molecular life sciences CMLS 2009, 66, 3111.
- [62] Y. Zeng, A. O. Charkowski, *Phytopathology* **2021**, *111*, 600.
- [63] A. L. Davidson, E. Dassa, C. Orelle, J. Chen, *Microbiology and molecular biology reviews MMBR* **2008**, *72*, 317-64, table of contents.
- [64] E. Schneider, S. Hunke, FEMS microbiology reviews 1998, 22, 1.
- [65] D. A. Rodionov, P. Hebbeln, A. Eudes, J. ter Beek, I. A. Rodionova, G. B. Erkens, D. J. Slotboom, M. S. Gelfand, A. L. Osterman, A. D. Hanson, T. Eitinger, *Journal of bacteriology* 2009, 191, 42.
- [66] L. J. Y. M. Swier, A. Guskov, D. J. Slotboom, *Nature communications* **2016**, *7*, 11072.
- [67] F. Finkenwirth, F. Kirsch, T. Eitinger, Journal of bacteriology 2013, 195, 4105.
- [68] J. A. Santos, S. Rempel, S. T. Mous, C. T. Pereira, J. ter Beek, J.-W. de Gier, A. Guskov, D. J. Slotboom, *eLife* **2018**, *7*.
- [69] A. Eudes, G. B. Erkens, D. J. Slotboom, D. A. Rodionov, V. Naponelli, A. D. Hanson, *Journal of bacteriology* **2008**, *190*, 7591.
- [70] J. Song, C. Ji, J. Z. H. Zhang, Scientific reports **2013**, *3*, 3566.
- [71] M. Zhang, Z. Bao, Q. Zhao, H. Guo, K. Xu, C. Wang, P. Zhang, *Proceedings of the National Academy of Sciences of the United States of America* **2014**, *111*, 18560.
- [72] G. B. Erkens, R. P.-A. Berntsson, F. Fulyani, M. Majsnerowska, A. Vujičić-Žagar, J. ter Beek, B. Poolman, D. J. Slotboom, *Nature structural & molecular biology* 2011, 18, 755.
- [73] Y. Yu, M. Zhou, F. Kirsch, C. Xu, L. Zhang, Y. Wang, Z. Jiang, N. Wang, J. Li, T. Eitinger, M. Yang, *Cell research* **2014**, *24*, 267.
- [74] Z. Bao, X. Qi, S. Hong, K. Xu, F. He, M. Zhang, J. Chen, D. Chao, W. Zhao, D. Li, J. Wang, P. Zhang, Cell research 2017, 27, 675.
- [75] G. B. Henderson, E. M. Zevely, *Journal of bacteriology* **1978**, *133*, 1190.

- [76] G. B. Henderson, E. M. Zevely, F. M. Huennekens, *Journal of Biological Chemistry* **1977**, *252*, 3760.
- [77] G. B. Henderson, E. M. Zevely, F. M. Huennekens, *Journal of bacteriology* **1979**, 139, 552.
- [78] G. B. Henderson, E. M. Zevely, F. M. Huennekens, *Journal of bacteriology* **1979**, *137*, 1308.
- [79] G. B. Henderson, E. M. Zevely, R. J. Kadner, F. M. Huennekens, *Journal of supramolecular structure* **1977**, 6, 239.
- [80] D. A. Rodionov, P. Hebbeln, M. S. Gelfand, T. Eitinger, *Journal of bacteriology* **2006**, *188*, 317.
- [81] P. Hebbeln, D. A. Rodionov, A. Alfandega, T. Eitinger, *Proceedings of the National Academy of Sciences of the United States of America* **2007**, *104*, 2909.
- [82] M. S. Gelfand, D. A. Rodionov, *Physics of Life Reviews* **2008**, 5, 22.
- [83] D. J. Slotboom, Nature reviews. Microbiology 2014, 12, 79.
- [84] K. Schauer, J. Stolz, S. Scherer, T. M. Fuchs, *Journal of bacteriology* **2009**, *191*, 2218.
- [85] J. I. Glass, N. Assad-Garcia, N. Alperovich, S. Yooseph, M. R. Lewis, M. Maruf, C. A. Hutchison, H. O. Smith, J. C. Venter, *Proceedings of the National Academy of Sciences of the United States of America* 2006, 103, 425.
- [86] J.-H. Song, K. S. Ko, Methods in molecular biology (Clifton, N.J.) 2008, 416, 401.
- [87] R. A. Forsyth, R. J. Haselbeck, K. L. Ohlsen, R. T. Yamamoto, H. Xu, J. D. Trawick, D. Wall, L. Wang, V. Brown-Driver, J. M. Froelich, K. G. C, P. King, M. McCarthy, C. Malone, B. Misiner, D. Robbins, Z. Tan, Z. Zhu Zy, G. Carr, D. A. Mosca, C. Zamudio, J. G. Foulkes, J. W. Zyskind, *Molecular microbiology* 2002, 43, 1387.
- [88] G. B. Erkens, M. Majsnerowska, J. ter Beek, D. J. Slotboom, *Biochemistry* **2012**, 51, 4390.
- [89] S. Bousis, I. Setyawati, E. Diamanti, D. J. Slotboom, A. K. H. Hirsch, *Advanced Therapeutics* **2019**, *2*.
- [90] N. K. Karpowich, D.-N. Wang, *Proceedings of the National Academy of Sciences of the United States of America* **2013**, *110*, 2534.

- [91] S. Rempel, W. K. Stanek, D. J. Slotboom, *Annual review of biochemistry* **2019**, *88*, 551.
- [92] J. ter Beek, A. Guskov, D. J. Slotboom, *The Journal of general physiology* **2014**, *143*, 419.
- [93] A. L. Davidson, E. Dassa, C. Orelle, J. Chen, *Microbiology and molecular biology reviews MMBR* **2008**, *72*, 317-64, table of contents.
- [94] O. Neubauer, C. Reiffler, L. Behrendt, T. Eitinger, PloS one 2011, 6, e29087.
- [95] L. Monjas, L. J. Y. M. Swier, I. Setyawati, D. J. Slotboom, A. K. H. Hirsch, *ChemMedChem* **2017**, *12*, 1693.
- [96] N. K. Karpowich, J. M. Song, N. Cocco, D.-N. Wang, *Nature structural & molecular biology* **2015**, *22*, 565.
- [97] D. A. Rodionov, P. Hebbeln, A. Eudes, J. ter Beek, I. A. Rodionova, G. B. Erkens, D. J. Slotboom, M. S. Gelfand, A. L. Osterman, A. D. Hanson, T. Eitinger, *Journal of bacteriology* 2009, 191, 42.
- [98] C. Thangaratnarajah, M. Nijland, L. Borges-Araújo, A. Jeucken, J. Rheinberger, S. J. Marrink, P. C. T. Souza, C. Paulino, D. J. Slotboom, *Nature communications* 2023, 14, 4484.
- [99] I. Setyawati, W. K. Stanek, M. Majsnerowska, L. J. Y. M. Swier, E. Pardon, J. Steyaert, A. Guskov, D. J. Slotboom, *eLife* **2020**, 9.
- [100] S. Bousis, S. Winkler, J. Haupenthal, F. Fulco, E. Diamanti, A. K. H. Hirsch, International journal of molecular sciences **2022**, 23.
- [101] A. Volkamer, D. Kuhn, F. Rippmann, M. Rarey, *Bioinformatics (Oxford, England)* **2012**, *28*, 2074.
- [102] E. Diamanti, I. Setyawati, S. Bousis, I. mojas, I. Swier, J. Haupenthal, P. Gibson, c. volz, w. stanek, m. Jaeger, j. herrmann, veening, r. müller, D. J. Slotboom, A. K. Hirsch 2020.
- [103] E. Diamanti, I. Setyawati, S. Bousis, P. C. T. Souza, I. mojas, I. Swier, J. Haupenthal, P. Gibson, c. volz, w. stanek, m. Jaeger, j. herrmann, S. Marrink, veening, r. müller, D. J. Slotboom, A. K. Hirsch **2021**.
- [104] E. Diamanti, P. C. T. Souza, I. Setyawati, S. Bousis, L. Monjas, L. J. Y. M. Swier,
 A. Shams, A. Tsarenko, W. K. Stanek, M. Jäger, S. J. Marrink, D. J. Slotboom, A. K.
 H. Hirsch, Communications biology 2023, 6, 1182.

- [105] A. F. Kiefer, S. Bousis, M. M. Hamed, E. Diamanti, J. Haupenthal, A. K. H. Hirsch, *Journal of medicinal chemistry* **2022**, 65, 8869.
- [106] R. Capela, R. Félix, M. Clariano, D. Nunes, M. d. J. Perry, F. Lopes, *International journal of molecular sciences* **2023**, *24*.
- [107] M. Pai, M. A. Behr, D. Dowdy, K. Dheda, M. Divangahi, C. C. Boehme, A. Ginsberg, S. Swaminathan, M. Spigelman, H. Getahun, D. Menzies, M. Raviglione, *Nature reviews*. *Disease primers* 2016, 2, 16076.
- [108] E. Cambau, M. Drancourt, Clinical microbiology and infection the official publication of the European Society of Clinical Microbiology and Infectious Diseases 2014, 20, 196.
- [109] I. Barberis, N. L. Bragazzi, L. Galluzzo, M. Martini, *Journal of preventive medicine and hygiene* **2017**, 58, E9-E12.
- [110] P. Warren, Canadian bulletin of medical history = Bulletin canadien d'histoire de la medecine **2006**, 23, 457.
- [111] S. H. Gillespie, Antimicrobial agents and chemotherapy 2002, 46, 267.
- [112] WHO Global tuberculosis report **2024**, https://www.who.int/teams/global-tuberculosis-programme/tb-reports.
- [113] S. Abbasnia, A. M. Hashem Asnaashari, H. Sharebiani, S. Soleimanpour, A. Mosavat, S. A. Rezaee, *Journal of clinical tuberculosis and other mycobacterial diseases* 2024, 36, 100458.
- [114] J. Yang, L. Zhang, W. Qiao, Y. Luo, *MedComm* **2023**, *4*, e353.
- [115] D. T. Hoagland, J. Liu, R. B. Lee, R. E. Lee, *Advanced drug delivery reviews* **2016**, *102*, 55.
- [116] K. C. Rahlwes, B. R. S. Dias, P. C. Campos, S. Alvarez-Arguedas, M. U. Shiloh, *Virulence* **2023**, *14*, 2150449.
- [117] K. Dheda, F. Mirzayev, D. M. Cirillo, Z. Udwadia, K. E. Dooley, K.-C. Chang, S. V. Omar, A. Reuter, T. Perumal, C. R. Horsburgh, M. Murray, C. Lange, *Nature reviews*. *Disease primers* 2024, 10, 22.
- [118] G. F. S. Fernandes, A. M. Thompson, D. Castagnolo, W. A. Denny, J. L. Dos Santos, *Journal of medicinal chemistry* **2022**, 65, 7489.

- [119] R. S. K. Sachan, V. Mistry, M. Dholaria, A. Rana, I. Devgon, I. Ali, J. Iqbal, S. M. Eldin, A. R. Mohammad Said Al-Tawaha, S. Bawazeer, J. Dutta, A. Karnwal, ACS omega 2023, 8, 32244.
- [120] A. Sharma, M. de Rosa, N. Singla, G. Singh, R. P. Barnwal, A. Pandey, *Journal of medicinal chemistry* **2021**, *64*, 4359.
- [121] H. Guo, G. M. Courbon, S. A. Bueler, J. Mai, J. Liu, J. L. Rubinstein, *Nature* 2021, 589, 143.
- [122] WHO, WHO targets elimination of TB in over 30 countries, https://www.who.int/news/item/03-07-2014-who-targets-elimination-of-tb-in-over-30-countries.
- [123] J.-M. Lehn, Chemical Society reviews 2007, 36, 151.
- [124] S. J. Rowan, S. J. Cantrill, G. R. L. Cousins, J. K. M. Sanders, J. F. Stoddart, Angew. Chem. Int. Ed. 2002, 41, 898.
- [125] P. T. Corbett, J. Leclaire, L. Vial, K. R. West, J.-L. Wietor, J. K. M. Sanders, S. Otto, *Chemical reviews* **2006**, *106*, 3652.
- [126] J.-M. Lehn, Aust. J. Chem. 2010, 63, 611.
- [127] J.-M. Lehn **2013**, *261*, 155.
- [128] Y. Zhang, M. Barboiu, *Chemical reviews* **2016**, *116*, 809.
- [129] J.-M. Lehn, *Progress in Polymer Science* **2005**, *30*, 814.
- [130] E. Kolomiets, J.-M. Lehn, *Chemical communications (Cambridge, England)* **2005**.
- [131] N. Roy, B. Bruchmann, J.-M. Lehn, Chemical Society reviews 2015, 44, 3786.
- [132] A. K. H. Hirsch, E. Buhler, J.-M. Lehn, *Journal of the American Chemical Society* **2012**, *134*, 4177.
- [133] Y. Liu, J.-M. Lehn, A. K. H. Hirsch, Accounts of chemical research 2017, 50, 376.
- [134] J.-M. Lehn, Topics in current chemistry **2012**, 322, 1.
- [135] J. F. Folmer-Andersen, E. Buhler, S.-J. Candau, S. Joulie, M. Schmutz, J.-M. Lehn, *Polymer International* **2010**, *59*, 1477.
- [136] Y. Zhang, Y. Qi, S. Ulrich, M. Barboiu, O. Ramström, *Materials chemistry frontiers* **2020**, *4*, 489.
- [137] J. Haggett, D. W. Domaille **2023**.

- [138] S. V. Wanasinghe, O. J. Dodo, D. Konkolewicz, *Angewandte Chemie* (International ed. in English) **2022**, 61, e202206938.
- [139] C. Godoy-Alcántar, A. K. Yatsimirsky, J.-M. Lehn, *J of Physical Organic Chem* **2005**, *18*, 979.
- [140] V. T. Bhat, A. M. Caniard, T. Luksch, R. Brenk, D. J. Campopiano, M. F. Greaney, Nature chemistry **2010**, *2*, 490.
- [141] A.-E. Dascalu, L. Halgreen, A. Torres-Huerta, H. Valkenier, *Chemical communications (Cambridge, England)* **2022**, 58, 11103.
- [142] D. K. Kölmel, E. T. Kool, Chemical reviews 2017, 117, 10358.
- [143] J. Collins, Z. Xiao, M. Müllner, L. A. Connal, *Polym. Chem.* **2016**, *7*, 3812.
- [144] Y. Jin, L. Song, Y. Su, L. Zhu, Y. Pang, F. Qiu, G. Tong, D. Yan, B. Zhu, X. Zhu, *Biomacromolecules* **2011**, *12*, 3460.
- [145] N. Sreenivasachary, D. T. Hickman, D. Sarazin, J.-M. Lehn, *Chemistry* (Weinheim an der Bergstrasse, Germany) **2006**, *12*, 8581.
- [146] R. E. Kleiner, Y. Brudno, M. E. Birnbaum, D. R. Liu, *Journal of the American Chemical Society* **2008**, *130*, 4646.
- [147] Y. Brudno, M. E. Birnbaum, R. E. Kleiner, D. R. Liu, *Nature chemical biology* **2010**, 6, 148.
- [148] Y. Ruff, J.-M. Lehn, *Biopolymers* **2008**, 89, 486.
- [149] Y. Ruff, E. Buhler, S.-J. Candau, E. Kesselman, Y. Talmon, J.-M. Lehn, *Journal of the American Chemical Society* **2010**, *132*, 2573.
- [150] Y. Liu, M. C. A. Stuart, E. Buhler, J.-M. Lehn, A. K. H. Hirsch, *Adv Funct Materials* **2016**, *26*, 6297.
- [151] Y. Liu, M. C. A. Stuart, E. Buhler, A. K. H. Hirsch, *Macromolecular rapid communications* **2018**, 39, e1800099.
- [152] S. Lee, C. Kaya, H. Jang, M. Koch, B. Loretz, E. Buhler, C.-M. Lehr, A. K. H. Hirsch, *Materials chemistry frontiers* **2020**, *4*, 905.
- [153] S. Lee, S. Nasr, S. Rasheed, Y. Liu, O. Hartwig, C. Kaya, A. Boese, M. Koch, j. herrmann, r. müller, B. Loretz, E. Buhler, A. K. H. Hirsch, C.-M. Lehr, *Journal of controlled release official journal of the Controlled Release Society* **2023**, *353*, 915.

- [154] Y. Liu, S. Ashmawy, L. Latta, A.-V. Weiss, A. F. Kiefer, S. Nasr, B. Loretz, A. K. H. Hirsch, S. Lee, C.-M. Lehr, *Biomacromolecules* **2023**, *24*, 3742.
- [155] Y. Liu, T. Hamm, T. R. Eichinger, W. Kamm, H. A. Wieland, B. Loretz, A. K. H. Hirsch, S. Lee, C.-M. Lehr, *International journal of nanomedicine* **2024**, *19*, 4429.
- [156] L. Zeroug-Metz, S. Lee, *Drug delivery and translational research* **2024**, *14*, 3599.
- [157] L. Zeroug-Metz, M. A. M. Kamal, J. Bassil, K. Elamaldeniya, B. H. Ryu, E. Buhler, S. Lee, *RSC Appl. Polym.* **2024**, *2*, 1124.
- [158] M. A. M. Kamal, J. Bassil, B. Loretz, A. K. H. Hirsch, S. Lee, C.-M. Lehr, European journal of pharmaceutics and biopharmaceutics official journal of Arbeitsgemeinschaft fur Pharmazeutische Verfahrenstechnik e.V 2024, 200, 114336.

2 Results & Discussion

2.1 Chapter A

Discovery of Picolinic Acid Derivatives as a New Class of Energy-Coupling Factor Transporter (ECF-T) Inhibitors

<u>Justine Bassil</u>^{1,2,3†}, Ioulia. A. Exapicheidou^{1,2,3†}, Katja Stefan⁴, Aleksei Tsarenko⁵, Ayanda I. Zulu^{1,3}, Andreas M. Kany^{1,3}, Jörg Haupenthal^{1,3}, Sven Marcel Stefan^{4,6}, Dirk J. Slotboom⁵, Mostafa M. Hamed^{1,3}, Anna K. H. Hirsch^{1,2,3*}

- ¹ Helmholtz Institute for Pharmaceutical Research Saarland (HIPS) Helmholtz Centre for Infection Research (HZI), Campus Building E 8.1, D-66123, Saarbrücken, Germany
- ² Saarland University, 66123 Saarbrücken, Germany
- ³ PharmaScienceHub (PSH), Campus Building A, D-66123 Saarbrücken, Germany
- ⁴ University of Lübeck and University Medical Center Schleswig-Holstein, Lübeck Institute of Experimental Dermatology, Medicinal Chemistry and Systems Polypharmacology, Ratzeburger Allee 160, 23538 Lübeck, Germany
- ⁵ Biomolecular Sciences and Biotechnology Institute University of Groningen Nijenborgh 4, 9747AG Groningen, The Netherlands.
- ⁶ Medical University of Lublin, Department of Biopharmacy, Chodzki 4a, 20-093 Lublin, Poland

[†]Both authors contributed equally

This manuscript will be submitted at European Journal of Medicinal Chemistry

Contribution to the presented work

Author's Contribution:

The author contributed to the conception and design of this study. She was responsible for the synthesis and characterization of the compounds, analyzing and interpreting the resulting data. She contributed to conceiving and writing the manuscript.

Contributions by others:

loulia. A. Exapicheidou contributed to the conception of this project, designed, synthesized and characterized the compounds. She also contributed to conceiving and writing of the manuscript. Aleksei Tsarenko executed the proteoliposome uptake assay of the frontrunners. Ayanda I. Zulu assisted in the synthesis of some compounds. Katja Stefan and Sven Marcel Stefan performed the inhibitory activity against the human ABC transporters. Andreas M. Kany coordinated and evaluated the ADMET profiling, which was performed by Jannine Seelbach and Tabea Wittmann. Jörg Haupenthal coordinated the whole-cell uptake assay, which was performed by Jeannine Jung. Mostafa M. Hamed and Anna K. H. Hirsch contributed to the conceptualization, conceiving, design, and supervision of the project and proofreading of the manuscript.

All authors contributed to writing, reviewing, and approving the final manuscript.

Abstract

This study presents picolinic acid derivatives as a novel class of energy-coupling factor transporters (ECF-T) inhibitors, thereby enriching the landscape of existing ECF-T inhibitors library. ECF-T are integral transmembrane proteins responsible for the uptake of various micronutrients mainly in Gram-positive species. Due to their critical role in bacterial growth as well as their absence in human cells, ECF-T are considered to be promising and selective antimicrobial target. Picolinic acid derivatives were identified through experimental screening of in-house and external compound libraries. A comprehensive structure–activity relationship (SAR) study yielded potent inhibitors. The most promising derivatives translated their ECF-T inhibition into strong antibacterial activity, and in addition, showed no cytotoxicity as well as high metabolic and plasma stability. These results pave the ground for combating infections by Gram-positive bacteria addressing novel bacterial drug targets with drug candidates.

Keywords: antimicrobial resistance, AMR, ECF-T; picolinic acid; inhibition; antibacterial activity

Introduction

Antimicrobial resistance (AMR) of virulent pathogens poses an ever-growing health threat worldwide, necessitating both the identification of novel drug targets and the development of new classes of antibiotics [1]. The World Health Organization (WHO) has classified resistant bacteria into priority lists, emphasizing the treatment of multidrug-resistant pathogens such as Streptococcus pneumoniae [2]. Grampositive bacteria can obtain essential vitamins for their survival and growth either through de novo biosynthesis or via a prokaryote-specific class of transmembrane proteins. These transmembrane proteins, referred to as energy-coupling factor transporters (ECF-T), belong to the superfamily of adenosine-triphosphate (ATP)-binding cassette (ABC) transporters [3]. ECF-T are responsible for the uptake of B-type vitamins such as folate, pantothenate, riboflavin, as well as metal ions into bacteria. Their predominance in Gram-positive species, coupled with their absence in humans, make them promising targets for antimicrobial drugs [4,5].

ECF-T consists of a substrate-specific binding protein (S-component) and an energy-coupling module (Ecf module). The latter is composed of a transmembrane protein (T-component, EcfT) and two cytosolic nucleotide binding proteins (EcfA and EcfA') [6]. This amongst ABC transporters unique architecture allows a single S-component to interact either with a 'dedicated' Ecf module (Group I ECF-T) [7], or various S-components with a 'common' Ecf module (Group II ECF-T; Figure 1) [8].

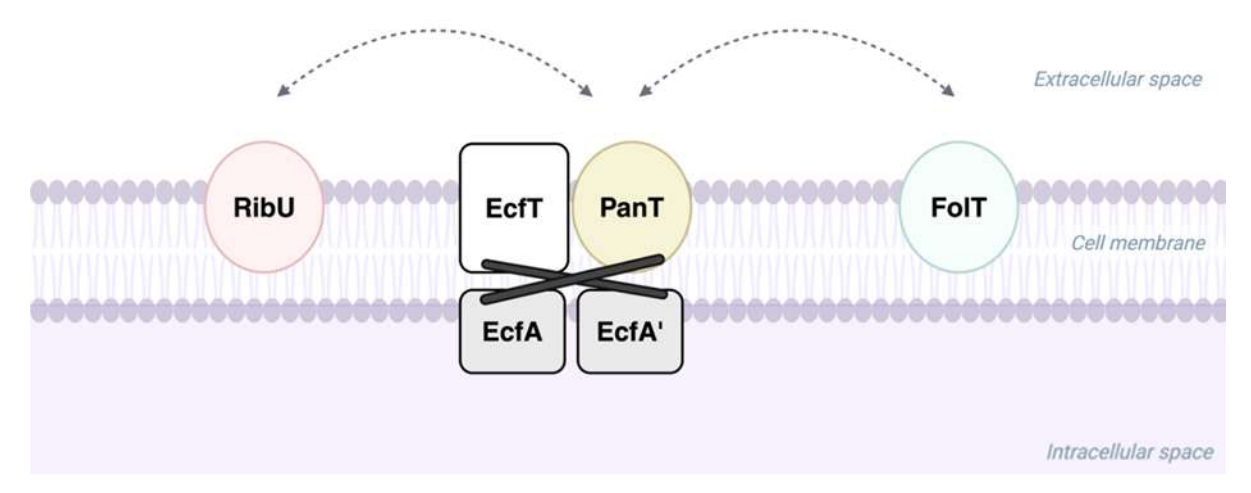


Figure 1. Group-II ECF-T architecture. A shared Ecf module interacts with exchangeable S-components for specific micronutrient substrates [e.g., pantothenic acid (PanT; yellow), folic acid (FolT; green), or riboflavin (RibU; red)] to form a functional ECF-T.

ECF-T employ a toppling mechanism, where the S-component tightly binds to the substrate pocket and subsequently undergoes a 90-degree rotation within the membrane. In this toppled state, the S-component binds to the Ecf module, leading to substrate release into the cytoplasm. ATP hydrolysis through the cytosolic EcfA and EcfA' subunits induces a conformational change in the Ecf module re-orientating the S-component to toward the extracellular space, initiating a new transport cycle [5,9]. Our research focuses on identifying new inhibitors that target group-II ECF-T and thus, inhibiting the uptake of multiple vitamins using one single inhibitor.

Several series of ECF-T inhibitors have been reported so far. The first ECF-T inhibitors were discovered through a structure-based virtual screening (SBVS) approach using the X-ray crystal structure of the folate-specific transporter ECF-FolT2 from Lactobacillus delbrueckii (L. delbrueckii) (PDB ID: 5JSZ). Unbiased coarse-grained molecular dynamics simulation with the hit compound provided its binding mode and mechanism of action which suggested a binding site at the interface between S-

component and Ecf module [10]. In-depth structure—activity relationship (SAR) study led to improved ECF-T inhibitors with enhanced antimicrobial activities [11]. Hit optimization for the two chemical classes derived from the SBVS campaign was achieved via target-directed dynamic combinatorial chemistry (tdDCC) addressing the pantothenate ECF-T (ECF-PanT) in S. pneumoniae [12]. In 2022, a SBVS approach merged with a newly derived whole-cell assay provided ureidotheiophenes as very potent inhibitors of ECF-FolT2 [13,14]. Finally, we reported very recently on a new target repurposing approach which provided various structurally diverse drugs and drug-like compounds as potent ECF-T inhibitors, with moxidectin as the most potent representative known so far [15].

Here, we report a promising new chemical class for ECF-T inhibition discovered through screening applying our functional whole-cell uptake assay. This class contains a picolinic acid (PA) moiety linked to a phenoxy phenyl group via an amide bond. PA is a pyridine derivative containing a carboxylic acid function at position 2 and is associated with immunological, neuroprotective, and antiproliferative properties [16,17], and furthermore, showed antimicrobial activity against Mycobacterium avium [18]. In this regard, PA represented an excellent starting point for further investigation and optimization. We performed an SAR study to enhance both ECF-T inhibitory activity and antibacterial activity, ultimately leading to the identification of novel antimicrobial agents to tackle the challenge of AMR.

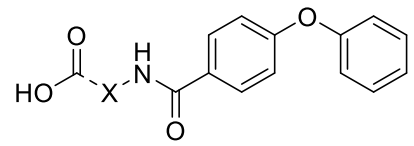
Results and discussion

Discovery of hit compound

This study aimed to identify novel ECF-T inhibitors using experimental screening of inhouse and external compound libraries. The initial screening provided compound 1 as a hit showing 18% inhibition at 50 μ M in our whole-cell uptake assay. Analogs from our in-house library bearing similar structural features provided compounds 2–5 containing a pyridine carboxylate scaffold in the Western part of the molecule (Table 1). All analogs differed only in the position of the aromatic nitrogen, where compound 5 (ortho to carboxylic acid, para to the amide linker) emerged as the most potent analog, achieving 100% and 91% inhibition at 50 μ M and 12.5 μ M, respectively. The

determined half-maximal inhibition concentration (IC $_{50}$) value of 5.2 μ M qualified it as one of the most potent ECF-T inhibitors identified so far [14,15]. Thus, compound **5** served as template for further optimization.

Table 1. Inhibitory activities of hit compounds **1–5** in the whole-cell uptake assay.



Compound	X	% uptake inhibition at 50 μM	IC ₅₀ ± SD (μM)
1		18 ± 3.1	n.d.
2	, N	< 10	n.d.
3) \ \ \ \ \ \ \ \ \ \ \ \ \ \ \ \ \ \ \	< 10	n.d.
4		< 10	n.d.
5	Z	100 ± 0.9	5.2 ± 0.8

S.D.: Standard deviation derived from two independent experiments, n.d.: Not determined

Chemistry

The synthesis of compounds **5–24**, featuring variations in the Western part, Eastern part, and middle ring of the molecule was achieved through a two-step synthetic approach (Scheme 1). The first step involved an amide coupling reaction between the commercially available carboxylic acids (**5b**, **9b–24b**) and either methyl 4-aminopicolinate (**5c**) or amino derivatives (**6c–8c**), using propane phosphonic acid anhydride (T_3P) as the coupling reagent. If applicable, resulting esters were hydrolyzed in the second step to yield the final derivatives (**9–24**).

Scheme 1. Synthesis of compound **5** derivatives that vary in the Western part (**5a**, **6–8**), the Eastern part (**9–22**) and the middle ring (**23–24**). Reagent and conditions: (i) EtOAc, pyridine, T₃P, 40 °C, 12 h; (ii) ester, THF, LiOH, rt, 15 min.

In addition, a synthetic route was developed to substitute the amide bond of compound 5 with bioisosteric functional groups as shown in Scheme 2. The reversed amide 25 was synthesized through a two-step approach as described earlier. This involved an amide coupling reaction between commercially available 2-(methoxycarbonyl) isonicotinic acid (25c) and 4-phenoxyaniline (25b), followed by treatment with lithium hydroxide (LiOH) to give the desired derivative 25. The reaction between 1-(bromomethyl)-4-phenoxybenzene (26b) and 5c in the presence of a base resulted in methylamine derivative 26. Methyl 4-bromopicolinate (27c) exposed to 25b using Xantphos reagent and cesium carbonate (CsCO₃) directly afforded derivative 27 after purification by preparative HPLC. By combining 5c with phenoxybenzene isocyanate (28b) in DMF at room temperature and subsequent

treatment with LiOH the urea derivative **28** was obtained. On the other and, combining **5c** with 4-phenoxybenzenesulfonyl chloride (**29b**) in the presence of K₂CO₃ and subsequent hydrolysis (LiOH) resulted in the sulfonamide derivative **29**. To access the triazole moiety, compound **27c** was first reacted with sodium azide (NaN₃) in DMF at 80 °C, yielding the azide intermediate **30c**. This intermediate was then subjected to a click reaction with the commercially available alkyne 1-ethynyl-4-phenoxybenzene, forming triazole **30a** with an ester group, which after hydrolysis, gave the desired triazole **30**. Conversely, compound **27c** could undergo a Sonogashira reaction followed by desilylation with tetrabutylammoniumfluorid (TBAF) to provide the corresponding alkyne **31c**. On the other hand, azidation of **25b** under Sandmeyer conditions with TMSN₃ provided the azide intermediate **31b**. The combination of compounds **31b** and **31c** yielded in the desired reversed triazole **31** after hydrolysis *via* LiOH.

Scheme 2. Synthesis of amide linker derivatives **25–31.** Reagents and conditions: (i) EtOAc, pyridine, T_3P , 40 °C, 12 h (**25**); (ii) K_2CO_3 , THF, rt, 16 h (**26**); (iii) Xantphos, palladium (II) acetate, Cs_2CO_3 , butanol, 95 °C, 16 h (**27**); (iv) **5c**, DMF, rt, 1 h (**28**); (v) **5c**, K_2CO_3 , ACN, 80 °C, 16 h (**29**); (vi) azide derivative, corresponding alkyne, THF/H₂O (2:1) (**30**) or MeOH (**31**), sodium ascorbate, $CuSO_4 \cdot 5H_2O$, 2 d, 65 °C (**30**) or 12 h, rt (**31**); (vii) ester, THF, LiOH, rt 15 min (**25**, **28**, **29**) or 16 h (**31**); (viii) ester, MeOH, NaOH, 65 °C (**30**).

Structure-activity relationship study

Compound **5** represented the template molecule for a comprehensive SAR study to further optimize and develop ECF-T inhibitors, which included four primary modification areas: (i) the Western part; (ii) the Eastern part; (iii) the middle ring; and (iv) the amide linker (Figure 2). Initially, all synthesized compounds were assessed in

our whole-cell uptake assay for their inhibition of the radiolabeled folic acid uptake into Lactobacillus casei at 12.5 μ M. Compounds with more than 80% inhibition were evaluated in-depth for their IC50 values.

Figure 2. Chemical structure of hit compound **5**. The scaffold was divided into four subunits: (i) Western part; (ii) Eastern part; (iii) middle ring; and (iv) amide linker.

We first investigated the importance of the carboxylic acid group in the Western part of the molecule using a small set of compounds (compounds **5a**, **6–8**; Scheme 1). Removal of the carboxylic acid group (**6**), its methyl esterification (**5a**), and its replacement by methyl (**7**) or trifluoromethyl (**8**) led to a significant loss of the inhibitory activity (Table 2). These results underscore the critical role of the carboxylic acid group with respect to ECT-T inhibition, and thus, was left unchanged in the following SAR.

Table 2. Inhibitory activities of compounds with Western part modifications (**5a** and **6-8**) in the wholecell uptake assay.

Compound	R	% uptake inhibition at 12.5 µM	
		at 12.5 μ14	
5a	COOCH₃	13.6 ± 2.9	
6	Н	< 10	
7	CH₃	13.0 ± 1.7	
8	CF₃	< 10	

S.D.: Standard deviation derived from two independent experiments, n.d.: Not determined

A series of modifications at the Eastern part and the middle ring of the molecule included three key changes: at the terminal phenyl ring (9–14, 19–22); the ether linker (15–18); and the middle ring (23–24) (Scheme 1, Table 3).

Diverse electron-withdrawing (EWG) and electron-donating groups (EDG) at *para* position of the Eastern part provided varying effects on the potency against ECF-T. The trifluoromethoxy (OCF₃) group (14) was the most potent, showing comparable activity to the non-substituted hit 5 (IC₅₀: $4.8 \,\mu\text{M}$), followed by OCH₃ (9) > CF₃ (13) > F (11). In contrast, cyano (10) and chloro (12) derivatives led to decreased activities. Replacing the ether linker at the Eastern part by different functional groups led to a reduction [methylene (15) and oxymethylene (16) derivatives] or (almost) complete loss [carbonyl (17), and amino (18) derivatives] of biological activities at the tested concentrations, which also resulted after complete removal of the terminal phenoxy group (19). Interestingly, the position of the phenoxy group affected the biological activity: While the *ortho* position (20) resulted in decreased potency, the *meta* position (21) retained almost similar activity as the *para* position (5). Introduction of a pyridine at the eastern part (22) abolished biological activity. Finally, we replaced the middle ring by heterocycles: The furan derivative 23 reduced the biological activity almost by half, while the pyridine derivative 24, led to an entire loss of activity.

Table 3. Inhibitory activities of compounds with modifications in the Eastern part and the middle ring (9–24) in the whole-cell uptake assay.

$$\begin{array}{c|c} O & H \\ \hline \\ HO & N \end{array} \begin{array}{c} R \\ \hline \\ O \end{array}$$

Compound	R	% uptake inhibition at 12.5 μM	IC ₅₀ (μΜ)
9	OCH ₃	80.8 ± 5.6	6.7 ± 1.1
10	CN	21.3 ± 9.8	n.d.

11) O	81.6 ± 7.7	8.2 ± 0.7
12	O	48.0 ± 7.8	n.d.
13	O CF ₃	85.6 ± 0.6	7.7 ± 0.3
14	OCF ₃	97.6 ± 1.4	4.8 ± 0.2
15		49.3 ± 5.8	n.d.
16		68.0 ± 2.8	n.d.
17		16.6 ± 13.4	n.d.
18	T T T T T T T T T T T T T T T T T T T	<10	n.d.
19		<10	n.d.
20		28.3 ± 4.8	n.d.
21		85.8 ± 1.6	6.1 ± 0.3
22		<10	n.d.
23	0	56 ± 6.3	n.d.
24	viction derived from two independen	<10	n.d.

S.D.: Standard deviation derived from two independent experiments, n.d.: Not determined

The final set of modifications aimed to design bioisosteric replacements to replicate the properties of the amide bond. However, the synthesized bioisosteres [e.g., reversed amide (25), methylamine (26), secondary amine (27), urea (28) and sulfonamide (29)] failed to enhance inhibitory activity. Nevertheless, introducing a triazole moiety (30) significantly increased activity by two-fold against ECF-T (IC $_{50}$: 2.1 μ M), revealing it to be one of the most potent ECF-T reported until today [14,15]. These results support the idea that a 1,4-substituted 1,2,3-triazole moiety is proficient in mimicking the configuration and activity of an amide bond [19]. Finally, reversing the triazole moiety (31) did not show an improvement in activity, suggesting that the specific orientation and electronic properties of the triazole are critical for maintaining the desired potency.

Table 4. Inhibitory activities of compounds with modifications at the amide linker (**25–31**) in the whole-cell uptake assay.

Compound	R	% uptake inhibition	IC ₅₀ ± S.D
Compound		at 12.5 µM	(µM)
25	O ZT	30.8 ± 1	n.d.
26	H	<10	n.d.
27	N H	<10	n.d.
28	O N H	<10	n.d.
29	O N H	<10	n.d.
30	, N = N	98.0 ± 1.2	2.1 ± 0.5
31	\N \ N	86.0 ± 5.4	6.0 ± 4.7

S.D.: Standard deviation derived from two independent experiments, n.d.: Not determined

Proteoliposome uptake assay

As a next step, the initial hit compound $\mathbf{5}$, and the triazole derivative $\mathbf{30}$ were selected for evaluation in a proteoliposome uptake assay employing L. delbrueckii ECF-FolT2 and radiolabeled folic acid [20] (Figure 3). Both compounds showed IC₅₀ values in the low micromolar range comparable to those determined in the whole-cell uptake assay (Table 5).

Compound	Structure	ECF-FolT2 IC ₅₀ (µM)
5	HO NO	12.3
30	HO N N N N N N N N N N N N N N N N N N N	6.9

Table 5. Inhibitory activities of 5 and 30 in a proteoliposome uptake assay using ECF-FolT2.

S. D.: Standard deviation derived from two independent experiments, n.d.: Not determined

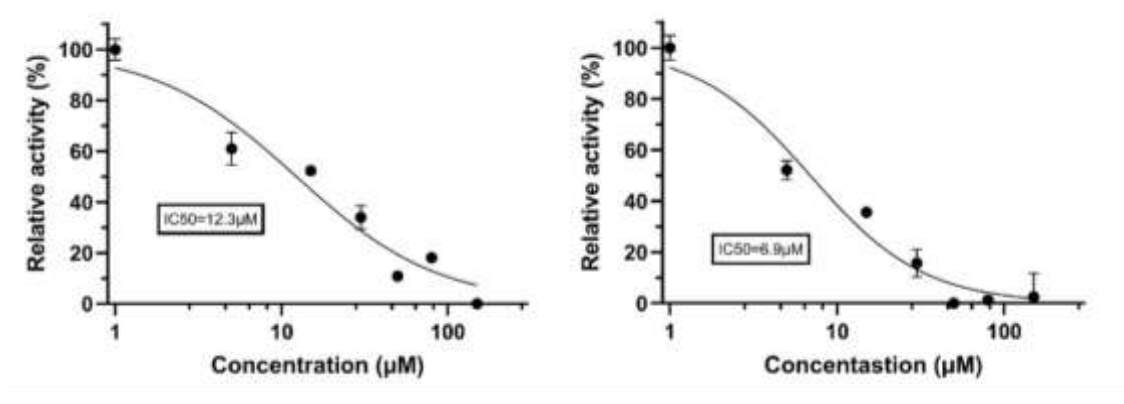


Figure 3. Concentration-effect curves of compounds 5 (left) and 30 (right) in the proteoliposome uptake assay.

Antibacterial profile

The most potent inhibitors identified through our SAR study were assessed against a panel of Gram-positive pathogens for their antimicrobial profile (Table 6). Compound $\bf 5$ exhibited low micromolar activities against S. pneumoniae strains, while it displayed no effects against Enterococcus species. In a similar manner, analog $\bf 14$ was inactive against the Enterococcus species, but demonstrated a slightly stronger antimicrobial effect against penicillin-resistant and wild-type S. pneumoniae [minimum inhibitory concentration (MIC) values: $2~\mu M$ and $16~\mu M$, respectively]. Surprisingly, compound $\bf 30$ showed minor activity against S. pneumoniae strains; one

strain exhibited a complete loss of activity, while the other penicillin-resistant strain showed an MIC of 16 μ M.

Table 6. Determination of minimum inhibitory concentration (MIC) values of compounds **5**, **14** and **30** against a panel of Gram-positive bacteria.

MIC (μM)	Compound		
	5	14	30
PR- Streptococcus pneumoniae DSM-11865 ^[a]	4	2	16
Streptococcus pneumoniae DSM-20566	32	16	>128
Enterococcus faecalis DSM-20478	>128	>128	>128
Enterococcus faecalis DSM-20477	>128	>128	>128

[[]a] PRSP: Penicillin-resistant Streptococcus pneumoniae.

In vitro ADMET profiling

The selected frontrunners **5**, **14**, and **30** were further evaluated for their *in vitro* ADMET profile. All compounds were found to be stable (>2 h) in both murine and human liver microsomes and no instability in plasma was observed over 4 h. Furthermore, low cytotoxicity was determined for **14** with 50% cytotoxic concentration (CC_{50}) around 100 μ M, while **5** and **30** did not impair HepG2 viability at 100 μ M, which is a concentration far above the determined IC_{50} and MIC_{50} values. Additionally, **14** and **30** showed reduced solubility compared to compound **5**. Hence, in view of the similar antibacterial and on-target activity of the three compounds tested, **5** seems to be more favorable for further development.

Table 2. In vitro ADMET profile for derivatives 5, 14, and 30.

Properties	species	Compound		
		5	14	30
logD _{7.4}		2.01	3.41	1.51
Kinetic Solubility 5% DMSO/PBS [μΜ]		130 ± 25	22.4 ± 0.5	20 ± 8
Kinetic Solubility 1% DMSO/PBS [µM]		25 ± 3	8 ± 4	3.9 ± 1.5

Cytotoxicity HepG2, viability @100 µM [%]		92 ± 18	41 ± 15 102 ± 26 (CC ₅₀ ^a)	110 ± 3
Liver Microsomes	mouse	>120 / <11.6	>120 / <11.6	>120 / <11.6
t _{1/2} ^b [min] / Cl _{int} ^c [µL/min/mg]	human	>120 / <11.6	>120 / <11.6	>120 / <11.6
Diagna + b[min]	mouse	>240	>240	>240
Plasma, t _{1/2} ^b [min]	human	>240	>240	>240

^aConcentration at which cell viability is reduced by 50% [μM]. ^b Half-life. ^cIntrinsic clearance. Means ± S.D.: Standard deviation derived from at least two independent experiments.

ABC transporter selectivity

Another important factor in ADMET profiling is the potential interaction of the drug candidates with human ABC transporters at biological barriers, which would significantly influence their pharmacokinetics and could also lead to undesired off-target effects. Thus, lead compounds **5** and **30** as the most potent ECF-T inhibitors were assessed against the most prominent ABC transporters ABCB1 [P-glycoprotein (P-gp)], ABCC1 [multidrug resistance-associated protein 1 (MRP1)], and ABCG2 [breast cancer resistance protein (BCRP)]. Both compounds showed no biological activity against any of the transporters assessed, and thus ABC transporter-related pharmacokinetic constraints and/or toxicity could not be expected from compounds **5** and **30**.

Conclusions

In summary, we have identified picolinic acid analog as a new class of ECF-T inhibitors through experimental screening using in-house and external compound libraries. In terms of structure-guided optimization, we have conducted a comprehensive SAR study to get valuable insights into the chemical features required for optimal inhibitory potency of this chemical class. In addition, we successfully proved the selectivity of our series towards ECF-T over the human ABC transporters ABCB1, ABCC1, and ABCG2. ADMET profiling of the frontrunner compounds highlighted high metabolic and plasma stability of this series without any critical cytotoxic effects. The compounds also exhibited potent antibacterial activity against

S. pneumoniae with even stronger effect on the penicillin-resistant strain. Further investigation and optimization of this class is needed to refine and enhance solubility and antibacterial activity.

Author Information

Justine Bassil - Helmholtz Institute for Pharmaceutical Research Saarland (HIPS) – Helmholtz Centre for Infection Research (HZI), Campus Building E 8.1, D-66123, Saarbrücken, Germany; Saarland University, Saarbrücken, Germany.

Ioulia Exapicheidou - Helmholtz Institute for Pharmaceutical Research Saarland (HIPS) - Helmholtz Centre for Infection Research (HZI), Campus Building E 8.1, D-66123, Saarbrücken, Germany; Saarland University, Saarbrücken, Germany.

Katja Stefan - University of Lübeck and University Medical Center Schleswig-Holstein, Lübeck Institute of Experimental Dermatology, Medicinal Chemistry and Systems Polypharmacology, Ratzeburger Allee 160, 23538 Lübeck, Germany.

Ayanda I. Zulu - Helmholtz Institute for Pharmaceutical Research Saarland (HIPS) – Helmholtz Centre for Infection Research (HZI), Campus Building E 8.1, D-66123, Saarbrücken, Germany; Saarland University, PharmaScienceHub (PSH), Saarbrücken, Germany.

Aleksei Tsarenko - Biomolecular Sciences and Biotechnology Institute University of Groningen Nijenborgh 4, 9747AG Groningen, The Netherlands.

Andreas M. Kany - Helmholtz Institute for Pharmaceutical Research Saarland (HIPS) – Helmholtz Centre for Infection Research (HZI), Campus Building E 8.1, D-66123,

Saarbrücken, Germany; PharmaScienceHub (PSH), Saarbrücken, Germany.

Jörg Haupenthal - Helmholtz Institute for Pharmaceutical Research Saarland (HIPS)

– Helmholtz Centre for Infection Research (HZI), Campus Building E 8.1, D-66123, Saarbrücken, Germany; PharmaScienceHub (PSH), Saarbrücken, Germany.

Sven Marcel Stefan - University of Lübeck and University Medical Center Schleswig-Holstein, Lübeck Institute of Experimental Dermatology, Medicinal Chemistry and Systems Polypharmacology, Ratzeburger Allee 160, 23538 Lübeck, Germany; Medical University of Lublin, Department of Biopharmacy, Chodzki 4a, 20-093 Lublin, Poland.

Dirk J. Slotboom - Biomolecular Sciences and Biotechnology Institute University of Groningen Nijenborgh 4, 9747AG Groningen, The Netherlands.

Mostafa M. Hamed - Helmholtz Institute for Pharmaceutical Research Saarland (HIPS) - Helmholtz Centre for Infection Research (HZI), Campus Building E 8.1, D-66123, Saarbrücken, Germany; PharmaScienceHub (PSH), Saarbrücken, Germany.

Corresponding Author

Anna K. H. Hirsch Helmholtz Institute for Pharmaceutical Research Saarland (HIPS) – Helmholtz Centre for Infection Research (HZI), Campus Building E 8.1, D-66123, Saarbrücken, Germany; Saarland University; PharmaScienceHub (PSH), Saarbrücken, Germany, e-mail: anna.hirsch@helmholtz-hips.de

Author Contributions

The manuscript was written through contributions of all authors. All authors have given approval to the final version of the manuscript. †These authors contributed equally.

Justine Bassil† and Ioulia Exapicheidou†: Writing – review & editing, Writing – original draft, Visualization, Validation, Investigation, Methodology, Formal analysis, Data curation, Conceptualization. Katja Stefan: Investigation, Writing – review and editing, Visualization, Funding acquisition. Aleksei Tsarenko: Writing – review & editing, Validation, Investigation. Ayanda I. Zulu: Review & editing, Methodology, Investigation. Andreas M. Kany: Writing – review & editing, Methodology. Jörg Haupenthal: Review & editing, Methodology. Sven Marcel Stefan: Formal analysis, Resources, Writing, Review and editing, Visualization, Supervision, Funding acquisition. Dirk J. Slotboom: Writing – review & editing, Supervision. Mostafa M. Hamed: Writing – review & editing, Supervision, Project administration, Conceptualization. Anna K.H. Hirsch: Writing – review & editing, Supervision, Project administration, Funding acquisition, Conceptualization.

Funding Sources

Any funds used to support the research of the manuscript should be placed here (per journal style). Work by I. A. E. was supported by the GradUS program and from Saarland University. K.S. received a Walter Benjamin Return Grant from the German

Research Foundation (DFG, Germany; #537276156). S.M.S. is supported by the Research Grant Programme of the DFG [#504079349 (PANABC)]. A. K. H. H. gratefully acknowledges funding from the European Research Council (ERC Starting grant 757913) and from the Helmholtz Association's Initiative and Networking Fund.

Acknowledgments

The authors would like to thank Jeannine Jung, Jannine Seelbach and Tabea Wittmann for excellent technical support in the performance of the cell-based folate uptake assay and ADMET assays. Katja Stefan was supported by the German Research Foundation (DFG, Germany; #537276156). Sven Marcel Stefan appreciates support by the DFG (Germany; #504079349, PANABC).

References

- [1] A.H. Fairlamb, N.A.R. Gow, K.R. Matthews, A.P. Waters, Drug resistance in eukaryotic microorganisms, Nat. Microbiol. 1 (2016) 16092. https://doi.org/10.1038/nmicrobiol.2016.92.
- [2] WHO, WHO bacterial priority pathogens list, 2024.
- [3] S. Rempel, W.K. Stanek, D.J. Slotboom, ECF-Type ATP-Binding Cassette Transporters, Annu. Rev. Biochem. 88 (2019) 551–576. https://doi.org/10.1146/annurev-biochem-013118-111705.
- [4] G.B. Erkens, M. Majsnerowska, J. ter Beek, D.J. Slotboom, Energy coupling factor-type ABC transporters for vitamin uptake in prokaryotes, Biochemistry 51 (2012) 4390–4396. https://doi.org/10.1021/bi300504v.
- [5] D.J. Slotboom, Structural and mechanistic insights into prokaryotic energy-coupling factor transporters, Nat. Rev. Microbiol. 12 (2014) 79–87. https://doi.org/10.1038/nrmicro3175.
- [6] D.A. Rodionov, P. Hebbeln, A. Eudes, J. ter Beek, I.A. Rodionova, G.B. Erkens, D.J. Slotboom, M.S. Gelfand, A.L. Osterman, A.D. Hanson, T. Eitinger, A novel class of modular transporters for vitamins in prokaryotes, J. Bacteriol. 191 (2009) 42–51. https://doi.org/10.1128/JB.01208-08.
- [7] D.A. Rodionov, P. Hebbeln, M.S. Gelfand, T. Eitinger, Comparative and functional genomic analysis of prokaryotic nickel and cobalt uptake transporters:

- evidence for a novel group of ATP-binding cassette transporters, J. Bacteriol. 188 (2006) 317–327. https://doi.org/10.1128/JB.188.1.317-327.2006.
- [8] A. Eudes, G.B. Erkens, D.J. Slotboom, D.A. Rodionov, V. Naponelli, A.D. Hanson, Identification of genes encoding the folate- and thiamine-binding membrane proteins in Firmicutes, J. Bacteriol. 190 (2008) 7591–7594. https://doi.org/10.1128/JB.01070-08.
- [9] T. Wang, G. Fu, X. Pan, J. Wu, X. Gong, J. Wang, Y. Shi, Structure of a bacterial energy-coupling factor transporter, Nature 497 (2013) 272–276. https://doi.org/10.1038/nature12045.
- [10] E. Diamanti, P.C.T. Souza, I. Setyawati, S. Bousis, L. Monjas, L.J.Y.M. Swier, A. Shams, A. Tsarenko, W.K. Stanek, M. Jäger, S.J. Marrink, D.J. Slotboom, A.K.H. Hirsch, Identification of inhibitors targeting the energy-coupling factor (ECF) transporters, Commun. Biol. 6 (2023) 1182. https://doi.org/10.1038/s42003-023-05555-x.
- [11] E. Diamanti, I. Setyawati, S. Bousis, P.C.T. Souza, I. mojas, I. Swier, J. Haupenthal, P. Gibson, c. volz, w. stanek, m. Jaeger, j. herrmann, S. Marrink, veening, r. müller, D.J. Slotboom, A.K. Hirsch, Targeting the energy-coupling factor (ECF) transporters: identification of new tool compounds (2021). https://doi.org/10.26434/chemrxiv-2021-xq08b-v2.
- [12] I.A. Exapicheidou, A. Shams, H. Ibrahim, A. Tsarenko, M. Backenköhler, M.M. Hamed, E. Diamanti, A. Volkamer, D.J. Slotboom, A.K.H. Hirsch, Hit optimization by dynamic combinatorial chemistry on Streptococcus pneumoniae energy-coupling factor transporter ECF-PanT, Chem. Commun. (Camb) 60 (2024) 870–873. https://doi.org/10.1039/D3CC04738E.
- [13] S. Bousis, S. Winkler, J. Haupenthal, F. Fulco, E. Diamanti, A.K.H. Hirsch, An Efficient Way to Screen Inhibitors of Energy-Coupling Factor (ECF) Transporters in a Bacterial Uptake Assay, Int. J. Mol. Sci. 23 (2022). https://doi.org/10.3390/ijms23052637.
- [14] A.F. Kiefer, S. Bousis, M.M. Hamed, E. Diamanti, J. Haupenthal, A.K.H. Hirsch, Structure-Guided Optimization of Small-Molecule Folate Uptake Inhibitors Targeting the Energy-Coupling Factor Transporters, J. Med. Chem. 65 (2022) 8869–8880. https://doi.org/10.1021/acs.jmedchem.1c02114.

- [15] J. Haupenthal, M. Rafehi, A.M. Kany, A. Lespine, K. Stefan, A.K.H. Hirsch, S.M. Stefan, Target repurposing unravels avermectins and derivatives as novel antibiotics inhibiting energy-coupling factor transporters (ECFTs), Arch. Pharm. (Weinheim) 357 (2024) e2400267. https://doi.org/10.1002/ardp.202400267.
- [16] A.A.-B. Badawy, Kynurenine Pathway of Tryptophan Metabolism: Regulatory and Functional Aspects, Int. J. Tryptophan Res. 10 (2017) 1178646917691938. https://doi.org/10.1177/1178646917691938.
- [17] S. Bousis, I. Setyawati, E. Diamanti, D.J. Slotboom, A.K.H. Hirsch, 2019. Energy-Coupling Factor Transporters as Novel Antimicrobial Targets. Advanced Therapeutics 2, 1800066. https://doi.org/10.1002/adtp.201800066.
- [18] T. Shimizu, H. Tomioka, Activity of picolinic acid in combination with the antiprotozoal drug quinacrine against Mycobacterium avium complex, Antimicrob. Agents Chemother. 50 (2006) 3186–3188. https://doi.org/10.1128/AAC.01510-05.
- [19] S. Kumari, A.V. Carmona, A.K. Tiwari, P.C. Trippier, Amide Bond Bioisosteres: Strategies, Synthesis, and Successes, J. Med. Chem. 63 (2020) 12290–12358. https://doi.org/10.1021/acs.jmedchem.0c00530.
- [20] I. Setyawati, W.K. Stanek, M. Majsnerowska, L.J.Y.M. Swier, E. Pardon, J. Steyaert, A. Guskov, D.J. Slotboom, In vitro reconstitution of dynamically interacting integral membrane subunits of energy-coupling factor transporters, Elife 9 (2020). https://doi.org/10.7554/eLife.64389.

2.1.1 Supplementary information

Discovery of picolinic acid derivatives as a new class of energy-coupling factor transporters (ECF-T) inhibitors

Justine Bassil^{1,2,3†}, Ioulia. A. Exapicheidou^{1,2,3†}, Katja Stefan⁴, Aleksei Tsarenko⁵, Ayanda I. Zulu^{1,3}, Andreas M. Kany^{1,3}, Jörg Haupenthal^{1,3}, Sven Marcel Stefan^{4,6}, Dirk J. Slotboom⁵, Mostafa M. Hamed^{1,3}, Anna K. H. Hirsch^{1,2,3*}

¹Helmholtz Institute for Pharmaceutical Research Saarland (HIPS) – Helmholtz Centre for Infection Research (HZI), Campus Building E 8.1, D-66123, Saarbrücken, Germany

² Saarland University, 66123 Saarbrücken, Germany

³ PharmaScienceHub (PSH), campus building A, D-66123 Saarbrücken, Germany

⁴University of Lübeck and University Medical Center Schleswig-Holstein, Lübeck

Institute of Experimental Dermatology, Medicinal Chemistry and Systems

Polypharmacology, Ratzeburger Allee 160, 23538 Lübeck, Germany

⁵Biomolecular Sciences and Biotechnology Institute University of Groningen Nijenborgh 4, 9747AG Groningen, The Netherlands.

⁶Medical University of Lublin, Department of Biopharmacy, Chodzki 4a, 20-093 Lublin, Poland

[†] Both authors contributed equally

Chemicals, materials and methods

NMR experiments were run on a Bruker Avance Neo 500 MHz spectrometer. Spectra were acquired at 300 K, using deuterated solvents. Chemical shifts for ¹H and ¹³C spectra were recorded in parts per million (ppm) using the residual non-deuterated solvent as the internal standard. Coupling constants (*J*) are given in Hertz (Hz). Data are reported as follows: chemical shift, multiplicity (s = singlet, d =doublet, t = triplet, m = multiplet, br = broad and combinations of these) coupling constants and integration. Flash chromatography was performed using the automated flash chromatography system CombiFlash Rf+ (Teledyne Isco, Lincoln, NE, USA) equipped with RediSepRf silica columns (Axel Semrau, Sprockhövel Germany). TLC was performed with aluminum-backed silica TLC plates (Macherey-Nagel MN ALUGRAM Sheets SIL G/UV 254 20 x 20cm 818133) with a suitable solvent system and was visualized using UV fluorescence (254 & 366 nm). All reactions were carried out in oven-dried glassware under an atmosphere of argon. Anhydrous DMF was purchased from Aldrich and used directly.

Liquid chromatography-mass spectrometry was performed on a LC-MS system, consisting of a Dionex UltiMate 3000 pump, autosampler, column compartment and MWD or DAD detector (Thermo Fisher Scientific, Dreieich, Germany) and ESI quadrupole MS (MSQ Plus or ISQ EC, Thermo Fisher Scientific, Dreieich, Germany). Columns used: 1) Hypersil Gold column, 100 x 2.1 mm, 3 µm. At a flow rate of 700 μL/min, the gradient of H₂O (0.1% FA) and ACN (0.1% FA) starting from 5% ACN and then increased to 100% over 7 min. 2) Hypersil Gold column, 100 x 1.9 mm, 2.1 μm. At a flow rate of 600 μL/min, the gradient of H₂O (0.1% FA) and ACN (0.1% FA) starting from 5% ACN and then increased to 100% over 5.5 min. The mass spectrum was measured in positive and negative mode in a range from 100-600 m/z. The UV spectrum was recorded at 254 nm. High-resolution mass spectra (HR-MS) were recorded with a ThermoScientific system where a Dionex Ultimate 3000 RSLC was coupled to a Q Exactive Focus mass spectrometer with an electrospray ion (ESI) source. An Acquity UPLC® BEH C8, 150 x 2.1 mm, 1.7 µm column equipped with a VanGuard Pre-Column BEH C8, 5 x 2.1 mm, 1.7 µm (Waters, Germany) was used for separation. At a flow rate of 250 μ L/min, the gradient of (A) H₂O + 0.1% FA and (B) ACN + 0.1% FA was held at 10% B for 1 min and then increased to 95% B over 4 min. It was held there for 1.2 min before the gradient was decreased to 10% B over 0.3 min where it was held for 1 min. The mass spectrum was measured in positive mode in a range from 120–1000 m/z. UV spectrum was recorded at 254 nm.

Preparative RP-HPLC was performed using an UltiMate 3000 Semi-Preparative System (Thermo Fisher Scientific) with nucleodur® C18 Gravity (250 mm × 16 mm, 5 μ m). Separation was done using gradient 5–100% CH₃CN + 0.05% HCOOH in water + 0.05% HCOOH in 53 min at a flow rate of 10 mL/min and end with a 5 min step at 100% CH₃CN. The sample was dissolved in DMSO and manually injected to the HPLC system.

Abbreviations

Acetonitrile (ACN), chloroform (CHCl₃), copper (II) sulfate pentahydrate (CuSO₄·5H₂O), dichloromethane (DCM), dimethylsulfoxide (DMSO), ethyl acetate (EtOAc), formic acid (HCO₂H), hydrochloric acid (HCl), *iso*propanol (*i*-PrOH), lithium hydroxide (LiOH), methanol, CH₃OH, propanephosphonic acid cyclic anhydride 50% in ethyl acetate (T_3P), sodium sulfate (Na₂SO₄), tetrahydrofuran (THF), trifluoroacetic acid (TFA), water (H₂O). Other abbreviations used are: aqueous (aq.), calculated (calcd), equivalents (equiv.) hours (h), HRMS (high-resolution mass spectrometry), minutes (min), room temperature (rt), on (overnight), saturated (sat.) part(s) per million (ppm).

Synthesis and characterization of compounds 5–31

General procedure for amide coupling (GP1) (5a, 9a-24a):

To a solution of the respective carboxylic acid (1 equiv.) and methyl 4-aminopicolinate (**5c**) (1.1 equiv.) in EtOAc (0.15 M) and pyridine (70 equiv.), T₃P (11 equiv.) was added. The reaction mixture was stirred at 40 °C overnight. After cooling to rt, the reaction mixture was poured into concentrated aq. Na₂CO₃ solution and extracted with EtOAc (3 x). The combined organic layers were dried over Na₂SO₄, filtered and concentrated under vacuum. The crude material was purified by preparative HPLC to afford the respective methyl esters.

General procedure for basic-methyl ester hydrolysis (GP2):

To a suspension of the corresponding ester (1 equiv.) in THF (0.3 M), an aq. solution of LiOH (4M) was added and the reaction mixture was stirred at rt for 15–30 min. After completion of the reaction, THF was removed under vacuum and the reaction mixture was treated with 2M HCl (3–4) and the aq. phase was extracted with a mixture of CHCl $_3$ /i-PrOH (3:1). The combined organic layers were dried over Na $_2$ SO $_4$, filtered and concentrated under vacuum. The crude material was purified by preparative HPLC to afford the respective acid.

Compounds 1-4 were synthesized according to the reported procedures [1].

methyl 4-(4-phenoxybenzamido)picolinate (5a)

aminopicolinate (**5c**) (117.2 mg, 0.77 mmol) in EtOAc (4 mL) and pyridine (4 mL, 49.0 mmol) to afford after preparative HPLC **5a** (130 mg, 52%) as a transparent oil. ¹**H NMR** (500 MHz, DMSO- d_6) δ 10.77 (s, 1H), 8.60 (d, J = 5.5 Hz, 1H), 8.52 (d, J = 2.0 Hz, 1H), 8.08 – 8.03 (m, 3H), 7.51 – 7.43 (m, 2H), 7.25 (t, J = 7.4 Hz, 1H), 7.17 – 7.10 (m, 4H), 3.89 (s, 3H). ¹³**C NMR** (126 MHz, DMSO- d_6) δ 165.71, 165.30, 160.47, 155.29, 150.56, 148.26, 147.13, 130.34, 128.26, 124.60, 119.75, 117.38, 116.62, 115.20, 52.91. **LC-MS** calcd for $C_{20}H_{16}N_2O_4$ [M+H]*: 349.10, found 349.10.

4-(4-phenoxybenzamido)picolinic acid (5)

HPLC compound **5** (10 mg, 0.14 mmol, 35%) as a white solid. **¹H NMR** (500 MHz, DMSO- d_6) δ 10.74 (s, 1H), 8.57 (d, J = 5.5 Hz, 1H), 8.48 (s, 1H), 8.04 (d, J = 8.5 Hz, 3H), 7.47 (t, J = 7.9 Hz, 2H), 7.25 (t, J = 7.4 Hz, 1H), 7.12 (dd, J = 8.2, 6.3 Hz, 4H). ¹³**C NMR** (126 MHz, DMSO- d_6) δ 166.33, 166.20, 160.94, 155.77, 150.16, 147.97, 130.81, 128.98, 128.76, 128.29, 125.07, 120.22, 117.86, 116.76, 115.37. **HR-MS** calcd for $C_{19}H_{15}N_2O_4$ [M+H]*: 335.10263, found 335.10134.

4-phenoxy-N-(63yridine-4-yl)benzamide (6)

In a round bottom flask containing **5b** (150 mg, 0.70 mmol), HATU (400 mg, 1.05 mmol), DIPEA (0.37 mL, 2.10 mmol) in 5 mL of DMF were added and the reaction was stirred for 5 min before adding the 63yridine-4-amine (**6c**) (79.1 mg, 0,84 mmol) . The reaction was then left to stir at rt for 16 h. After completion, the mixture was diluted with 50 mL water and acidified to pH =3. The mixture was then extracted with ethyl acetate (2 x 50 mL), organic layers were combined and dried over MgSO4, concentrated in vacuo and purified on the FlashHPLC column. The desired fractions were combined and dried on a freeze dryer to achieve **6** (58 mg, 29%) as white powder. ¹**H NMR** (500 MHz, DMSO-
$$d_6$$
) δ 10.55 (s, 1H), 8.47 (d, J = 5.4 Hz, 2H), 8.01 (d, J = 8.4 Hz, 2H), 7.78 (d, J = 6.4 Hz, 2H), 7.46 (t, J = 7.8 Hz, 2H), 7.24 (t, J = 7.4 Hz, 1H), 7.12 (t, J = 7.5 Hz, 4H). ¹³**C NMR** (126 MHz, DMSO- d_6) δ 165.72, 160.34, 155.40, 150.31, 146.10, 130.40, 130.33, 128.72, 124.62, 119.77, 117.44, 114.02. **HR-MS** calcd for C₁₈H₁₅N₂O₂ [M+H]*: 291.11280, found 291.09959.

N-(2-methylpyridin-4-yl)-4-phenoxybenzamide (7)

mmol), HATU (400 mg, 1.05 mmol), DIPEA (0.37 mL, 2.1 mmol) in 5 mL of DMF were added and the reaction was stirred for 5 min before adding 2-methylpyridin-4-amine (**7c**) (90.87 mg, 0,84 mmol) . The reaction was then left to stir at rt for 16 h. After completion, the mixture was diluted with 50 mL water and acidified to pH =3. The mixture was then extracted with ethyl acetate (2 x 50 mL), organic layers were combined and dried over MgSO4, concentrated in vacuo and purified on the FlashHPLC column. The desired fractions were combined and dried on a freeze dryer to achieve **7** (36 mg, 17%) as white powder. ¹**H NMR** (500 MHz, DMSO-
$$d_6$$
) δ 10.51 (s, 1H), 8.35 (d, J = 5.7 Hz, 1H), 8.00 (d, J = 8.6 Hz, 2H), 7.70 (s, 1H), 7.61 (d, J = 5.7 Hz, 1H), 7.46 (t, J = 7.8 Hz, 2H), 7.24 (t, J = 7.4 Hz, 1H), 7.12 (t, J = 8.1 Hz, 4H), 2.45 (s, 3H). ¹³**C NMR** (126 MHz, DMSO- d_6) δ 165.68, 160.35, 158.21, 155.40, 149.07, 146.81, 130.40, 130.32, 128.70, 124.63, 119.77, 117.44, 113.05, 111.59, 24.08. **HR-MS** calcd for $C_{19}H_{17}N_2O_2$ [M+H]*: 305.12854, found 305.11321.

In a round bottom flask containing **5b** (150 mg, 0.70

4-phenoxy-N-(2-(trifluoromethyl)64yridine-4-yl)benzamide (8)

According to **GP1**, T_3P (2.27 mL, 7.70 mmol) was added to a solution of **5b** (150 mg, 0.70 mmol) and 2-(trifluoromethyl)64yridine-4-amine (**8c**) (124.8 mg,

0.77 mmol) in EtOAc (4 mL) and pyridine (4 mL, 49.0 mmol) to afford after preparative HPLC **8** (90 mg, 36%) as a brown oil. ¹**H NMR** (500 MHz, DMSO- d_6) δ 10.86 (s, 1H), 8.66 (d, J = 5.6 Hz, 1H), 8.31 (d, J = 2.0 Hz, 1H), 8.04 (t, J = 7.6 Hz, 3H), 7.47 (t, J = 7.7 Hz, 2H), 7.24 (t, J = 8.1 Hz, 1H), 7.13 (d, J = 8.7 Hz, 4H). ¹³**C NMR** (126 MHz, DMSO- d_6) δ 165.89, 160.61, 155.26, 151.10, 147.70, 147.29 (q, J = 33.1 Hz), 130.39, 130.34, 128.08, 124.63, 121.67 (q, J = 273.9 Hz), 119.77, 117.41, 116.38, 110.61 (q, J = 3.2 Hz). ¹⁹**F NMR** (470 MHz, DMSO- d_6) δ -66.89. **HR-MS** calcd for C₁₉H₁₂F₃N₂O₂ [M-H]⁻: 357.08564, found 357.08578.

methyl 4-(4-(4-methoxyphenoxy)benzamido)picolinate (9a)

According to **GP1**, T_3P (2.0 mL, 6.76 mmol) was added to a solution of 4-(3-methoxyphenoxy)benzoic acid (**9b**) (150 mg, 0.61 mmol) and **5c** (102.8 mg, 0.67

mmol) in EtOAc (3.5 mL) and pyridine (3.5 mL, 42.99 mmol) to afford after preparative HPLC **9a** (100 mg, 43%) as a white powder. ¹**H NMR** (500 MHz, DMSO- d_6) δ 10.71 (s, 1H), 8.60 (d, J = 5.5 Hz, 1H), 8.51 (d, J = 2.1 Hz, 1H), 8.05 (dd, J = 5.5, 2.1 Hz, 1H), 8.01 (d, J = 8.7 Hz, 2H), 7.14 – 7.07 (m, 2H), 7.05 – 7.00 (m, 4H), 3.89 (s, 3H), 3.78 (s, 3H). ¹³**C NMR** (126 MHz, DMSO- d_6) δ 165.73, 165.28, 156.30, 150.51, 148.21, 148.10, 147.20, 130.27, 127.56, 121.54, 116.61, 116.30, 115.30, 115.20, 55.45, 52.44. **LC-MS** calcd for C₂₁H₁₉N₂O₅ [M+H]*: 379.13, found 379.20.

4-(4-(4-methoxyphenoxy)benzamido)picolinic acid (9)

According to **GP2**, to a suspension of **9a** (50 mg, 0.13 mmol) in THF (0.4 mL), an aq. Solution of LiOH (0.4 mL) was added to

afford after preparative HPLC compound **9** (12 mg, 29%) as a white solid. ¹**H NMR** (500 MHz, DMSO- d_6) δ 10.71 (s, 1H), 8.58 (d, J = 5.5 Hz, 1H), 8.48 (d, J = 2.0 Hz, 1H),

8.05 (dd, J = 5.6, 1.9 Hz, 1H), 8.02 (d, J = 8.7 Hz, 2H), 7.12 – 7.08 (m, 2H), 7.06 – 7.01 (m, 4H), 3.79 (s, 3H). ¹³**C NMR** (126 MHz, DMSO- d_6) δ 165.91, 165.73, 161.60, 156.30, 149.65, 148.11, 147.49, 130.29, 127.61, 121.53, 116.30, 116.20, 115.30, 114.86, 55.46. **HR-MS** calcd for $C_{20}H_{17}N_2O_5[M+H]^+$: 365.11320, 365.11191.

methyl 4-(4-(3-cyanophenoxy)benzamido)picolinate (10a)

According to **GP1**, T_3P (2.03 mL, 6.90 mmol) was added to a solution of 4-(3-cyanophenoxy)benzoic acid (**10b**) (150 mg,

0.63 mmol) and **5c** (104.9 mg, 0.69 mmol) in EtOAc (3.5 mL) and pyridine (3.5 mL, 43.90 mmol) to afford after preparative HPLC **10a** (93 mg, 40%) as a white powder. ¹**H NMR** (500 MHz, DMSO- d_6) δ 10.81 (s, 1H), 8.62 (d, J = 5.5 Hz, 1H), 8.53 (d, J = 1.9 Hz, 1H), 8.11 (d, J = 8.7 Hz, 2H), 8.06 (dd, J = 5.5, 2.1 Hz, 1H), 7.95 – 7.88 (m, 2H), 7.30 (d, J = 8.7 Hz, 2H), 7.24 (d, J = 8.7 Hz, 2H), 3.90 (s, 3H). ¹³**C NMR** (126 MHz, DMSO- d_6) δ 165.77, 165.46, 160.08, 158.36, 150.77, 148.47, 147.21, 135.02, 130.73, 130.18, 119.55, 119.39, 118.75, 116.83, 115.39, 106.37, 52.62. **LC-MS** calcd for C₂₁H₁₆N₃O₄ [M+H]⁺: 374.11, found 374.09.

4-(4-(3-cyanophenoxy)benzamido)picolinic acid (10)

According to **GP2**, to a suspension of **10a** (50 mg. 0.13 mmol) in THF (0.4 mL), an aq. solution of LiOH (0.4 mL) was added to

afford after preparative HPLC compound **10** (15 mg, 31%) as a transparent oil. ¹**H NMR** (500 MHz, DMSO- d_6) δ 10.81 (br s, 1H), 8.59 (d, J = 5.3 Hz, 1H), 8.48 (d, J = 1.8 Hz, 1H), 8.11 (d, J = 7.6 Hz, 2H), 8.05 (dd, J = 5.5, 2.0 Hz, 1H), 7.92 (d, J = 7.8 Hz, 2H), 7.30 (d, J = 8.9 Hz, 2H), 7.24 (d, J = 7.8 Hz, 2H). ¹³**C NMR** (126 MHz, DMSO- d_6) δ 165.84, 160.15, 158.37, 153.26, 149.84, 147.57, 135.07, 130.82, 130.30, 119.60, 119.44, 118.83, 116.24, 115.05, 106.39. **HR-MS** calcd for C₂₀H₁₂N₃O₄ [M-H]⁻: 358.08333, found 358.0834.

methyl 4-(4-(4-fluorophenoxy)benzamido)picolinate (11a)

According to **GP1**, T_3P (2.09 mL, 7.11 mmol) was added to a solution of 4-(3-fluorophenoxy)benzoic acid (**11b**) (150 mg, 0.65 mmol) and **5c** (108.1 mg, 0.71 mmol) in

EtOAc (3.6 mL) and pyridine (3.6 mL, 45.2 mmol) to afford after preparative HPLC **11a** (140 mg, 59%) as a white powder. ¹**H NMR** (500 MHz, DMSO- d_6) δ 10.75 (s, 1H), 8.60 (d, J = 5.5 Hz, 1H), 8.52 (d, J = 2.1 Hz, 1H), 8.06 – 8.01 (m, 3H), 7.31 (t, J = 8.7 Hz, 2H), 7.20 (dd, J = 9.0, 4.5 Hz, 2H), 7.10 (d, J = 8.6 Hz, 2H), 3.89 (s, 3H). ¹³**C NMR** (126 MHz, DMSO- d_6) δ 165.74, 165.35, 160.87, 158.92 (d, J = 240.4 Hz), 151.26 (d, J = 2.3 Hz), 150.64, 148.29, 147.17, 130.42, 128.21, 121.96 (d, J = 8.3 Hz), 117.00, 116.99 (d, J = 23.4 Hz), 116.67, 115.24, 52.51. ¹⁹**F NMR** (470 MHz, DMSO- d_6) δ -118.30. **LC-MS** calcd for C₂₀H₁₆FN₂O₄ [M+H]*: 367.11, found 367.20.

4-(4-(4-fluorophenoxy)benzamido)picolinic acid (11)

According to **GP2**, to a suspension of **11a** (50 mg, 0.14) in THF (0.5 mL), an aq. solution of LiOH (0.5 mL) was added to afford after

preparative HPLC compound **11** (18 mg, 37%) as a white powder. ¹**H NMR** (500 MHz, DMSO- d_6) δ 10.75 (s, 1H), 8.58 (d, J = 5.6 Hz, 1H), 8.49 (d, J = 2.2 Hz, 1H), 8.04 (d, J = 8.3 Hz, 3H), 7.30 (t, J = 8.6 Hz, 2H), 7.19 (dd, J = 9.0, 4.5 Hz, 2H), 7.10 (d, J = 8.4 Hz, 2H). ¹³**C NMR** (126 MHz, DMSO) δ 166.04, 165.85, 160.96, 159.98, 158.07, 151.41 (d, J = 2.3 Hz), 149.88, 147.63, 130.54, 128.41, 122.07, 122.00, 117.18, 117.15, 116.99, 116.44, 115.07. ¹⁹**F NMR** (470 MHz, DMSO- d_6) δ -118.38. **HR-MS** calcd for C₁₉H₁₄FN₂O₄ [M+H]⁺: 353.09321, found 353.09198.

methyl 4-(4-(4-chlorophenoxy)benzamido)picolinate (12a)

According to **GP1**, T_3P (1.95 mL, 6.64 mmol) was added to a solution of 4-(3-chlorophenoxy)benzoic acid (**12b**) (150 mg,

0.60 mmol) and **5c** (101.0 mg, 0.66 mmol) in EtOAc (3.4 mL) and pyridine (3.4 mL, 42.2 mmol) to afford after preparative HPLC **12a** (110 mg, 46%) as a white powder. ¹H NMR

(500 MHz, DMSO- d_6) δ 10.77 (s, 1H), 8.61 (d, J = 5.5 Hz, 1H), 8.53 (d, J = 2.1 Hz, 1H), 8.10 – 8.03 (m, 3H), 7.54 – 7.49 (m, 2H), 7.20 – 7.14 (m, 4H), 3.89 (s, 3H). ¹³**C NMR** (126 MHz, DMSO- d_6) δ 165.65, 165.30, 160.02, 154.34, 150.58, 148.28, 147.09, 130.40, 130.19, 128.69, 128.36, 121.43, 117.69, 116.63, 115.21, 52.44. **LC-MS** calcd for $C_{20}H_{16}ClN_2O_4$ [M+H]*: 383.08, found 383.20.

4-(4-(4-chlorophenoxy)benzamido)picolinic acid (12)

According to **GP2**, to a suspension of **12a** (50 mg, 0.13 mmol) in THF (0.4 ml), an aq. solution of LiOH (0.4 mL) was added to afford

after preparative HPLC compound **12** (31 mg, 32%) as a white powder. ¹**H NMR** (500 MHz, DMSO- d_6) δ 10.78 (s, 1H), 8.58 (d, J = 5.6 Hz, 1H), 8.48 (d, J = 2.1 Hz, 1H), 8.07 – 8.04 (m, 2H), 8.03 (d, J = 2.3 Hz, 1H), 7.52 – 7.49 (m, 2H), 7.17 – 7.13 (m, 4H). ¹³**C NMR** (126 MHz, DMSO- d_6) δ 165.97, 165.77, 160.08, 154.40, 149.67, 147.54, 130.50, 130.26, 128.80, 128.44, 121.51, 117.75, 116.25, 114.93. **HR-MS** calcd for C₁₉H₁₄ClN₂O₅ [M+H]⁺: 369.06366, found 369.06264.

methyl 4-(4-(3-(trifluoromethyl)phenoxy)benzamido)picolinate (13a)

According to **GP1**, T3P (1.72 mL, 5.85 mmol) was added to a solution of 4-(3-(trifluoromethyl)phenoxy)benzoic acid

(13b) (150 mg, 0.53 mmol) and 5c (89.0 mg, 0.58 mmol) in EtOAc (3 mL) and pyridine (3 mL, 37.2 mmol) to afford after preparative HPLC 13a (90 mg, 41%) as a white powder. 1 H NMR (500 MHz, DMSO- d_6) δ 10.80 (s, 1H), 8.61 (d, J = 5.4 Hz, 1H), 8.52 (s, 1H), 8.09 (d, J = 8.7 Hz, 2H), 8.05 (dd, J = 3.6, 2.0 Hz, 1H), 7.81 (d, J = 8.4 Hz, 2H), 7.30 – 7.25 (m, 4H), 3.89 (s, 3H). 13 C NMR (126 MHz, DMSO- d_6) δ 165.64, 165.30, 159.17, 158.76, 150.60, 148.30, 147.07, 130.54, 129.65, 127.71 (q, J = 3.9 Hz), 124.34 (q, J = 32.1 Hz), 124.21 (q, J = 271.6 Hz), 119.18, 119.01, 116.67, 115.23, 52.46. 19 F NMR (470 MHz, DMSO- d_6) δ -60.29. **LC-MS** calcd for $C_{21}H_{16}F_3N_2O_4$ [M+H] $^+$: 417.11, found 417.10.

4-(4-(4-(trifluoromethyl)phenoxy)benzamido)picolinic acid (13)

According to **GP2**, to a suspension of **13a** (50 mg, 0.12 mmol) in THF (0.4 mL), an aq. solution of LiOH (0.4 mL) was added to

afford after preparative HPLC compound **13** (13 mg, 27%) as an off-white powder. ¹**H NMR** (500 MHz, DMSO- d_6) δ 10.82 (s, 1H), 8.60 (d, J = 5.5 Hz, 1H), 8.50 (dd, J = 1.8 Hz, 1H), 8.11 (d, J = 8.7 Hz, 2H), 8.06 (dd, J = 5.3, 2.1 Hz, 1H), 7.81 (d, J = 8.5 Hz, 2H), 7.28 (dd, J = 8.8, 2.5 Hz, 4H). ¹³**C NMR** (126 MHz, DMSO- d_6) δ 167.39, 165.51, 159.24, 158.61, 156.83, 148.59, 147.23, 130.55, 129.91, 127.71 (q, J = 3.9 Hz), 124.29 (q, J = 32.2 Hz), 124.22 (q, J = 271.2 Hz), 119.16, 118.98, 114.54, 114.03. ¹⁹**F NMR** (470 MHz, DMSO- d_6) δ -60.29. **HR-MS** calcd for C₂₀H₁₄F₃N₂O₄ [M+H]⁺: 403.09002, found 403.08866.

methyl 4-(4-(trifluoromethoxy)phenoxy)benzamido)picolinate (14a)

According to **GP1**, T_3P (1.63 mL, 5.53 mmol) was added to a solution of 4-(3-(trifluoromethoxy)phenoxy)benzoic acid (14b) (150 mg, 0.50 mmol) and 5c (84.2

mg, 0.55 mmol) in EtOAc (2.8 mL) and pyridine (2.8 mL, 35.20 mmol) to afford after preparative HPLC **14a** (80.5 mg, 37%) as a white powder. ¹**H NMR** (500 MHz, DMSO- d_6) δ 10.79 (s, 1H), 8.61 (d, J = 5.5 Hz, 1H), 8.52 (d, J = 2.1 Hz, 1H), 8.09 – 8.03 (m, 3H), 7.47 (d, J = 8.6 Hz, 2H), 7.24 (d, J = 9.0 Hz, 2H), 7.19 (d, J = 8.7 Hz, 2H), 3.89 (s, 3H). ¹³**C NMR** (126 MHz, DMSO) δ 165.72, 165.35, 159.90, 154.45, 150.66, 148.30, 147.14, 130.51, 128.92, 123.30, 120.14 (q, J = 256.0 Hz) 117.99, 116.69, 115.25, 52.52. ¹⁹**F NMR** (470 MHz, DMSO- d_6) δ -57.10. **LC-MS** calcd for C₂₁H₁₆F₃N₂O₅ [M+H]⁺: 433.10, found 433.20.

4-(4-(4-(trifluoromethoxy)phenoxy)benzamido)picolinic acid (14)

According to **GP2**, to a suspension of **14a** (50 mg, 0.12 mmol) in THF (0.4 mL), an aq. solution of LiOH (0.4 mL) was added

to afford after preparative HPLC compound 14 (19 mg, 39%) as a white solid. 1H NMR

(500 MHz, DMSO- d_6) δ 10.82 (s, 1H), 8.57 (d, J = 5.5 Hz, 1H), 8.49 (s, 1H), 8.06 (t, J = 6.8 Hz, 3H), 7.46 (d, J = 8.5 Hz, 2H), 7.24 (d, J = 8.8 Hz, 2H), 7.18 (d, J = 8.4 Hz, 2H). ¹³**C NMR** (126 MHz, DMSO- d_6) δ 166.06, 165.76, 163.29, 159.91, 154.47, 149.66, 147.57, 144.47 (q, J = 4.8 Hz), 130.58, 128.97, 123.32, 121.09, 120.17 (q, J = 256.0 Hz), 117.99, 116.24, 114.92. ¹⁹**F NMR** (470 MHz, DMSO- d_6) δ -57.12. **HR-MS** calcd for C₂₀H₁₄F₃N₂O₅ [M+H]*: 419.08493, found 419.08347.

methyl 4-(4-benzylbenzamido)picolinate (15a)

According to **GP1**, T_3P (2.3 mL, 7.77 mmol) was added to a solution of 4-benzylbenzoic acid (**15b**) (150 mg, 0.70 mmol) and **5c** (118.3 mg,

0.78 mmol) in EtOAc (4.0 mL) and pyridine (4.0 mL, 49.47 mmol) to afford after preparative HPLC **15a** (125 mg, 51%) as a white powder. ¹**H NMR** (500 MHz, DMSO- d_6) δ 10.72 (s, 1H), 8.60 (d, J = 5.4 Hz, 1H), 8.51 (d, J = 2.1 Hz, 1H), 8.03 (dd, J = 5.4, 2.1 Hz, 1H), 7.92 (d, J = 8.1 Hz, 2H), 7.42 (d, J = 8.0 Hz, 2H), 7.34 – 7.25 (m, 4H), 7.20 (t, J = 7.2 Hz, 1H), 4.04 (s, 2H), 3.88 (s, 3H). ¹³**C NMR** (126 MHz, DMSO- d_6) δ 166.92, 165.79, 151.07, 148.78, 147.58, 146.57, 141.14, 132.17, 129.35, 129.26, 129.04, 128.69, 126.68, 117.09, 115.67, 52.93, 41.39. **LC-MS** calcd for C₂₁H₁₉N₂O₃ [M+H]⁺: 347.14, found 347.11.

4-(4-benzylbenzamido)picolinic acid (15)

According to **GP2**, to a suspension of **15a** (50 mg, 0.14 mmol) in THF (0.5 mL), an aq. solution of LiOH (0.5 mL) was added to afford after

preparative HPLC compound **15** (21 mg, 43%) as a white solid. ¹**H NMR** (500 MHz, DMSO- d_6) δ 10.73 (s, 1H), 8.58 (d, J = 5.5 Hz, 1H), 8.48 (d, J = 2.2 Hz, 1H), 8.03 (dd, J = 5.6, 2.2 Hz, 1H), 7.92 (d, J = 8.3 Hz, 2H), 7.42 (d, J = 8.2 Hz, 2H), 7.32 – 7.24 (m, 4H), 7.22 – 7.17 (m, 1H), 4.04 (s, 2H). ¹³**C NMR** (126 MHz, DMSO- d_6) δ 166.45, 165.84, 149.74, 149.25, 147.46, 146.08, 140.65, 131.70, 128.86, 128.77, 128.55, 128.22, 126.19, 116.31, 114.91, 40.90. **HR-MS** calcd for C₂₀H₁₇N₂O₃ [M+H]⁺: 333.12337, found 333.12242.

methyl 4-(4-(benzyloxy)benzamido)picolinate (16a)

According to **GP1**, T_3P (2.1 mL, 7.23 mmol) was added to a solution of 4-(benzyloxy)benzoic acid (**16b**) (150 mg, 0.66 mmol) and **5c** (110 mg, 0.72 mmol) in

EtOAc (3.7 mL) and pyridine (3.7 mL, 46.0 mmol) to afford after preparative HPLC **16a** (142 mg, 60%) as a beige solid. ¹**H NMR** (500 MHz, DMSO- d_6) δ 10.88 (s, 1H), 8.62 (d, J = 15.4 Hz, 2H), 8.17 (dd, J = 5.8, 2.2 Hz, 1H), 8.02 (d, J = 8.9 Hz, 2H), 7.48 (d, J = 7.2 Hz, 2H), 7.41 (t, J = 7.5 Hz, 2H), 7.35 (t, J = 7.3 Hz, 1H), 7.19 (d, J = 8.8 Hz, 2H), 5.23 (s, 2H), 3.92 (s, 3H). ¹³**C NMR** (126 MHz, DMSO- d_6) δ 165.92, 164.42, 161.70, 149.37, 148.46, 146.82, 136.52, 130.12, 128.51, 128.03, 127.83, 125.79, 116.63, 115.30, 114.69, 69.50, 52.72. **LC-MS** calcd for C₂₁H₁₉N₂O₄ [M+H]⁺: 363.13, found 363.03.

4-(4-(benzyloxy)benzamido)picolinic acid (16)

$$HO \longrightarrow HO \longrightarrow HO$$

According to **GP2**, to a suspension of **16a** (50 mg, 0.14 mmol) in THF (0.5 mL), an aq. solution of LiOH (0.5 mL) was added to afford after preparative HPLC compound

16 (17 mg, 35%) as a white solid. ¹**H NMR** (500 MHz, DMSO- d_6) δ 10.66 (br s, 1H), 8.57 (d, J = 5.3 Hz, 1H), 8.48 (br s, 1H), 8.07 – 8.03 (m, 1H), 8.00 (d, J = 8.4 Hz, 2H), 7.48 (d, J = 7.5 Hz, 2H), 7.41 (t, J = 7.5 Hz, 2H), 7.35 (t, J = 7.3 Hz, 1H), 7.18 (d, J = 8.6 Hz, 2H), 5.22 (s, 2H). ¹³**C NMR** (126 MHz, DMSO- d_6) δ 165.94, 165.83, 161.56, 149.53, 147.64, 147.61, 136.56, 130.03, 128.51, 128.02, 127.83, 126.06, 116.08, 114.80, 114.64, 69.49. **HR-MS** calcd for $C_{20}H_{15}N_2O_4[M-H]^-$: 347.10373, found 347.10385.

methyl 4-(4-benzoylbenzamido)picolinate (17a)

According to **GP1**, T₃P (2.1 mL, 7.29 mmol) was added to a solution of 4-benzoylbenzoic acid (**17b**) (150 mg, 0.66 mmol) and **5c** (111.0 mg, 0.73 mmol) in EtOAc (3.7 mL) and pyridine (3.7

mL, 46.41 mmol) to afford after preparative HPLC **17a** (105 mg, 44%) as a white powder. ¹**H NMR** (500 MHz, DMSO- d_6) δ 11.01 (s, 1H), 8.64 (d, J = 5.4 Hz, 1H), 8.55 (d,

J = 2.0 Hz, 1H), 8.16 (d, J = 8.2 Hz, 2H), 8.07 (dd, J = 5.5, 2.1 Hz, 1H), 7.90 (d, J = 8.2 Hz, 2H), 7.79 (dd, J = 7.7, 1.4 Hz, 2H), 7.76 – 7.70 (m, 1H), 7.61 (t, J = 7.7 Hz, 2H), 3.90 (s, 3H). 13 **C NMR** (126 MHz, DMSO- d_6) δ 195.51, 166.07, 165.42, 150.85, 148.53, 147.03, 140.27, 137.23, 136.68, 133.37, 129.95, 129.76, 128.92, 128.31, 116.93, 115.46, 52.64. **LC-MS** calcd for $C_{21}H_{17}N_2O_4$ [M+H]⁺: 361.12, found 361.13.

4-(4-benzoylbenzamido)picolinic acid (17)

According to **GP2**, to a suspension of **17a** (50 mg, 0.12 mmol) in THF (0.4 mL), an aq. solution of LiOH (0.4 mL) was added to afford after preparative HPLC compound **17** (10 mg, 25%) as

a white solid. ¹H NMR (500 MHz, DMSO- d_6) δ 11.01 (s, 1H), 8.63 (d, J = 5.5 Hz, 1H), 8.53 (d, J = 2.1 Hz, 1H), 8.18 – 8.14 (m, J = 8.1 Hz, 2H), 8.08 (dd, J = 5.4, 1.9 Hz, 1H), 8.15 (d, J = 8.0 Hz, 2H), 8.07 (dd, J = 5.6, 2.2 Hz, 1H), 7.90 (d, J = 8.0 Hz, 2H), 7.78 (d, J = 7.6 Hz, 2H), 7.73 (t, J = 7.4 Hz, 1H), 7.60 (t, J = 7.6 Hz, 2H). ¹³**C NMR** (126 MHz, DMSO- d_6) δ 195.35, 165.91, 165.89, 150.00, 149.29, 147.12, 140.10, 137.10, 136.51, 133.20, 129.78, 129.59, 128.75, 128.16, 116.50, 115.04. **HR-MS** calcd for C₂₀H₁₅N₂O₄ [M+H]⁺: 347.10263, 347.11708.

methyl 4-(4-(phenylamino)benzamido)picolinate (18a)

According to **GP1**, T_3P (2.3 mL, 7.74 mmol) was added to a solution of 4-(phenylamino)benzoic acid (**18b**) (150 mg, 0.70 mmol) and **5c** (117.8 mg, 0.77 mmol) in EtOAc (4 mL) and pyridine (4

mL, 49.24 mmol) to afford after preparative HPLC **18a** (96 mg, 39%) as a white powder. ¹**H NMR** (500 MHz, DMSO- d_6) δ 10.52 (s, 1H), 8.77 (s, 1H), 8.58 (d, J = 5.5 Hz, 1H), 8.53 (d, J = 2.1 Hz, 1H), 8.05 (dd, J = 5.5, 2.1 Hz, 1H), 7.94 – 7.90 (m, 2H), 7.36 – 7.31 (m, 2H), 7.23 – 7.17 (m, 2H), 7.15 – 7.09 (m, 2H), 6.99 (t, J = 7.3 Hz, 1H), 3.89 (s, 3H). ¹³**C NMR** (126 MHz, DMSO- d_6) δ 165.50, 165.06, 150.12, 147.87, 147.52, 147.14, 141.15, 129.51, 129.03, 122.81, 121.38, 118.73, 116.14, 114.77, 113.74, 52.08. **LC-MS** calcd for C₂₀H₁₈N₃O₃ [M+H]⁺: 348.13, found 348.20.

4-(4-(phenylamino)benzamido)picolinic acid (18)

According to **GP2**, to a suspension of **18a** (50 mg, 0.14 mmol) in THF (0.5 mL), an aq. solution of LiOH (0.5 mL) was added to afford after preparative HPLC compound **18** (16 mg, 33%) as

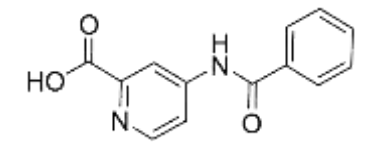
a white solid. ¹**H NMR** (500 MHz, DMSO- d_6) δ 10.50 (s, 1H), 8.76 (s, 1H), 8.52 (d, J = 1.0 Hz, 1H), 8.45 (s, 1H), 8.07 – 8.02 (m, 1H), 7.92 (d, J = 1.0 Hz, 2H), 7.33 (t, J = 7.8 Hz, 2H), 7.20 (d, J = 7.9 Hz, 2H), 7.12 (d, J = 8.7 Hz, 2H), 6.99 (t, J = 7.4 Hz, 1H). ¹³**C NMR** (126 MHz, DMSO- d_6) δ 166.08, 165.80, 149.17, 147.84, 147.81, 141.51, 129.85, 129.37, 123.22, 121.69, 119.04, 115.68, 114.57, 114.08. **HR-MS** calcd for C₁₉H₁₆N₃O₃ [M+H]*: 334,11862 found 334.11754.

tert-butyl 4-benzamidopicolinate (19a)

According to **GP1**, T_3P (4 mL, 13.51 mmol) was added to a solution of benzoic acid (**19b**) (150 mg, 1.23 mmol) and **5c** (205.6 mg, 1.35 mmol) in EtOAc (6.9 mL) and pyridine (6.9

mL, 85.98 mmol) to afford after preparative HPLC **19a** (145 mg, 46%) as a white powder. ¹**H NMR** (500 MHz, DMSO- d_6) δ 10.81 (s, 1H), 8.61 (d, J = 5.5 Hz, 1H), 8.54 (d, J = 2.1 Hz, 1H), 8.06 (dd, J = 5.5, 2.1 Hz, 1H), 8.00 (dd, J = 8.2, 1.4 Hz, 2H), 7.65 (t, J = 7.3 Hz, 1H), 7.57 (t, J = 7.6 Hz, 2H), 3.89 (s, 3H). ¹³**C NMR** (126 MHz, DMSO- d_6) δ 166.59, 165.30, 150.59, 148.31, 147.07, 133.88, 132.36, 128.57, 127.93, 116.67, 115.24, 52.44. **LC-MS** calcd for C₁₄H₁₃N₂O₃ [M+H]⁺: 257.09, found 257.10.

4-benzamidopicolinic acid (19)



According to **GP2**, to a suspension of **19a** (50 mg, 0.19 mmol) in THF (0.6 mL), an aq. solution of LiOH (0.6 mL) was added to afford after preparative HPLC compound **19** (15

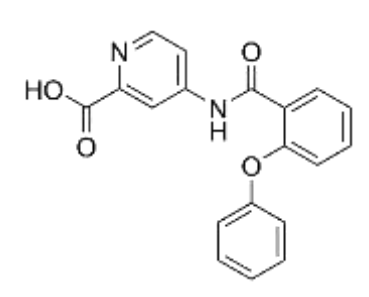
mg, 37%) as a white crystallize powder. ¹**H NMR** (500 MHz, DMSO-d₆) δ 10.83 (s, 1H), 8.61 (d, J = 5.5 Hz, 1H), 8.52 (s, 1H), 8.07 (dd, J = 1.0 Hz, 1H), 8.01 (d, J = 7.9 Hz, 2H), 7.65 (t, J = 1.0 Hz, 1H), 7.58 (t, J = 7.2 Hz, 2H). ¹³**C NMR** (126 MHz, DMSO- d_6) δ 166.79, 166.01, 149.95, 149.38, 147.62, 134.07, 132.54, 128.76, 128.13, 116.58, 115.15. **HR-MS** calcd for C₁₃H₁₁N₂O₃ [M+H]⁺: 243.07642, found 243.07574.

methyl 4-(2-phenoxybenzamido)picolinate (20a)

According to **GP1**, T_3P (2.27 mL, 7.70 mmol) was added to a solution of 2-phenoxybenzoic acid (**20b**) (150 mg, 0.70 mmol) and **5c** (117.2 mg, 0.77 mmol) in EtOAc (4 mL) and pyridine (4 mL, 49.0 mmol) to afford after preparative HPLC **20a** (160 mg, 66%) as a transparent oil. ¹**H NMR** (500

MHz, DMSO- d_6) δ 10.96 (s, 1H), 8.56 (d, J = 5.3 Hz, 1H), 8.39 (s, 1H), 7.84 (dd, J = 5.3, 1.7 Hz, 1H), 7.68 (d, J = 6.7 Hz, 1H), 7.54 (t, J = 7.8 Hz, 1H), 7.37 (t, J = 7.9 Hz, 2H), 7.29 (t, J = 7.5 Hz, 1H), 7.13 (t, J = 7.4 Hz, 1H), 7.04 (d, J = 8.1 Hz, 2H), 6.98 (d, J = 8.2 Hz, 1H), 3.87 (s, 3H). ¹³**C NMR** (126 MHz, DMSO- d_6) δ 166.21, 165.66, 156.82, 154.16, 151.10, 148.87, 147.09, 132.84, 130.50, 130.09, 128.51, 124.28, 124.09, 119.42, 119.21, 116.68, 115.07, 52.90. **LC-MS** calcd for $C_{20}H_{17}N_2O_4$ [M+H]⁺: 349.12, found 349.10.

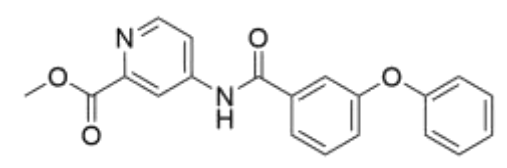
4-(2-phenoxybenzamido)picolinic acid (20)



According to **GP2**, to a suspension of **20a** (50 mg, 0.14 mmol) in THF (0.4 mL), an aq. solution of LiOH (0.4 mL) was added to afford after preparative HPLC compound **20** (25 mg, 52%) as a beige solid. ¹**H NMR** (500 MHz, DMSO- d_6) δ 10.89 (s, 1H), 8.44 (d, J = 5.5 Hz, 1H), 8.27 (d, J = 2.2 Hz,

1H), 7.82 (dd, J = 5.5, 2.2 Hz, 1H), 7.68 (dd, J = 7.6, 1.7 Hz, 1H), 7.56 – 7.49 (m, 1H), 7.37 (t, J = 7.9 Hz, 2H), 7.28 (t, J = 7.5 Hz, 1H), 7.13 (t, J = 7.4 Hz, 1H), 7.05 (d, J = 8.1 Hz, 2H), 6.97 (d, J = 8.3 Hz, 1H). ¹³**C NMR** (126 MHz, DMSO- d_6) δ 166.58, 165.66, 163.72, 156.34, 153.72, 149.27, 146.80, 132.28, 130.04, 129.65, 128.15, 123.84, 123.59, 118.86, 118.81, 114.97, 113.87. **HR-MS** calcd for C₁₉H₁₅N₂O₄ [M+H]⁺: 335.10263, found 335.10134.

Methyl 4-(3-phenoxybenzamido)picolinate (21a)



According to **GP1**, T_3P (2.27 mL, 7.70 mmol) was added to a solution of 3-phenoxybenzoic acid (**21b**) (150 mg, 0.70 mmol) and **5c** (117.2

mg, 0.77 mmol) in EtOAc (4 mL) and pyridine (4 mL, 49.0 mmol) to afford after preparative HPLC **21a** (152 mg, 6 %) as a yellowish oil. 1 H NMR (500 MHz, DMSO- d_6)

 δ 10.81 (s, 1H), 8.61 (d, J = 5.5 Hz, 1H), 8.50 (s, 1H), 8.04 (dd, J = 5.6, 2.1 Hz, 1H), 7.79 (d, J = 9.3 Hz, 1H), 7.63 (s, 1H), 7.58 (t, J = 7.9 Hz, 1H), 7.44 (t, J = 7.9 Hz, 2H), 7.27 (dd, J = 8.2, 2.5 Hz, 1H), 7.20 (t, J = 7.4 Hz, 1H), 7.08 (d, J = 7.9 Hz, 2H), 3.88 (s, 3H). ¹³**C NMR** (126 MHz, DMSO- d_6) δ 165.71, 165.26, 156.88, 156.18, 150.62, 148.30, 146.91, 135.68, 130.41, 130.27, 124.00, 122.91, 122.34, 119.33, 118.93, 116.75, 115.32, 52.46. **LC-MS** calcd for C₂₀H₁₇N₂O₄ [M+H]*: 349.12, found 349.10.

4-(3-phenoxybenzamido)picolinic acid (21)

According to **GP2**, to a suspension of **21a** (50 mg, 0.12 mmol) in THF (0.4 mL), an aq. solution of LiOH (0.4 mL) was added to afford after preparative HPLC compound **21** (20 mg, 42%) as a brown solid. ¹H **NMR** (500 MHz, DMSO-
$$d_6$$
) δ 10.83 (s, 1H), 8.52 (s, 1H), 8.43 (s, 1H), 8.02 (s, 1H), 7.80 (d, J = 7.7 Hz, 1H), 7.64 (s, 1H), 7.58 (t, J = 8.0 Hz, 1H), 7.43 (t, J = 7.7 Hz, 2H), 7.27 (d, J = 8.2 Hz, 1H), 7.19 (t, J = 7.4 Hz, 1H), 7.08 (d, J = 7.9 Hz, 2H). ¹³**C NMR** (126 MHz, DMSO- d_6) δ 166.58, 165.72, 156.90, 156.23, 152.02, 149.49, 147.17, 135.83, 130.45, 130.32, 124.04, 123.00, 122.34, 118.98, 117.83, 115.82, 114.78. **HR-MS** calcd for C₁₉H₁₅N₂O₄ [M+H]⁺: 335.10263, found 335.09702.

methyl 4-(4-(pyridin-3-yloxy)benzamido)picolinate (22a)

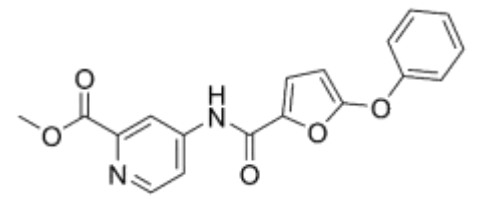
and **5c** (116.6 mg, 0.77 mmol) in EtOAc (4 mL) and pyridine (4 mL, 48.80 mmol) to afford after preparative HPLC **22a** (112 mg, 46 %) as a white powder. ¹**H NMR** (500 MHz, DMSO- d_6) δ 10.77 (s, 1H), 8.60 (d, J = 5.5 Hz, 1H), 8.52 (d, J = 2.1 Hz, 1H), 8.49 – 8.44 (m, 2H), 8.06 (s, 1H), 7.59 (dd, J = 8.4, 2.0 Hz, 1H), 7.50 (dd, J = 8.4, 4.6 Hz, 1H), 7.19 (d, J = 8.7 Hz, 2H), 3.89 (s, 3H). ¹³**C NMR** (126 MHz, DMSO- d_6) δ 165.45, 165.13, 159.67, 151.90, 150.42, 148.11, 146.91, 145.47, 141.67, 130.31, 128.75, 126.92, 124.78, 117.44, 116.47, 115.05, 52.27. **LC-MS** calcd for C₁₉H₁₆N₃O₄ [M+H]⁺: 350.11, found 350.14.

4-(4-(pyridin-3-yloxy)benzamido)picolinic acid (22)

According to **GP2**, to a suspension of **22a** (50 mg, 0.14 mmol) in THF (0.5 mL), an aq. solution of LiOH (0.5 mL) was added to afford after

preparative HPLC compound **22** (17 mg, 35%) as a white powder. ¹**H NMR** (500 MHz, DMSO- d_6) δ 10.79 (s, 1H), 8.59 (d, J = 5.5 Hz, 1H), 8.50 (d, J = 2.1 Hz, 1H), 8.49 – 8.45 (m, 2H), 8.10 – 8.03 (m, 3H), 7.59 (ddd, J = 8.4, 2.9, 1.3 Hz, 1H), 7.50 (dd, J = 8.3, 4.7 Hz, 1H), 7.22 – 7.17 (m, 2H). ¹³**C NMR** (126 MHz, DMSO- d_6) δ 13C NMR (126 MHz, DMSO) δ 165.84, 165.68, 159.86, 152.11, 149.75, 149.24, 147.51, 145.66, 141.84, 130.53, 128.97, 127.12, 124.99, 117.64, 116.40, 114.98. **HR-MS** calcd for C₁₈H₁₄N₃O₄ [M+H]*: 336.09788, found 336.09666.

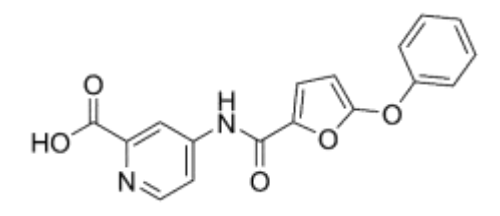
methyl 4-(5-phenoxyfuran-2-carboxamido)picolinate (23a)



According to **GP1**, T_3P (2.4 mL, 8.08 mmol) was added to a solution of 5-phenoxyfuran-2-carboxylic acid (23b) (150 mg, 0.73 mmol) and 5c (123.0 mg, 0.81

mmol) in EtOAc (4.1 mL) and pyridine (4.1 mL, 51.42 mmol) to afford after preparative HPLC **23a** (115 mg, 46%) as a white powder. ¹**H NMR** (500 MHz, DMSO- d_6): δ 10.64 (s, 1H), 8.58 (d, J = 5.5 Hz, 1H), 8.47 (d, J = 2.1 Hz, 1H), 8.01 (dd, J = 5.5, 2.1 Hz, 1H), 7.52 – 7.45 (m, 3H), 7.31 – 7.26 (m, 1H), 7.24 (dd, J = 8.1, 1.5 Hz, 2H), 5.93 (d, J = 3.6 Hz, 1H), 3.88 (s, 3H). ¹³**C NMR** (126 MHz, DMSO- d_6): δ 165.26, 158.38, 156.26, 155.00, 150.56, 148.25, 146.69, 138.45, 130.35, 125.28, 118.99, 117.79, 116.50, 115.08, 91.25, 52.43. **LC-MS** calcd for C₁₈H₁₅N₂O₅ [M+H]⁺: 339.10, found 339.05.

4-(5-phenoxyfuran-2-carboxamido)picolinic acid (23)



According to **GP2**, to a suspension of **23a** (50 mg, 0.15 mmol) in THF (0.5 mL), an aq. solution of LiOH (0.5 mL) was added to afford after preparative HPLC compound **23** (13 mg, 27%) as

a yellow solid. ¹**H NMR** (500 MHz, DMSO- d_6) δ 10.65 (br s, 1H), 8.57 (d, J = 5.5 Hz, 1H), 8.45 (d, J = 2.0 Hz, 1H), 8.01 (dd, J = 5.5, 2.0 Hz, 1H), 7.54 – 7.46 (m, 3H), 7.31 – 7.21 (m, 3H), 5.93 (d, J = 3.7 Hz, 1H). ¹³**C NMR** (126 MHz, DMSO- d_6) δ 166.31, 158.88, 156.73, 155.47, 150.19, 149.82, 147.51, 138.94, 130.82, 125.76, 119.48, 118.27,

116.65, 115.24, 91.70. **HR-MS** calcd for $C_{17}H_{13}N_2O_5$ [M+H]⁺: 325.08190, found 325.08085.

methyl 4-(6-phenoxynicotinamido)picolinate (24a)

According to **GP1**, T_3P (2.3 mL, 7.67 mmol) was added to a solution of 6-phenoxynicotinic acid (**24b**) (150 mg, 0.70 mmol) and **5c** (116.6 mg,

0.77 mmol) in EtOAc (4 mL) and pyridine (4 mL, 48.80 mmol) to afford after preparative HPLC **24a** (120 mg, 49%) as a white powder. ¹**H NMR** (500 MHz, DMSO- d_6) δ 10.86 (s, 1H), 8.75 (d, J = 2.5 Hz, 1H), 8.62 (d, J = 5.5 Hz, 1H), 8.49 (d, J = 2.1 Hz, 1H), 8.40 (dd, J = 8.7, 2.5 Hz, 1H), 8.02 (dd, J = 5.5, 2.1 Hz, 1H), 7.47 (t, J = 7.8 Hz, 2H), 7.28 (t, J = 7.4 Hz, 1H), 7.20 (dd, J = 8.5, 3.5 Hz, 3H), 3.89 (s, 3H). ¹³**C NMR** (126 MHz, DMSO- d_6) δ 165.10, 165.03, 164.38, 153.05, 150.45, 148.09, 148.00, 146.72, 139.75, 129.68, 125.03, 124.85, 121.32, 116.47, 115.01, 110.75, 52.31. **LC-MS** calcd for C₁₉H₁₆N₃O₄ [M+H]⁺: 350.11, found 350.20.

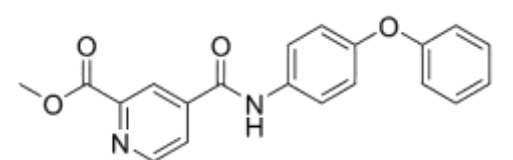
4-(6-phenoxynicotinamido)picolinic acid (24)

$$HO \xrightarrow[N]{} H \xrightarrow[O]{} O$$

According to **GP2**, to a suspension of **24a** (50 mg, 0.14 mmol) in THF (0.5 mL), an aq. solution of LiOH (0.5 mL) was added to afford after

preparative HPLC compound **24** (18 mg, 38%) as a white solid. ¹**H NMR** (500 MHz, DMSO- d_6) δ 10.86 (s, 1H), 8.76 (d, J = 2.3 Hz, 1H), 8.61 (d, J = 5.5 Hz, 1H), 8.47 (d, J = 1.8 Hz, 1H), 8.41 (dd, J = 8.7, 2.4 Hz, 1H), 8.03 (dd, J = 5.5, 2.0 Hz, 1H), 7.47 (t, J = 7.9 Hz, 2H), 7.28 (t, J = 7.5 Hz, 1H), 7.21 (dd, J = 8.1, 4.1 Hz, 3H). ¹³**C NMR** (126 MHz, DMSO- d_6) δ 165.84, 165.26, 164.56, 153.22, 149.94, 149.25, 148.17, 147.14, 139.95, 129.85, 125.19, 125.06, 121.49, 116.37, 114.93, 110.92. **HR-MS** calcd for C₁₈H₁₄N₃O₄ [M+H]⁺: 336.0978, found 336.09659.

methyl 4-((4-phenoxyphenyl)carbamoyl)picolinate (25a)



According to **GP1**, T_3P (2.7 mL, 9.11 mmol) was added to a solution of 2-(methoxycarbonyl)isonicotinic acid (**25c**) (150

mg, 0.83 mmol) and 4-phenoxyaniline (25b) (168.7 mg, 0.91 mmol) in EtOAc (4.7 mL)

and pyridine (4.7 mL, 58.0 mmol) to afford after preparative HPLC **25a** (160 mg, 57%) as a white powder. ¹**H NMR** (500 MHz, DMSO- d_6) δ 10.60 (s, 1H), 9.17 (s, 1H), 8.80 (d, J = 15.3 Hz, 2H), 8.04 (d, J = 8.4 Hz, 2H), 7.46 (t, J = 7.7 Hz, 2H), 7.24 (t, J = 7.4 Hz, 1H), 7.15 – 7.10 (m, 4H), 3.91 (s, 2H). ¹³**C NMR** (126 MHz, DMSO- d_6) δ 165.64, 165.51, 160.61, 155.73, 145.74, 144.88, 136.39, 130.67, 130.50, 128.77, 127.47, 125.74, 124.88, 120.03, 117.79, 52.87. **LC-MS** calcd for C₂₀H₁₇N₂O₄ [M+H]⁺: 349.12, found 349.20.

4-((4-phenoxyphenyl)carbamoyl)picolinic acid (25)

According to **GP2**, to a suspension of **25a** (50 mg, 0.14 mmol) in THF (0.5 mL), an aq. solution of LiOH (0.5 mL) was added to afford after preparative HPLC

compound **25** (29 mg, 60%) as a yellow solid. ¹**H NMR** (500 MHz, DMSO- d_6) δ 10.70 (s, 1H), 8.91 (d, J = 4.9 Hz, 1H), 8.53 (d, J = 1.6 Hz, 1H), 8.09 (dd, J = 5.0, 1.7 Hz, 1H), 7.80 (d, J = 8.9 Hz, 2H), 7.39 (t, J = 7.9 Hz, 2H), 7.13 (t, J = 7.4 Hz, 1H), 7.09 – 7.03 (m, 2H), 7.01 (d, J = 8.1 Hz, 2H). ¹³**C NMR** (126 MHz, DMSO- d_6) δ 165.87, 162.99, 157.11, 152.74, 150.35, 149.27, 143.09, 134.24, 130.04, 124.80, 123.22, 122.34, 122.30, 119.23, 118.15. **HR-MS** calcd for C₁₉H₁₅N₂O₄ [M+H][†]: 335.10263, found 335.10127.

4-((4-phenoxybenzyl)amino)picolinic acid (26)

In a round bottom flask, 1-(bromomethyl)-4-phenoxybenzene **26b** (100 mg, 0.38 mmol, 1 equiv.) and **5c** (63.6 mg, 0.42 mmol, 1.1 equiv.)

were dissolved in 8 mL THF. Followed by the addition of K_2CO_3 (105 mg, 0.76 mmol, 2 equiv.). The mixture was refluxed at 65 °C for 16 h. After reaction completion, K_2CO_3 was filtered and THF was removed using a rotavap. The crude mixture was purified using preparative HPLC to get the already hydrolyzed desired product **26** (25 mg, 21%) as a white powder. ¹**H NMR** (500 MHz, DMSO- d_6) δ 8.05 (d, J = 7.2 Hz, 1H), 7.94 (d, J = 20.4 Hz, 2H), 7.38 (t, J = 7.4 Hz, 4H), 7.14 (t, J = 7.4 Hz, 1H), 6.98 (t, J = 8.6 Hz, 4H), 6.80 (d, J = 2.8 Hz, 1H), 6.69 (dd, J = 7.3, 2.8 Hz, 1H), 5.61 (s, 2H). ¹³**C NMR** (126 MHz, DMSO- d_6) δ 162.25, 158.93, 156.63, 156.35, 154.80, 142.91, 131.59, 130.17, 130.14, 123.75,

118.83, 118.67, 108.82, 107.29, 55.95. **HR-MS** calcd for $C_{19}H_{15}N_2O_3$ [M–H]⁻: 319.10882, found 319.10895.

4-((4-phenoxyphenyl)amino)picolinic acid (27)

$$HO \bigvee_{O} \bigvee_{H} \bigcap_{O} \bigcirc$$

A seal tube containing methyl 4-bromopicolinate (27c) (200 mg, 0.93 mmol), 4-phenoxyaniline (27b) (205.7 mg 1.11 mmol), Xantphos (53.6 mg, 0.09 mmol), palladium (II)

acetate (41.6 mg, 0.18 mmol) and Cs_2CO_3 (905 mg, 2.78 mmol) in 1-butanol (8 mL) was degassed with N_2 gas for 5 min. The tube was then sealed and placed on a heating block while stirring and heating at 95 °C for 16 h. After completion, the mixture was passed through a bed of celite and purified using preparative HPLC to afford compound **27** (50 mg, 18%) as a white powder. ¹H NMR (500 MHz, DMSO- d_6) δ 10.26 (s, 1H), 8.05 (d, J = 6.7 Hz, 1H), 7.45 – 7.39 (m, 3H), 7.34 (d, J = 8.4 Hz, 2H), 7.17 (t, J = 7.4 Hz, 1H), 7.09 (dd, J = 18.2, 8.2 Hz, 4H), 7.01 (dd, J = 6.8, 2.7 Hz, 1H). ¹³C NMR (126 MHz, DMSO- d_6) δ 160.34, 156.74, 156.51, 154.62, 148.81, 140.72, 133.02, 130.23, 125.36, 123.80, 119.74, 118.87, 108.59, 107.33. HR-MS calcd for $C_{18}H_{13}N_2O_3[M-H]^-$: 305.09317, found 305.09347.

methyl 4-(3-(4-phenoxyphenyl)ureido)picolinate (28a)

In a round bottom flask, to a solution of **5c** (150 mg, 0.98 mmol) in DMF (2 mL) was added 1-isocyanato-4-phenoxybenzene

(28b) (312.4 mg, 1.48 mmol). The mixture was left stirring at rt for 1 h to afford after preparative HPLC 28a (135 mg, 38 %) as a white powder. ¹H NMR (500 MHz, DMSO- d_6) δ 9.41 (s, 1H), 8.97 (s, 1H), 8.47 (d, J = 5.5 Hz, 1H), 8.24 (d, J = 2.2 Hz, 1H), 7.58 (dd, J = 5.6, 2.2 Hz, 1H), 7.49 (d, J = 8.8 Hz, 2H), 7.37 (t, J = 7.7 Hz, 2H), 7.10 (t, J = 7.4 Hz, 1H), 6.99 (dd, J = 19.0, 8.4 Hz, 4H), 3.87 (s, 3H). ¹³C NMR (126 MHz, DMSO- d_6) δ 165.47, 157.51, 152.16, 151.39, 150.35, 148.24, 147.79, 134.84, 130.04, 122.99, 120.69, 119.76, 117.83, 115.06, 113.43, 52.47. **LC-MS** calcd for C₂₀H₁₈N₃O₄ [M+H]⁺: 364.13, found 364.20.

4-(3-(4-phenoxyphenyl)ureido)picolinic acid (28)

According to **GP2**, to a suspension of **28a** (50 mg, 0.14 mmol) in THF (0.5 mL), an aq. solution of LiOH (0.5 mL) was added to afford

after preparative HPLC compound **28** as (19 mg, 40%) a white solid. ¹**H NMR** (500 MHz, DMSO- d_6) δ 8.45 (d, J = 6.0 Hz, 1H), 8.13 (s, 2H), 7.64 (d, J = 8.5 Hz, 2H), 7.37 (t, J = 7.9 Hz, 2H), 7.09 (t, J = 7.4 Hz, 1H), 6.99 (dd, J = 17.4, 8.4 Hz, 4H). ¹³**C NMR** (126 MHz, DMSO- d_6) δ 165.51, 163.59, 157.58, 152.33, 151.27, 149.27, 135.27, 130.02, 122.92, 120.77, 119.73, 117.75, 116.65, 113.81, 112.87. **HR-MS** calcd for C₁₉H₁₄N₃O₄ [M-H]⁻: 348.09898, found 348.09910.

methyl 4-((4-phenoxyphenyl)sulfonamido)picolinate (29a)

To a solution of $\mathbf{5c}$ (100 mg, 0.66 mmol, 1 equiv.) and K_2CO_3 (227 mg, 1.64 mmol, 2.5 equiv.) in ACN, 4-phenoxybenzenesulfonyl

chloride (**29b**) (265 mg, 0.98 mmol, 1.5 equiv.) was added and the reaction mixture was heated at 80 °C for 16 h. Once the reaction was completed, the mixture was diluted with EtOAc and washed with sat. NaHCO₃ (x 3) solution. The combined organic layers were dried over MgSO₄ to obtain after preparative HPLC **29a** (58 mg, 2 %) as a white powder. ¹**H NMR** (500 MHz, DMSO- d_6) δ 11.34 (s, 1H), 8.43 (s, 1H), 7.87 (d, J = 8.6 Hz, 2H), 7.73 (s, 1H), 7.45 (t, J = 7.8 Hz, 2H), 7.26 (q, J = 7.4, 6.6 Hz, 2H), 7.11 (dd, J = 12.9, 8.4 Hz, 4H), 3.85 (s, 3H). ¹³**C NMR** (126 MHz, DMSO- d_6) δ 161.82, 154.85, 130.92, 130.38, 129.79, 128.09, 125.70, 120.86, 118.05, 115.16, 113.82. **LC-MS** calcd for C₁₉H₁₇N₂O₅S [M+H]⁺:385.09, found 385.10.

4-((4-phenoxyphenyl)sulfonamido)picolinic acid (29)

According to **GP2**, to a suspension of **29a** (50 mg, 0.13 mmol) in THF (0.5 mL), an aq. solution of LiOH (0.5 mL) was added to afford after preparative

HPLC compound **29** (25 mg, 52%) as a white powder. ¹**H NMR** (500 MHz, DMSO- d_6) δ 8.26 (d, J = 6.1 Hz, 1H), 7.89 – 7.83 (m, 2H), 7.65 (d, J = 2.4 Hz, 1H), 7.43 (t, J = 7.8 Hz, 2H), 7.22 (t, J = 7.4 Hz, 1H), 7.19 (dd, J = 6.1, 2.4 Hz, 1H), 7.12 – 7.04 (m, 4H). ¹³**C NMR** (126 MHz, DMSO- d_6) δ 164.33, 160.84, 154.71, 134.51, 130.48, 129.14, 125.10,

120.28, 117.62, 114.76, 113.87. **HR-MS** calcd for $C_{18}H_{13}N_2O_5S$ [M-H]⁻: 369.05507 found, 369.05524.

methyl 4-azidopicolinate (30c)

To a solution of methyl 4-bromopicolinate (**27c**) (500 mg, 2.77 mmol, 1 equiv.) in DMF/ H_2O (20:1, 0.8 M) NaN₃ (215 mg, 3.30 mmol, 1.2 equiv.) was added portion wise and the reaction mixture was heated at 80 °C overnight. Once the reaction was completed the mixture was diluted with EtOAc and washed with sat. aq. NaHCO₃ (x 3). The combined organic layers were dried over MgSO₄ to obtain after evaporation methyl **30c** (400 mg, 83%) as a yellow oil. ¹H **NMR** (500 MHz, DMSO- d_6) δ 8.63 (d, J = 5.4 Hz, 1H), 7.67 (d, J = 2.2 Hz, 1H), 7.41 (dd, J = 5.3, 2.3 Hz, 1H), 3.89 (s, 3H). ¹³C **NMR** (126 MHz, DMSO- d_6) δ 164.69, 151.12, 149.62, 149.02, 117.54, 115.30, 52.63. **LC-MS** calcd for $C_7H_7N_4O_2$ [M+H]⁺:179.06, found 179.1.

To a solution of **30c** (200 mg, 1.12 mmol, 1.0

methyl 4-(4-(4-phenoxyphenyl)-1H-1,2,3-triazol-1-yl)picolinate (30a)

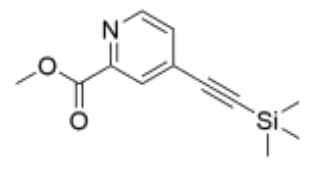
and 1-ethynyl-4-phenoxybenzene equiv.) (**30b**) (218.05 mg, 1.12 mmol, 1.0 equiv.) in (THF/ H_2O , 2:1, 0.4 M) sodium ascorbate (88.96 mg, 0.45 mmol, 0.4 equiv.) was added, followed by the addition of CuSO₄·5H₂O (56 mg, 0.22 mmol, 0.2 equiv.). The reaction mixture was vigorously stirred for 2 d at 65 °C. After completion of the reaction, THF was removed under vacuum, and the aqueous phase was extracted with EtOAc (3x). The combined organic layers were dried over MgSO4 and concentrated in vacuo to afford after preparative HPLC 30a (250 mg, 60%) as a white solid. ¹**H NMR** (500 MHz, CD₃CN) δ 8.87 (d, J = 5.3 Hz, 1H), 8.80 (s, 1H), 8.53 (d, J = 2.1 Hz, 1H), 8.06 (dd, J = 5.3, 2.3 Hz, 1H), 7.92 (d, J = 7.8 Hz, 2H), 7.42 (t, J = 7.3 Hz, 2H), 7.18 (t, J = 7.4 Hz, 1H), 7.12 – 7.06 (m, 4H), 3.97 (s, 3H). ¹³**C NMR** (126 MHz,CD₃CN) δ 165.9, 158.9, 157.8, 152.8, 151.3, 149.0, 145.2, 131.3, 131.1, 128.4, 126.1, 124.9, 120.2, 120.0, 119.5, 117.5, 115.8, 53.6. **LC-MS** calcd for $C_{21}H_{17}N_4O_3$ [M+H]⁺: 373.13, found 373.29.

4-(4-(4-phenoxyphenyl)-1H-1,2,3-triazol-1-yl)picolinic acid (30)

To a stirred suspension of **30a** (160 mg, 0.43 mmol, 1 equiv.) in CH₃OH (0.2 M), 10% aq. NaOH (43 μ L, 2.15 mmol, 5 equiv.) was added and the solution was stirred at 65 °C. After

completion of the reaction, CH₃OH was removed under vacuum and the crude residue was dissolved in EtOAc. Aq. HCl (2 M) was added, and the aqueous phase was extracted with EtOAc (3×). The combined organic layers were dried over MgSO₄ and concentrated in vacuo to afford after preparative HPLC compound **30** (90 mg, 58%) as a yellow solid. 1 H NMR (500 MHz DMSO- d_6) δ 9.64 (s, 1H), 8.94 (d, 1H, J=5.3 Hz), 8.61 (d, 1H, J=2.1 Hz), 8.26 (dd, 1H, J=2.2, 5.4 Hz), 7.99 (d, 2H, J=7.7 Hz), 7.44 (t, 2H, J=7.3 Hz), 7.1-7.2 (m, 3H), 7.10 (d, 2H, J=7.8 Hz). 13 C NMR (126 MHz, DMSO- d_6) δ 165.46, 157.10, 156.24, 151.64, 150.67, 147.48, 143.66, 130.18, 127.26, 124.89, 123.85, 119.35, 119.01, 118.98, 116.17, 114.12. HR-MS calcd for C₂₀H₁₃N₄O₃ [M-H]⁻: 357.09931, found 357.09947.

methyl 4-((trimethylsilyl)ethynyl)picolinate (31d)



To a solution of methyl 4-bromopicolinate (**27c**) (300 mg, 1.39 mmol, 1 equiv.) in dry ACN (3 mL), DIPEA (0.48 mL, 2.79 mmol, 2 equiv.), CuI (24 mg, 0.13 mmol, 0.1 equiv.), Pd(PPh₃)₂Cl₂

(29.33 mg, 0.04 mmol, 0.03 equiv.) and ethynyltrimethylsilane (0.59 mL, 4.26 mmol, 3 equiv.) were added in a seal tube and placed on a heating block. The mixture was degassed with N₂ gas before sealing the tube and heated to 90 °C for 16 h. Then, the mixture was filtered over a pad of celite and rinsed with ethyl acetate. The organic phase was washed with water (x2), dried over MgSO₄ and concentrated in vacuo. The crude material was purified by column chromatography on silica using PE:EtOAc to afford compound **31d** (300 mg, 92%) as a yellow oil. 1 H **NMR** (500 MHz, MeOD- d_4) δ 8.64 (d, J = 5.1 Hz, 1H), 8.08 (d, J = 1.5 Hz, 1H), 7.61 (d, J = 5.0 Hz, 1H), 3.98 (s, 3H), 0.28 (s, 9H). 13 C **NMR** (126 MHz, MeOD- d_4) δ 166.01, 165.99, 150.90, 149.00, 134.36, 130.30, 128.20, 102.75, 101.92, 53.41, 0. **LC-MS** calcd for C₁₂H₁₆NO₂Si [M+H]⁺: 234.09, found 234.01.

methyl 4-ethynylpicolinate (31c)

A solution of **31d** (300 mg, 1.29 mmol, 1 equiv.) in 3 mL THF was cooled to 0 °C using an ice batch. Acetic acid (0.1 mL, 1.77 mmol, 1.4 equiv.) and TBAF (0.6 mL, 1.93 mmol, 1.5 equiv.) were added.

And the reaction mixture was left stirring for 1 h. The solvent was removed in *vacuo*, the crude was then extracted with EtOAc (3x). The combined organic layer were dried over MgSO₄ and concentrated in vacuo to afford after purification by column chromatography using PE:EtOAc the desired product **31c** (155 mg, 75%) as an offwhite solid. ¹**H NMR** (500 MHz, MeOD- d_4) δ 8.66 (d, J = 5.0 Hz, 1H), 8.12 (d, J = 1.5 Hz, 1H), 7.67 (d, J = 5.0 Hz, 1H), 4.10 (s, 1H), 3.98 (s, 3H). ¹³**C NMR** (126 MHz, MeOD- d_4) δ 165.95, 150.92, 149.07, 133.91, 130.69, 128.48, 85.89, 80.83, 53.41. **LC-MS** calcd for C₉H₈NO₂ [M+H]⁺: 162.05, found 162.20.

1-azido-4-phenoxybenzene (31b)

A solution of 4-phenoxyaniline (200 mg, 1.08 mmol, 1 equiv.) in ACN (8 mL) was cooled to 0 °C using an ice-bath. tert-butyl nitrite (0.3 mL, 2.70 mmol, 2.5 equiv.) was added dropwise

to the solution, followed by the dropwise addition of azidotrimethylsilane (0.2 mL, 1.62 mmol, 1.5 equiv.). The mixture was left stirring at 0 °C for 15 min, then at rt for 1 h. After reaction completion, the mixture was diluted with water (30 mL) and extracted with diethyl ether (2x). The combined organic layers were dried over MgSO₄ and concentrated in *vacuo* to get the compound **31b** (198 mg, 87%) as a brown oil, which was used in the next step without any further purification. On the LC-MS, the ionization was not clearly observed for this compound, hence it is not recorded. ¹H NMR (500 MHz, DMSO- d_6) δ 7.42 – 7.36 (m, 2H), 7.17 – 7.12 (m, 3H), 7.08 – 7.04 (m, 2H), 7.00 (d, J = 8.7 Hz, 2H). ¹³C NMR (126 MHz, DMSO- d_6) δ 156.76, 153.80, 134.48, 130.09, 123.51, 120.70, 120.33, 118.38.

methyl 4-(1-(4-phenoxyphenyl)-1H-1,2,3-triazol-4-yl)picolinate (31a)

$$0 \longrightarrow N=N$$

To a solution of **31c** (150 mg, 0.93 mmol, 1.0 equiv.) and **31b** (197 mg, 0.93 mmol, 1.0 equiv.) in 10 mL MeOH, sodium ascorbate

(74 mg, 0.37 mmol, 0.4 equiv.) was added, followed by the addition of CuSO₄ · 5H₂O (93 mg, 0.37 mmol, 0.4 equiv.). The reaction mixture was stirred at rt for 16 h. After completion of the reaction, MeOH was concentrated under vacuo and the crude was then diluted with water. A precipitate that formed was filtered and purified on column chromatography using DCM:MeOH (9:1) to afford compound **31a** (117 mg, 34%) as a yellow solid. ¹**H NMR** (500 MHz, DMSO- d_6) δ 9.64 (s, 1H), 8.82 (d, J = 5.0 Hz, 1H), 8.55 (d, J = 1.6 Hz, 1H), 8.13 (dd, J = 5.0, 1.7 Hz, 1H), 7.96 (d, J = 8.9 Hz, 2H), 7.46 (t, J = 7.8 Hz, 2H), 7.24 (t, J = 8.1 Hz, 3H), 7.13 (d, J = 8.0 Hz, 2H), 3.93 (s, 3H). ¹³**C NMR** (126 MHz, DMSO- d_6) δ 165.09, 157.28, 155.91, 150.71, 148.42, 144.20, 138.85, 131.73, 130.29, 124.24, 122.58, 122.38, 122.18, 120.48, 119.31, 119.25, 52.56. **LC-MS** calcd for $C_{21}H_{17}N_4O_3$ [M+H]*: 373.13, found 373.20.

4-(4-(4-phenoxyphenyl)-1H-1,2,3-triazol-1-yl)picolinic acid (31)

$$HO$$
 $N=N$
 $N=N$

In a round bottom flask containing **31a** (100 mg, 0.27 mmol, 1 equiv.) in 10 mL THF: water (2:1) mixture, LiOH (32.15 mg, 1.34 mmol, 5 equiv.) was added. The reaction was stirred at

room temperature for 16 h. After reaction completion, the crude was purified using prep HPLC to get the desired compound **31** (12 mg, 12.5%) as a cream-white powder. **1H NMR** (500 MHz, DMSO- d_6) δ 9.64 (s, 1H), 8.80 (d, J = 5.0 Hz, 1H), 8.55 (s, 1H), 8.11 (d, J = 5.0 Hz, 1H), 7.97 (d, J = 8.6 Hz, 2H), 7.45 (t, J = 7.8 Hz, 2H), 7.23 (t, J = 8.4 Hz, 3H), 7.12 (d, J = 7.9 Hz, 2H). **13C NMR** (126 MHz, DMSO- d_6) δ 166.16, 157.29, 155.95, 150.36, 149.73, 144.41, 138.84, 131.79, 130.33, 124.27, 122.34, 122.21, 120.38, 119.35, 119.28. HRMS calcd for $C_{20}H_{13}N_4O_3$ [M-H]⁻: 357.09931, found 357.09949.

Biological evaluation

Whole-cell bacterial uptake assay (ECF-T assay)

The ECF inhibitors and their inhibitory effect on folate uptake in the Grampositive model organism *Lactobacillus casei* were studied in a whole-cell uptake assay as recently published in our group [2]. For this purpose, 20 μ L of inhibitor was added to the wells of a MultiScreen HTS Filter Plate containing 175 μ L of *L. casei* culture diluted in citrate buffer. The blank was determined

with 185 μ L citrate buffer and 10 μ L of DMSO. 5 μ L of radiolabeled folic acid was added to each well (2 μ M, Moravek Biochemicals, Brea, CA). Using this method, we determined the percentage of inhibition at 12.5, 50, 100 and 200 μ M for the compounds and the IC₅₀ values for our best compounds. The assay was performed in both technical and biological duplicate ensuring the reliability and consistency of the data. Subsequently, the gathered data were analyzed using GraphPad Prism, version 10 (GraphPad Software, San Diego, CA, USA).

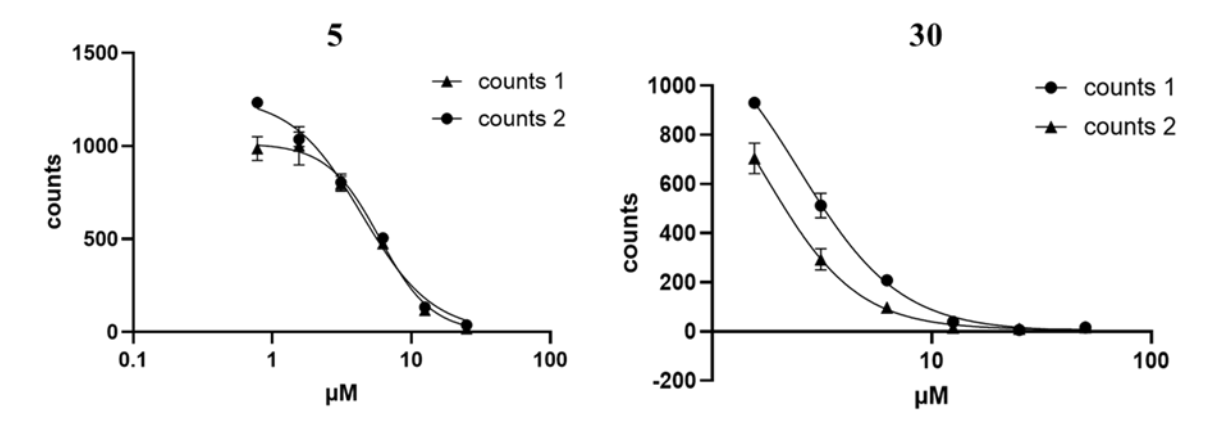


Figure S1. Half maximal inhibitory concentration (IC $_{50}$) values for the best compound 5 and 30.

Proteoliposome uptake assay

Purification of Ld_ECF-FolT2 and Ld_ECF-PanT

For Ld_ECF-FolT2 and Ld_ECF-PanT, 2 mL of membrane vesicles were resuspended in 20 mL of solubilization buffer (50 mM KPi pH 7.5, 300 mM NaCl, 1% (w/v) DDM) and solubilized for approximately 60 minutes under gentle agitation. Insoluble material was removed by ultracentrifugation (MLA-80 rotor, 4°C, 80,000 rpm, 30 min). In parallel, 1.5 mL of 50% Ni2+-sepharose slurry was equilibrated with ~15 mL of wash buffer (50 mM KPi pH 7.5, 300 mM NaCl, 50 mM Imidazole pH 8.0, 0.05% (w/v) DDM) after ethanol removal and washing with ~25 mL Milli-Q water (MQ).

The equilibrated Ni2+-sepharose beads were incubated with solubilized membrane vesicles for less than 1 hour with gentle rocking. The suspension was applied to a 10 mL poly-prep Bio-Rad column, washed with 15 mL wash buffer, and proteins were eluted with elution buffer (50 mM KPi pH 7.5, 300 mM NaCl, 500 mM Imidazole pH 8.0, 0.05% (w/v) DDM) in defined fractions. The elution fraction with the highest

protein concentration was further purified by SEC using a Superdex 200 10/300 GL column (GE Healthcare) equilibrated with gel filtration buffer (50 mM KPi pH 7.5, 150 mM NaCl, 0.05% (w/v) DDM).

Protein reconstitution into liposomes

For reconstitution into liposomes, a lipid mixture (3:1 w/w E. coli polar lipids: egg phosphatidylcholine) was prepared at 20 mg/mL in 50 mM KPi pH 7.5. Liposomes were generated by extrusion through a 0.4 µm polycarbonate filter and destabilized with Triton X-100 until ~50-60% of the initial absorbance at 540 nm was achieved. Purified protein was incorporated at a 1:250 (w/w) protein:lipid ratio, followed by sequential Bio-Bead SM-2 treatments to remove detergent. Proteoliposomes were harvested by ultracentrifugation, aliquoted, flash-frozen, and stored in liquid nitrogen.

Radiolabelled-substrate uptake assay

Radiolabelled substrate uptake assays were performed to assess the inhibitory effects of compounds on LdECF-FolT2 transporters. Proteoliposomes containing Mg-ATP were exposed to radiolabelled folic acid, and uptake was monitored over 4 minutes at five time points. The transport activity was quantified as picomoles of substrate per microgram of transporter protein.

Uptake assay with ECF transporters

To facilitate active substrate import, proteoliposomes containing Ld_ECF-FolT2 were loaded with Mg-ATP or Mg-ADP (10 mM) and 50 mM KPi, pH 7.5, in a final volume of 0.5–1 mL. Nucleotides were enclosed within the lumen of the proteoliposomes, and protein orientation was scrambled by subjecting the samples to three freeze-thaw cycles (flash-freezing in liquid nitrogen followed by thawing on a metal block). Homogeneity in proteoliposome size distribution was achieved by extruding the samples 11–13 times through a 0.4 μ m polycarbonate filter using a pre-equilibrated extruder (50 mM KPi, pH 7.5).

External nucleotides were removed by diluting the extruded proteoliposomes with 50 mM KPi, pH 7.5, to 6 mL, followed by ultracentrifugation (MLA-80 rotor, 4°C, 80,000 rpm, 30 min). The resulting proteoliposome pellet was resuspended in 50 mM KPi, pH

7.5. Subsequently, $8 \mu L$ of an inhibitory compound or DMSO (5%) was added to reach a final volume of 160 μL (0.03125 mg/mL protein). The proteoliposomes were incubated with the inhibitor on ice for at least 60 min.

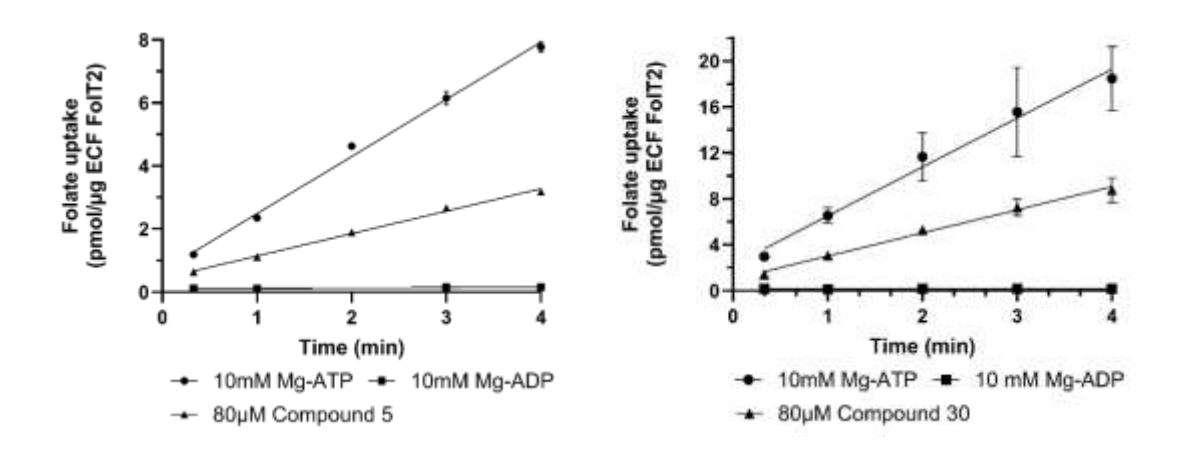
Uptake activity measurements were performed at five time points. A substrate buffer (713 μ L) supplemented with 37 μ L of inhibitory compound or DMSO (5%) was incubated at 30°C with stirring. For Ld_ECF-FolT2 proteoliposomes, the substrate buffer contained 50 mM KPi, pH 7.5, with 110 nM folic acid (104.5 nM cold and 5.5 nM 3H-radiolabeled).

The uptake reaction was initiated by adding proteoliposomes containing 2.5 μg of protein (75 μL of 160 μL) to the prewarmed substrate buffer. Samples (145 μL , containing 0.5 μg of protein) were collected at 20 s, 1 min, 2 min, 3 min, and 4 min. Reactions were quenched with 2 mL of ice-cold 50 mM KPi, pH 7.5, and filtered over a 450 nm BA-85 nitrocellulose filter (Cytiva). The filters were washed with an additional 2 mL of ice-cold KPi buffer and dissolved in 1.8 mL of Ultima Gold liquid scintillation cocktail. After at least 60 min of incubation at room temperature, samples were vortexed, and radioactivity was measured using a Perkin Elmer Tri-Carb 2800TR Scintillation Counter.

All measurements were performed in technical duplicates. For control experiments, substrate uptake by Mg-ATP-loaded proteoliposomes was assessed in the absence of inhibitory compounds. For inhibited uptake controls, Mg-ADP-loaded proteoliposomes were used without inhibitors, demonstrating that the absence of Mg-ATP prevents transporter complex resetting, halting substrate uptake.

Radioactivity was collected as counts per minute (CPM), reflecting atomic decays detected by the scintillation counter. To quantify imported substrate, CPM values were converted into picomoles by dividing the total concentration of hot and cold substrate by the average substrate sample counts. The transport activity of each sample was calculated by normalizing the imported substrate quantity to the protein concentration, resulting in picomoles of substrate per microgram of transporter protein.

The averaged data from duplicate measurements were plotted over time, and standard deviations were calculated. A linear trendline was fitted to the data, and slopes were utilized to determine relative inhibition percentages of substrate uptake.



IC₅₀ determination

The half-maximal inhibitory concentration (IC_{50}) of compounds was determined using uptake assays with varying compound concentrations. Data analysis was conducted using GraphPad Prism, employing a nonlinear regression model (log(inhibitor) vs. normalized response with variable slope) to calculate IC_{50} values.

In vitro ADMET assays

Kinetic turbidimetric solubility

The desired compounds were sequentially diluted in DMSO in a 96-well plate. 1.5 μ L of each well were transferred into another 96-well plate and mixed with 148.5 μ L of PBS to reach 1% DMSO/PBS. For determination of solubility in 5% DMSO/PBS, 7.5 μ L were mixed with 142.5 μ L PBS. Plates were shaken for 5 min at 600 rpm at room temperature (rt), and the absorbance at 620 nm was measured. Absorbance values were normalized by blank subtraction and plotted using GraphPad Prism. Solubility (S) was determined based on the First X value of AUC function using a threshold of 0.005.

Lipophilicity determination

 $Log D_{7.4}$ was analyzed using an HPLC-based method. The UV retention time of reference compounds with known $Log D_{7.4}$ was determined and plotted toward their

LogD_{7.4}. Linear regression was used to determine the LogD_{7.4} of unknown compounds. Analysis was performed using a Vanquish Flex HPLC system with variable wavelength detector (Thermo Fisher, Dreieich, Germany) with the following conditions: EC150/2 NUCLEODUR C18 Pyramid column, 5 μ M (Macherey Nagel, Düren, Germany); eluent A: 50 mM NH₄OAc pH 7.4, eluent B: acetonitrile, and flow: 0.6 mL/min. The gradient was set to 0–100% B from 0 to 2.5 min, 100% B from 2.5 to 3.0 min, 100–0% B from 3.0 to 3.2 min, and 0% B from 3.2–5.0.

Cytotoxicity

To obtain information regarding the toxicity of our compounds, their impact on the viability of human cells was investigated. HepG2 cells (2x104 cells per well) were seeded in 96-well, flat-bottomed culture plates in 100 µL culture medium (DMEM containing 10% fetal calve serum, 1% penicillin-streptomycin). Twenty-four hours after seeding the cells, medium was removed and replaced by medium containing test compounds in a final DMSO concentration of 1%. Compounds were tested in duplicates at a single concentration or, for CC50 determination, at 8 concentrations that were prepared via 2-fold serial dilutions in 1% DMSO/medium. Epirubicin and doxorubicin were used as positive controls in serial dilutions starting from 10 µM, and rifampicin was used as a negative control (at 100 μM). The living cell mass was determined 48 h after treatment with compounds by adding 0.1 volumes of 3-(4,5dimethylthiazol-2-yl)-2,5-diphenyltetrazolium bromide (MTT) solution (5 mg/mL sterile PBS) (Sigma, St. Louis, MO) to the wells. After incubating the cells for 30 min at 37 °C (atmosphere containing 5% CO2), medium was removed and MTT crystals were dissolved in 75 µL of a solution containing 10% SDS and 0.5% acetic acid in DMSO. The optical density (OD) of the samples was determined photometrically at 570 nm in a PHERAstar Omega plate reader (BMG labtech, Ortenberg, Germany). To obtain percent viability for each sample, their ODs were related to those of DMSO controls. At least two independent measurements were performed for each compound. The calculation of CC₅₀ was performed using the nonlinear regression function of GraphPad Prism 10 (GraphPad Software, San Diego, CA, USA) [3].

Metabolic stability in liver microsomes

For the evaluation of phase I metabolic stability, the compound (1 µM) was incubated with 0.5 mg/mL pooled mouse or human liver microsomes (Xenotech, Kansas City, USA), 2 mM NADPH, 10 mM MgCl₂ at 37 °C for 120 min on a microplate shaker (Eppendorf, Hamburg, Germany). The metabolic stability of testosterone, verapamil and ketoconazole were determined in parallel to confirm the enzymatic activity of mouse liver microsomes. For human liver microsomes, testosterone, diclofenac and propranolol were used. The incubation was stopped after defined time points by precipitation of aliquots of the incubation mixture with 2 volumes of cold acetonitrile containing internal standard (15 nM diphenhydramine). Samples were stored on ice until the end of the incubation and precipitated protein was removed by centrifugation (15 min, 4 °C, and 4,000 g). Concentration of the remaining test compound at the different time points was analyzed by HPLC-MS/MS (Vanquish Flex coupled to a TSQ Altis Plus, Thermo Fisher, Dreieich, Germany) and used to determine half-life (t_{1/2}).

Stability in plasma

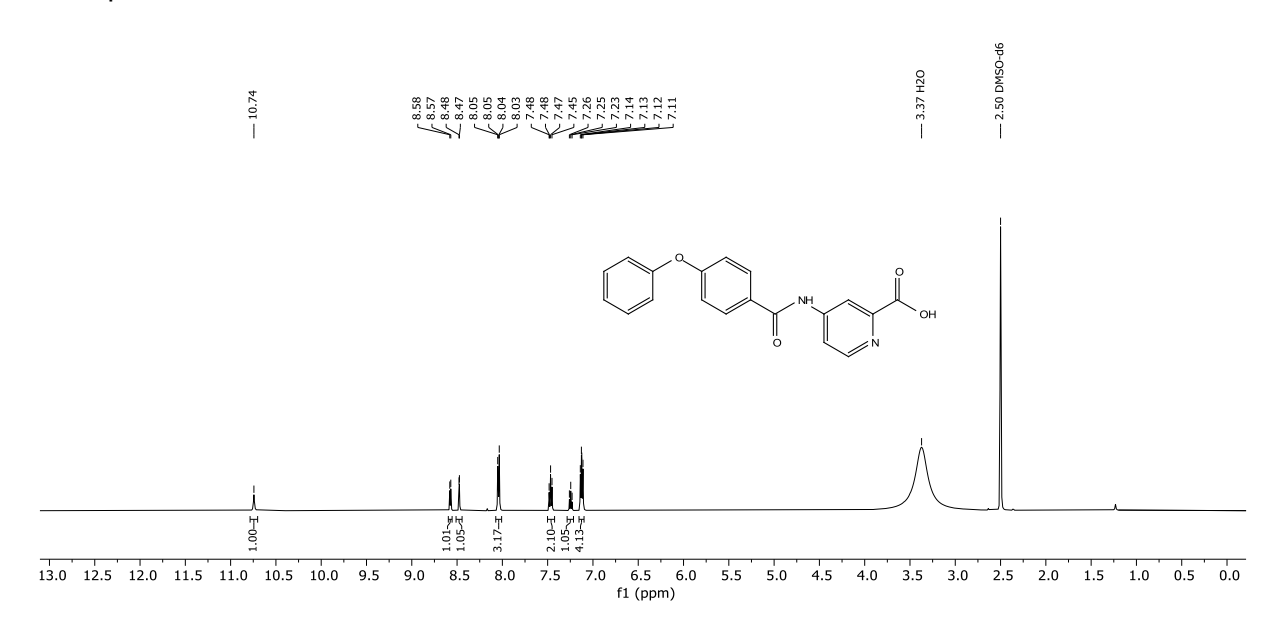
To determine stability in plasma, the compound (1 μ M) was incubated with pooled CD-1 mouse or human plasma (Neo Biotech, Nanterre, France). Samples were taken at defined time points by mixing aliquots with 4 volumes of acetonitrile containing internal standard (12.5 nM for Altis Plus measurements). Samples were stored on ice until the end of the incubation and precipitated protein was removed by centrifugation (15 min, 4 °C, 4,000 g, 2 centrifugation steps). Concentration of the remaining test compound at the different time points was analyzed by HPLC-MS/MS (Vanquish Flex coupled to a TSQ Altis Plus, Thermo Fisher, Dreieich, Germany) and used to determine half-life ($t_{1/2}$). The plasma stability of procain, propantheline and diltiazem were determined in parallel to confirm the enzymatic activity.

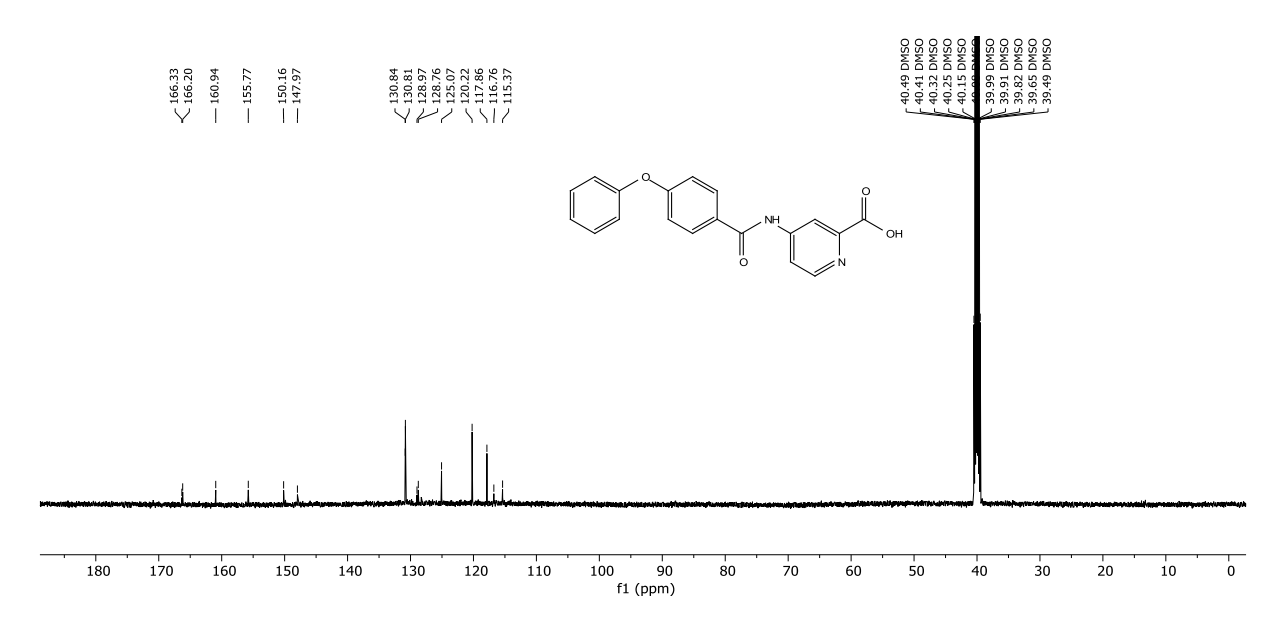
Inhibitory activity against the human ABC transporters ABCB1, ABCC1, and ABCG2

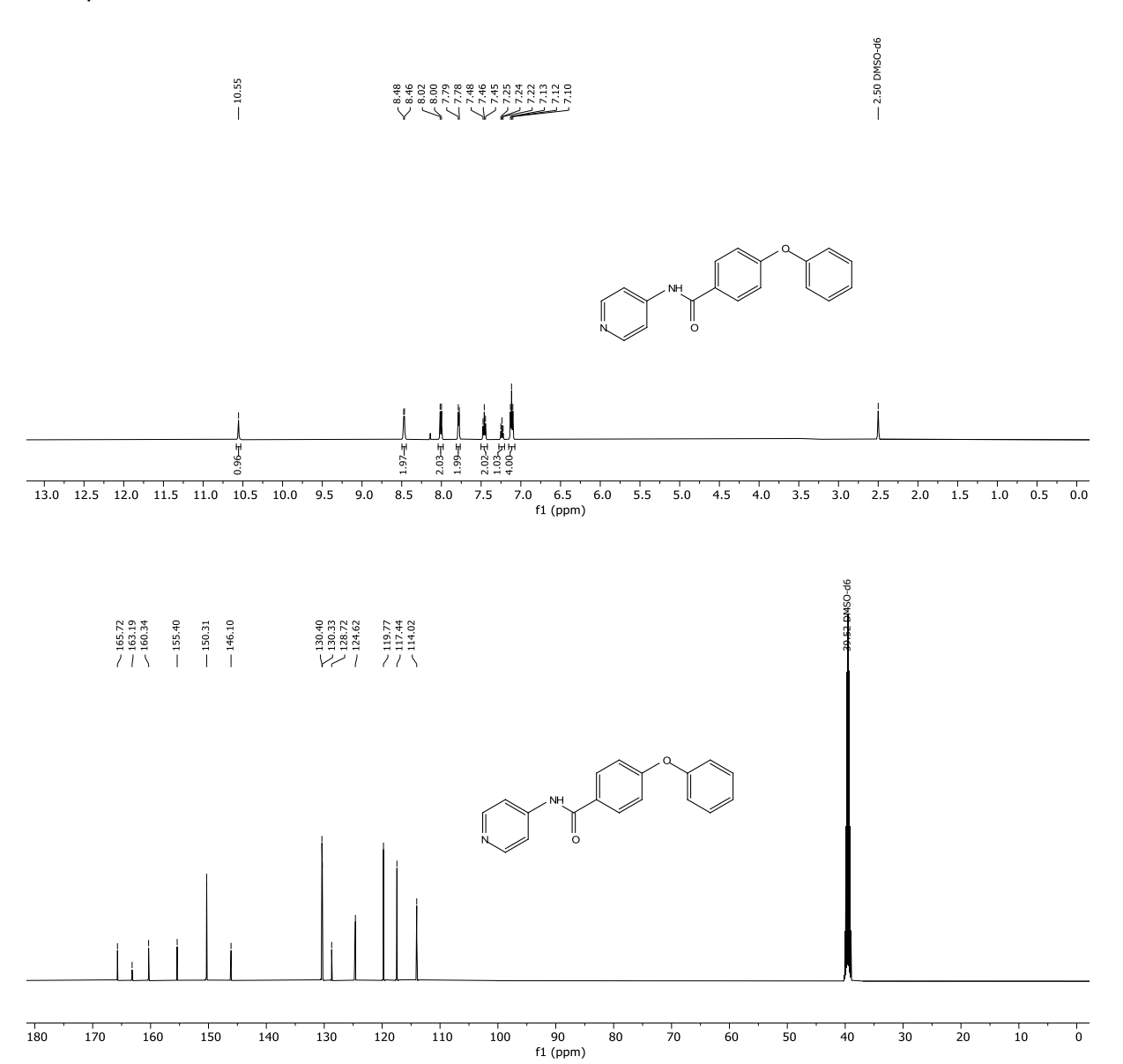
Calcein AM (ABCB1 and ABCC1), daunorubicin (ABCB1 and ABCC1), pheophorbide A (ABCG2), and Hoechst 33342 (ABCG2) assays were performed using ABCB1-expressing A2780/ADR, ABCC1-expressing H69AR, and ABCG2-expressing MDCK II

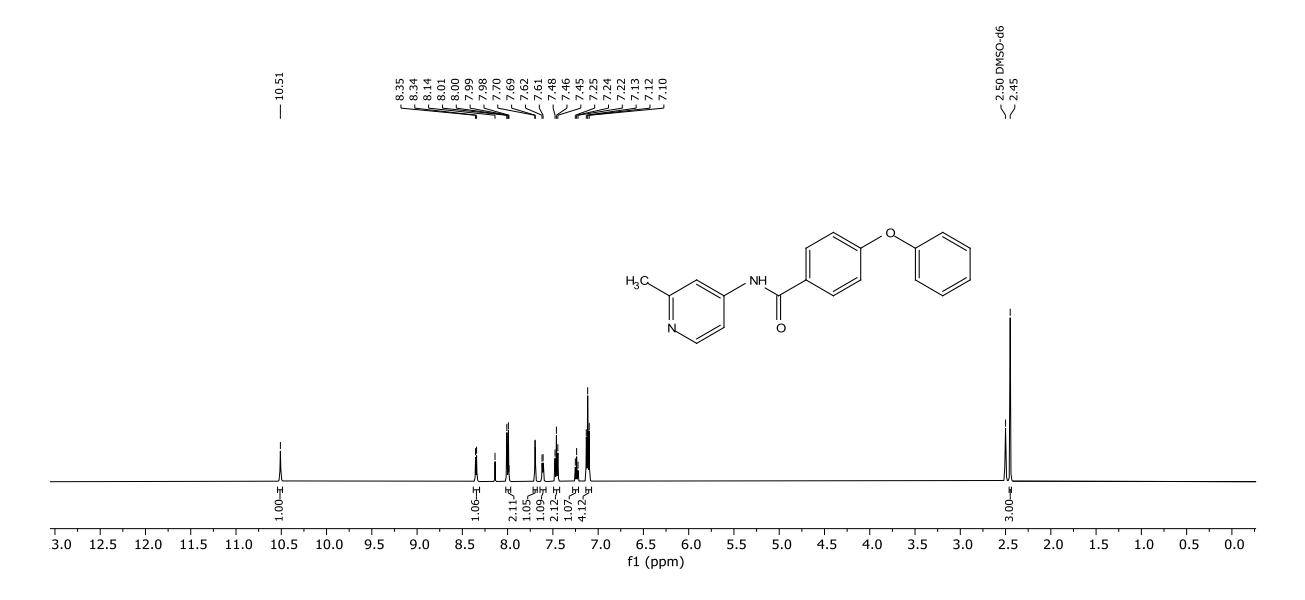
BCRP cells as described previously [4,5]. The cell lines were all a generous gift by Prof. Dr. Finn K. Hansen and Prof. Dr. Gerd Bendas (Pharmaceutical and Cellbiological Chemistry, University of Bonn, Germany). A volume of 20 µL of each test concentration of the compounds were transferred into clear (calcein AM, daunorubicin, and pheophorbide A) or black (Hoechst 33342) 96-well flat-bottom plates (Brand, Wertheim, Germany), and supplemented with 160 µL cell suspension (calcein AM: 30,000 cells/well; Hoechst 33342: 30,000 cells/well; daunorubicin: 45,000 cells/well; and pheophorbide A: 45,000 cells/well) in phenol red-free media (RPMI-1640: A2780/ADR and H69AR; DMEM: MDCK II BCRP) without other supplements. After pre-incubation (30 min) the respective fluorescence dye (20 μL) was added (calcein AM: 3.125 μ M; daunorubicin: 30 μ M; pheophorbide A: 5 μ M; and Hoechst 33342: 10 μ M), the fluorescence increase of each well was measured within 30 min in 30 s intervals (calcein AM assay; excitation: 485 nm, emission: 520 nm) using an Infinite M200 Pro microplate reader (Tecan, Männedorf, Switzerland), while the average steady-state fluorescence per well was measured after incubation (daunorubicin: 180 min; pheophorbide A: 180 min; and Hoechst 33342: 120 min) at excitation wave lengths of 360 nm (Hoechst 33342) and 488 nm (daunorubicin and pheophorbide A) and emission wave lengths of 460 nm [Infinite M200 Pro microplate reader (Tecan, Männedorf, Switzerland); Hoechst 33342] and 530/30 nm [FACSCalibur flow cytometer (Becton Dickinson, Franklin Lakes, New Jersey, USA); daunorubicin and pheophorbide A].

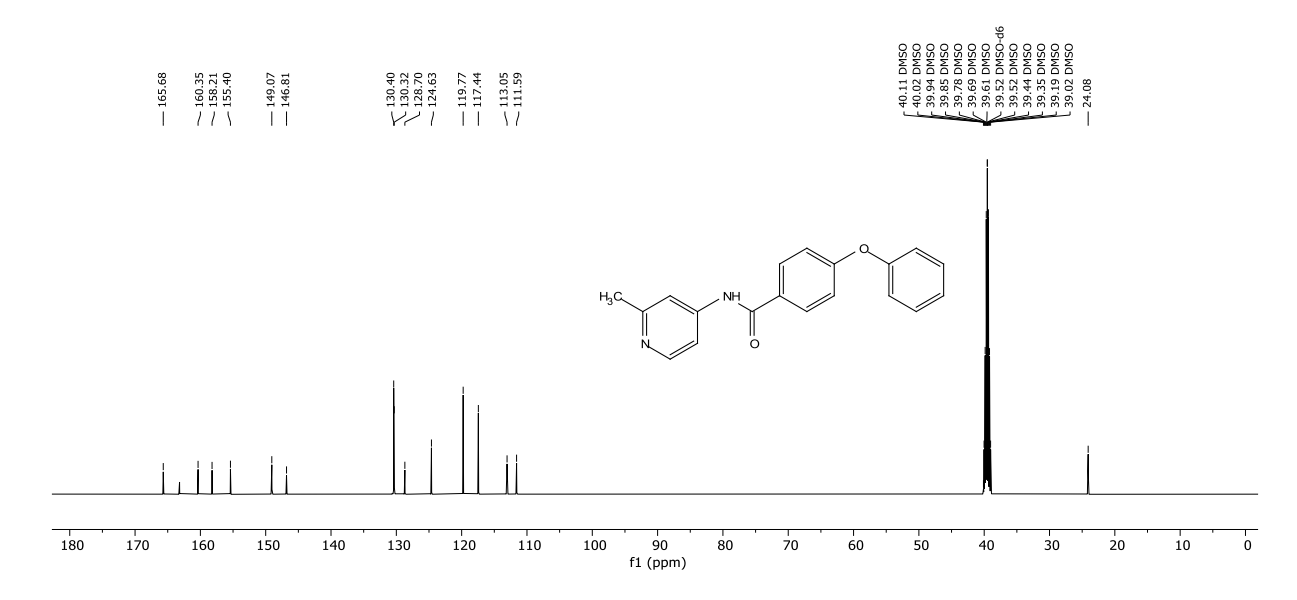
¹H- and ¹³C-NMR Spectra of the Final Compounds

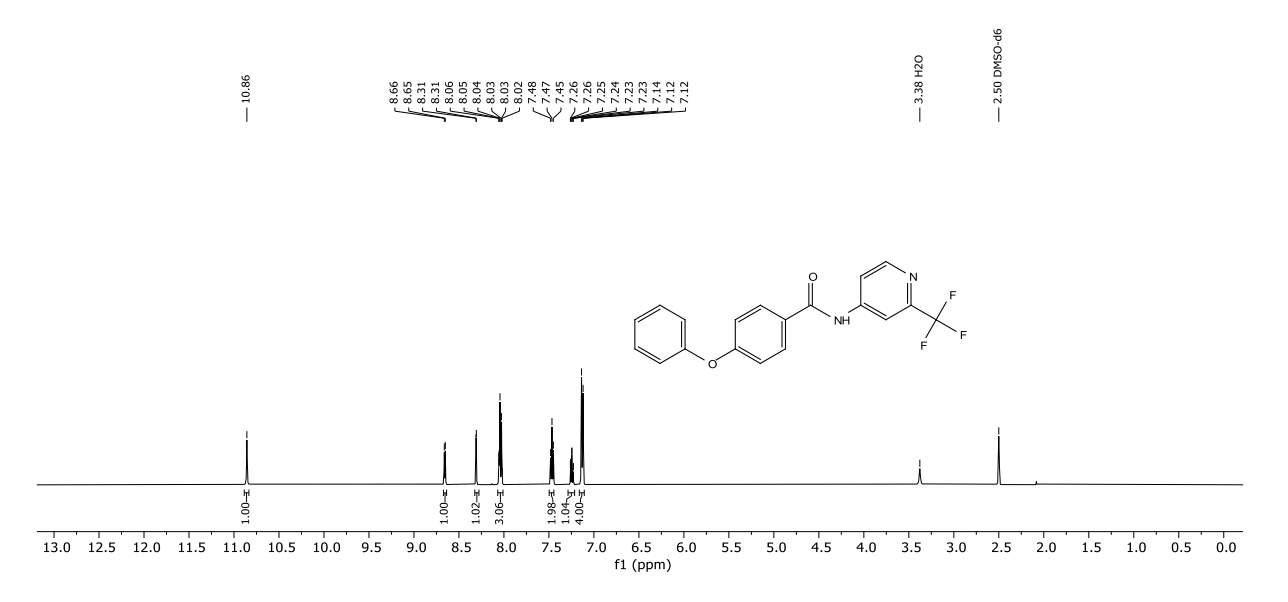


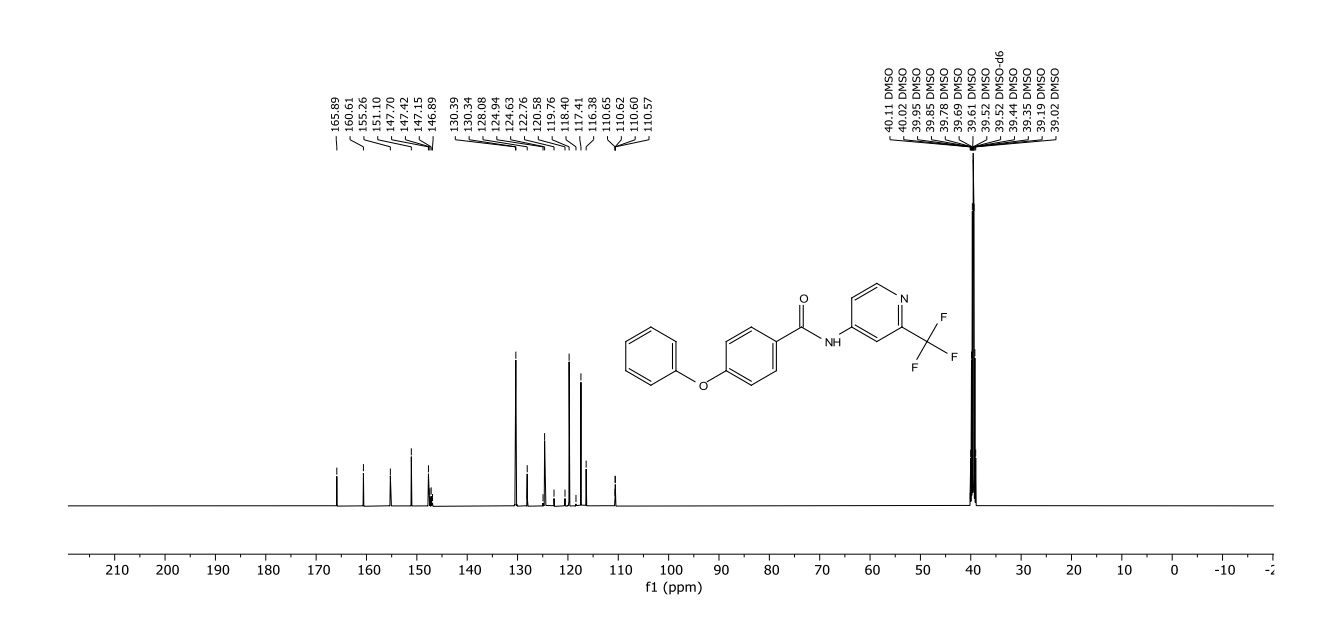


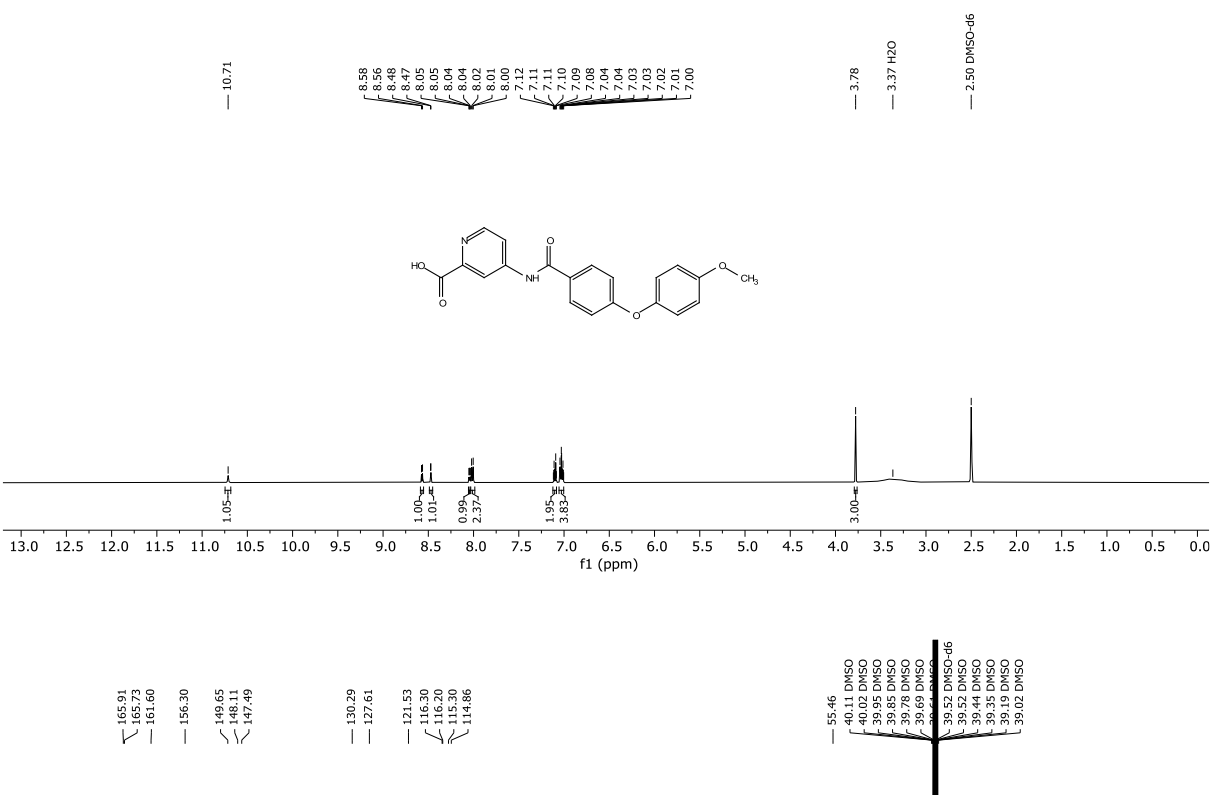


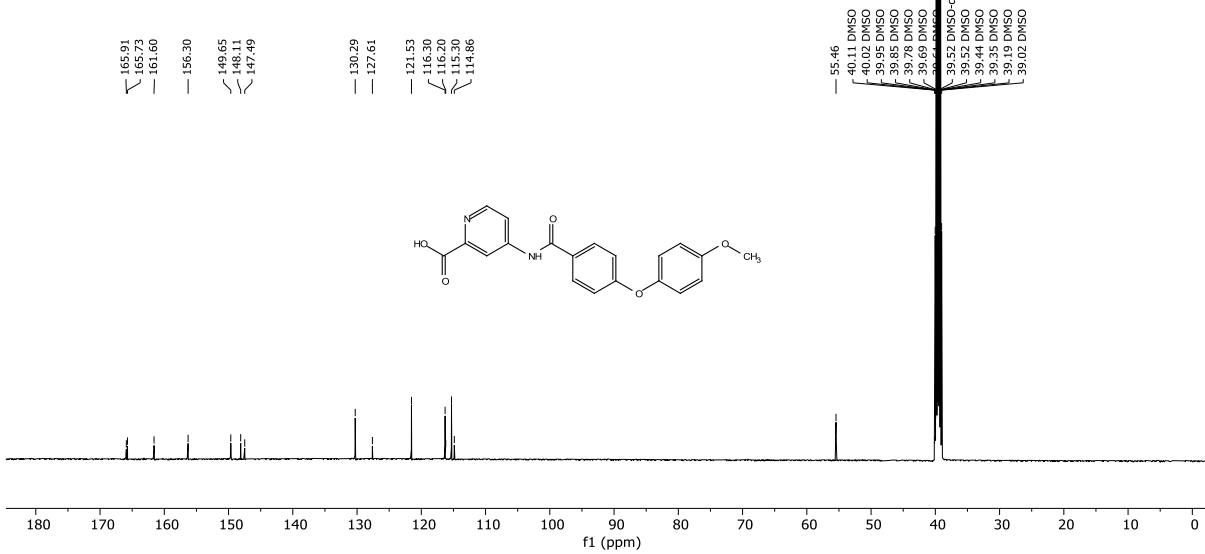


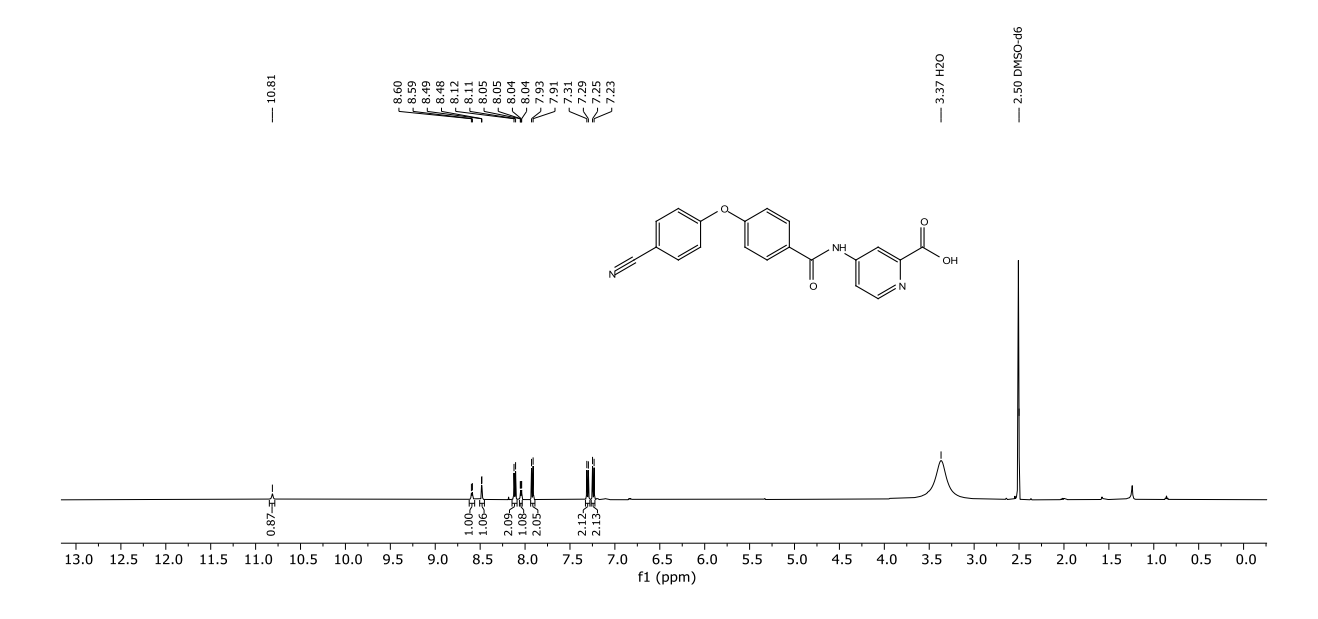


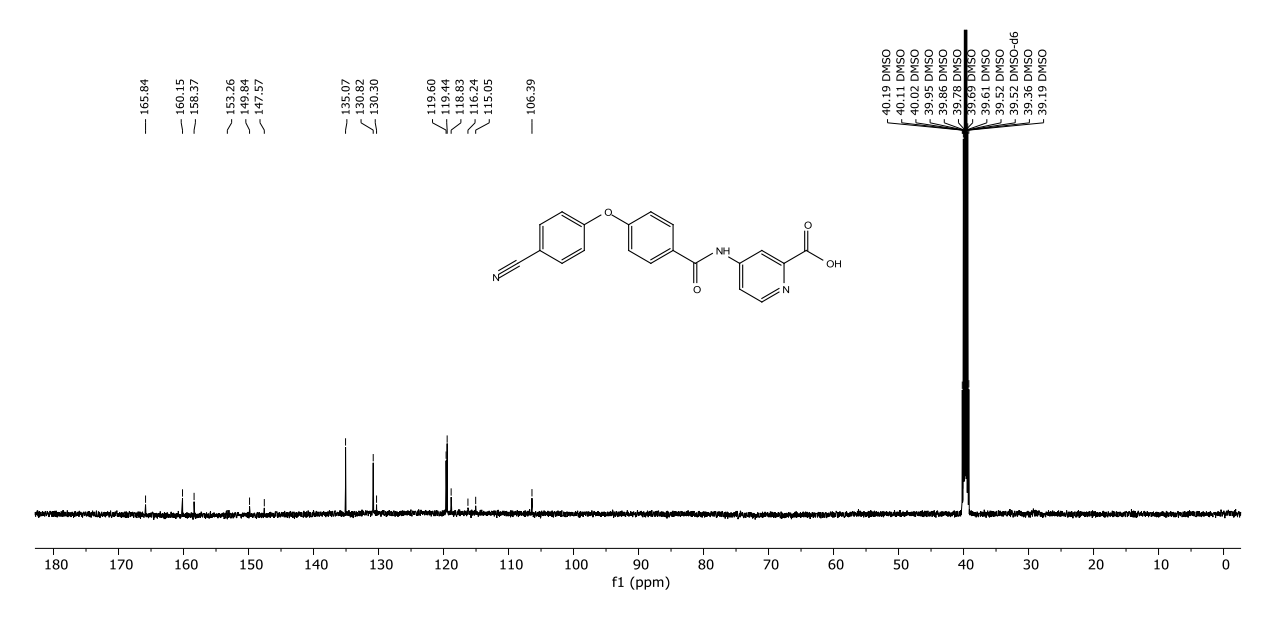


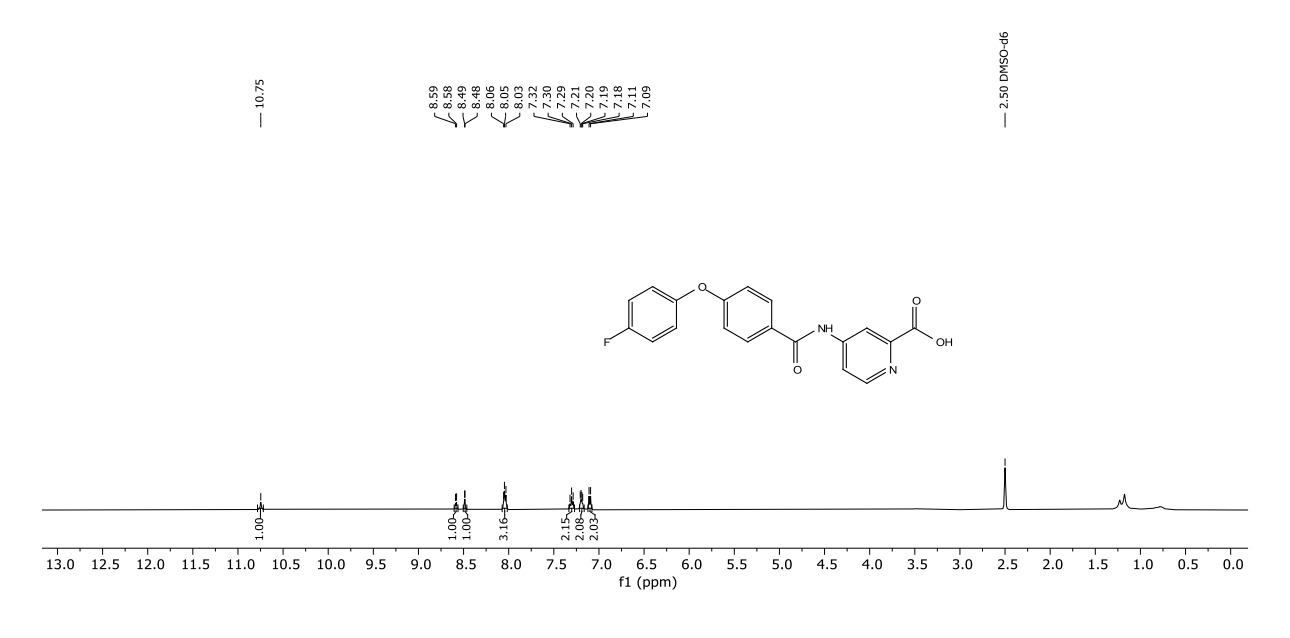


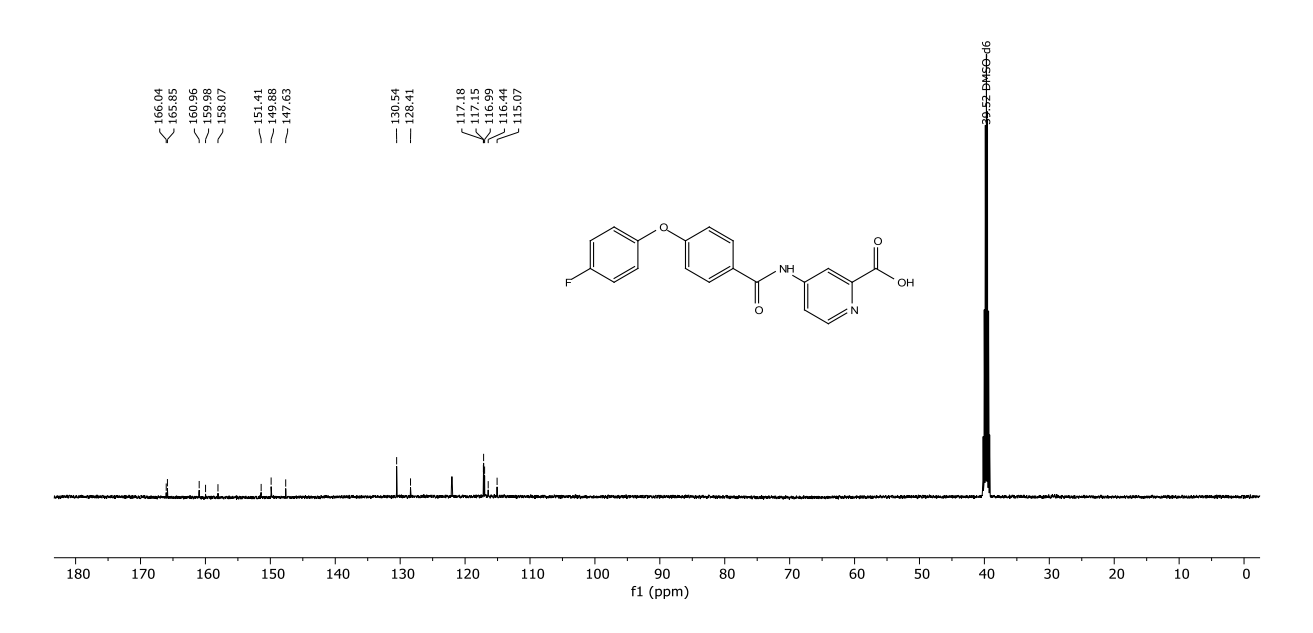


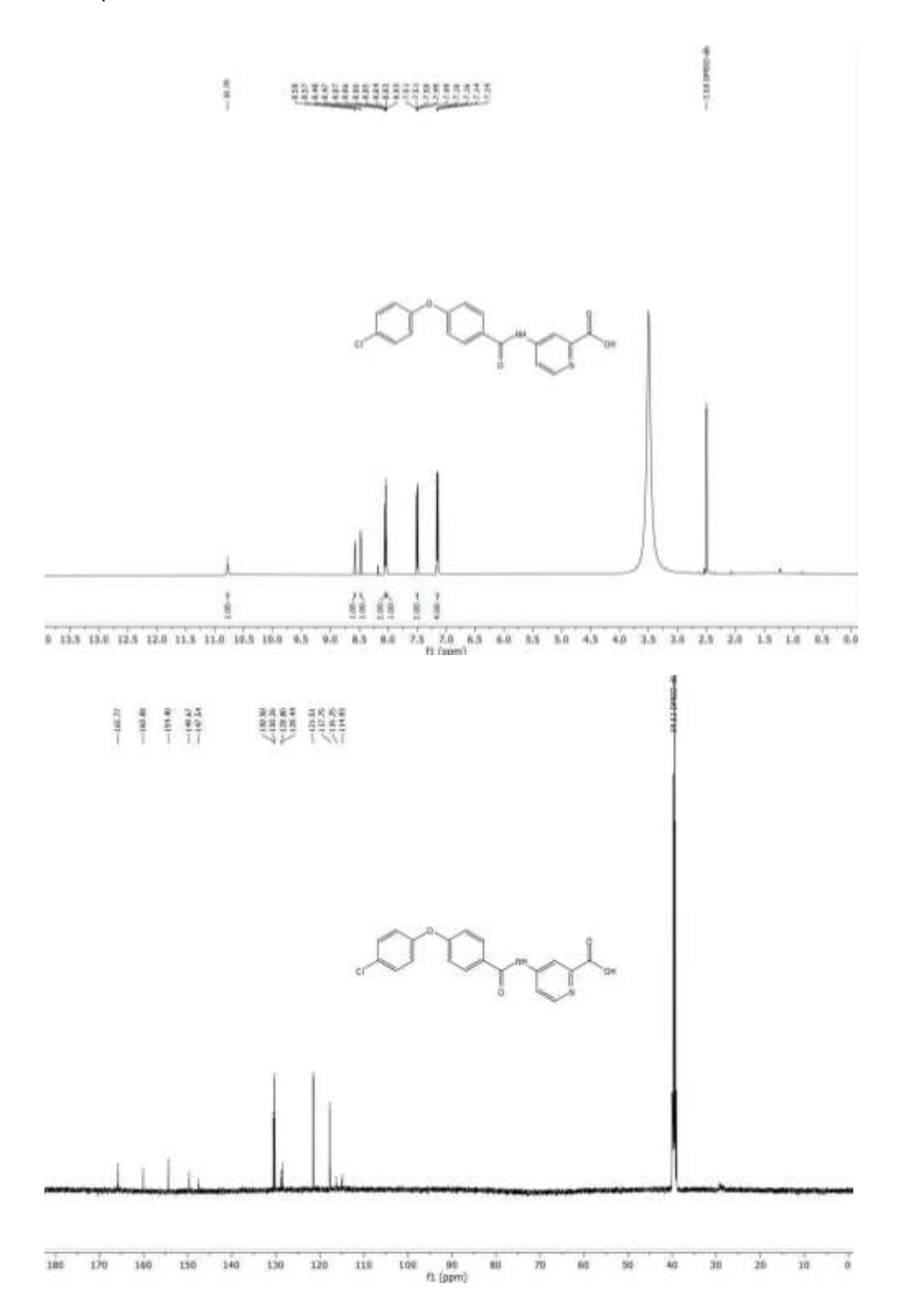


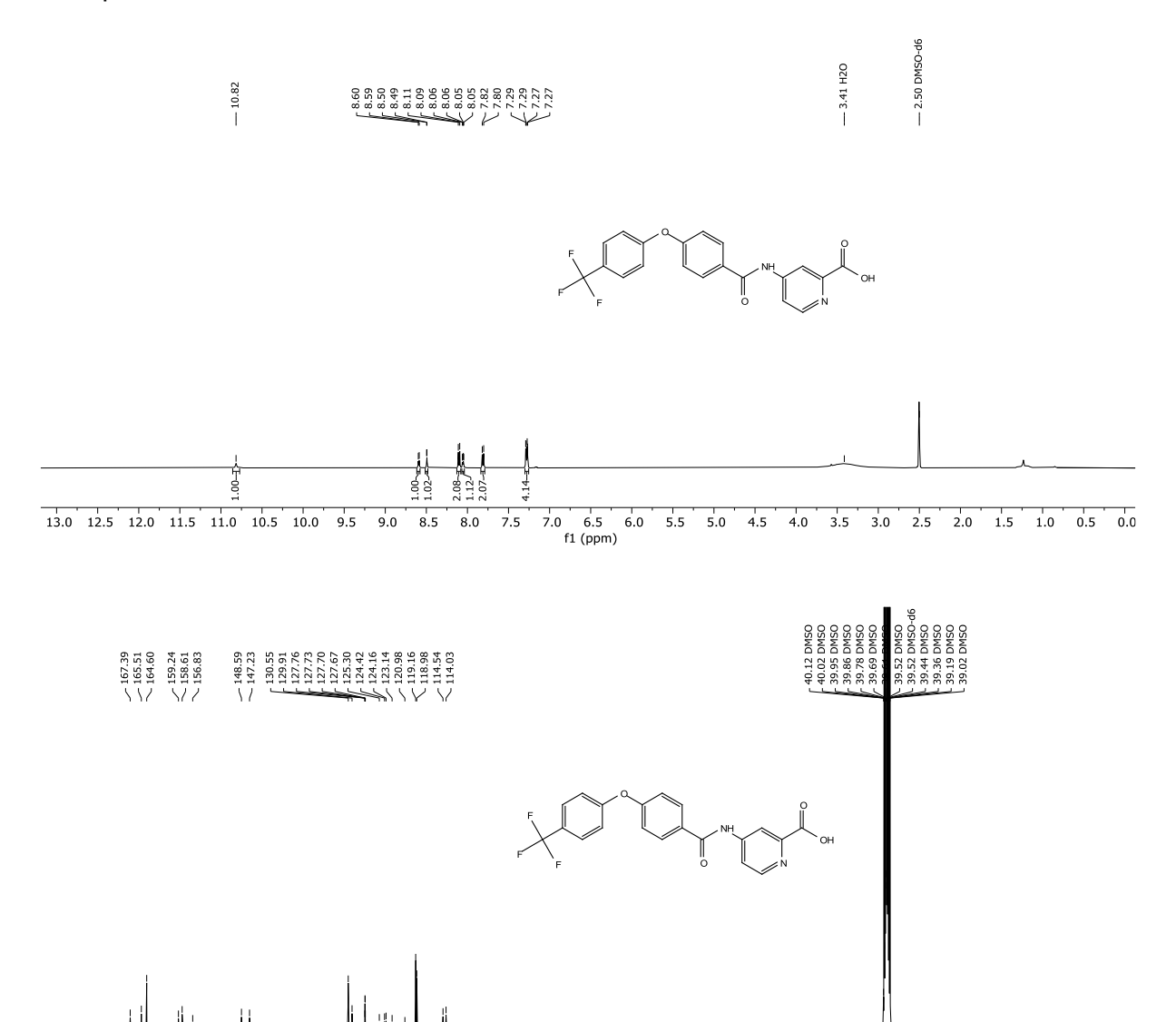




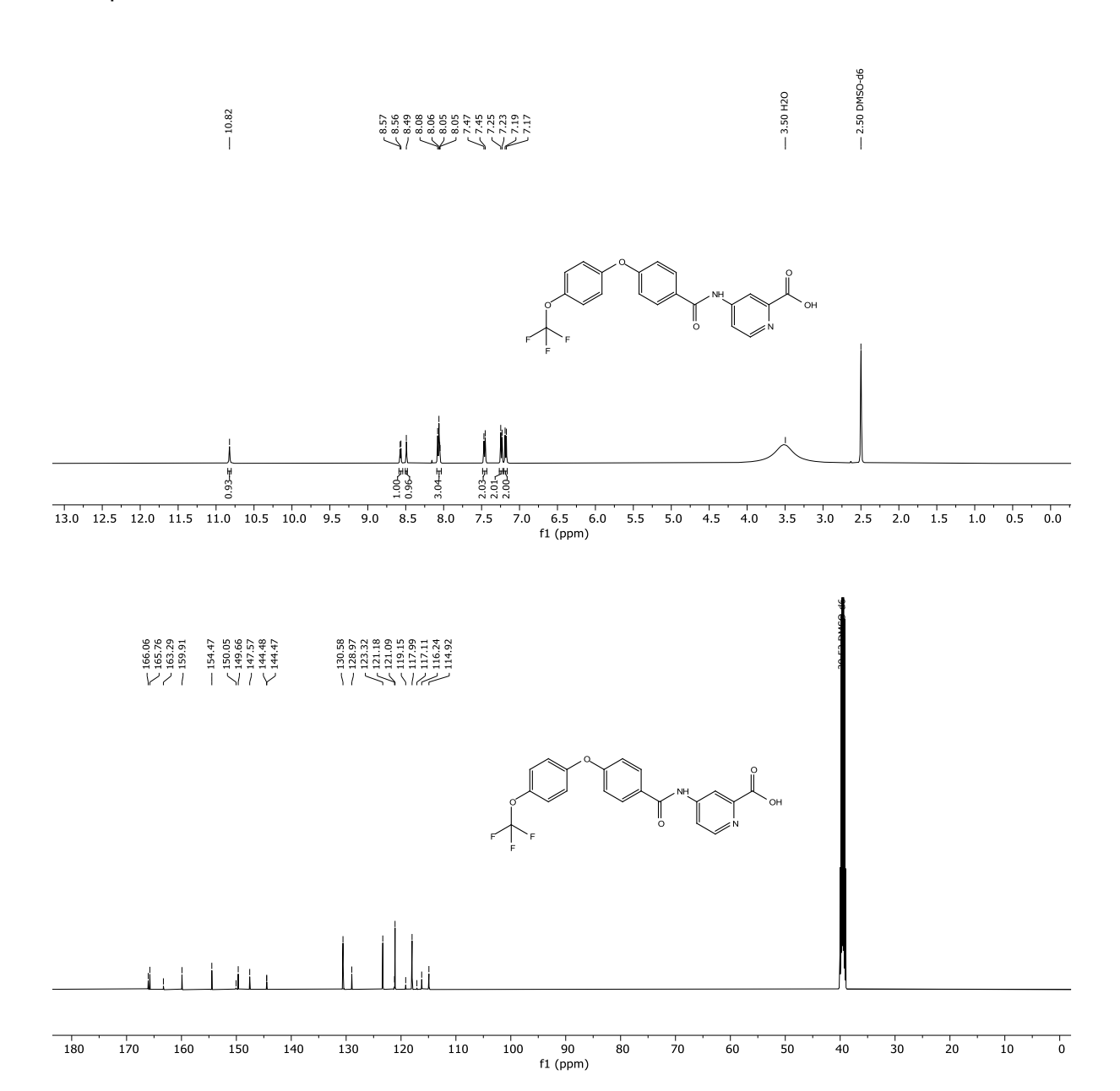


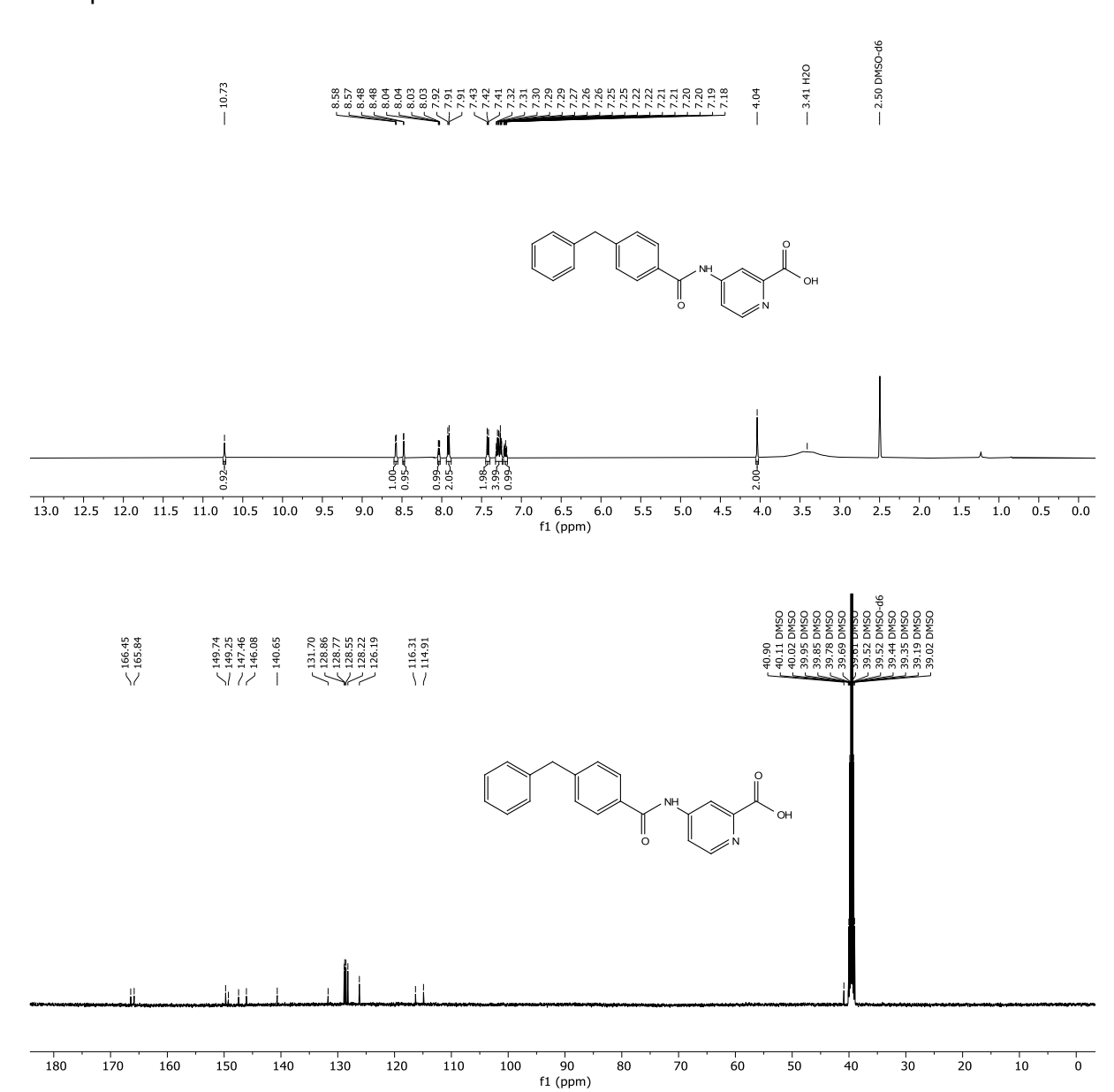


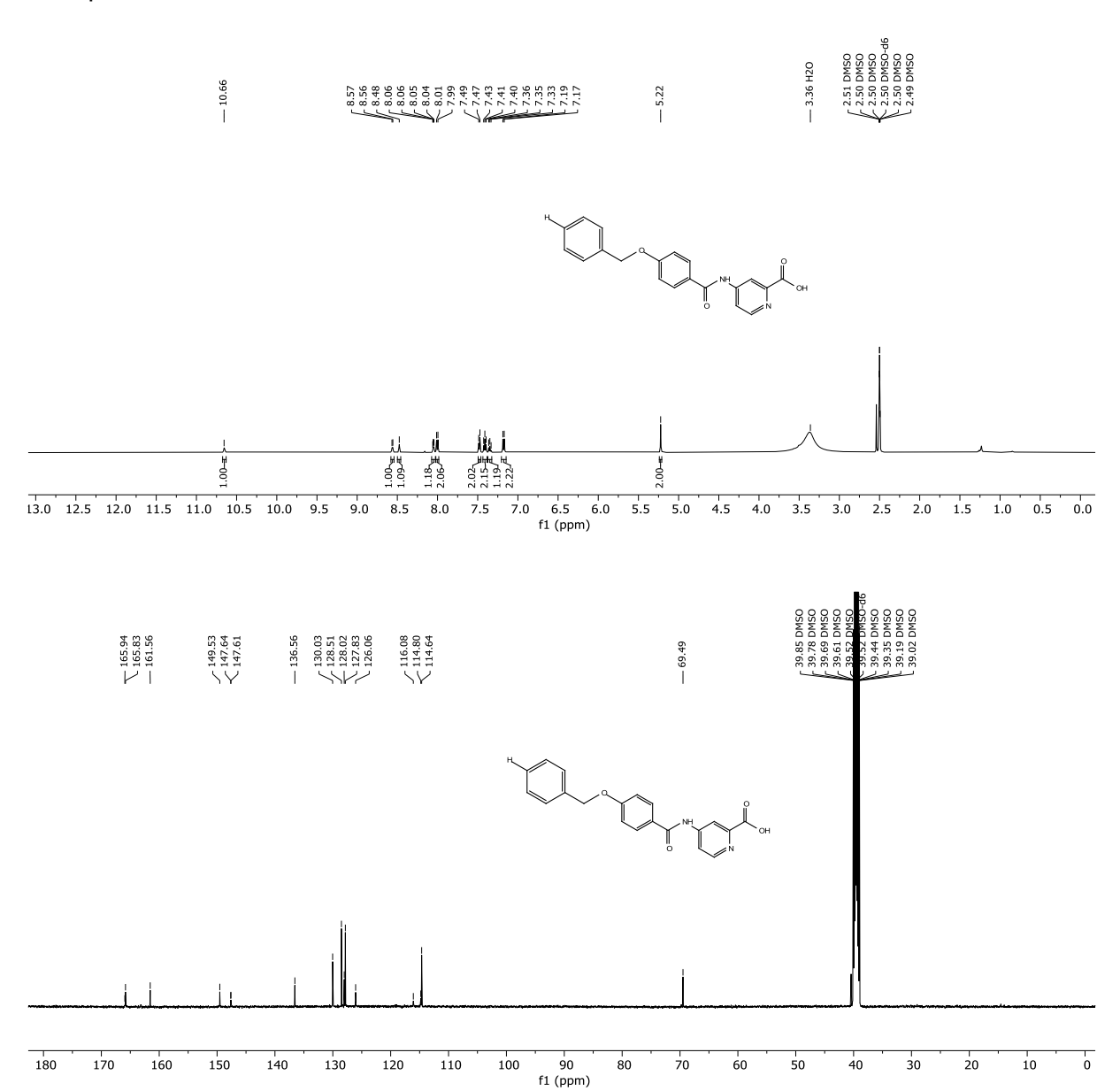


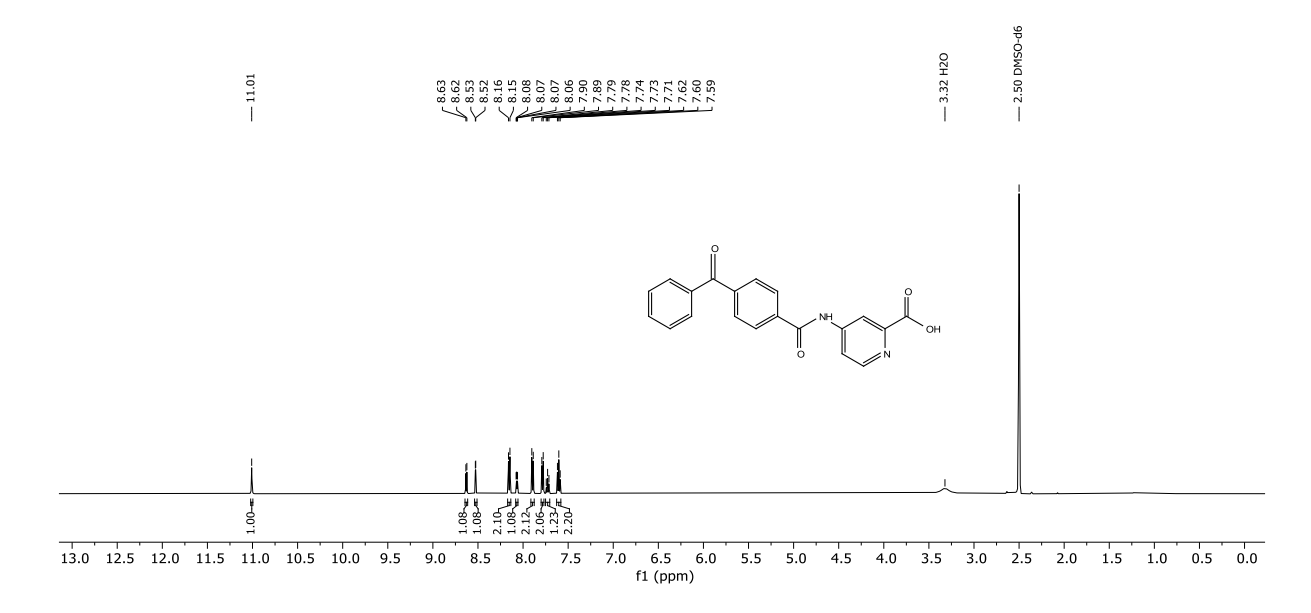


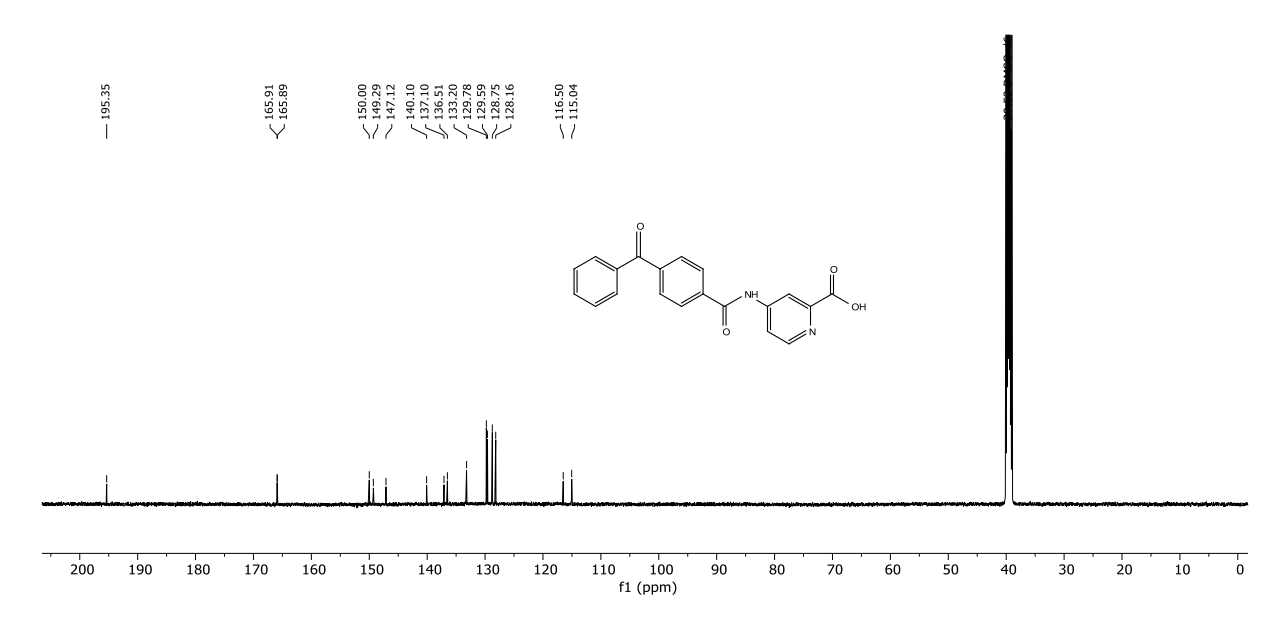
f1 (ppm)

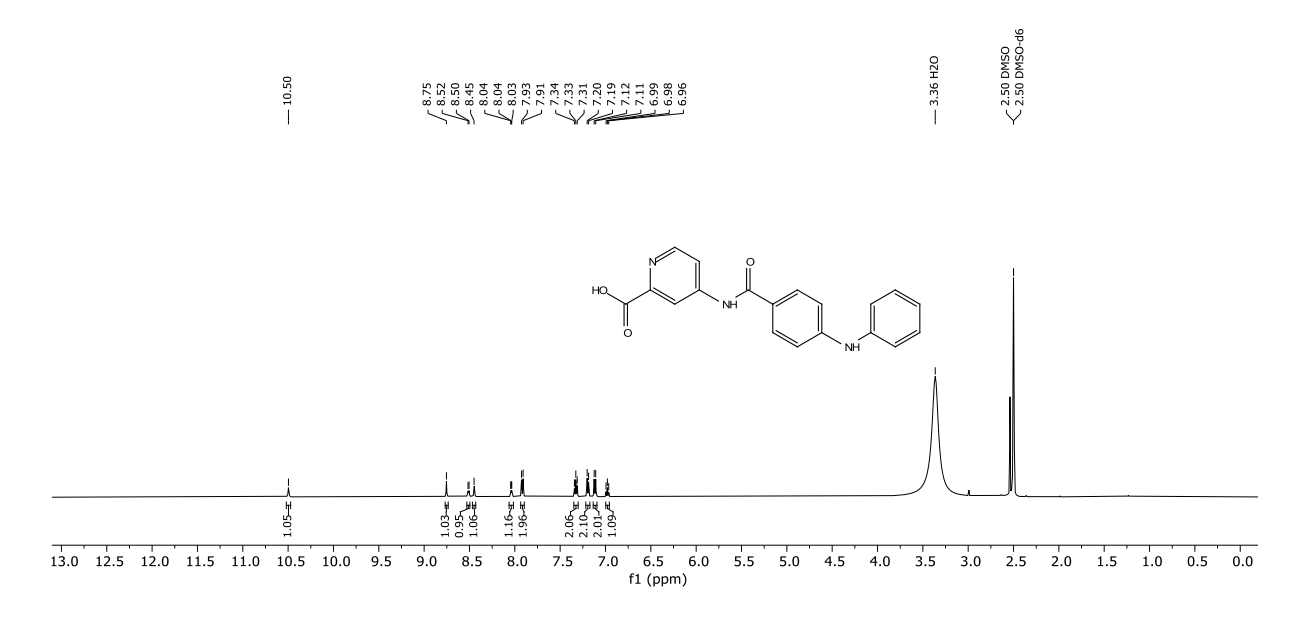


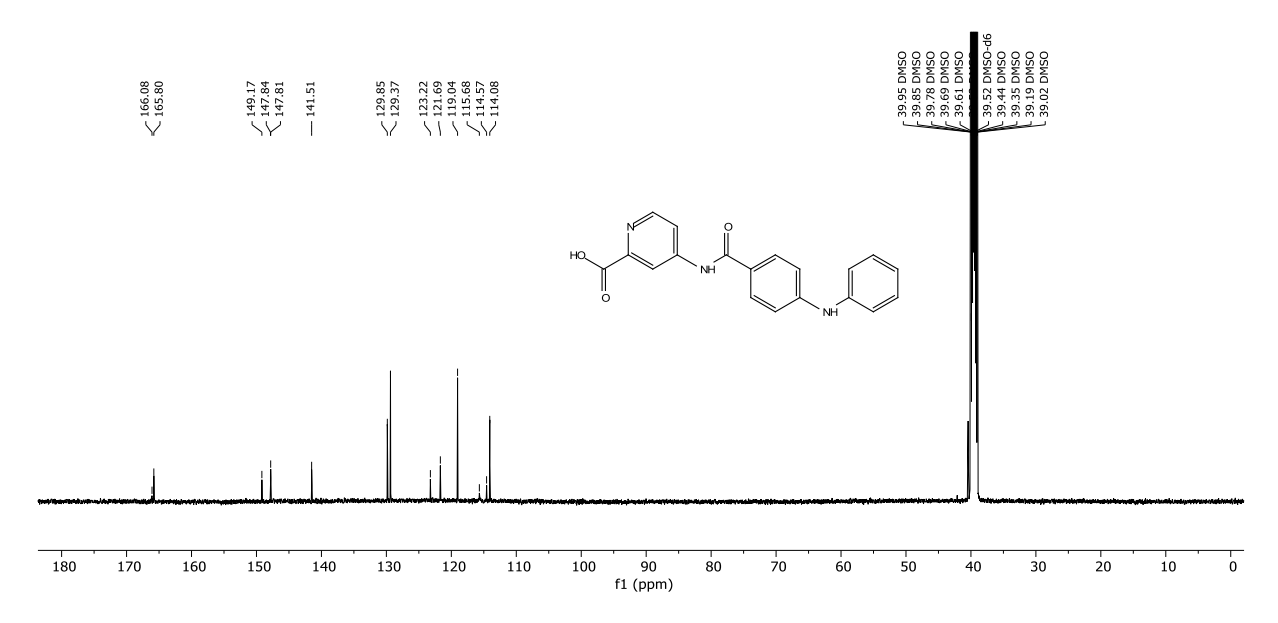


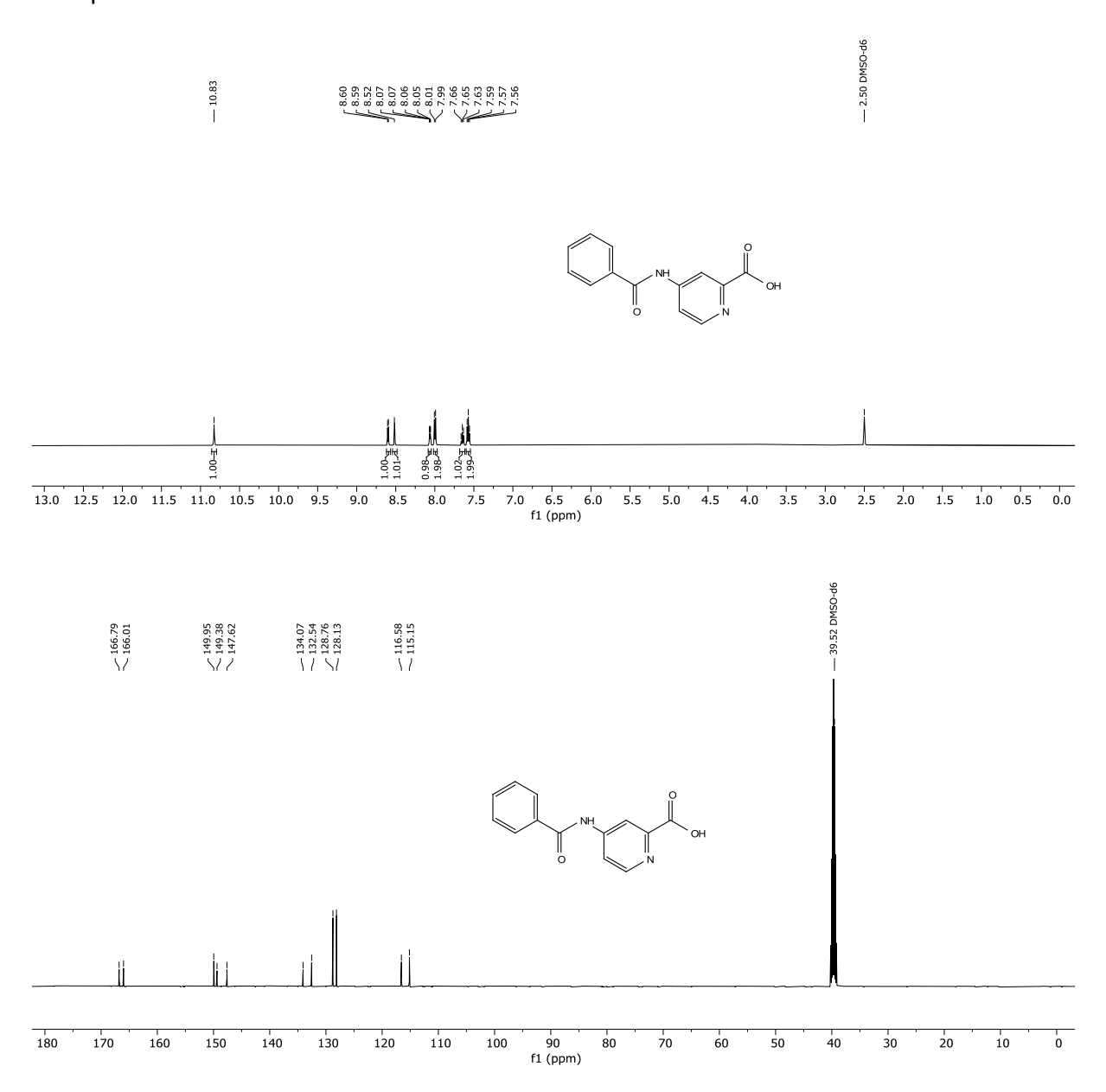


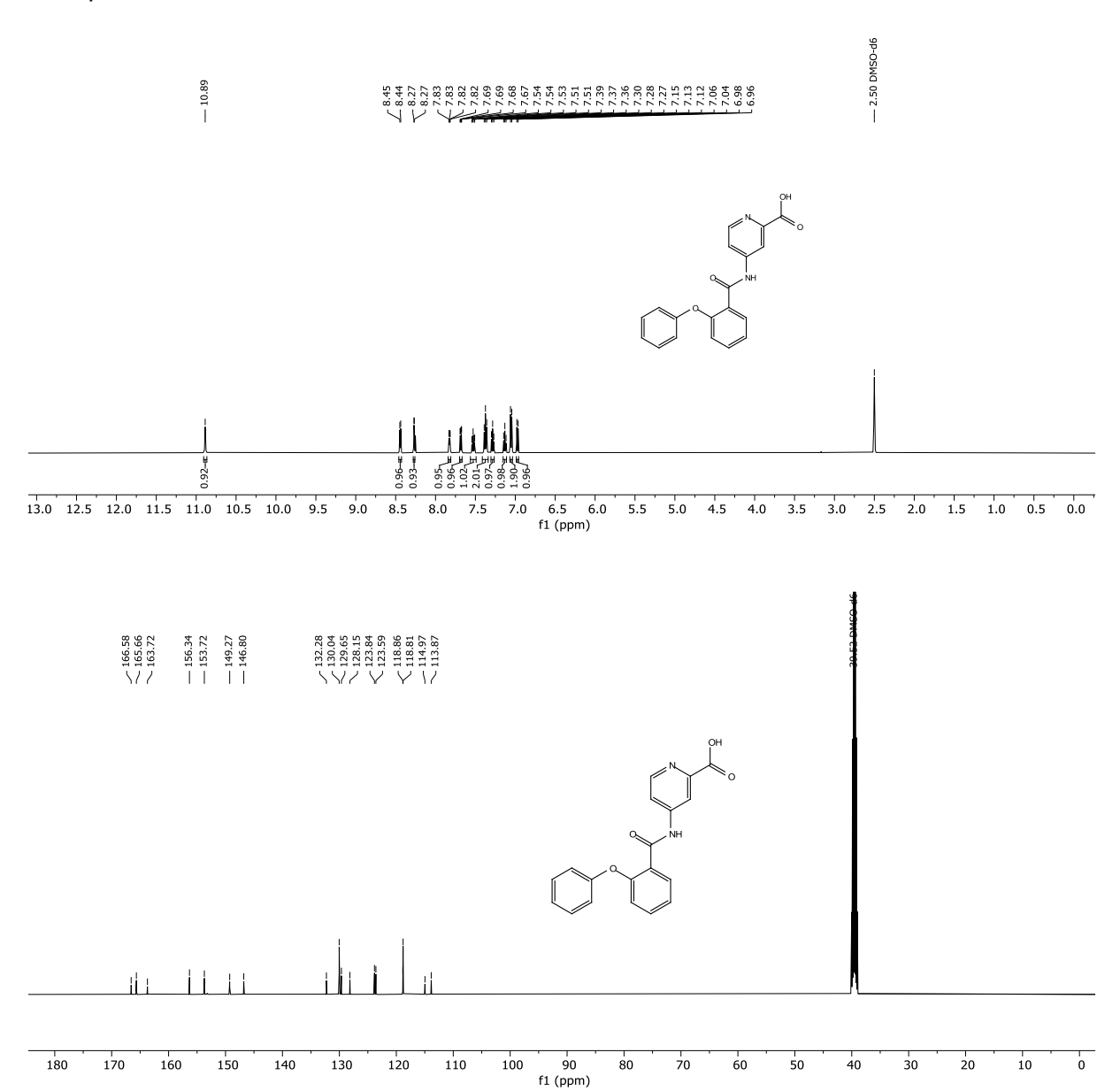


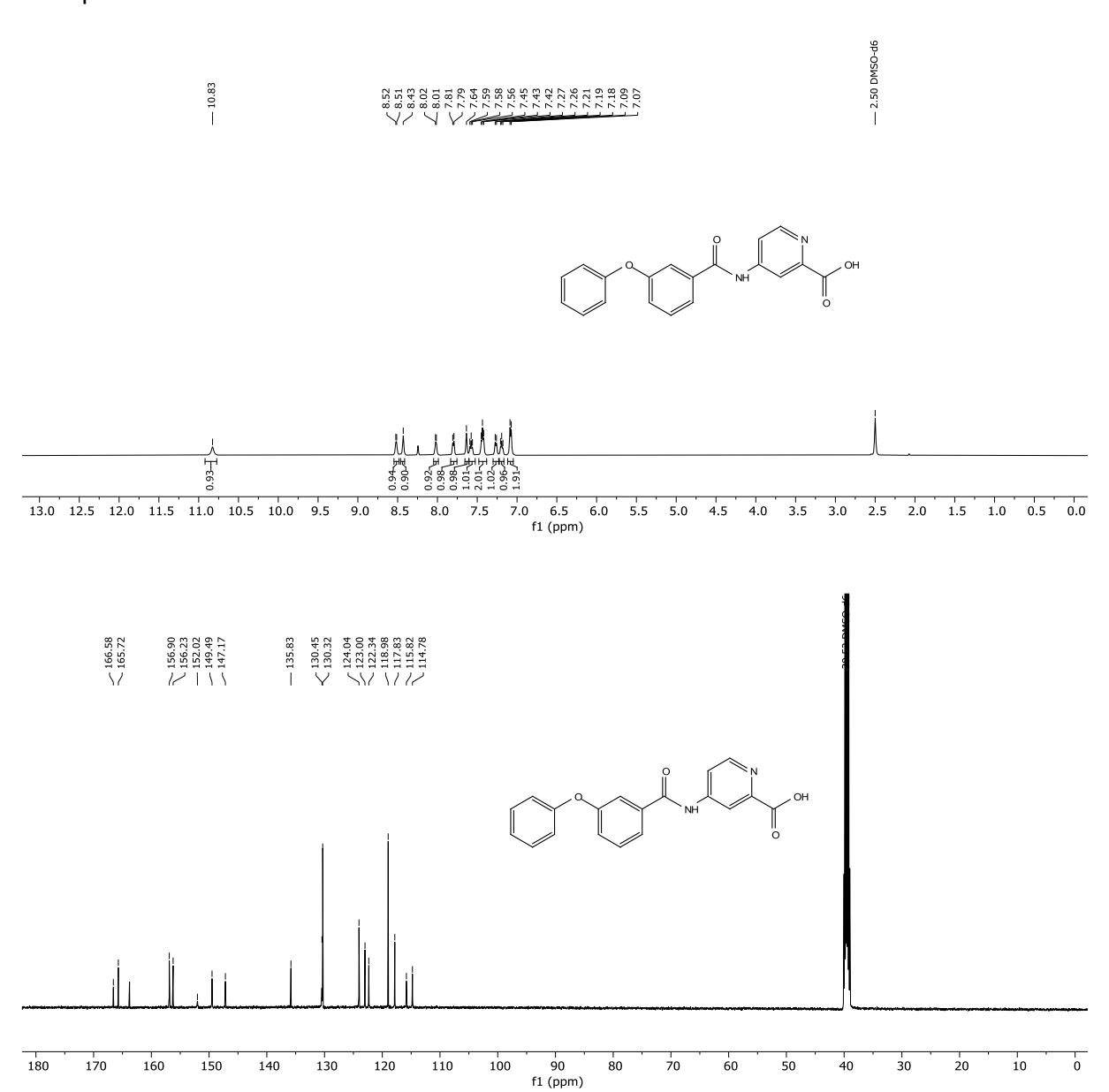


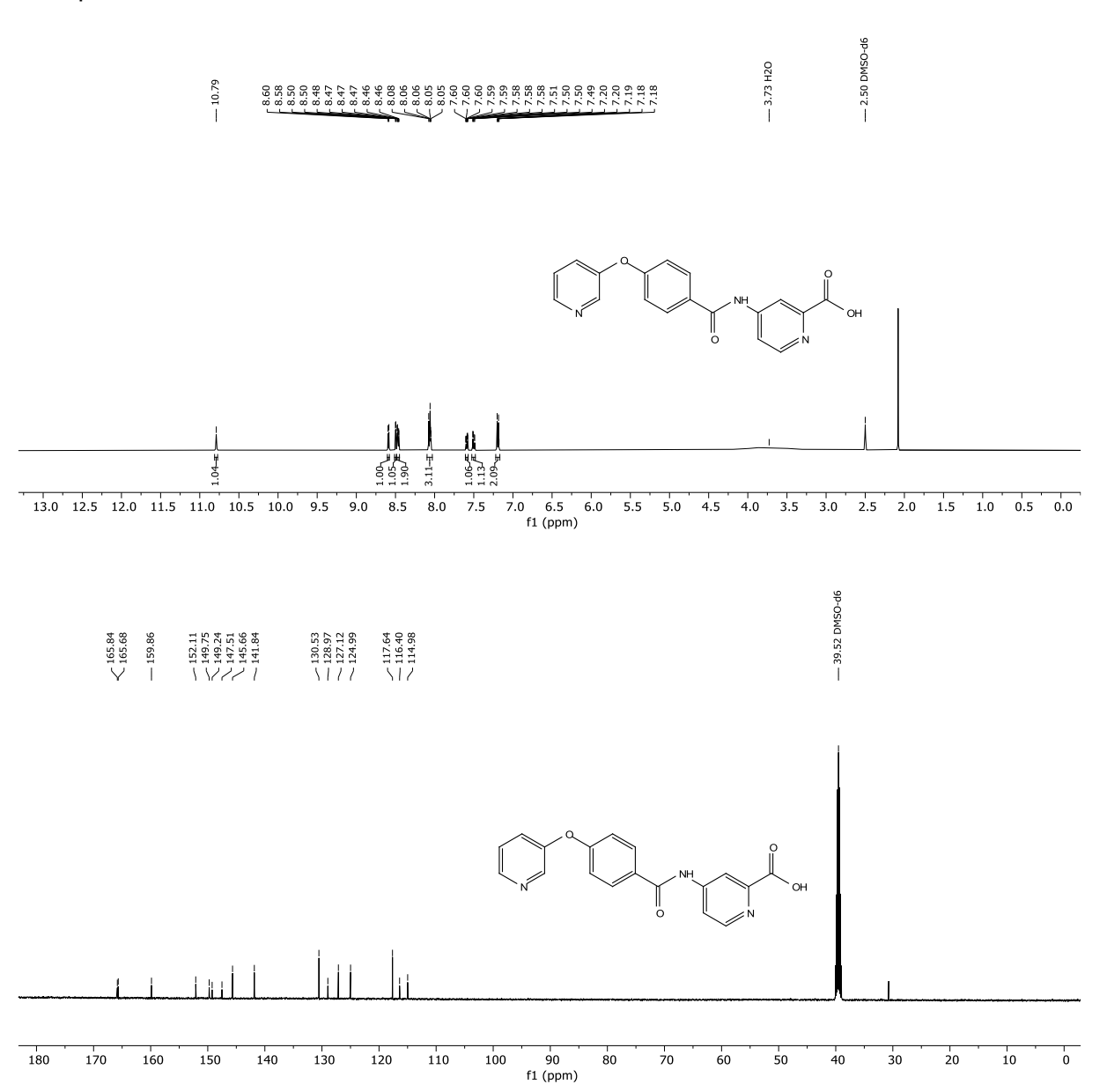


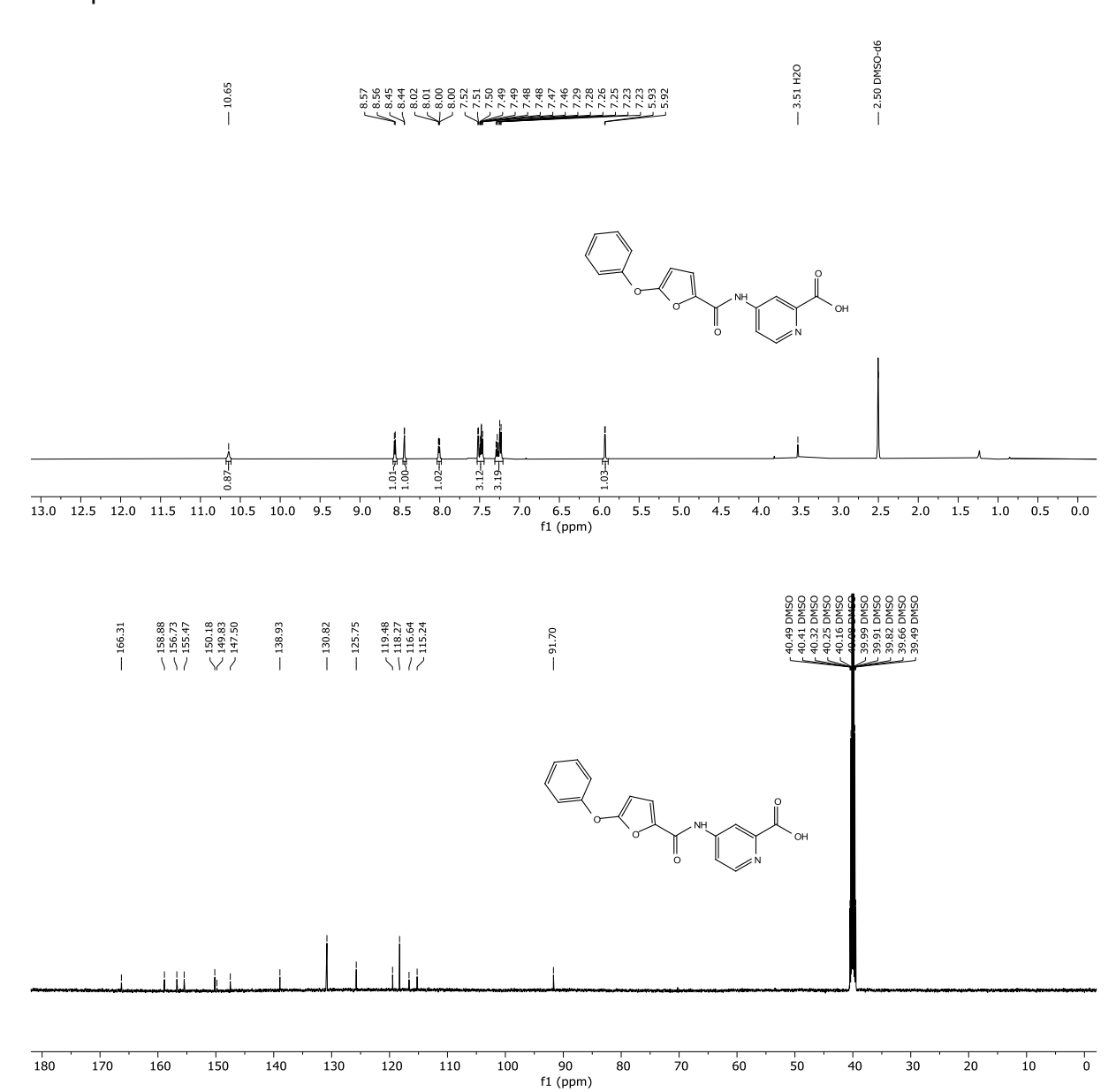


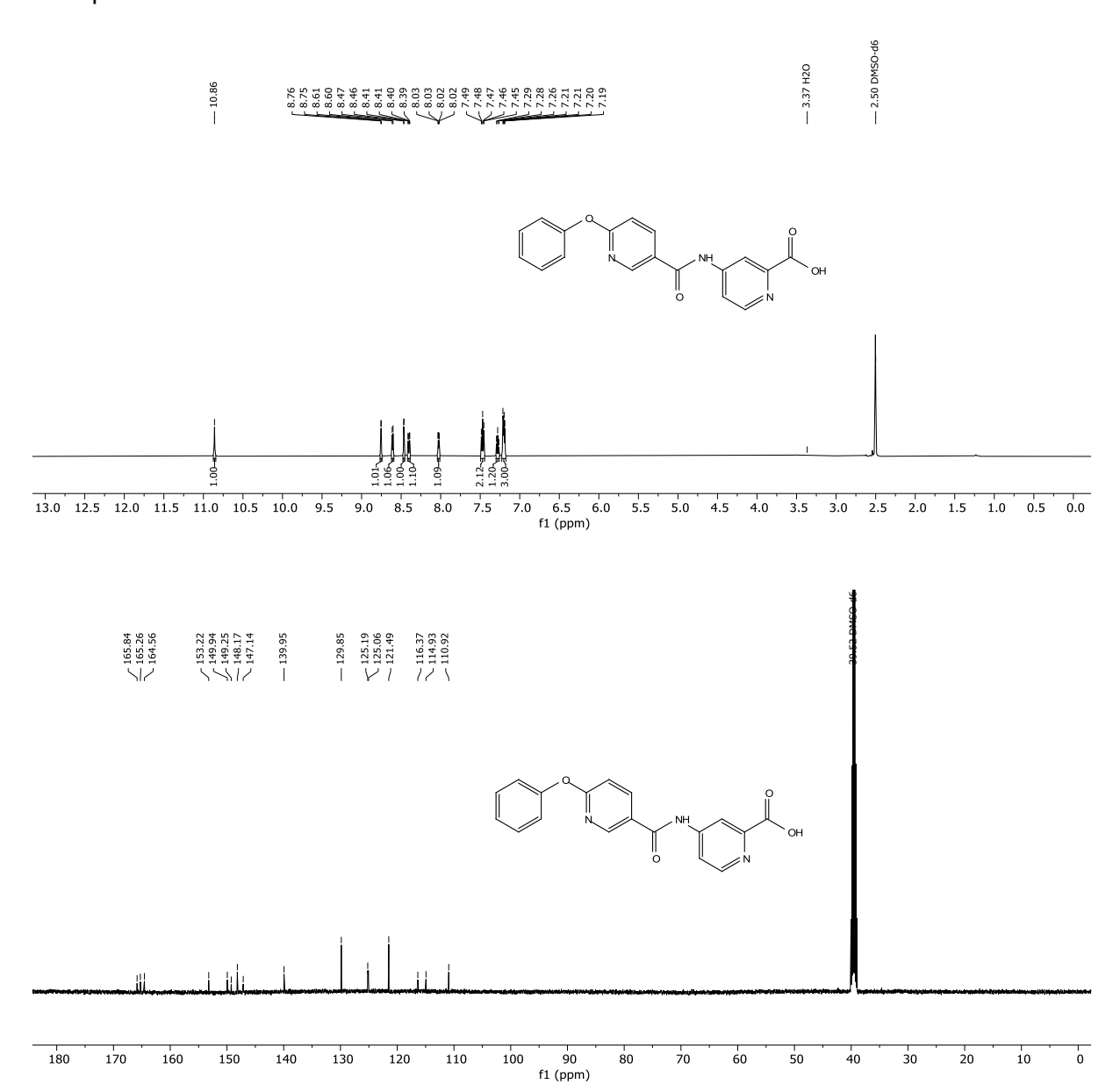


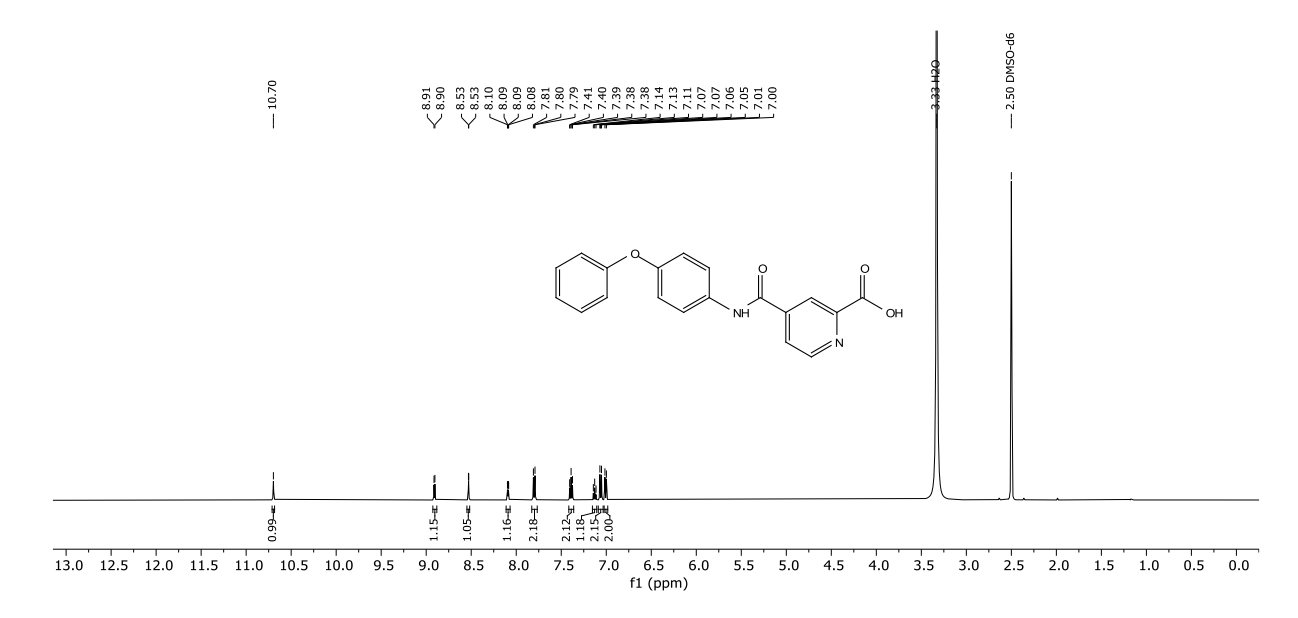


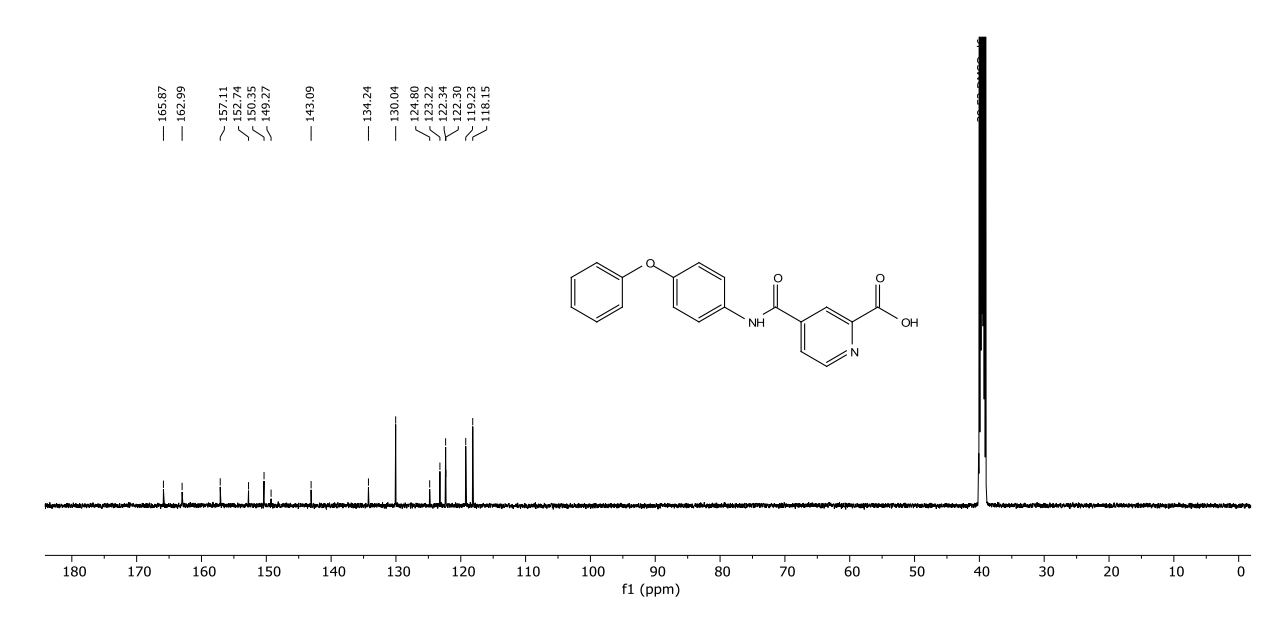


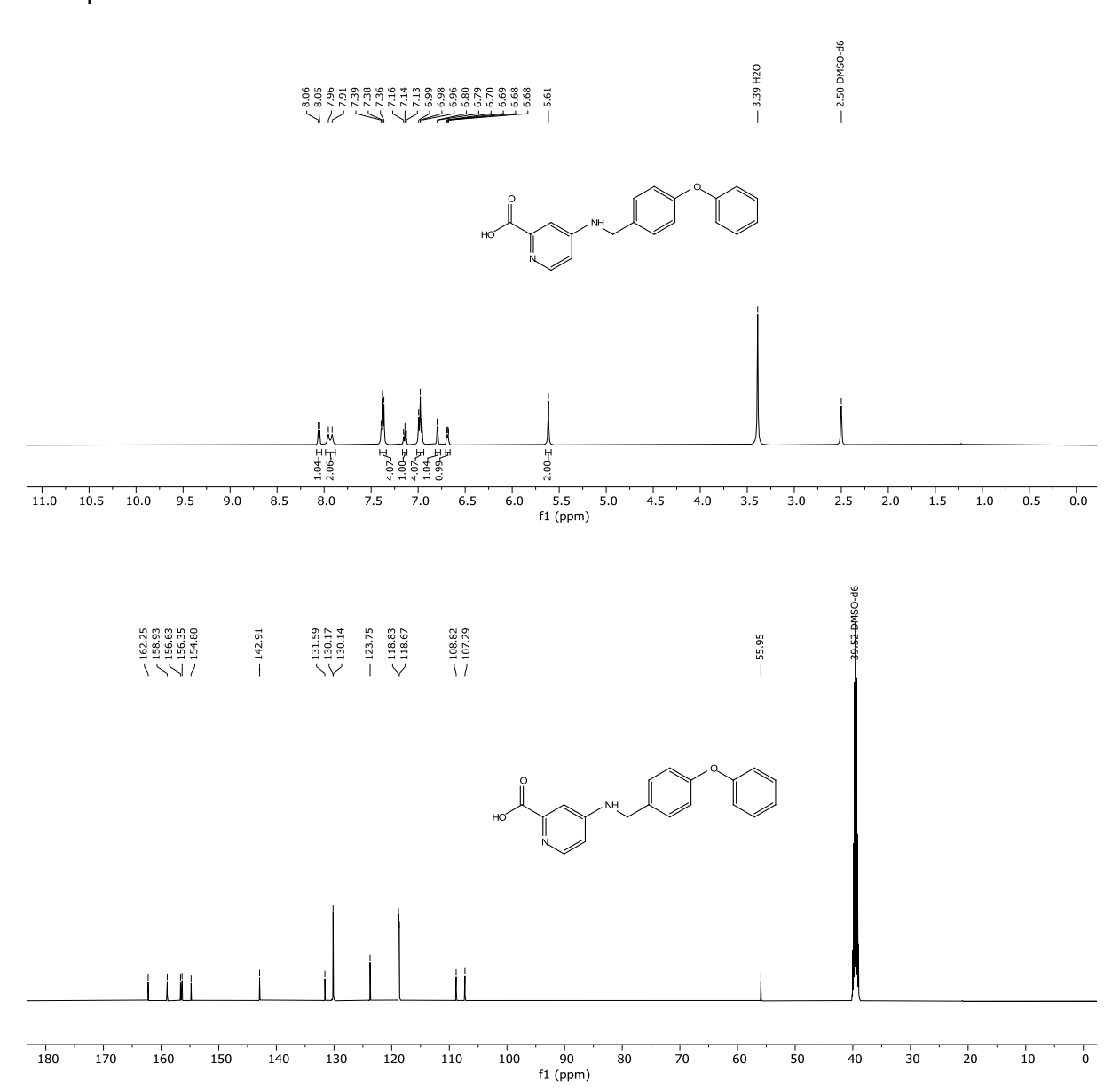


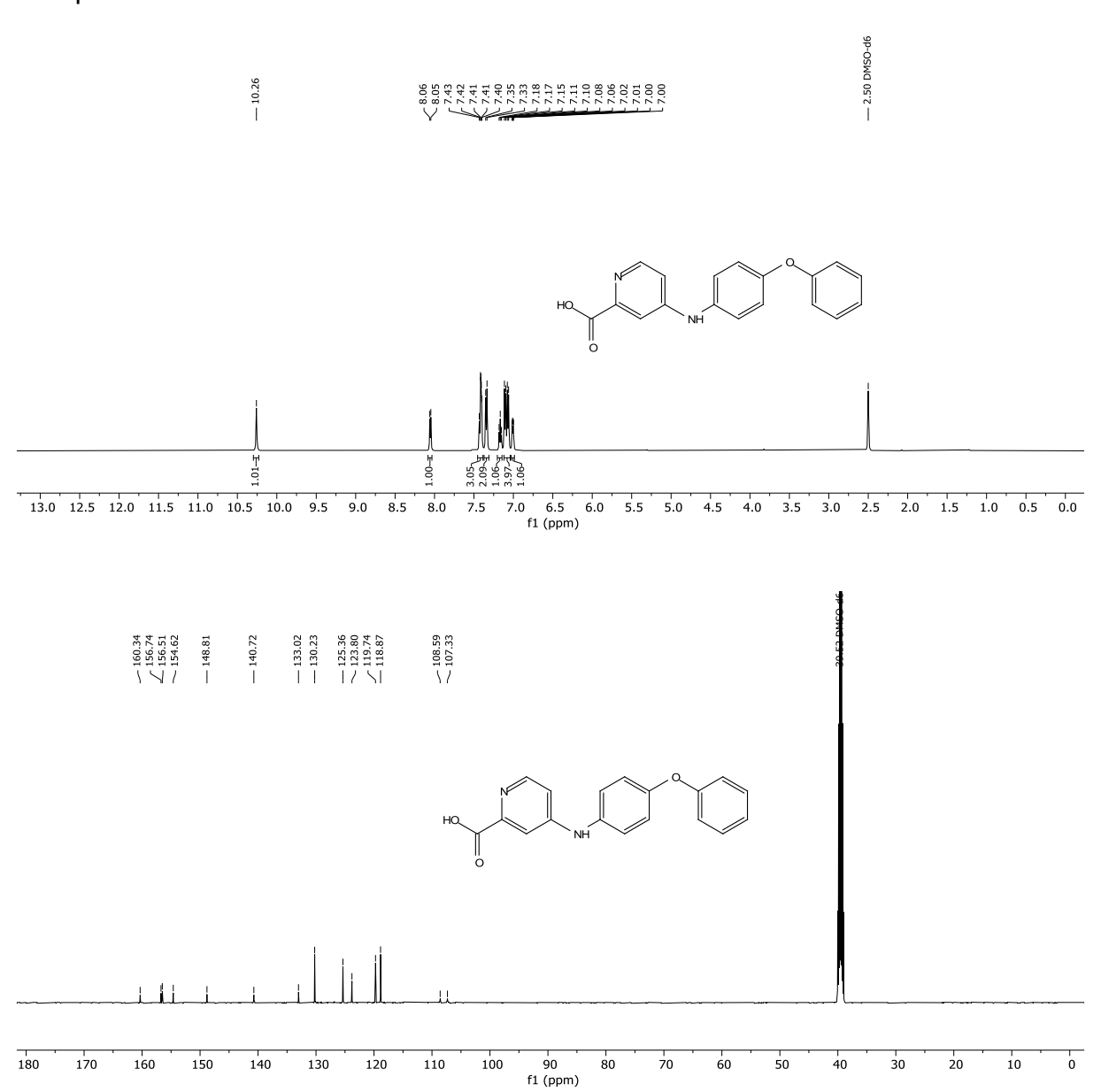


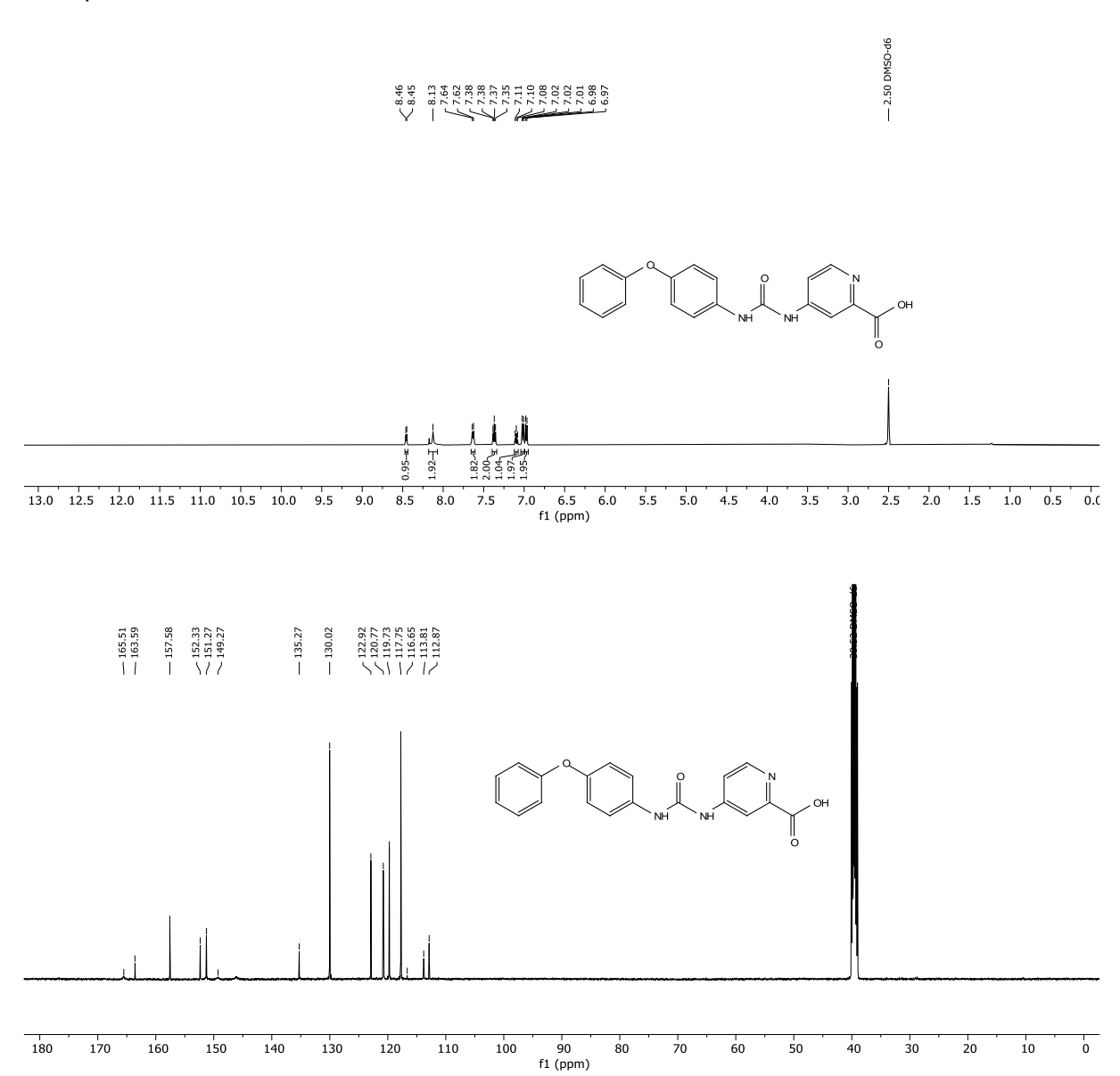


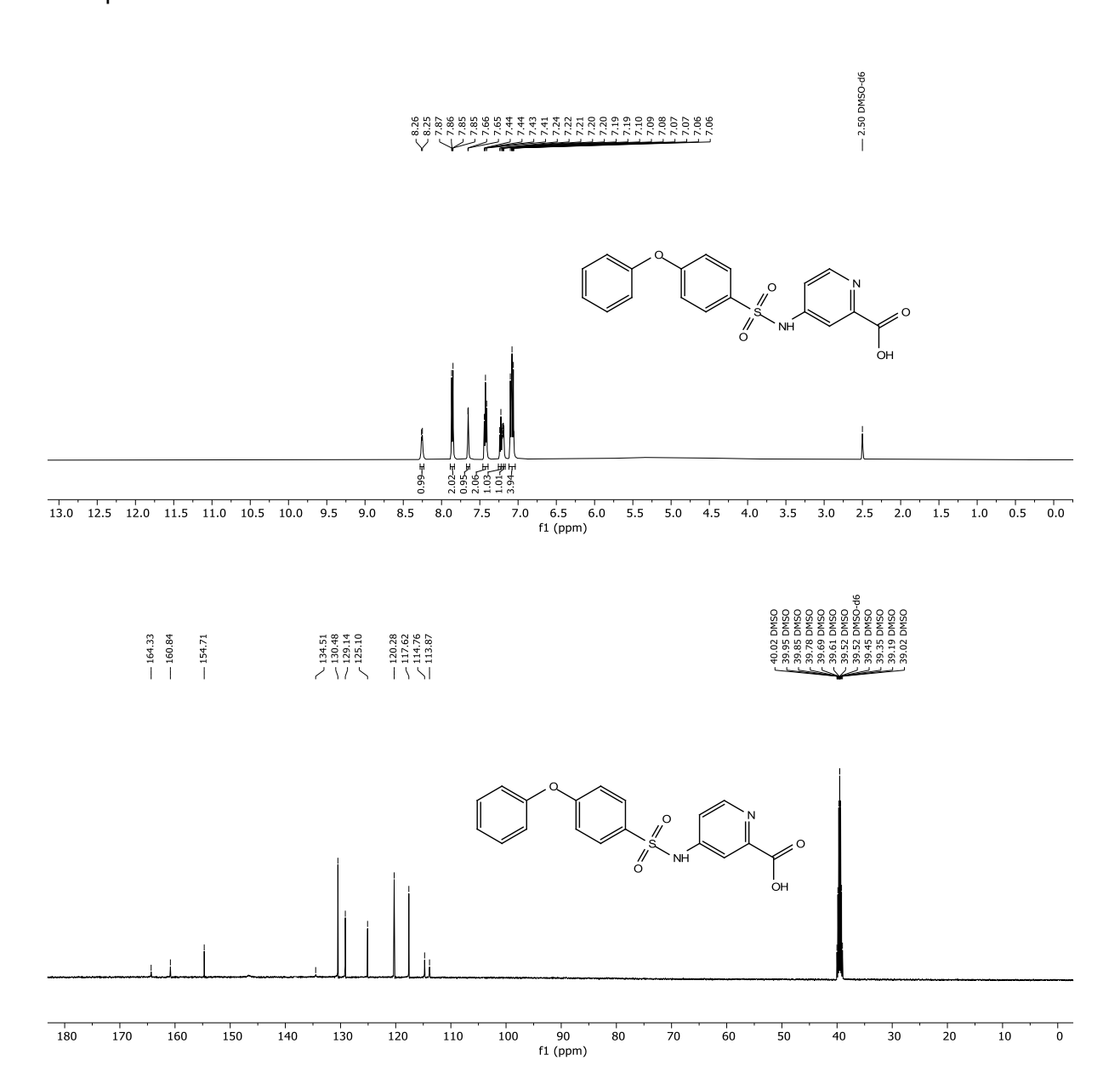


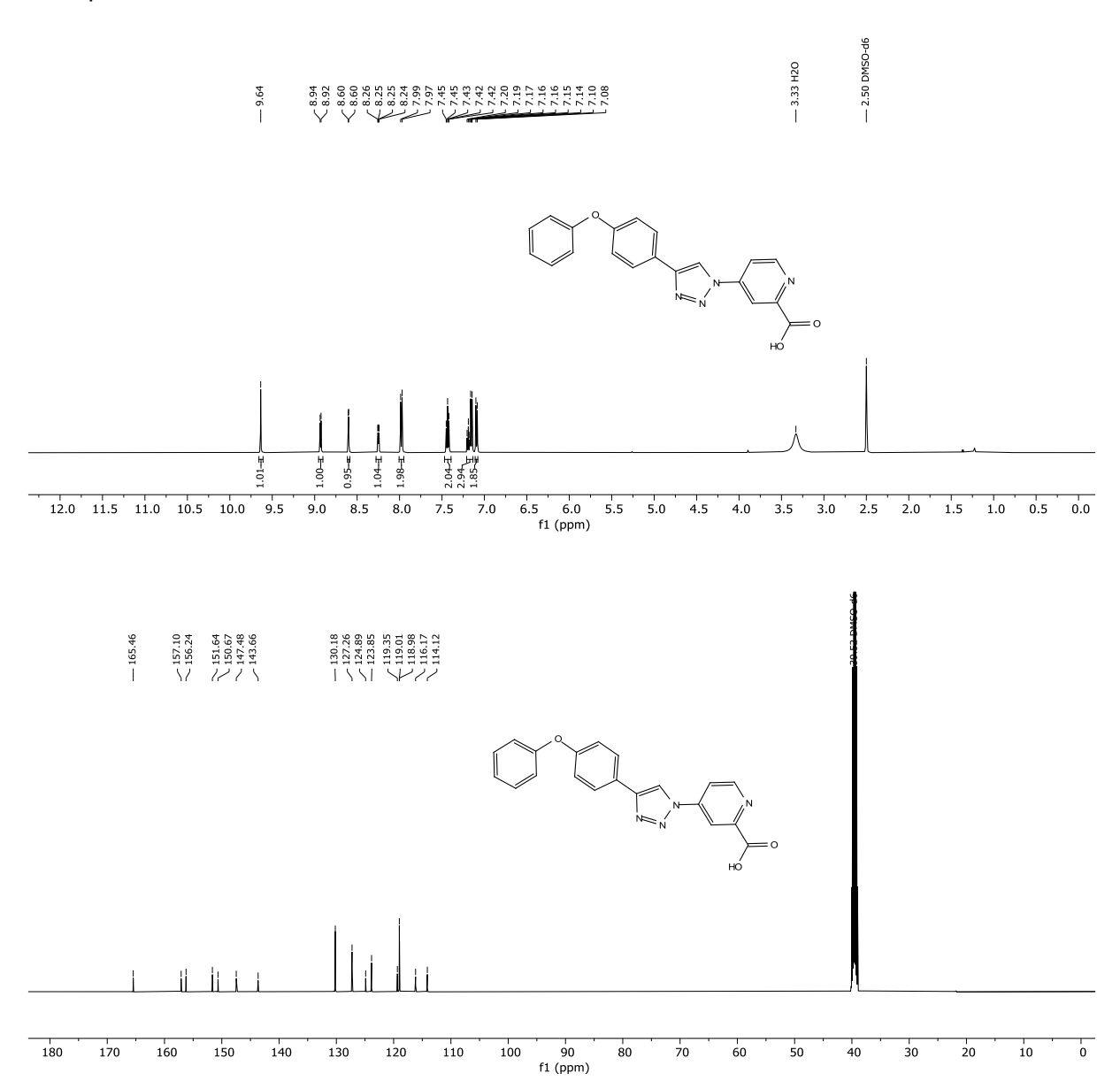


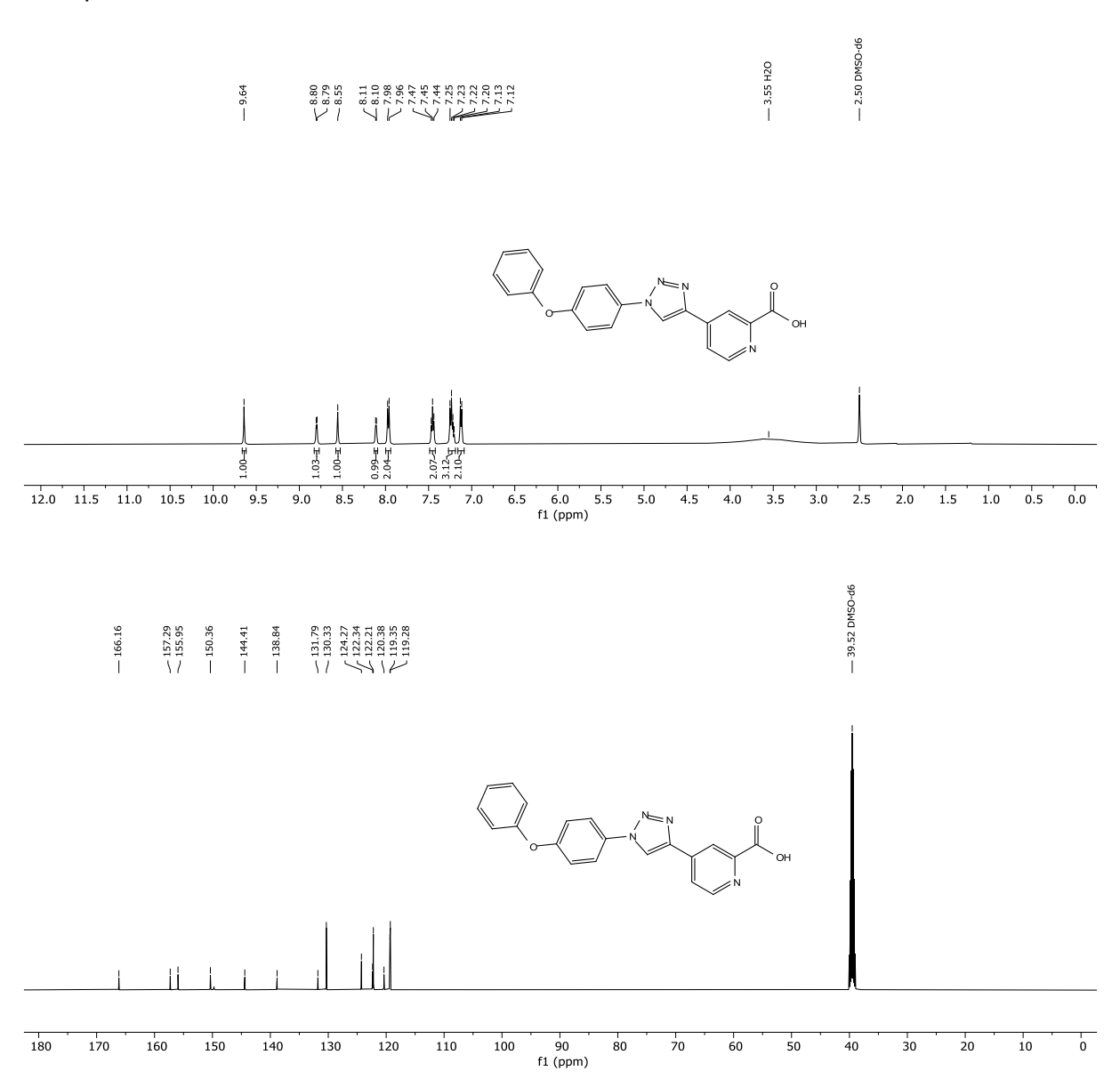












References

- [1] S. Schierle, J. Schmidt, A. Kaiser, D. Merk, Selective Optimization of Pranlukast to Farnesoid X Receptor Modulators, ChemMedChem 13 (2018) 2530–2545. https://doi.org/10.1002/cmdc.201800549.
- [2] S. Bousis, S. Winkler, J. Haupenthal, F. Fulco, E. Diamanti, A.K.H. Hirsch, An Efficient Way to Screen Inhibitors of Energy-Coupling Factor (ECF) Transporters in a Bacterial Uptake Assay, Int. J. Mol. Sci. 23 (2022). https://doi.org/10.3390/ijms23052637.
- [3] J. Haupenthal, C. Baehr, S. Zeuzem, A. Piiper, RNAse A-like enzymes in serum inhibit the anti-neoplastic activity of siRNA targeting polo-like kinase 1, Int. J. Cancer 121 (2007) 206–210. https://doi.org/10.1002/ijc.22665.
- [4] V. Namasivayam, K. Stefan, L. Gorecki, J. Korabecny, O. Soukup, P.J. Jansson, J. Pahnke, S.M. Stefan, Physicochemistry shapes bioactivity landscape of pan-ABC transporter modulators: Anchor point for innovative Alzheimer's disease therapeutics, Int. J. Biol. Macromol. 217 (2022) 775–791. https://doi.org/10.1016/j.ijbiomac.2022.07.062.
- [5] K. Stefan, S. Puri, M. Rafehi, G. Latambale, M. Neif, F. Tägl, N. S. Arlt, Z. N. Yazdi, E. Bakos, X. Chen, B. Zhang, W. I. Al-Khalil, H. Busch, Z.-S. Chen, C. Özvegy-Laczka, V. Namasivayam, K. Juvale, S. M. Stefan, Eur. J. Med. Chem. 2025, Just Accepted / In Print.

2.2 Chapter B

Discovery of a New Oxadiazole Derivative as Antitubercular Agents: Structure—Activity Relationship and Mode-of-Action Studies

Justine Bassil^{1,2,3†}, Gareth Prosser⁴, Mostafa M. Hamed^{1,3}, Norbert Reiling⁴, Anna K. H. Hirsch^{1,2,3*}

This manuscript is in preparation and will be finalized after the completion of the biological data and writing

¹ Helmholtz Institute for Pharmaceutical Research Saarland (HIPS) – Helmholtz Centre for Infection Research (HZI), Campus Building E 8.1, D-66123, Saarbrücken, Germany

² Saarland University, 66123 Saarbrücken, Germany

³ PharmaScienceHub (PSH), campus building A, D-66123 Saarbrücken, Germany

⁴ RG Microbial Interface Biology, Research Center Borstel, Leibniz Lung Center, Parkallee 1-40, 23845 Borstel, Germany

Contribution to the presented work

Author's Contribution:

The author contributed to the conception and design of this study. She performed all the synthesis and characterization of the compounds. She analyzed and interpreted the resulting data.

Contributions by others:

Gareth Prosser coordinated and evaluated the MIC assay against *Mtb*. Norbert Reiling was involved in supervising the project. Mostafa M. Hamed and Anna K. H. Hirsch contributed to the conceptualization, conceiving, design, and supervision of the project and proofreading of the manuscript.

Abstract

Tuberculosis is a major global health challenge, driven by the ongoing emergence of multidrug-resistant strains of *Mycobacterium tuberculosis*, which have rendered many existing treatments ineffective. Addressing this crisis has become a central focus of modern science, with an urgent need for innovative strategies and novel molecular inhibitors. In this study, we report on the identification, design, optimization, and detailed *in vitro* evaluation of the mode of action of a novel 1,3,4-oxadiazole-based TB inhibitors class, identified through experimental screening of inhouse and external libraries. A comprehensive structure—activity relationship (SAR) study led to new potent inhibitors, which exhibited promising properties, including enhanced antibacterial activity against *Mtb* and a range of Gram-positive pathogens, along with low cytotoxicity. Further evaluations of their selectivity, solubility and mode of action is needed.

Introduction

Despite the availability of antibiotics, Tuberculosis (TB), caused by *Mycobacterium tuberculosis* (*Mtb*), remains one of the deadliest infectious diseases worldwide.^[1] According to the World Health Organization (WHO), TB has reclaimed its position as the leading cause of death from a single infectious agent, surpassing coronavirus disease after three years.^[2] Each year, more than 10 million people develop TB, and 1.3 million lives are lost, underscoring its ongoing global health burden.^[3]

Mtb primarily spreads through aerial transmission and mostly affects alveolar macrophages in the lungs, though it can also impact other organs of the body. [4] A key feature of Mtb is its ability to invade and survive within human macrophages, enabling it to persist for an extended period in a dormant state, known as latent TB. Latent TB remains asymptomatic until the host's immune system becomes compromised. At this point, the infection may progress to active TB with clinical symptoms (e.g., cough, fever, fatigue) and transmissibility. Thus, upon infecting a susceptible host, Mtb can follow one of three pathways: it may be eliminated by the immune system, persist as latent TB, or develop into active TB. [5,6] Another known feature of Mtb is its very complex cell wall, which is composed of mycolic acids, lipoarabinomannan,

arabinogalactan, and peptidoglycans, which provides an effective protective barrier against various antibiotics.^[7]

The standard treatment of active TB involves a six-month regimen of four first-line drugs: isoniazid, rifampicin, pyrazinamide, and ethambutol, which has an approximate success rate of 85%. [8,9] However, the emergence of antibiotic-resistant *Mtb* strains over the years has posed significant challenges to this treatment approach. These strains, including multidrug-resistant TB (MDR-TB) and extensively drug-resistant TB (XDR-TB), are now recognized as major contributors to the global antimicrobial resistance (AMR) crisis. [10] MDR-TB refers to bacterial resistance against isoniazid and rifampicin, the two most potent first-line drugs, while XDR-TB exhibits resistance to MDR-TB drugs as well as additional second-line agents, such as fluoroquinolones and injectable antibiotics (amikacin, kanamycin). [4,11,12] Recent WHO reports indicated around half a million cases of MDR-TB, with an increased number of patients resistant to second-line drugs. [2] These cases typically require longer, more expensive treatments with more side effects, and lower success rates. Therefore, it is crucial to explore innovative therapies and develop new inhibitors to effectively combat this disease.

As an approach to overcome this deadly disease, we identified a promising chemical class bearing a 1,3,4-oxadiazole scaffold as potential antitubercular agent through our library screening. Molecules containing oxadiazole core have demonstrated diverse pharmacological activities, such as antibacterial, anti-TB, antifungal, anti-inflammatory, antiviral and anticancer. [13,14] This provided an excellent starting point for further investigation of this chemical class. Hence, we initiated a structure—activity relationship (SAR) study to enhance potency and identify new, highly effective TB inhibitors. The most active derivatives were subsequently optimized and evaluated *in vitro* to determine their mode of action.

Results and discussion

Medicinal chemistry-driven optimization

To find novel inhibitors with antituberculosis activity, we performed experimental screening of in-house and external libraries against *Mtb*. Among these, compound **1**

displayed an MIC value of 3.12 μ M against MtbH37Rv when cultured in a medium containing bovine serum albumin (BSA) and <0.049 μ M in its absence. BSA promotes the growth of Mtb by providing nutritional support, binding fatty acids and facilitating biofilm formation. Additionally, it serves as a stabilizing agent and is an essential component in understanding Mtb metabolism and developing effective treatments. [15,16]

Core Part

$$N-N$$
 O
 CF_3

1

Eastern Part

Figure 1. Chemical structure of Hit compound **1** obtained from in-house library screening. SAR is divided into two regions: the core and the Eastern part.

Through SAR analysis, we explored how structural modifications can impact drug efficacy against *Mtb*H37RV, focusing on two key regions of the molecule: the core and the Eastern part (Figure 1). Systematic modifications of these regions revealed key structural features of hit **1** that are critical for antitubercular potency. All synthesized compounds were evaluated for their antitubercular activity against *Mtb*H37Rv in presence and absence of BSA. Compounds showing low micromolar activity were further assessed for their cytotoxicity on HepG2 cells.

For the optimization of hit **1**, our investigation initially focused on core of the molecule by varying it with different heterocycles (**2–6**). Substituting with benzoxazole (**2**), quinoline (**3**), quinazoline derivative (**4**), pyrimidine (**5**) or indole (**6**) resulted in a complete loss of activity both in the presence and absence of BSA. This finding highlights the important role of the oxidiazole-amide moiety in maintaining the anti-TB activity; therefore, this structural region was retained for subsequent modifications.

Table 1. Core modifications with their inhibition activity (MIC in µM) against Mtb H37RV.

$$F_3C^{O}$$
 R O OCF_3

		Mtb H37Rv		
Compound	R	MIC (μM)		
		7H9 ADNty ^a	7H9 CasDNTyb	
1	N-N N N N N N N N N N N N N N N N N N N	3.12	<0.049	
2	Z O	>50	>50	
3		>50	>50	
4	N N	>50	>50	
5	O H	>50	>50	
6	N	>50	>50	

^a 7H9 medium supplemented with 0.5% BSA, 0.4% dextrose, 0.08% NaCl, 0.05% Tyloxapol.

Modification of the Eastern part of the molecule revealed that replacing the electron-withdrawing OCF₃ group with donating groups such as methoxy (**7**) and methyl (**8**) led to a decrease in activity, while the alkyne derivative (**9**) showed a slight improvement in activity. Considering the relative potency of **1**, we evaluated various halogenated substituents (**10–13**). The results showed that, while all substituents exhibited similar potency to hit **1** in the absence of BSA, their activity varied in its presence. The brominated (**11**) and chlorinated (**12**) substituents slightly enhanced the activity, with MIC values of 1.56 and 2.34 μ M, respectively, whereas the trifluoromethyl (**10**) resulted in no change in activity. Interestingly, no difference in antitubercular activity

 $^{^{\}rm b}$ 7H9 medium supplemented with 0.3% Casamino acids, 0.4% dextrose, 0.085% NaCl, 0.05% Tyloxapol.

and cytotoxicity was observed between the mono- (12) and the di- (13) chlorinated derivatives. To explore the effect of the distance of the phenyl ring from the central oxidiazole-amide moiety on the activity, compound 14 was synthesized. Keeping the chloro group of compound 12 constant and adding a methyl spacer resulted in loss of activity, indicating that positioning the phenyl ring closer to the core is beneficial for antitubercular activity.

Notably, it was clear that introducing various heterocyclic groups leads to significant loss of activity compared to our initial hit **1**. Specifically, the position of the nitrogen atom in the pyridine derivatives affected the activity; the *para* position (**15**) resulted in less potent derivative than the *meta* position (**16**). Moreover, the latter showed nearly a two-fold increase in activity compared to pyrazine (**16** *vs* **17**) in the presence of BSA. Of the 5-membered ring derivatives, and in the absence of BSA, thiophene **18** was the most potent, followed by furan **19**.

Overall, most of the synthesized derivatives exhibit decreased activity against Mtb in the presence of BSA compared to their activity without it, indicating that BSA medium influences the pharmacological activity of these compounds by binding to them and potentially altering their bioavailability. Among the Eastern derivatives modification, compounds **12** and **13** are the most potent one against Mtb with no significant toxicity (IC₅₀ > 37 μ M).

Table 2. Eastern part modifications with their inhibition activity (MIC in μ M) against *Mtb*H37RV and cytoxicity values in HepG2 cell line.

Compound	R	Mtb H37Rv MIC (μM)		HepG2
		7H9 ADNty ^a	7H9 CasDNTy♭	IC ₅₀ (μΜ)
7		18.75	0.13	28.0 ± 7.5

8		12.5	0.098	>37
9	CZ	1.56	<0.049	3.3 ± 1.1
10	FF	3.12	<0.049	>37
11	ad————————————————————————————————————	1.56	<0.049	>37
12	<u>o</u>	2.34	<0.049	>37
13	CI	2.34	<0.049	>37
14	CI	>50	6.25	27.2 ± 7.2
15	Z	12.5	2.60	12.2 ± 0.2
16		18.75	1.56	11.8 ± 1.5
17	$\begin{pmatrix} z = \\ -z \end{pmatrix}$	37.5	6.25	>37
18	s	18.75	0.22	9.4 ± 0.3
19		>50	3.125	>37

⁸7H9 medium supplemented with 0.5% BSA, 0.4% dextrose, 0.085% NaCl, 0.05% Tyloxapol.

 $^{^{\}rm b}$ 7H9 medium supplemented with 0.3% Casamino acids, 0.4% dextrose, 0.085% NaCl, 0.05% Tyloxapol.

Antimicrobial Profiling

We evaluated the most potent inhibitors identified in our extensive SAR study for their antimicrobial activity against a panel of bacteria. Hit **1** generally demonstrated broader range of activity against most strains, with MIC values in the submicromolar range. However, its antibacterial activity against *Streptococcus pneumoniae* strains was significantly weaker compared to the other analogues. Compound **12** showed the highest potency across both strains of *S. pneumoniae* including the penicillinresistant strain, with nanomolar MIC value of 0.003 µM. Similarly, compound **13** exhibited comparable activity against *S. pneumoniae* strains but showed superior potency against *Bacillus subtilis* than compound **12**. These findings emphasize the structural and functional diversity within the series, offering distinct advantages for further optimization as antimicrobial agents.

Table 3. Antibacterial profile of compounds 1, 12 and 13 against a panel of bacteria.

MIC (μM)	Compound		
	1	12	13
PR-Streptococcus pneumoniae DSM-11865[a]	0.25–0.5	≤0.003	0.006
Streptococcus pneumoniae DSM-20566	≤0.06	0.0125	0.05
Enterococcus faecalis DSM-20478	0.25	>128	0.5
VR-Enterococcus faecium DSM-17050 ^[b]	0.25-0.5	>128	0.5
Enterococcus faecium DSM-20477	0.5–1	>128	4-8
Staphylococcus aureus Newman	0.125–0.25	0.5	0.25–0.5
Bacillus subtilis DSM-10	0.125	0.5	0.125

[a] PRSP: Penicillin resistant; [b] VR: Vancomycin-resistant

Chemistry

The synthesis of compounds **2–6** was achieved via the route described in Scheme 1. Notably, the preparation of the scaffold required for the core modifications involved a Suzuki–Miyaura cross-coupling reaction, followed by nucleophilic acyl substitution when necessary. Specifically, compounds **2–4** and intermediates **5a** and **6a** were synthesized by reacting the boronic acid **2b** with various aryl halides under Suzuki conditions using [Pd(PPh₃)₄] as the catalyst. Subsequently, acetyl substitution of the intermediates was performed in DMF in the presence of either TEA or NaH, yielding compounds **5** and **6**, respectively.

Scheme 1. General scheme for the synthesis of compound **2–6**. Reagents and conditions: i) aryl halide derivative, (3-(trifluoromethoxy)phenyl)boronic acid **2b**, [Pd(PPh₃)₄], Na₂CO₃, dioxane/H₂O 4:1, 120 °C. ii) 3-(trifluoromethoxy)benzoyl chloride, TEA or NaH, DMF, r.t.

We used diverse carboxylic acid derivatives to generate the derivatives **7–19**, featuring variations in the Eastern part of the molecule. Starting with the commercially available 3-(trifluoromethoxy)benzoyl chloride, it was converted to the thiosemicarbazide intermediate **1c**, followed by cyclization using 1,3-dibromo-5,5-dimethylhydantoin (DBDMH) to obtain the respective oxidiazole-amine **1a**. Final amide coupling with a variety of carboxylic acids was carried out using propane

phosphonic acid anhydride (T₃P) as the coupling reagent, to provide derivatives **7–19** in high purity (Scheme 2).

$$\begin{array}{c} \text{O} \\ \text{CF}_3 \end{array} \begin{array}{c} \text{In} \\ \text{N} \\$$

Scheme 2. General scheme for the synthesis of compounds **1**, **7–19**. Reagents and conditions: *i)* hydrazinecarbothioamide, 3-(trifluoromethoxy)benzoyl chloride, THF, 24 h, r.t. *ii)* **1c**, IPA, KI (0 °C), 5M NaOH, DBDMH, 1 h at <10 °C. *iii)* **1a**, acid derivatives, EtOAc, pyridine, T₃P, 40 °C, 18 h.

Conclusions

In conclusion, we have identified an oxadiazole derivative as antitubercular agent through experimental screening using in-house and external libraries. We successfully obtained through a comprehensive SAR study two potent derivatives 12 and 13 with enhanced antibacterial activity against *Mtb* (with and without the presence of the bovine serum albumin) and a range of Gram-positive pathogens, along with low cytotoxicity. Further biological evaluation and investigation of these two frontrunners is currently ongoing to determine their mode of action against *Mtb* as well as their ADMET profiling.

References

- [1] A. Kumar, S. Chettiar, B. S. Brown, J. Early, J. Ollinger, M. Files, M. A. Bailey, A. Korkegian, D. Dennison, M. McNeil, J. Metz, A. Osuma, M. Curtin, A. Kunzer, G. Freiberg, M. Bruncko, D. Kempf, T. Parish, Scientific reports 2022, 12, 14879.
- [2] WHO, Global tuberculosis report 2024, https://iris.who.int/bitstream/handle/10665/379339/9789240101531eng.pdf?sequ ence=1
- [3] WHO, Health Topic, Tuberculosis, https://www.who.int/health-topics/tuberculosis#tab=tab_1.

- [4] A. Sharma, M. de Rosa, N. Singla, G. Singh, R. P. Barnwal, A. Pandey, Journal of medicinal chemistry 2021, 64, 4359.
- [5] R. Capela, R. Félix, M. Clariano, D. Nunes, M. d. J. Perry, F. Lopes, International journal of molecular sciences 2023, 24.
- [6] S. Kiazyk, T. B. Ball, Canada communicable disease report = Releve des maladies transmissibles au Canada 2017, 43, 62.
- [7] X. Du, V. Sonawane, B. Zhang, C. Wang, B. de Ruijter, A. S. S. Dömling, N. Reiling, M. R. Groves, ChemMedChem 2023, 18, e202300279.
- [8] A. Richter, R. W. Seidel, R. Goddard, T. Eckhardt, C. Lehmann, J. Dörner, F. Siersleben, T. Sondermann, L. Mann, M. Patzer, C. Jäger, N. Reiling, P. Imming, ACS medicinal chemistry letters 2022, 13, 1302.
- [9] C. Duan, Q. Jiang, X. Jiang, H. Zeng, Q. Wu, Y. Yu, X. Yang, Molecules (Basel, Switzerland) 2022, 27.
- [10] WHO, Global Research Agenda for Antimicrobial Resistance in Human Health. World Health Organization.
- [11] G. S. Shetye, S. G. Franzblau, S. Cho, Translational research the journal of laboratory and clinical medicine 2020, 220, 68.
- [12] A. Chauhan, M. Kumar, A. Kumar, K. Kanchan, Life sciences 2021, 274, 119301.
- [13] A. Maure, E. Lawarée, F. Fiorentino, A. Pawlik, S. Gona, A. Giraud-Gatineau, M. J. G. Eldridge, A. Danckaert, D. Hardy, W. Frigui, C. Keck, C. Gutierrez, O. Neyrolles, N. Aulner, A. Mai, M. Hamon, L. B. Barreiro, P. Brodin, R. Brosch, D. Rotili, L. Tailleux, PLoS biology 2024, 22, e3002259.
- [14] S. S. De, M. P. Khambete, M. S. Degani, Bioorganic & medicinal chemistry letters 2019, 29, 1999.
- [15] M. Lynn, A. R. Wilson, M. Solotorovsky, Applied and environmental microbiology 1979, 38, 806.
- [16] Y. Morishige, Y. Murase, K. Chikamatsu, H. Yamada, A. Aono, Y. Igarashi, K. Kamada, Y. Shimomura, M. Hosoya, A. Takaki, S. Mitarai 2021.

2.2.1 Supplementary information

Discovery of a New Oxadiazole Derivative as Antitubercular Agents: Structure—Activity Relationship and Mode-of-Action Studies

Justine Bassil^{1,2,3†}, Gareth Prosser⁴, Mostafa M. Hamed^{1,3}, Norbert Reiling⁴, Anna K. H. Hirsch^{1,2,3*}

¹ Helmholtz Institute for Pharmaceutical Research Saarland (HIPS) – Helmholtz Centre for Infection Research (HZI), Campus Building E 8.1, D-66123, Saarbrücken, Germany

² Saarland University, 66123 Saarbrücken, Germany

³ PharmaScienceHub (PSH), campus building A, D-66123 Saarbrücken, Germany

⁴ RG Microbial Interface Biology, Research Center Borstel, Leibniz Lung Center, Parkallee 1-40, 23845 Borstel, Germany

Materials and methods

Starting materials and solvents were purchased from commercial suppliers and used without further purification. Reaction progress was monitored using TLC silica gel 60 F254 aluminum sheets with a suitable solvent mixture and was visualized using UV fluorescent at 254 nm.

Proton (¹H) and carbon (¹³C) nuclear magnetic resonance spectra were recorded on a Bruker AV 500 MHz spectrometer (¹H at 500.0 MHz; ¹³C at 126.0 MHz) instrument. The chemical shifts are recorded as δ values in parts per million (ppm) and the coupling constants (J) in Hertz (Hz) and referenced against residual deuterated solvent peak (Chloroform (CDCl₃): δ = 7.26, 77.2; Dimethyl sulfoxide (DMSO- d_6): δ = 2.50, 39.5; acetone- d_6 (((CD₃)₂CO): δ = 2.05, 29.84). Data are reported as follows: chemical shift, multiplicity (s: singlet, br s: broad singlet, d: doublet, dd: doublet of doublets, t: triplet, dt: doublet of triplets, q: quartet, m: multiplet) coupling constants and integration.

Purification of products was performed via different methods: 1) Flash chromatography using the automated flash chromatography system CombiFlash Rf+ (Teledyne Isco, Lincoln, NE, USA) equipped with RediSepRf silica columns (Axel Semrau, Sprockhövel Germany). 2) Preparative high-performance liquid chromatography (HPLC) using an UltiMate 3000 Semi-Preparative System (Thermo Fisher Scientific) with nucleodur® C18 Gravity (250 mm × 16 mm, 5 μ m). Separation was done using gradient 5–100% ACN + 0.05% FA in H₂O + 0.05% FA in 53 min at a flow rate of 10 mL/min and end with a 5 min step at 100% ACN. The sample was dissolved in DMSO and manually injected to the HPLC system.

Liquid chromatography-mass spectrometry was performed on a LC-MS system, consisting of a Dionex UltiMate 3000 pump, autosampler, column compartment and MWD or DAD detector (Thermo Fisher Scientific, Dreieich, Germany) and ESI quadrupole MS (MSQ Plus or ISQ EC, Thermo Fisher Scientific, Dreieich, Germany). Columns used: 1) Hypersil Gold column, $100 \times 2.1 \text{ mm}$, 3 µm. At a flow rate of 700 µL/min, the gradient of H_2O (0.1% FA) and ACN (0.1% FA) starting from 5% ACN and then increased to 100% over 7 min. 2) Hypersil Gold column, $100 \times 1.9 \text{ mm}$, 2.1 µm. At a flow rate of 600 µL/min, the gradient of H_2O (0.1% FA) and ACN (0.1% FA) started

from 5% ACN and then increased to 100% over 5.5 min. The mass spectrum was measured in positive and negative mode in a range from 100–600 m/z. The UV spectrum was recorded at 254 nm.

High-resolution mass spectra (HR-MS) were recorded with a ThermoScientific system where a Dionex Ultimate 3000 RSLC was coupled to a Q Exactive Focus mass spectrometer with an electrospray ion (ESI) source. An Acquity UPLC® BEH C8, 150 x 2.1 mm, 1.7 μ m column equipped with a VanGuard Pre-Column BEH C8, 5 x 2.1 mm, 1.7 μ m (Waters, Germany) was used for separation. At a flow rate of 250 μ L/min, the gradient of (A) H₂O + 0.1% FA and (B) ACN + 0.1% FA was held at 10% B for 1 min and then increased to 95% B over 4 min. It was held there for 1.2 min before the gradient was decreased to 10% B over 0.3 min where it was held for 1 min. The mass spectrum was measured in positive or negative mode in a range from 120–1000 m/z. UV spectrum was recorded at 254 nm. The purity of the final compounds was determined by using the area percentage method on the UV trace and found to be >95%.

Abbreviations

Acetone ((CD₃)₂CO), acetonitrile (ACN), chloroform (CDCl₃), cesium carbonate (Cs₂CO₃), dichloromethane (DCM), dimethylformamide (DMF), dimethylsulfoxide (DMSO), ethyl acetate (EtOAc), formic acid (FA), hydrochloric acid (HCl), isopropanol (IPA), lithium hydroxide (LiOH), methanol (MeOH), sodium hydride (NaH), sodium hydroxide (NaOH) propanephosphonic acid cyclic anhydride 50% in ethyl acetate (T_3P), sodium sulfate (Na₂SO₄), tetrahydrofuran (THF), Tetrakis(triphenylphosphine)palladium (Pd(PPh₃)₄), trifluoroacetic acid (TFA), water (H₂O). Other abbreviations used are: aqueous (aq.), calculated (calcd), equivalents (equiv.) hours (h), HRMS (high-resolution mass spectrometry), minutes (min), room temperature (rt), saturated (sat.) part(s) per million (ppm).

Synthesis procedure of compounds 1-19

General procedure for amide coupling (GP1) using carboxylic acid derivatives (1, 7–19):

$$N-N$$
 $N-N$
 $N+R_1$
 O
 CF_3
 $N-N$
 R_1
 O
 CF_3
 $N-N$
 R_1
 O
 CF_3

In a round-bottomed flask, the corresponding acid (1 equiv.) and 5-(3-(trifluoromethoxy)phenyl)-1,3,4-oxadiazol-2-amine ($\mathbf{1a}$) (1.1 equiv.) were dissolved in EtOAc (0.15 M) and pyridine (70 equiv). Propylphosphonic anhydride (T_3P) 50% solution in EtOAc (14 equiv.) was then added, and the reaction was stirred at 40 °C for 18 h. Afterwards, The mixture was poured onto water (25 mL), acidified by HCl (1 M) to pH 5–6 and was extracted with EtOAc (30 mL × 3). The organic layers were dried over MgSO₄, filtered, and the solvent was removed under reduced pressure. The crude obtained was purified by preparative HPLC (Gradient flow "10mL/min", H_2O :ACN+0.1% FA, 5% to 100% ACN) to afford the respective product.

General procedure for suzzuki coupling (GP-2) (2-4, 5a and 6a):

In a microwave-compatible reaction vial, aryl halide (1 equiv.), aryl boronic acid ((3-(trifluoromethoxy)phenyl)boronic acid) **2b** (2 equiv. or 3.5 equiv), Na₂CO₃ (4 equiv) and [Pd(PPH₃)₄] (0.05 equiv.) were dissolved in dioxane/water (4:1) solvent mixture. The vial was placed in the microwave, and the reaction mixture was irradiated at 120 °C for 45 min. After cooling, the reaction was poured into H₂O, and extracted with DCM. The organic layers were dried over MgSO₄, filtered and the solvent was removed under reduced pressure. The crude obtained was purified by preparative HPLC (Gradient flow "10mL/min", H₂O:ACN + 0.1% FA, 5% to 100% ACN) or by automated flash chromatography (PE/EtOAc, 100:0 \rightarrow 0:100) to afford the respective product.

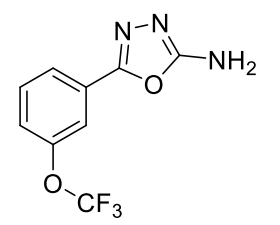
2-(3-(Trifluoromethoxy)benzoyl)hydrazine-1-carbothioamide (1c)

$$\bigcup_{O_{\mathsf{CF}_3}}^{\mathsf{O}} \bigvee_{\mathsf{H}}^{\mathsf{H}} \bigvee_{\mathsf{S}}^{\mathsf{NH}_2}$$

To hydrazine carbothio amide (2 g, 8.9 mmol) and THF (30 mL), 3-(trifluoromethoxy) benzoyl chloride (1.217 g, 13.35 mmol) was added dropwise at 0 $^{\circ}$ C using an ice bath. The mixture was stirred at room temperature under nitrogen atmosphere for 24

h. The mixture was quenched by the addition of water and alkalized using a saturated aqueous solution of NaHCO₃. Afterward, THF was evaporated, and the product was washed with water, filtered under vacuum and collected as white powder (1.4 g, 70%). ¹**H NMR** (500MHz, DMSO- d_6) δ 10.56 (s, 2H), 9.38 (s, 2H), 7.92 (d, J = 7.2 Hz, 4H), 7.85 (s, 2H), 7.63 (t, J = 7.9 Hz, 2H), 7.58 (d, J = 6.9 Hz, 1H). ¹³**C NMR** (126 MHz, DMSO- d_6) δ 182.04, 164.41, 148.13, 134.84, 130.44, 126.98, 124.31, 120.

5-(3-(Trifluoromethoxy)phenyl)-1,3,4-oxadiazol-2-amine (1a)



Compound 1c (1 g, 3.58 mmol) was filled into a flask and suspended in IPA (20 mL). The suspension was mixed with a solution of potassium iodide (178.34 mg, 1.07 mmol) in water (1.5 mL). The reaction was cooled to 0 °C on an ice bath, and a 5

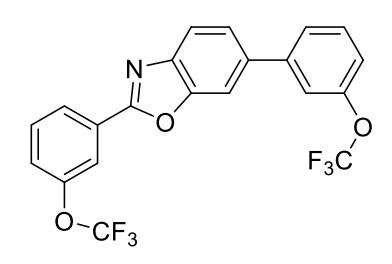
M solution of NaOH (214.86 mg, 5.37 mmol) was added. 1,3-Dibromo-5,5-dimethylimidazolidine-2,4-dione (767.94 mg, 2.68 mmol) dissolved in ACN (9 mL) was added dropwise while the temperature was maintained below 10 °C. Afterward, the reaction was aged for 1 h below 10 °C. The reaction mixture was quenched using NaHCO₃ saturated (0.25 mL), and water was added. The pH was adjusted to >12 using a saturated solution of NaHCO₃. Excess solvent was evaporated under reduced pressure, then water (30 mL) was added, and mixture was extracted with EtOAc (30 mL × 3). The organic solvent was then dried over MgSO₄, filtered and evaporated under reduced pressure. Purification was done using automated flash chromatography (PE/EtOAc, $100:0 \rightarrow 0:100$) affording compound **1a** (750 mg, 85%) as a yellow solid. ¹H NMR (500 MHz, DMSO- d_6) δ 7.82 (d, J = 7.9 Hz, 1H), 7.72 – 7.65 (m, 2H), 7.53 (d, J = 9.5 Hz, 1H), 7.39 (s, 2H). ¹³C NMR (126 MHz, DMSO- d_6) δ 164.34, 156.27, 148.87 (q, J = 2.3 Hz), 131.87, 126.56, 124.20, 122.95, 120.19 (q, J = 256.9 Hz), 117.19. **LC-MS** calcd for C₉H₇F₃N₃O₂ [M+H]*: 246.05 found 246.08.

3-(Trifluoromethoxy)-N-(5-(3-(trifluoromethoxy)phenyl)-1,3,4-oxadiazol-2-yl)benzamide (1)

According to **GP1**, T₃P (0.6 mL, 2.04 mmol) was added to a solution of 3-(trifluoromethoxy)benzoic acid (30 mg, 0.145 mmol) and amine **1a** (39.5 mg, 0.16 mmol) in EtOAc (0.9 mL) and pyridine (0.9 mL) to afford after preparative HPLC compound **1** (30 mg, 47%) as a white solid. ¹H NMR

(500 MHz, (CD₃)₂CO) δ 8.20 (d, J = 7.7 Hz, 1H), 8.07 (d, J = 8.3 Hz, 2H), 7.93 (s, 1H), 7.80 (t, J = 8.0 Hz, 1H), 7.74 (t, J = 8.0 Hz, 1H), 7.64 (t, J = 9.1 Hz, 2H). ¹³**C NMR** (126 MHz, (CD₃)₂CO) δ 150.36 (q, J = 2.1 Hz), 150.01 (q, J = 2.1 Hz), 132.52, 131.61, 128.25, 127.23, 126.82, 126.12, 126.00, 125.09, 121.86, 121.43 (q, J = 256.5 Hz), 119.45, 119.39 (q, J = 256.5 Hz). **HR-MS** calcd for C₁₇H₈F₆N₃O₄ [M-H]⁻: 432.04245 found 432.04250.

2,6-bis(3-(Trifluoromethoxy)phenyl)benzo[d]oxazole (2)



According to **GP2**, 2,6-dichlorobenzo[d]oxazole (100 mg, 0.53 mmol), **2b** (383.36 mg, 1.86 mmol), Na_2CO_3 (225.5 mg, 30.73 mmol) and [Pd(PPh₃)₄] (61.47 mg, 0.026 mmol) in 5 mL dioxan/H₂O mixture afforded after preparative HPLC compound **2** (85 mg, 36%) as an off-white solid. ¹H

NMR (500 MHz, CDCl₃) δ 8.21 (d, J = 7.8 Hz, 1H), 8.13 (s, 1H), 7.85 (d, J = 8.3 Hz, 1H), 7.79 (d, J = 1.6 Hz, 1H), 7.62 – 7.56 (m, 3H), 7.52 – 7.48 (m, 2H), 7.41 (d, J = 5.8 Hz, 1H), 7.27 – 7.22 (m, 1H). ¹³**C NMR** (126 MHz, CDCl₃) δ 162.38, 151.56, 149.93 (q, J = 1.8 Hz), 149.83 (d, J = 1.8 Hz), 142.92, 141.97, 137.99, 130.73, 130.45, 129.10, 126.06, 125.90, 124.63, 124.18, 120.68 (q, J = 257.4 Hz), 120.61 (q, J = 257.8 Hz), 120.62, 120.27, 120.15, 120.03, 109.49. **HR-MS** calcd for C₂₁H₁₂F₆NO₃ [M+H]*: 440.07159 found 440.0719.

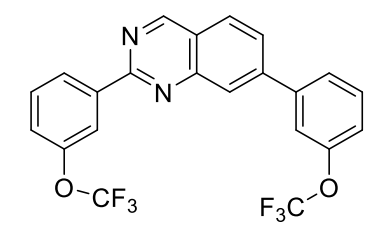
2,7-bis(3-(Trifluoromethoxy)phenyl)quinolone (3)

According to **GP2**, 7-bromo-2-chloroquinoline (100 mg, 0.412 mmol), **2b** (297.21 mg, 1.44 mmol), Na_2CO_3 (174.83 mg, 1.65 mmol) and $[Pd(PPh_3)_4]$ (23.83 mg, 0.02 mmol) in 5 mL dioxane/ H_2O mixture afforded after preparative HPLC compound **3** (118 mg,

64%) as a beige solid. ¹H NMR (500 MHz, CDCl₃) δ 8.40 (s, 1H), 8.27 (d, J = 8.5 Hz, 2H), 8.11 (d, J = 8.0 Hz, 2H), 7.93 (d, J = 8.4 Hz, 2H), 7.88 (d, J = 8.5 Hz, 2H), 7.79 (dd, J = 8.4, 1.8 Hz, 2H), 7.72 (d, J = 8.0 Hz, 1H), 7.64 (s, 2H), 7.55 (dt, J

= 13.8, 7.9 Hz, 3H), 7.34 (d, J = 8.1 Hz, 1H), 7.28 (d, J = 8.2 Hz, 1H). ¹³C NMR (126 MHz, CDCl₃) δ 156.37, 150.06 (q, J = 1.8 Hz), 150.01 (q, J = 2.0 Hz), 148.55, 142.53, 141.72, 141.15, 136.97, 130.49, 130.36, 128.36, 127.95, 126.97, 126.15, 125.96, 125.90, 121.89, 120.73 (q, J = 257.4 Hz), 120.70 (q, J = 257.4 Hz), 120.39, 120.34, 120.19, 119.10. ¹³C NMR (126 MHz, CDCl₃) δ 156.40, 150.04 (q, J = 6.4 Hz), 148.55, 142.54, 141.72, 141.19, 137.00, 130.51, 130.38, 128.38, 127.95, 126.98, 126.18, 125.97, 125.93, 121.91, 120.73 (q, J = 257.4 Hz), 120.70 (q, J = 257.4 Hz), 120.41, 120.36, 120.22, 119.13. **HR-MS** calcd for C₂₃H₁₄F₆NO₂ [M+H]⁺: 450.09232 found 450.0925.

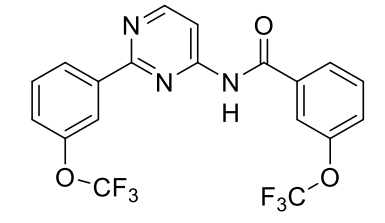
2,7-bis(3-(Trifluoromethoxy)phenyl)quinazoline (4)



According to **GP2**, 7-bromo-2-chloroquinazoline (100 mg, 0.410 mmol), **2b** (296 mg, 1.44 mmol), Na₂CO₃ (174.12 mg, 1.64 mmol) and [Pd(PPh₃)₄] (23.73 mg, 0.02 mmol) in 5 mL dioxane/H₂O mixture afforded after preparative

HPLC compound **4** (180 mg, 97%) as a white solid. ¹**H NMR** (500 MHz, CDCl₃) δ 9.49 (s, 1H), 8.59 (d, J = 7.9 Hz, 1H), 8.53 (s, 1H), 8.29 (s, 1H), 8.03 (d, J = 8.4 Hz, 1H), 7.87 (dd, J = 8.4, 1.8 Hz, 1H), 7.71 (d, J = 7.9 Hz, 1H), 7.62 (s, 1H), 7.57 (t, J = 8.0 Hz, 2H), 7.37 (d, J = 5.9 Hz, 1H), 7.33 (d, J = 8.3 Hz, 1H). ¹³C NMR (126 MHz, CDCl₃) δ 160.49, 160.32, 151.11, 150.06 (q, J = 2.0 Hz), 149.95 (q, J = 2.0 Hz), 145.53, 141.77, 140.23, 130.71, 130.12, 128.01, 127.25, 127.00, 126.77, 126.13, 123.21 (d, J = 1.8 Hz), 121.31, 121.14, 120.75 (q, J = 257.1 Hz), 120.67 (q, J = 257.8 Hz), 120.38. **HR-MS** calcd for C₂₂H₁₃F₆N₂O₂ [M+H]⁺:451.08757 found 451.0878.

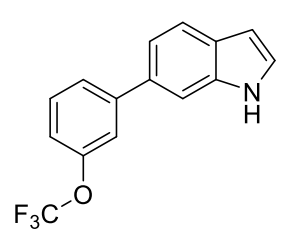
3-(Trifluoromethoxy)-N-(2-(3-(trifluoromethoxy)phenyl)pyrimidin-4-yl)benzamide (5)



In a round bottom flask, TEA (95.17 mg, 0.94 mmol, 3 equiv.) and 3-(trifluoromethoxy)benzoyl chloride (140.8 mg, 0.626 mmol, 2 equiv.) were added to a solution of compound **5a** (80 mg, 0.313 mmol, 1 equiv.) in 2 mL DMF.

The reaction was stirred at rt for 6 h. The reaction mixture was poured into H₂O and extracted with EtOAc. The organic layers were dried over MgSO₄, filtered and the solvent was removed under reduced pressure. The crude obtained was purified by preparative HPLC (Gradient flow "10mL/min", H₂O:ACN + 0.1% FA, 5% to 100% ACN) to afford the respective product **5** (30 mg, 21%) as a white solid. ¹**H NMR** (500 MHz, CDCl₃) δ 8.81 (dd, J = 5.8, 3.0 Hz, 1H), 8.59 (s, 1H), 8.39 (d, J = 7.7 Hz, 1H), 8.30 (s, 1H), 8.25 (dd, J = 5.6, 3.3 Hz, 1H), 7.89 (d, J = 7.3 Hz, 1H), 7.85 (s, 1H), 7.62 (td, J = 8.1, 3.0 Hz, 1H), 7.57 – 7.48 (m, 2H), 7.36 (d, J = 8.2 Hz, 1H). ¹³**C NMR** (126 MHz, CDCl₃) δ 164.80, 163.10, 159.46, 157.49, 149.94 (q, J = 1.8 Hz), 139.28, 135.56, 130.83, 130.10, 126.55, 125.42, 125.39, 123.50, 120.86, 120.60, 108.83. **HR-MS** calcd for C₁₉H₁₀F₆N₃O₃ [M-H]⁻: 442.06318 found 442.06320.

6-(3-(Trifluoromethoxy)phenyl)-1H-indole (6a)



According to **GP2,** 6-bromo-1H-indole (100 mg, 0.510 mmol), **2b** (210 mg, 1.02 mmol), Na_2CO_3 (216.25 mg, 2.04 mmol) and $[Pd(PPh_3)_4]$ (29.47 mg, 0.025 mmol) in 5 mL dioxane/ H_2O mixture afforded after automated flash chromatography **6a**

(121 mg, 85%) as a brown solid. ¹H NMR (500 MHz, CDCl₃) δ 8.26 (s, 1H), 7.72 (d, J = 8.2 Hz, 1H), 7.61 – 7.56 (m, 2H), 7.49 (s, 1H), 7.45 (t, J = 7.9 Hz, 1H), 7.36 (dd, J = 8.2, 1.6 Hz, 1H), 7.28 (t, J = 2.8 Hz, 1H), 7.17 (d, J = 8.2 Hz, 1H), 6.61 – 6.58 (m, 1H). ¹³C NMR (126 MHz, CDCl₃) δ 149.82 (q, J = 1.8 Hz), 144.59, 136.43, 134.09, 130.07, 127.89, 125.80, 125.40, 121.30, 119.72, 109.78, 119.49 (q, J = 257 Hz) 102.83. LCMS calcd for C₁₅H₁₁F₃NO [M+H]⁺: 278.078 found 278.10.

(3-(Trifluoromethoxy)phenyl)(6-(3-(trifluoromethoxy)phenyl)-1H-indol-1-yl)methanone (6)

In a round bottom flask, NaH was added to a solution of compound **6a** (100 mg, 0.36 mmol, 1 equiv.) in 5 mL DMF. The reaction was stirred at rt for 30 min and then 3-(trifluoromethoxy)benzoyl chloride (97.2 mg, 0.432 mmol, 1.2 equiv.) was added, and mixture was stirred at rt

overnight . The reaction mixture was poured into H_2O and extracted with EtOAc. The organic layers were dried over MgSO₄, filtered and the solvent was removed under reduced pressure. The crude obtained was purified by preparative HPLC (Gradient flow "10mL/min", H_2O :ACN + 0.1% FA, 40% to 100% ACN) to afford compound **6** (88 mg, 52.4%) as dark red oil. ¹**H NMR** (500 MHz, CDCl₃) δ 8.67 (d, J = 1.7 Hz, 1H), 7.71 – 7.66 (m, 2H), 7.65 – 7.61 (m, 2H), 7.61 – 7.56 (m, 2H), 7.53 (s, 1H), 7.48 (dd, J = 9.3, 6.7 Hz, 2H), 7.30 (d, J = 3.7 Hz, 1H), 7.22 (ddt, J = 8.2, 2.4, 1.2 Hz, 1H), 6.68 (d, J = 3.7 Hz, 1H). ¹³**C NMR** (126 MHz, CDCl₃) δ 167.09, 149.86 (q, J = 2.3 Hz), 149.39 (q, J = 2.3 Hz), 143.76, 137.20, 136.72, 136.41, 130.66, 130.49, 130.22, 127.99, 127.53, 125.99, 124.51, 123.83, 123.64, 121.87, 121.69 (q, J = 257.6 Hz), 121.55, 120.73 (q, J = 257.4 Hz), 120.21, 119.56, 115.29, 109.24. **HR-MS** calcd for C₂₃H₁₄F₆NO₃ [M+H]*: 466.08724 found 466.2642.

3-methoxy-N-(5-(3-(trifluoromethoxy)phenyl)-1,3,4-oxadiazol-2-yl)benzamide (7)

According to GP1, T_3P (0.9 mL, 3.22 mmol) was added to a solution of 3-methoxybenzoic acid (35 mg, 0.230 mmol)

and amine **1a** (62 mg, 0.253 mmol) in EtOAc (1.5 mL) and pyridine (1.5 mL) to afford after preparative HPLC compound **7** (25 mg, 29%) as a white solid. ¹**H NMR** (500 MHz, DMSO– d_6) δ 12.26 (s, 1H), 8.00 (d, J = 7.8 Hz, 1H), 7.85 (s, 1H), 7.78 (t, J = 8.0 Hz, 1H), 7.69 – 7.58 (m, 3H), 7.48 (t, J = 7.9 Hz, 1H), 7.23 (dd, J = 8.3, 2.5 Hz, 1H), 3.85 (s, 3H). ¹³**C NMR** (126 MHz, DMSO) δ 164.64, 159.68, 159.28, 158.41, 148.76 (q, J = 2.3 Hz), 133.58, 132.01, 129.87, 125.47, 125.20, 124.26, 120.63, 120.02 (q, J = 257.4 Hz), 119.11, 118.21, 113.09, 55.43. **HR-MS** calcd for C₁₇H₁₁F₃N₃O₄ [M-H]⁻: 378.07071 found 378.07090.

3-methyl-N-(5-(3-(trifluoromethoxy)phenyl)-1,3,4-oxadiazol-2-yl)benzamide (8)

According to GP1, T_3P (0.9 mL, 3.08 mmol) was added to a solution of 3-methylbenzoic acid (30 mg, 0.220 mmol) and amine **1a** (59.4 mg,

0.246 mmol) in EtOAc (1.5 mL) and pyridine (1.5 mL) to afford after preparative HPLC compound **8** (18 mg, 23%) as a white powder. ¹**H NMR** (500 MHz, DMSO– d_6) δ 12.19 (s, 1H), 8.00 (d, J = 7.8 Hz, 1H), 7.85 (dd, J = 14.3, 8.0 Hz, 3H), 7.78 (t, J = 8.1 Hz, 1H), 7.66 (d, J = 8.4 Hz, 1H), 7.47 (dt, J = 15.0, 7.6 Hz, 2H), 2.41 (s, 3H). ¹³**C NMR** (126 MHz, DMSO– d_6) δ 164.90, 159.80, 158.29, 148.75 (q, J = 2.3 Hz), 138.10, 133.62, 132.11, 132.01, 128.80, 128.59, 125.48, 125.20, 124.25, 120.02 (q, J = 257.1 Hz), 118.20, 20.88. **HR-MS** calcd for C₁₇H₁₁F₃N₃O₃ [M-H]⁻: 362.07580 found 362.07540.

3-ethynyl-N-(5-(3-(trifluoromethoxy)phenyl)-1,3,4-oxadiazol-2-yl)benzamide (9)

According to GP1, T_3P (1 mL, 3.35 mmol) was added to a solution of 3-ethynylbenzoic acid (35 mg, 0.240 mmol) and amine **1a** (64,6 mg, 0.263 mmol) in EtOAc (1.6 mL) and pyridine (1.6 mL)

to afford after preparative HPLC compound **9** (30 mg, 34%) as a white powder. ¹**H NMR** (500 MHz, DMSO- d_6) δ 8.46 (s, 1H), 8.33 (d, J = 7.9 Hz, 1H), 8.13 (d, J = 7.7 Hz, 1H), 8.00 (d, J = 7.8 Hz, 1H), 7.85 (s, 1H), 7.79 (td, J = 7.9, 4.2 Hz, 2H), 7.67 (d, J = 8.4 Hz, 1H). ¹³**C NMR** (126 MHz, DMSO- d_6) δ 158.73, 149.09 (q, J = 2.3 Hz), 136.43, 134.21, 133.37, 132.45, 132.36, 130.39, 125.68, 125.54, 124.68, 120.35 (q, J = 257.4 Hz), 118.53, 118.43, 112.11. **HR-MS** calcd for C₁₈H₉F₃N₃O₃ [M-H]⁻: 372.06015 found 373.0555.

N-(5-(3-(trifluoromethoxy)phenyl)-1,3,4-oxadiazol-2-yl) 3(trifluoromethyl)benzamide (10)

According to GP1, T_3P (1.3 mL, 4.42 mmol) was added to a solution of 3-(trifluoromethyl)benzoic acid (60 mg, 0.315

mmol) and amine **1a** (85.11 mg, 0.347 mmol) in EtOAc (2.1 mL) and pyridine (2.1 mL) to afford after preparative HPLC compound **10** (55 mg, 42%) as a white powder. ¹H

NMR (500 MHz, CDCl₃) δ 8.39 (d, J = 5.9 Hz, 1H), 8.33 (d, J = 7.4 Hz, 1H), 8.01 (dt, J = 15.8, 7.2 Hz, 2H), 7.86 – 7.73 (m, 3H), 7.66 (d, J = 7.3 Hz, 1H). ¹³**C NMR** (126 MHz, DMSO– d_6) δ 158.42, 148.76, 133.60, 132.51, 132.00, 130.02, 129.35 (q, J = 16.1 Hz), 127.11, 125.37, 125.18, 124.98 (q, J = 10.6 Hz), 124.30, 121.85 (q, J = 312.5 Hz), 119.39 (q, J = 256.9 Hz), 118.19. **HR-MS** calcd for C₁₇H₈F₆N₃O₃ [M–H]⁻: 416.04753 found 416.0478.

3-bromo-N-(5-(3-(trifluoromethoxy)phenyl)-1,3,4-oxadiazol-2-yl)benzamide (11)

According to GP1, T_3P (0.9 mL, 3.13 mmol) was added to a solution of 3-bromobenzoic acid (45 mg, 0.224 mmol) and amine **1a** (60.4 mg, 0.246

mmol) in EtOAc (1.5 mL) and pyridine (1.5 mL) to afford after preparative HPLC compound **12** (32 mg, 33%) as a white solid. ¹**H NMR** (500 MHz, DMSO– d_6) δ 12.40 (s, 1H), 8.23 (s, 1H), 8.02 (dd, J = 14.5, 7.6 Hz, 2H), 7.90 – 7.84 (m, 2H), 7.78 (t, J = 8.0 Hz, 1H), 7.67 (dd, J = 8.3, 2.4 Hz, 1H), 7.54 (t, J = 7.9 Hz, 1H). ¹³**C NMR** (126 MHz, DMSO– d_6) δ 163.65, 160.09, 158.38, 149.07, 135.97, 134.69, 132.36, 131.30, 131.24, 130.50, 127.82, 125.64 (d, J = 21.6 Hz), 124.66, 122.16, 120.35 (q, J = 257.4 Hz), 118.55. **HR-MS** calcd for C₁₆H₈BrF₃N₃O₃ [M–H]⁻: 425.97066 found 425.9712.

3-chloro-N-(5-(3-(trifluoromethoxy)phenyl)-1,3,4-oxadiazol-2-yl)benzamide (12)

According to GP1, T_3P (0.9 mL, 3.13 mmol) was added to a solution of 3-chlorobenzoic acid (35 mg, 0.223 mmol) and amine **1a** (60.3 mg, 0.246

mmol) in EtOAc (1.5 mL) and pyridine (1.5 mL) to afford after preparative HPLC compound **13** (16 mg, 19%) as a white solid. ¹**H NMR** (500 MHz, DMSO– d_6) δ 8.09 (s, 1H), 8.00 (d, J = 7.8 Hz, 2H), 7.84 (s, 1H), 7.77 (t, J = 8.0 Hz, 1H), 7.73 (d, J = 8.1 Hz, 1H), 7.66 (d, J = 10.5 Hz, 1H), 7.60 (t, J = 7.9 Hz, 1H). ¹³**C NMR** (126 MHz, DMSO– d_6) δ 159.12, 148.92 (q, J = 1.8 Hz), 133.52, 132.64, 132.17, 130.77, 129.14, 128.31, 127.29, 125.70, 125.32, 124.37, 120.19 (d, J = 257.4 Hz), 118.31. **HR-MS** calcd for $C_{16}H_8ClF_3N_3O_3[M-H]^-$: 382.02118 found 382.02150.

3,5-dichloro-N-(5-(3-(trifluoromethoxy)phenyl)-1,3,4-oxadiazol-2-yl)benzamide (13)

According to GP1, T_3P (0.86 mL, 2.93 mmol) was added to a solution of 3,5-dichlorobenzoic acid (40 mg, 0.209 mmol) and amine **1a** (56.5 mg, 0.230 mmol) in EtOAc

(1.4 mL) and pyridine (1.4 mL) to afford after preparative HPLC compound **9** (30 mg, 34%) as a white powder. ¹**H NMR** (500 MHz, DMSO– d_6) δ 8.05 (d, J = 1.9 Hz, 2H), 7.99 (d, J = 7.8 Hz, 1H), 7.94 (s, 1H), 7.84 (s, 1H), 7.78 (t, J = 8.0 Hz, 1H), 7.67 (d, J = 8.2 Hz, 1H). ¹³C NMR (126 MHz, DMSO– d_6) δ 158.83, 149.25 (q, J = 2.0 Hz), 134.99, 132.57, 132.53, 127.66, 125.79, 125.72, 124.89, 120.51 (d, J = 256.9 Hz), 118.71. **HR-MS** calcd for $C_{16}H_7Cl_2F_3N_3O_3$ [M–H]⁻: 415.98220 found 415.9826.

2-(4-chlorophenyl)-N-(5-(3-(trifluoromethoxy)phenyl)-1,3,4-oxadiazol-2-yl)acetamide (14)

$$F_3C$$

According to GP1, T₃P (0.97 mL, 3.28 mmol) was added to a solution of 2-(3-chlorophenyl)acetic acid (40 mg, 0.234

mmol) and amine **1a** (63.2 mg, 0.258 mmol) in EtOAc (1.6 mL) and pyridine (1.6 mL) to afford after preparative HPLC compound **14** (25 mg, 27%) as an off-white powder. **1H NMR** (500 MHz, DMSO– d_6) δ 7.93 (d, J = 7.8 Hz, 1H), 7.78 (s, 1H), 7.74 (t, J = 8.0 Hz, 1H), 7.63 (d, J = 8.4 Hz, 1H), 7.41 (d, J = 8.4 Hz, 2H), 7.35 (d, J = 8.4 Hz, 2H), 3.81 (s, 2H). **13C NMR** (126 MHz, DMSO– d_6) δ 168.43, 159.15, 157.76, 148.75 (q, J = 2.3 Hz), 133.51, 131.97, 131.65, 131.40, 128.31, 125.49, 125.09, 124.11, 120.00 (q, J = 257.4 Hz), 118.07, 41.51. **HR-MS** calcd for C₁₇H₁₀ClF₃N₃O₃ [M–H]: 396.03683 found 396.0369.

N-(5-(3-(trifluoromethoxy)phenyl)-1,3,4-oxadiazol-2-yl)isonicotinamide (15)

According to GP1, T_3P (1.2 mL, 3.98 mmol) was added to a solution of isonicotinic acid (35 mg, 0.284 mmol) and amine **1a** (77 mg, 0.313 mmol) in EtOAc (1.9 mL) and pyridine (1.9 mL) to afford after preparative HPLC compound **15** (29 mg, 29%) as a

$$F_3C$$

yellow powder. ¹**H NMR** (500 MHz, DMSO– d_6) δ 8.83 (d, J = 5.5 Hz, 2H), 8.00 (d, J = 7.8 Hz, 1H), 7.96 – 7.91 (m, 2H), 7.85 (s, 1H), 7.78 (t, J = 8.0 Hz,

1H), 7.67 (d, J = 8.3 Hz, 1H). ¹³C NMR (126 MHz, DMSO– d_6) δ 164.42, 159.19, 158.33, 150.53, 148.74 (q, J = 2.5 Hz), 139.85, 132.03, 125.35, 125.24, 124.37, 121.90, 120.02 (q, J = 257.1 Hz), 118.23. **HR-MS** calcd for C₁₅H₈F₃N₄O₃ [M-H]⁻: 349.05540 found 349.05560.

N-(5-(3-(trifluoromethoxy)phenyl)-1,3,4-oxadiazol-2-yl)nicotinamide (16)

$$F_3C$$

According to GP1, T₃P (1.2 mL, 3.98 mmol) was added to a solution of nicotinic acid (35 mg, 0.284 mmol) and amine **1a** (77 mg, 0.313 mmol)

in EtOAc (1.9 mL) and pyridine (1.9 mL) to afford after preparative HPLC compound **15** (25 mg, 25%) as a white powder. ¹**H NMR** (500 MHz, DMSO– d_6) δ 9.18 (d, J = 2.3 Hz, 1H), 8.82 (d, J = 5.0 Hz, 1H), 8.38 (dt, J = 8.0, 2.1 Hz, 1H), 8.01 (d, J = 7.8 Hz, 1H), 7.85 (s, 1H), 7.78 (t, J = 8.1 Hz, 1H), 7.67 (d, J = 8.3 Hz, 0H), 7.63 – 7.57 (m, 1H). ¹³C NMR (126 MHz, DMSO– d_6) δ 159.34, 158.42, 153.17, 149.34, 148.76, 148.75 (d, J = 2.2 Hz), 136.12, 132.02, 128.60, 125.41, 125.21, 124.31, 123.68, 120.02 (q, J = 257.4 Hz), 118.20. **HR-MS** calcd for $C_{15}H_8F_3N_4O_3$ [M–H]⁻: 349.05540 found 349.05560.

N-(5-(3-(trifluoromethoxy)phenyl)-1,3,4-oxadiazol-2-yl)pyrazine-2-carboxamide (17)

$$F_3C$$

According to GP1, T_3P (1 mL, 3.38 mmol) was added to a solution of pyrazine-2-carboxylic acid (30 mg, 0.242 mmol) and amine **1a** (65 mg, 0.266

mmol) in EtOAc (1.6 mL) and pyridine (1.6 mL) to afford after preparative HPLC compound **17** (35 mg, 41%) as a white powder. ¹**H NMR** (500 MHz, DMSO– d_6) δ 12.49 (s, 1H), 9.32 (d, J = 1.4 Hz, 1H), 8.99 (d, J = 2.5 Hz, 1H), 8.86 (t, J = 2.0 Hz, 1H), 8.01 (d, J = 7.8 Hz, 1H), 7.86 (s, 1H), 7.78 (t, J = 8.0 Hz, 1H), 7.66 (d, J = 8.2 Hz, 1H). ¹³**C NMR** (126 MHz, DMSO– d_6) δ 162.28, 160.08, 157.70, 148.76 (q, J = 4.6 Hz), 148.60, 144.59, 143.70, 143.60, 132.05, 125.36, 125.27, 124.39, 120.02 (q, J = 256.9 Hz), 118.28. **HR-MS** calcd for C₁₄H₇F₃N₅O₃ [M–H]⁻: 350.05065 found 350.0509.

N-(5-(3-(trifluoromethoxy)phenyl)-1,3,4-oxadiazol-2-yl)thiophene-3-carboxamide (18)

According to GP1, T_3P (0.96mL, 3.28 mmol) was added to a solution of thiophene-2-caroboxylic acid (30 mg, 0.234 mmol) and amine $\bf{1a}$ (63 mg,

0.258 mmol) in EtOAc (1.5 mL) and pyridine (1.5 mL) to afford after preparative HPLC compound **18** (28 mg, 34%) as a white solid. ¹**H NMR** (500 MHz, DMSO– d_6) δ 12.15 (s, 1H), 8.56 (d, J = 3.4 Hz, 1H), 8.00 (d, J = 7.8 Hz, 1H), 7.84 (s, 1H), 7.77 (t, J = 8.0 Hz, 1H), 7.74 – 7.62 (m, 3H). ¹³**C NMR** (126 MHz, DMSO– d_6) δ 159.65, 158.26, 148.76, 135.35, 132.43, 132.00, 127.67, 127.31, 125.52, 125.17, 124.21, 120.02 (q, J = 257.4 Hz), 118.17. **HR-MS** calcd for C₁₄H₇F₃N₃O₃S [M–H]⁻: 356.03112 found 356.0221.

N-(5-(3-(trifluoromethoxy)phenyl)-1,3,4-oxadiazol-2-yl)furan-2-carboxamide (19)

F₃C O NH O NH O

According to GP1, T_3P (1.1 mL, 3.75 mmol) was added to a solution of furan-2-carboxylic acid (30 mg, 0.268 mmol) and amine **1a** (72 mg, 0.294

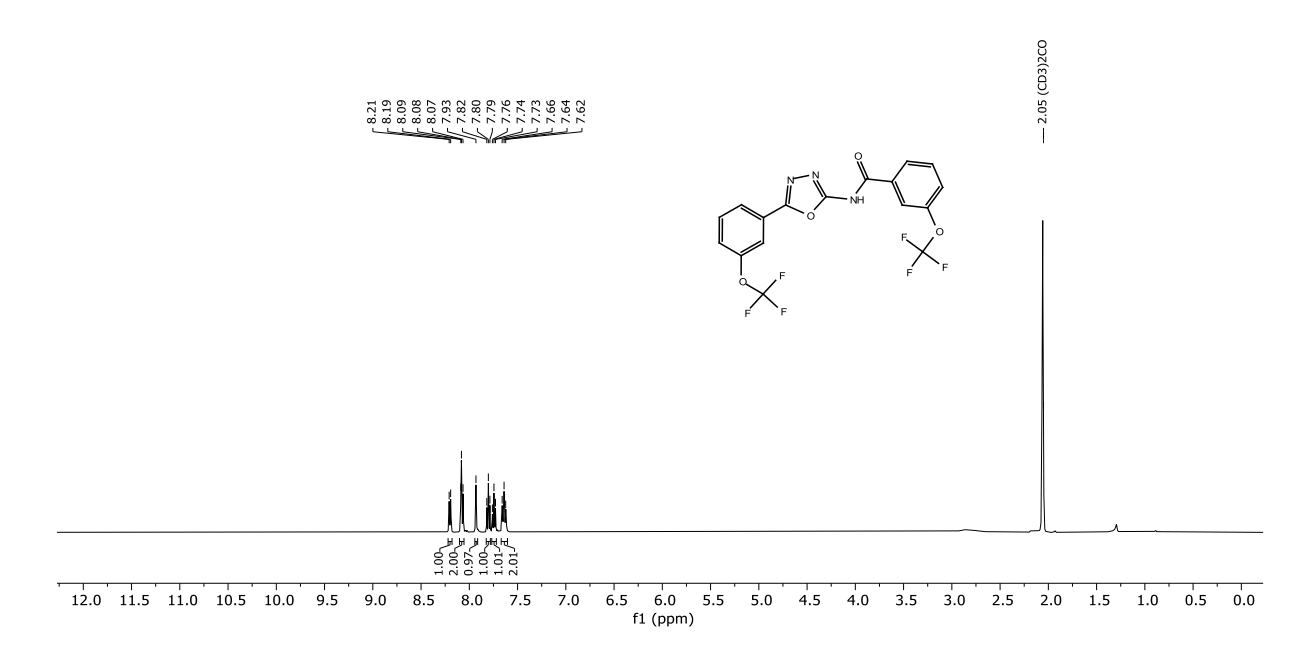
mmol) in EtOAc (1.8 mL) and pyridine (1.8 mL) to afford after preparative HPLC compound **19** (32 mg, 35%) as a white solid. ¹**H NMR** (500 MHz, DMSO– d_6) δ 12.28 (s, 1H), 8.04 (s, 1H), 7.99 (d, J = 7.7 Hz, 1H), 7.84 (s, 1H), 7.77 (t, J = 8.0 Hz, 1H), 7.66 (d, J = 8.4 Hz, 1H), 7.57 (s, 1H), 6.76 (s, 1H). ¹³C NMR (126 MHz, DMSO– d_6) δ 159.38, 158.04, 155.27, 148.75 (d, J = 2.0 Hz), 147.55, 145.87, 131.99, 125.47, 125.16, 124.21, 120.02 (d, J = 257.4 Hz), 118.16, 117.29, 112.49.**HR-MS** calcd for C₁₄H₇F₃N₃O₄ [M-H]⁻ 338.03941 found 338.03980.

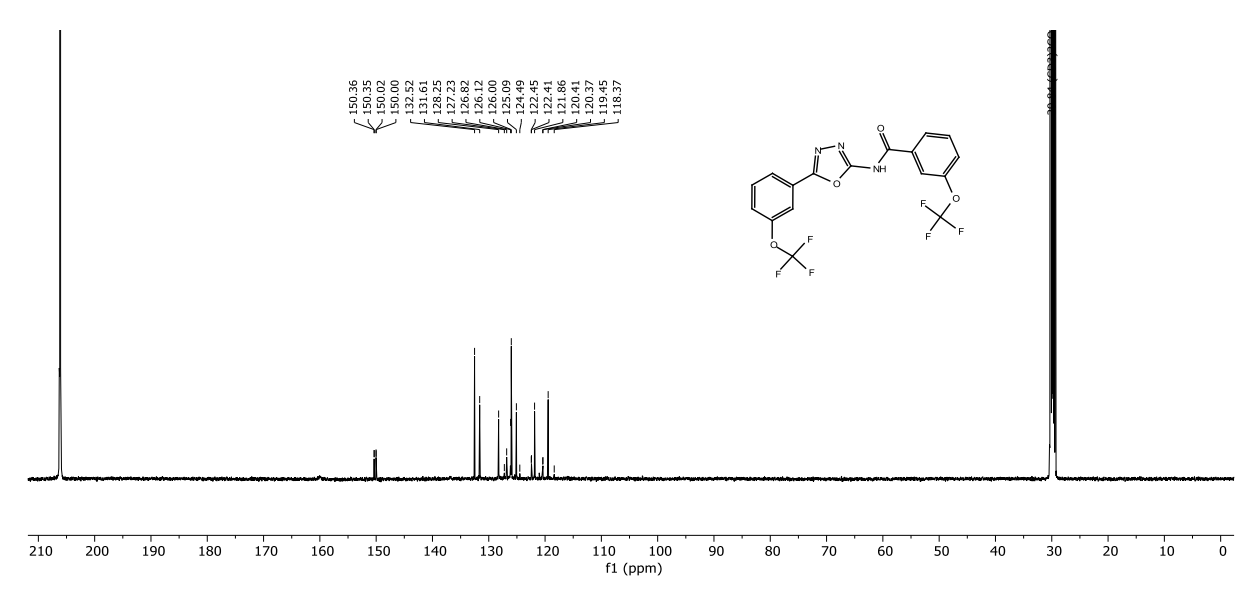
Biological evaluation

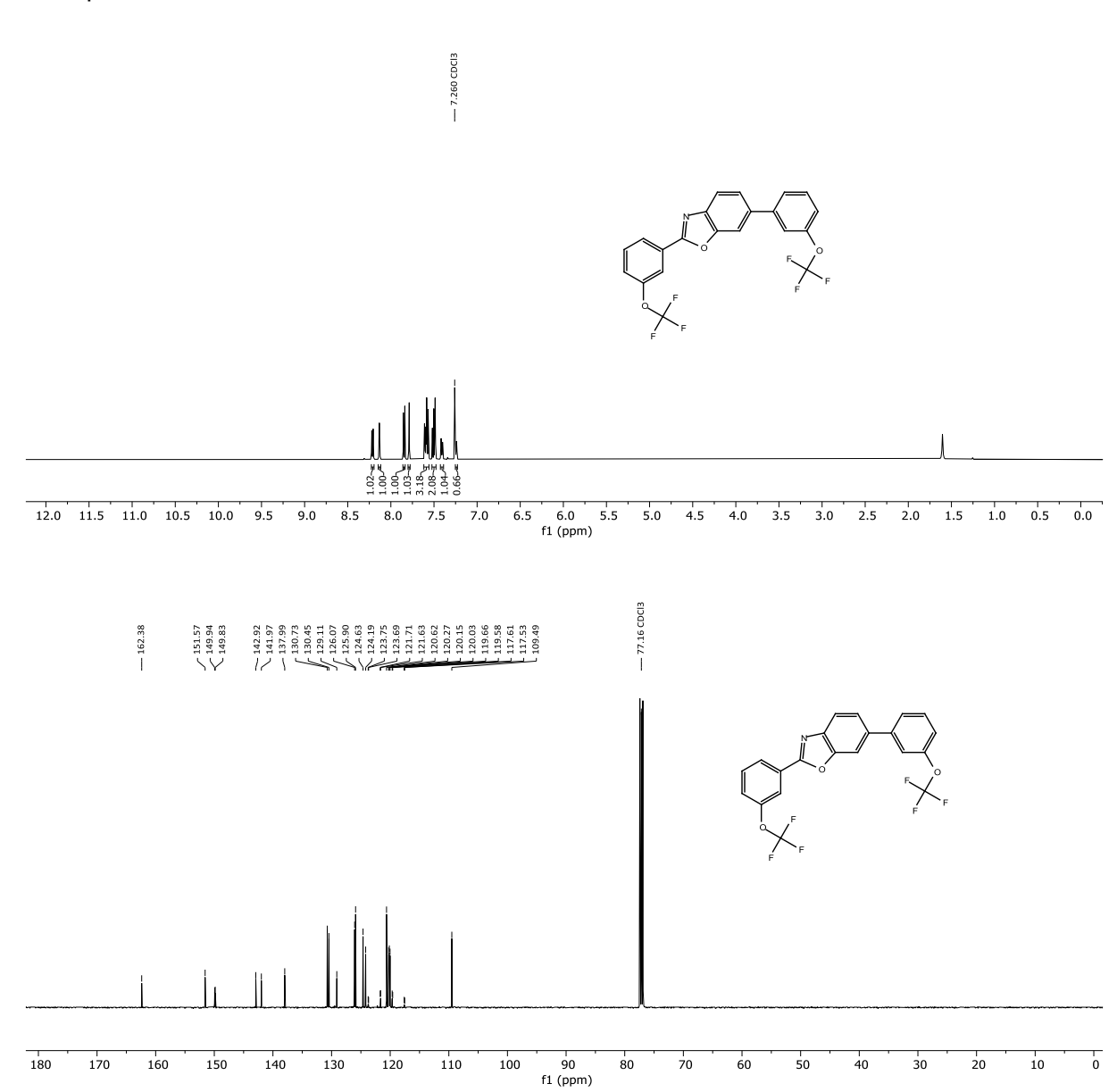
MIC determination in Mycobacterium tuberculosis

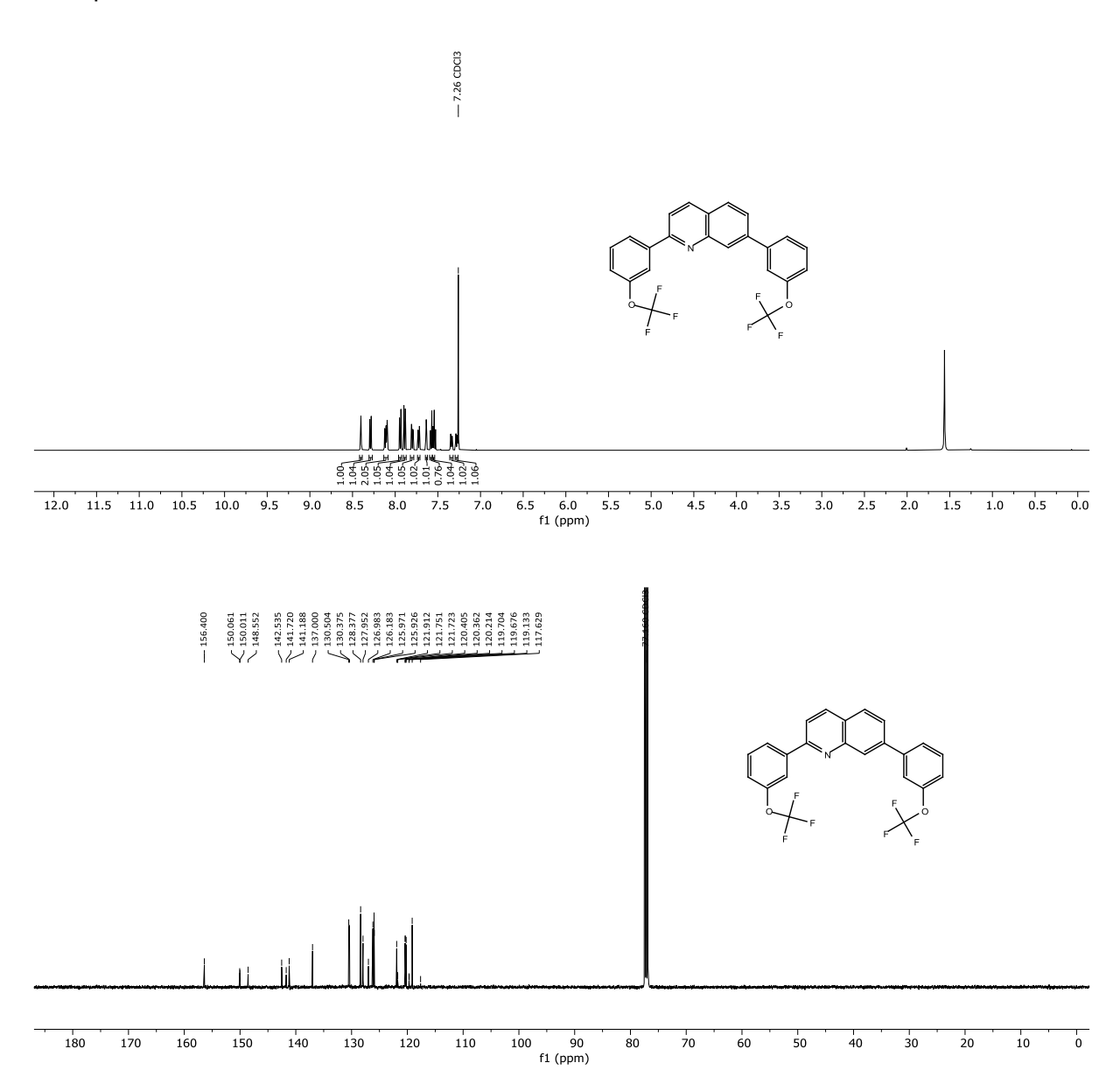
Mycobacterium tuberculosis strain H37Rv (ATCC 27294) was used for all compound efficacy testing. Cultures were routinely grown in, and MIC assays performed in, 7H9 medium supplemented with 0.4 % (w/v) glucose, 0.085 % (w/v) NaCl, 0.05 % (w/v) tyloxapol, and either 0.5 % (w/v) BSA ("ADNTy" media) or 0.3 % (w/v) casein hydrolysate ("CasDNTy" media). Compound efficacy was tested using a broth microdilution protocol, as previously described (PMID: 34235672) but with a few modifications. Briefly, clear, U-bottomed 96-well plates were prepared with each test compound present in an 11 point, 2-fold dilution series. Bacteria were diluted from an exponentially growing culture in the relevant medium to a final OD₆₀₀ of 0.001 in each well (~5000-10,000 cells per well), with each well containing a final volume of 100 µl. Final DMSO concentrations never exceeded 1 % (v/v). Plates were left to incubate at 37 °C, in ziplock bags within humidified sealed boxes for 7 days, prior to visual examination of bacterial growth using an inverted mirror device. MIC values were recorded as the lowest concentration of test compound that was able to inhibit bacterial growth >95 % relative to untreated controls. Each test compound was assayed in at least 2 independent experiments, with listed values being the average of all measurements.

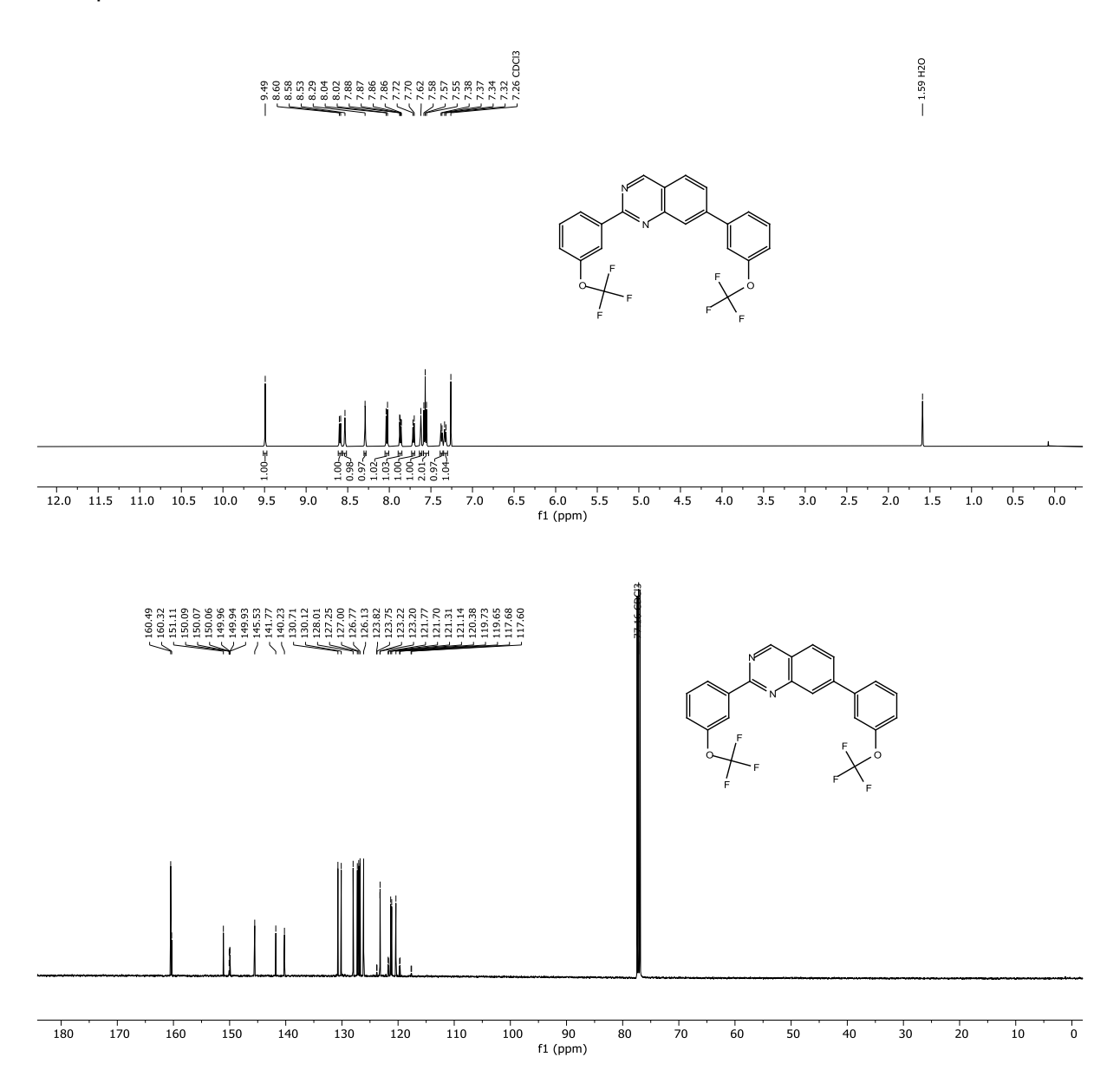
¹H- and ¹³C-NMR Spectra of the Synthesized Compounds

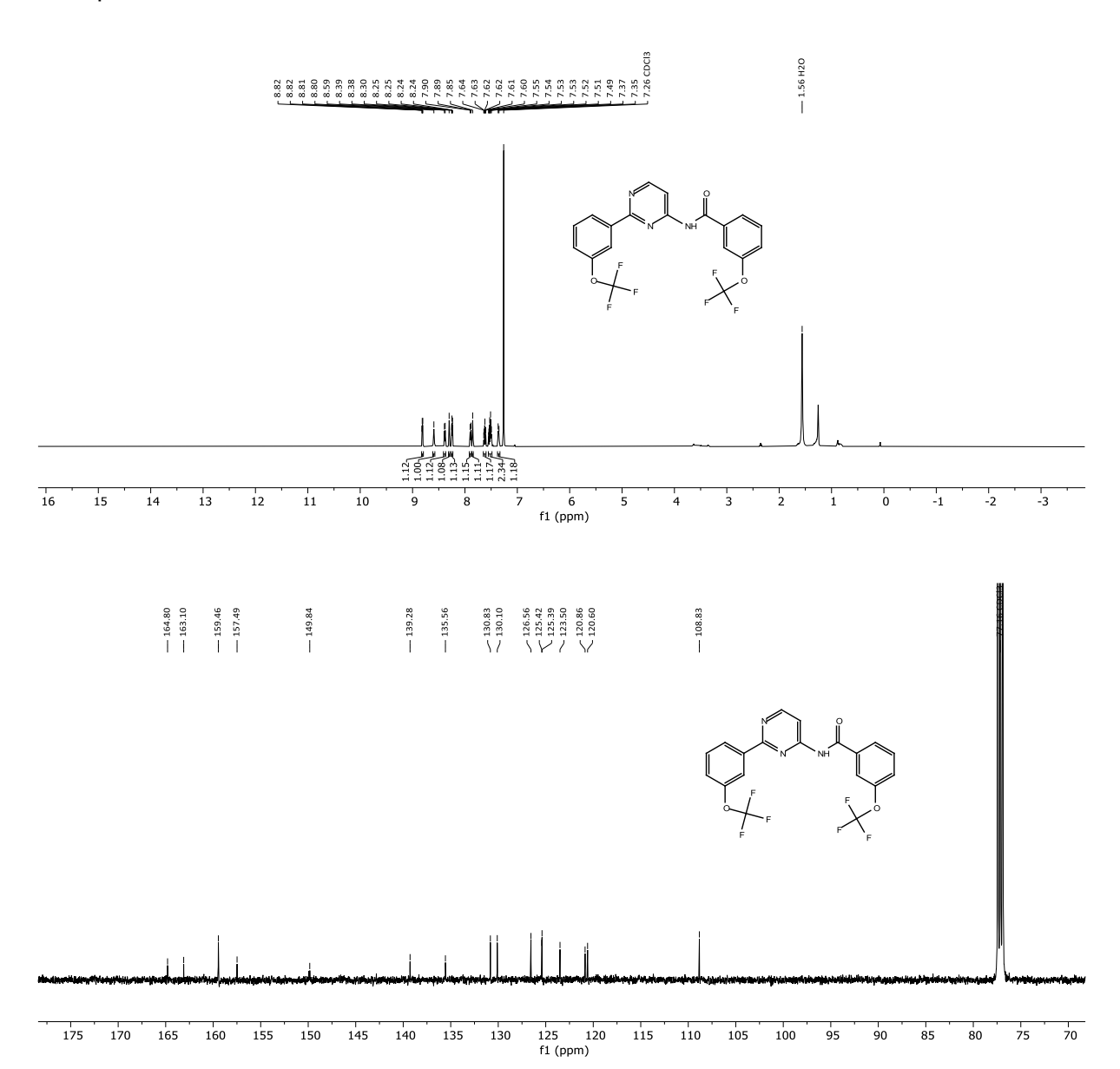


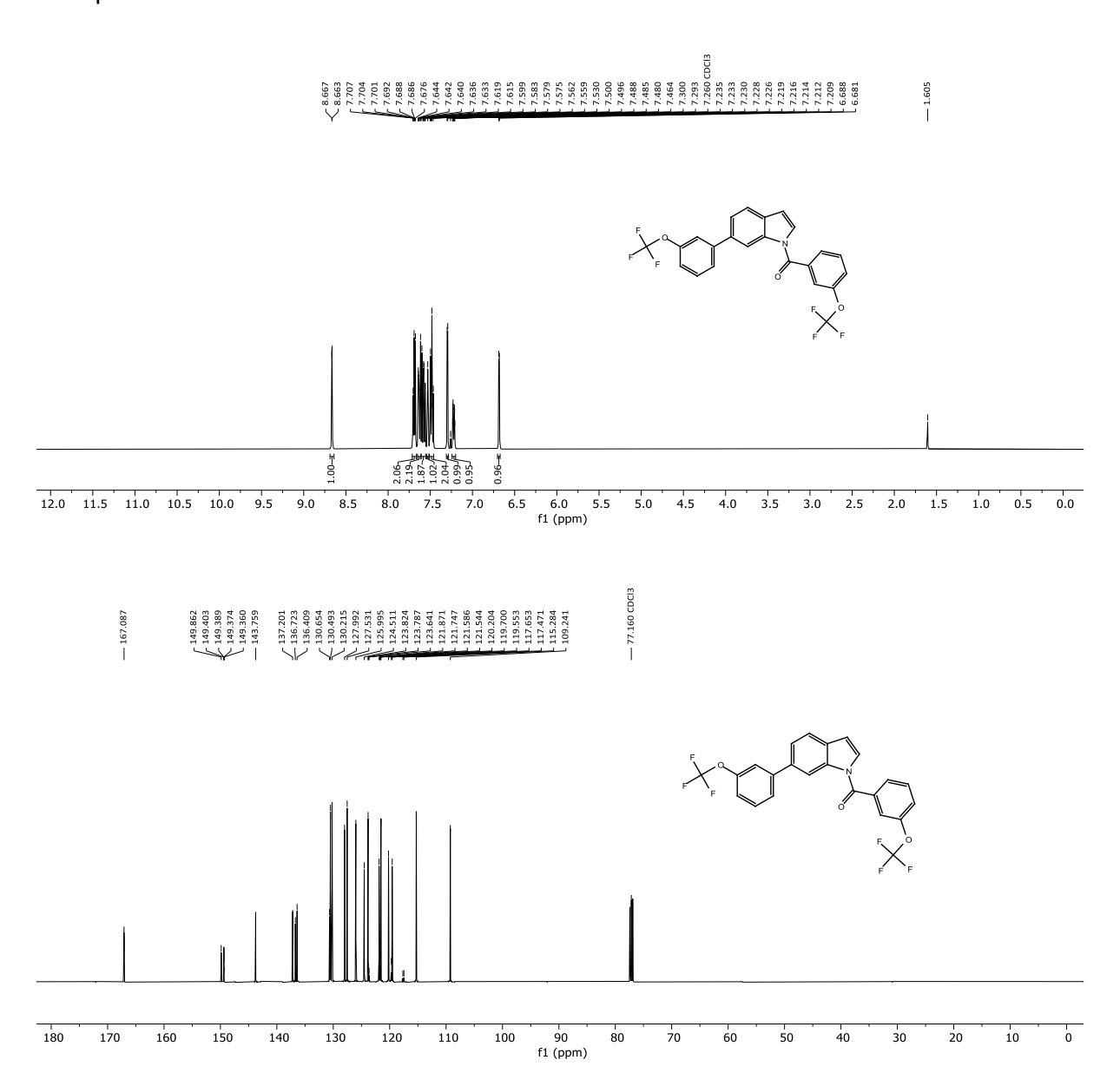


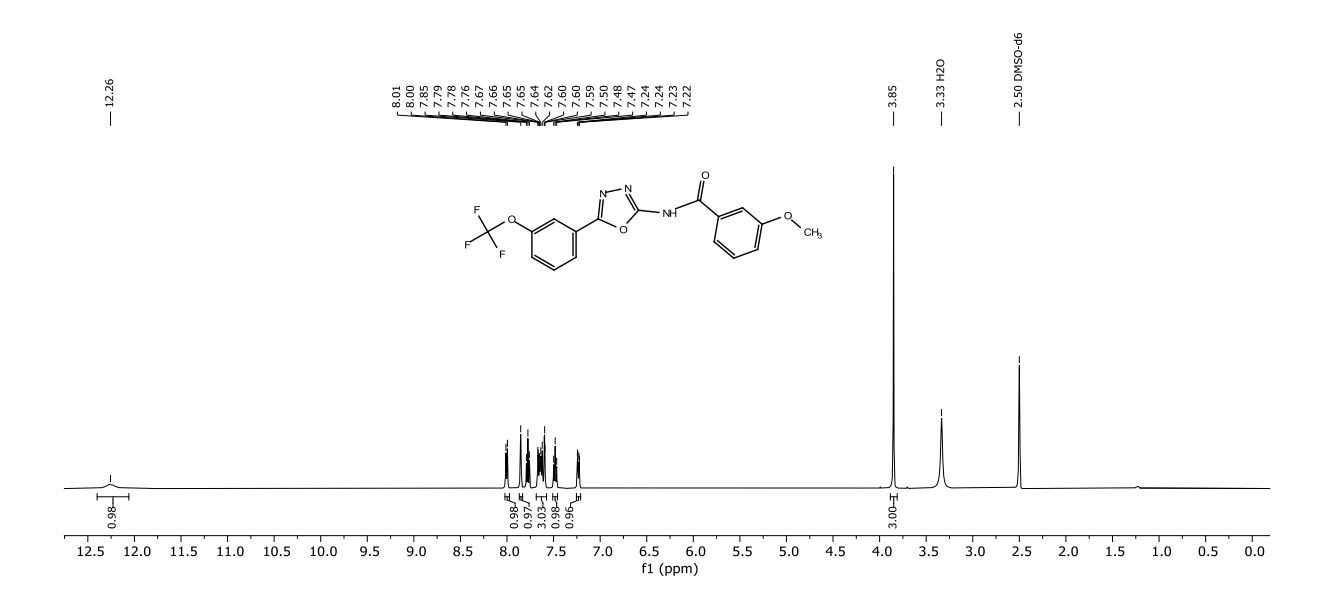


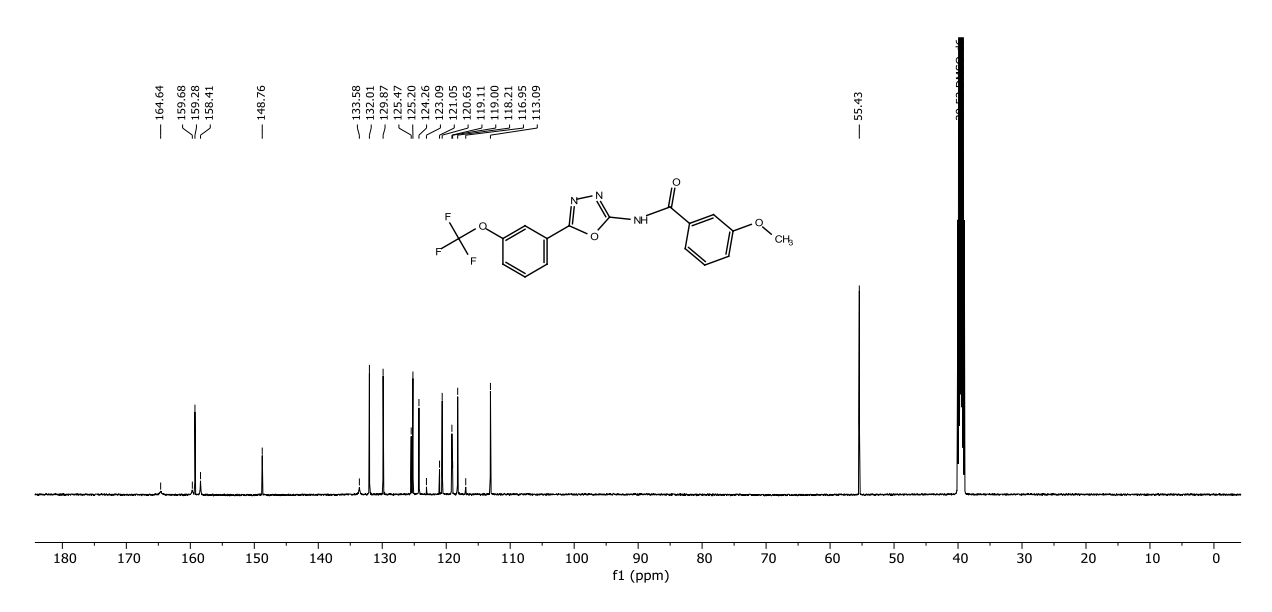


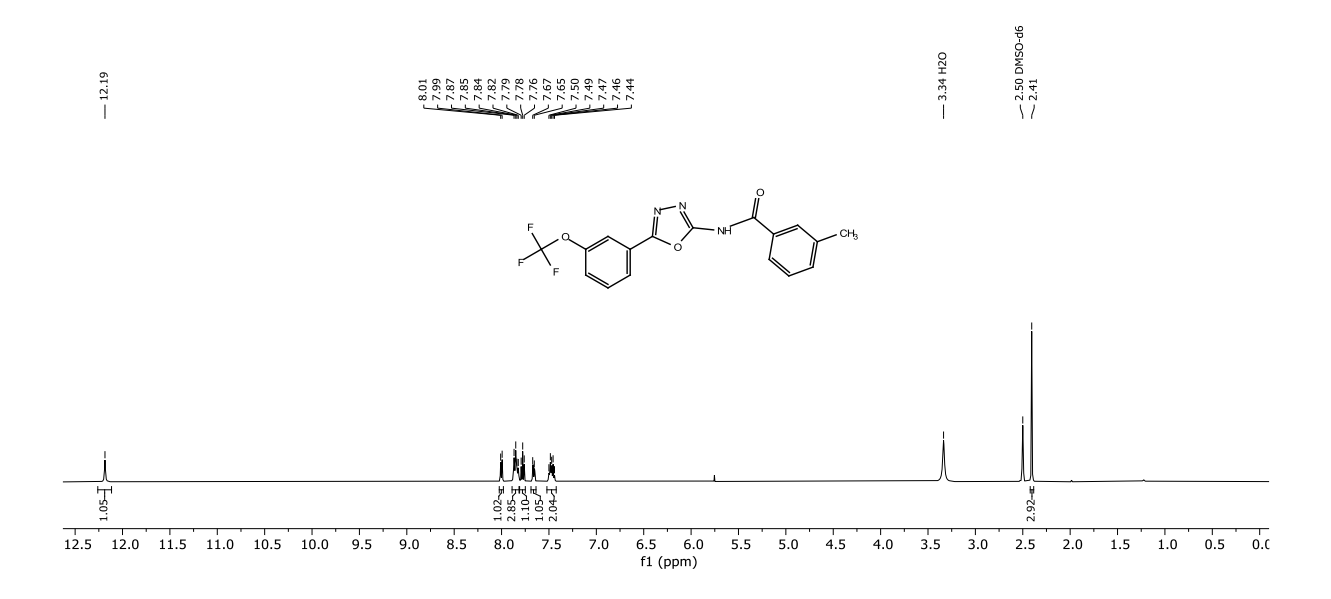


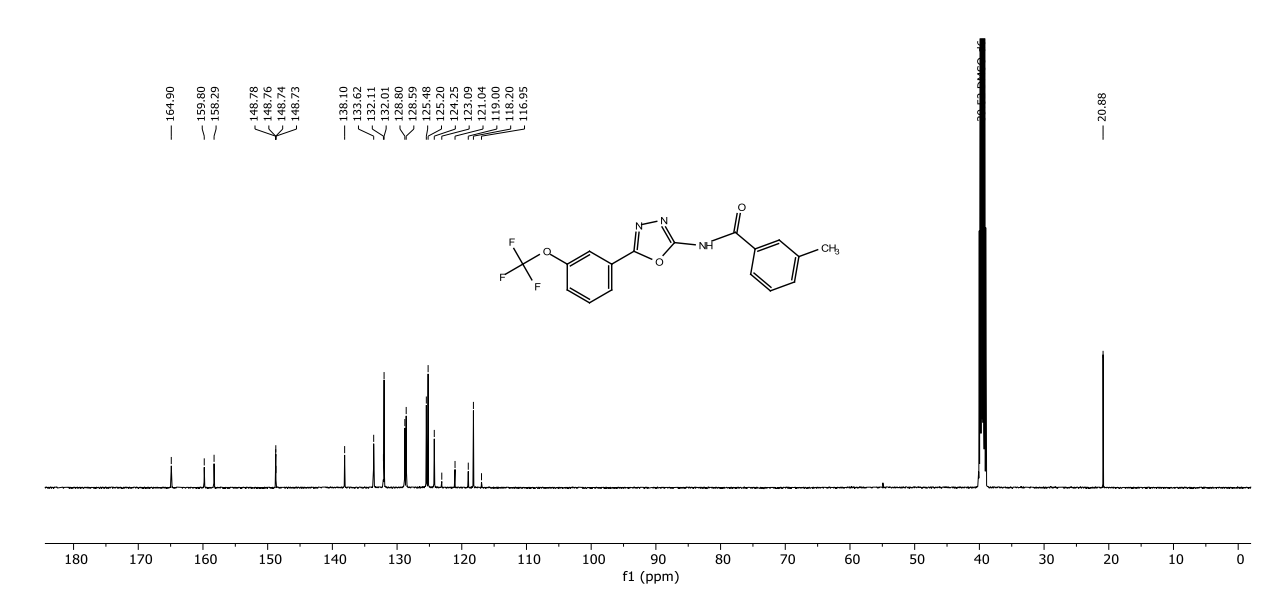


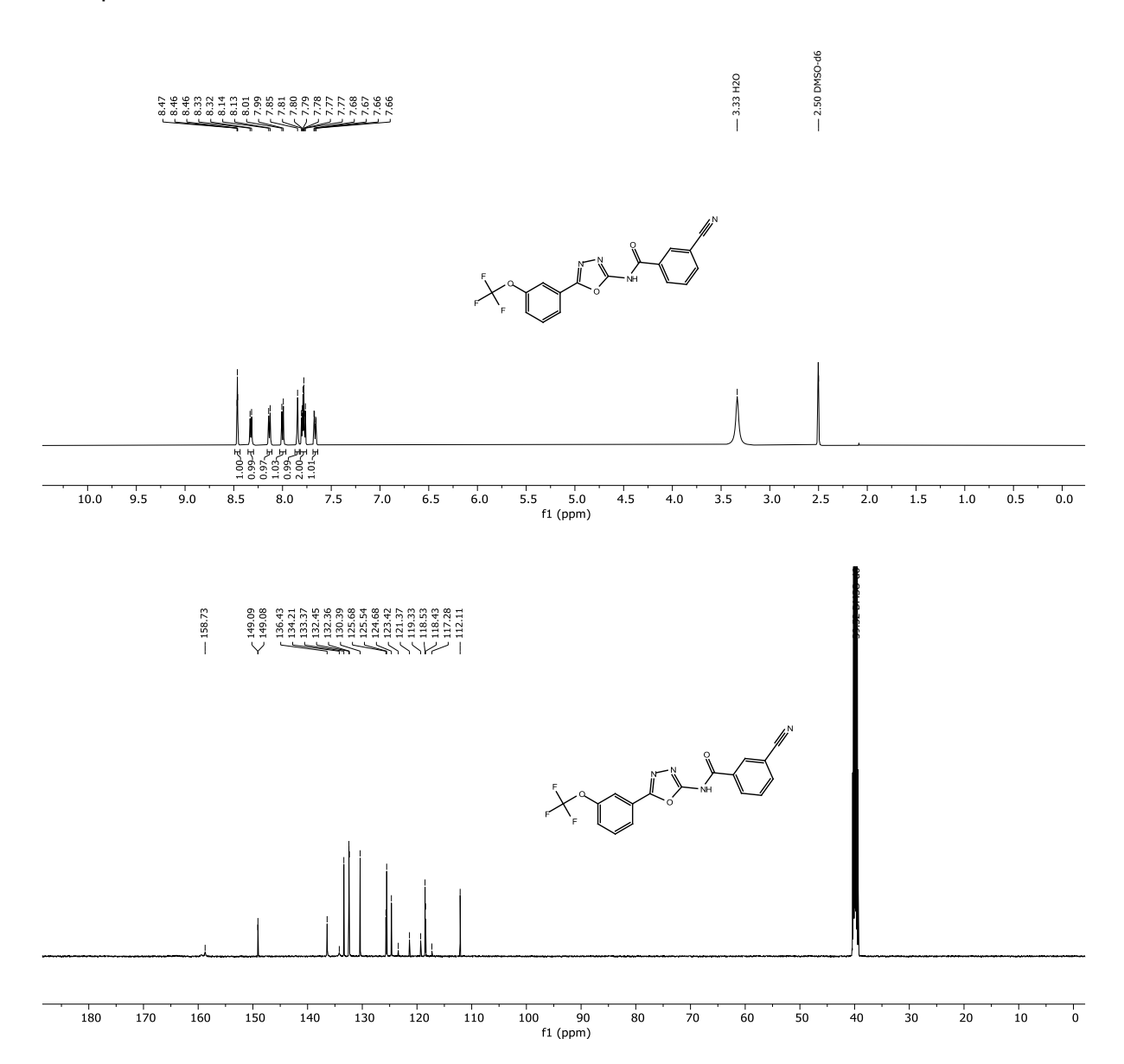


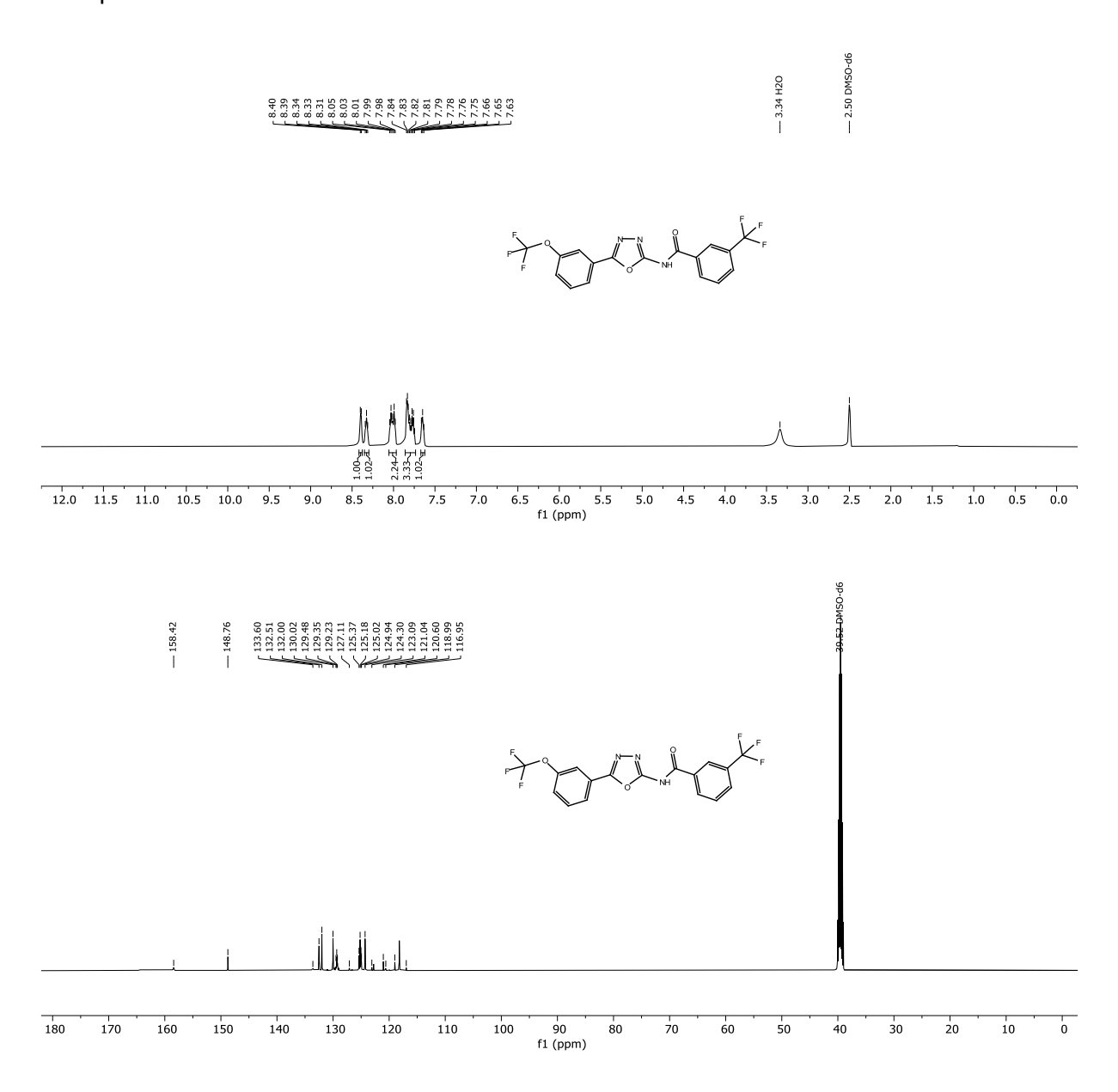


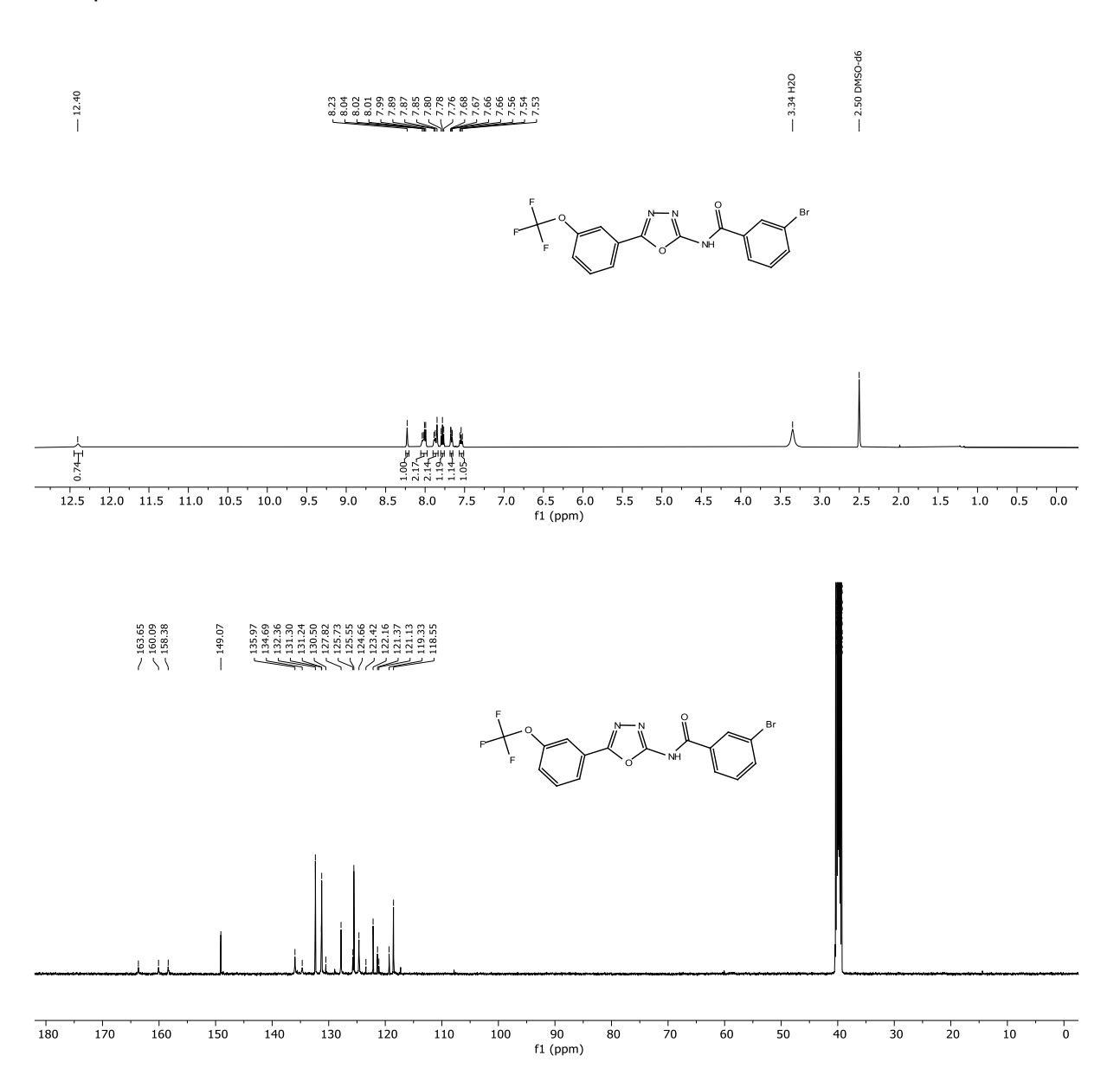


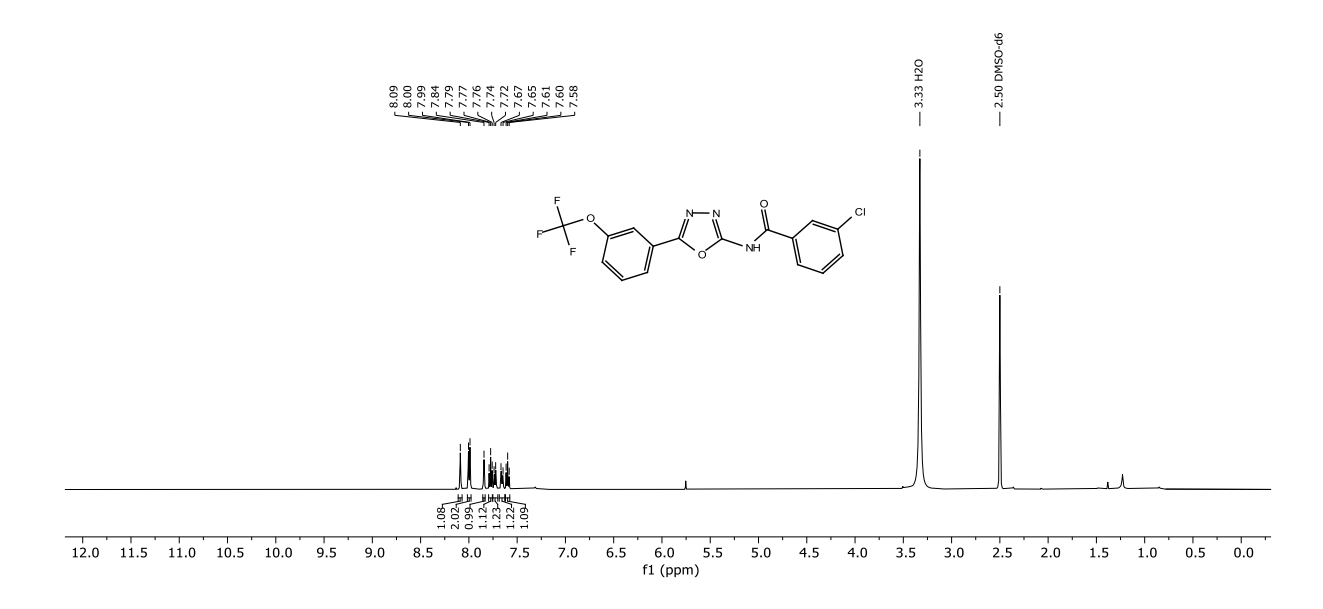


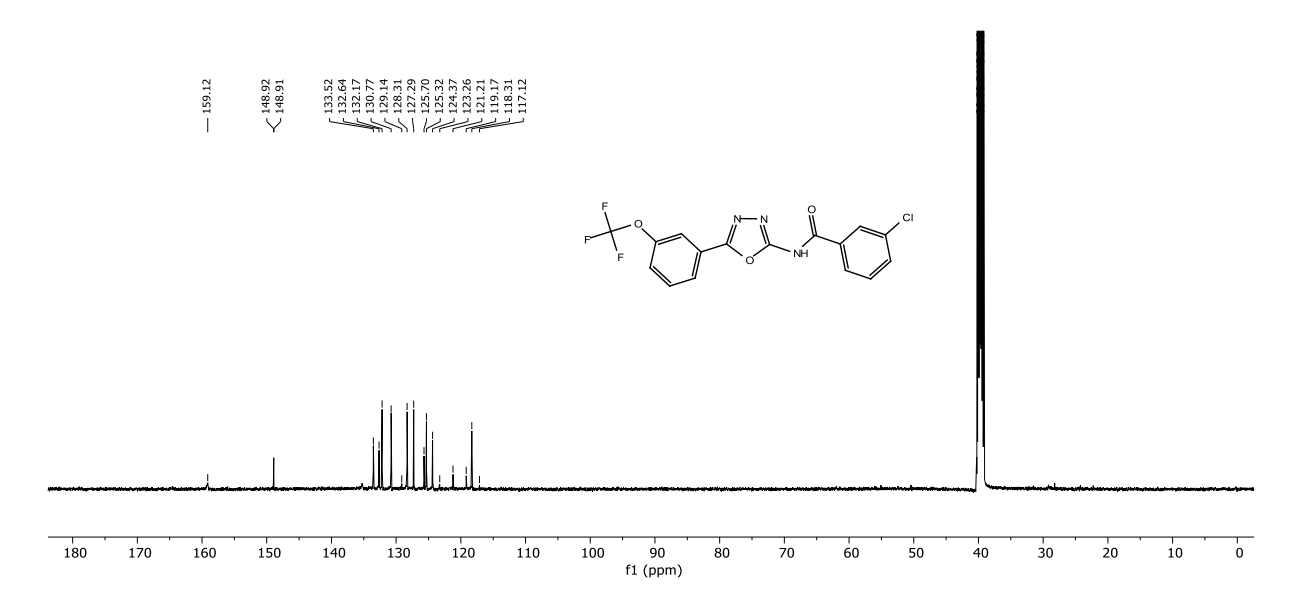


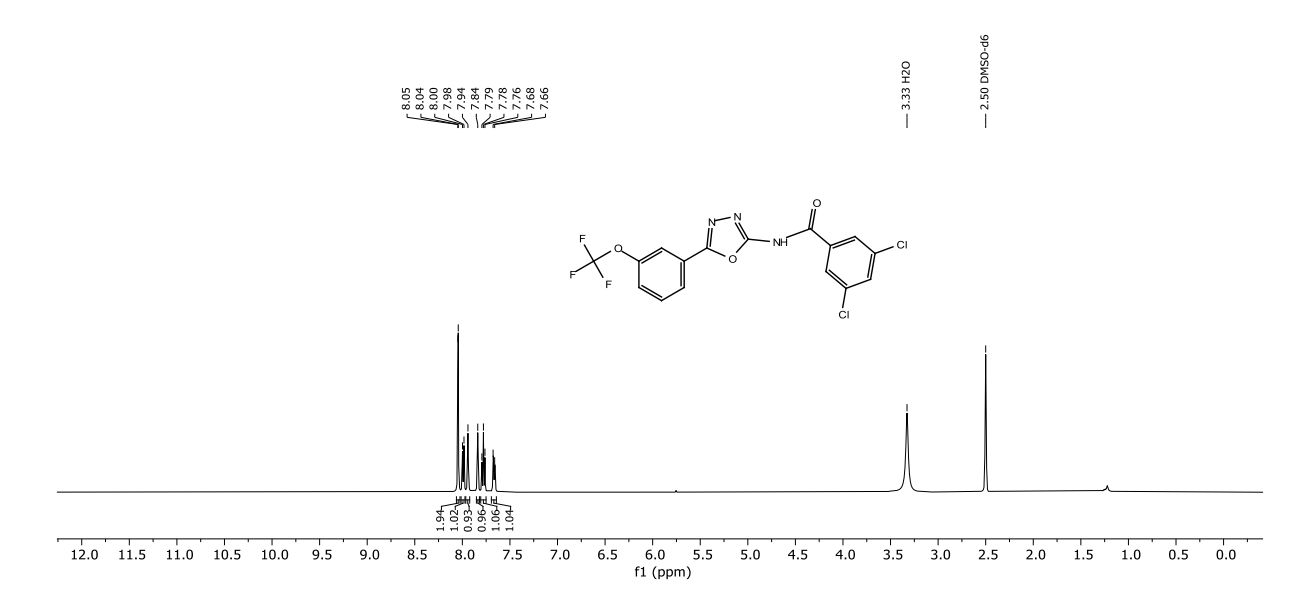


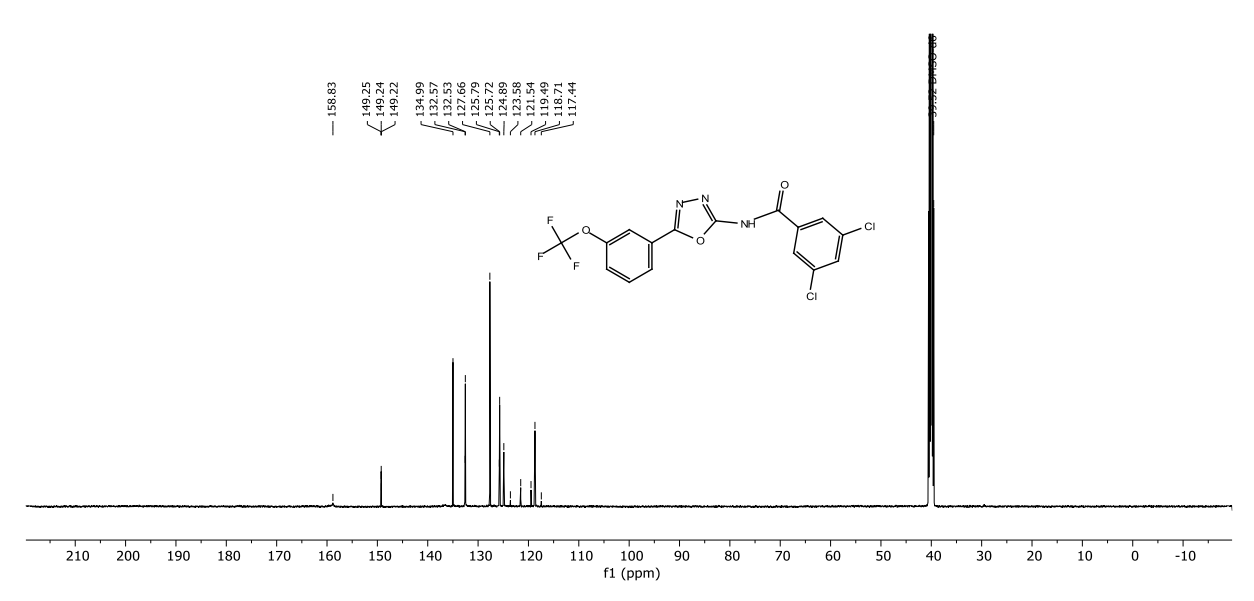


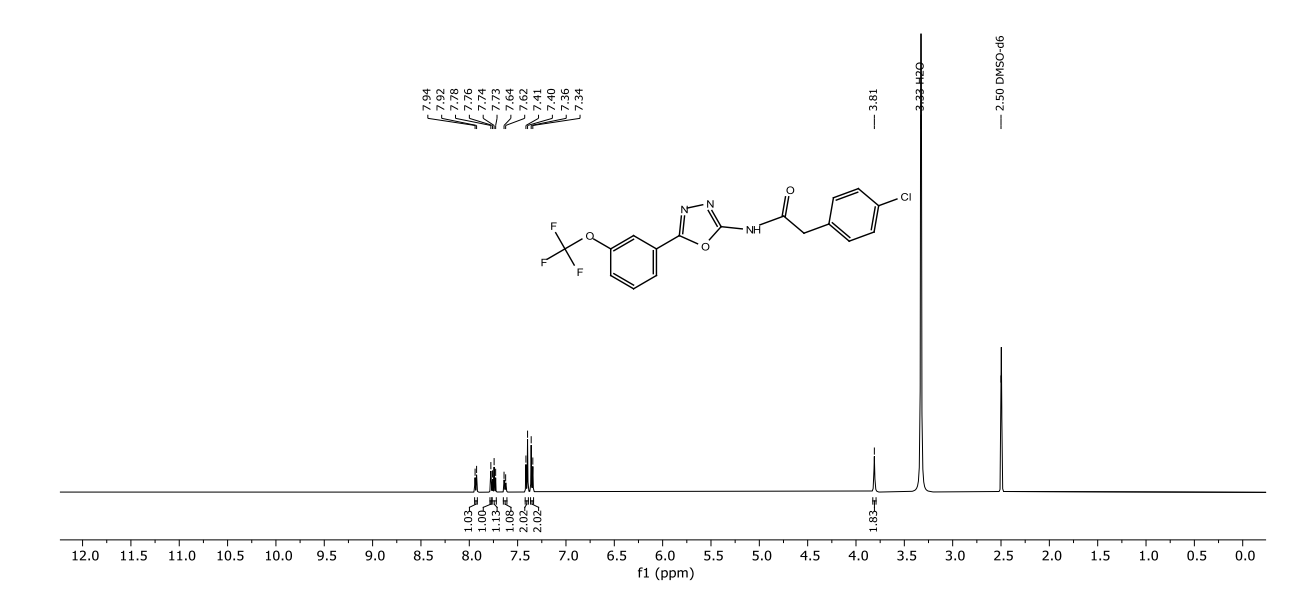


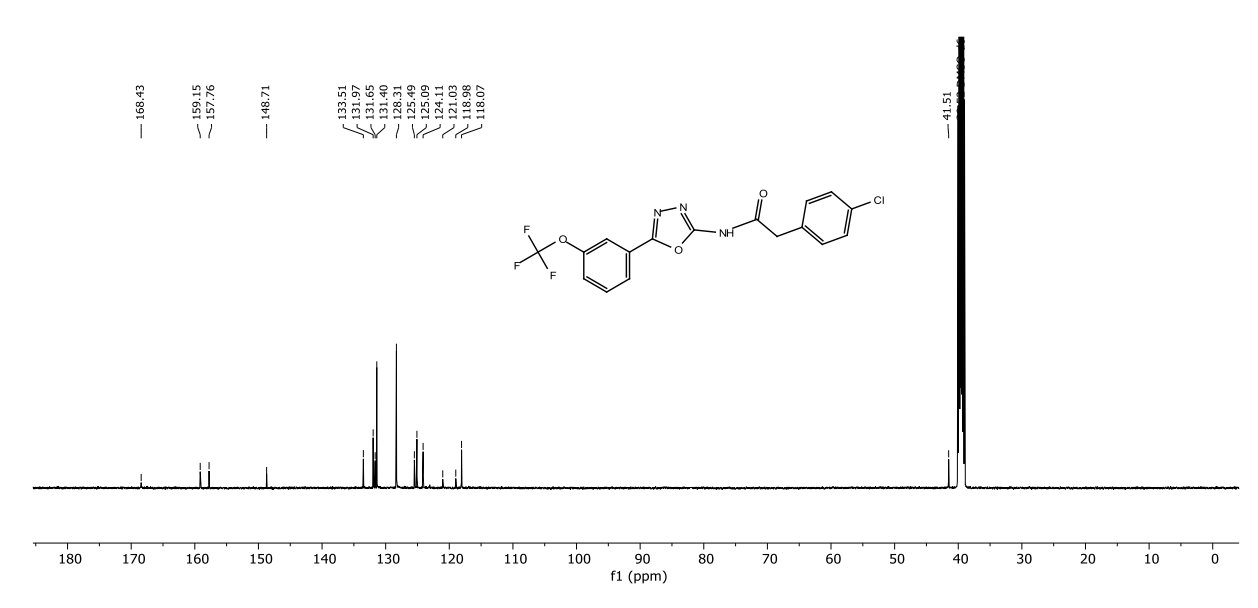


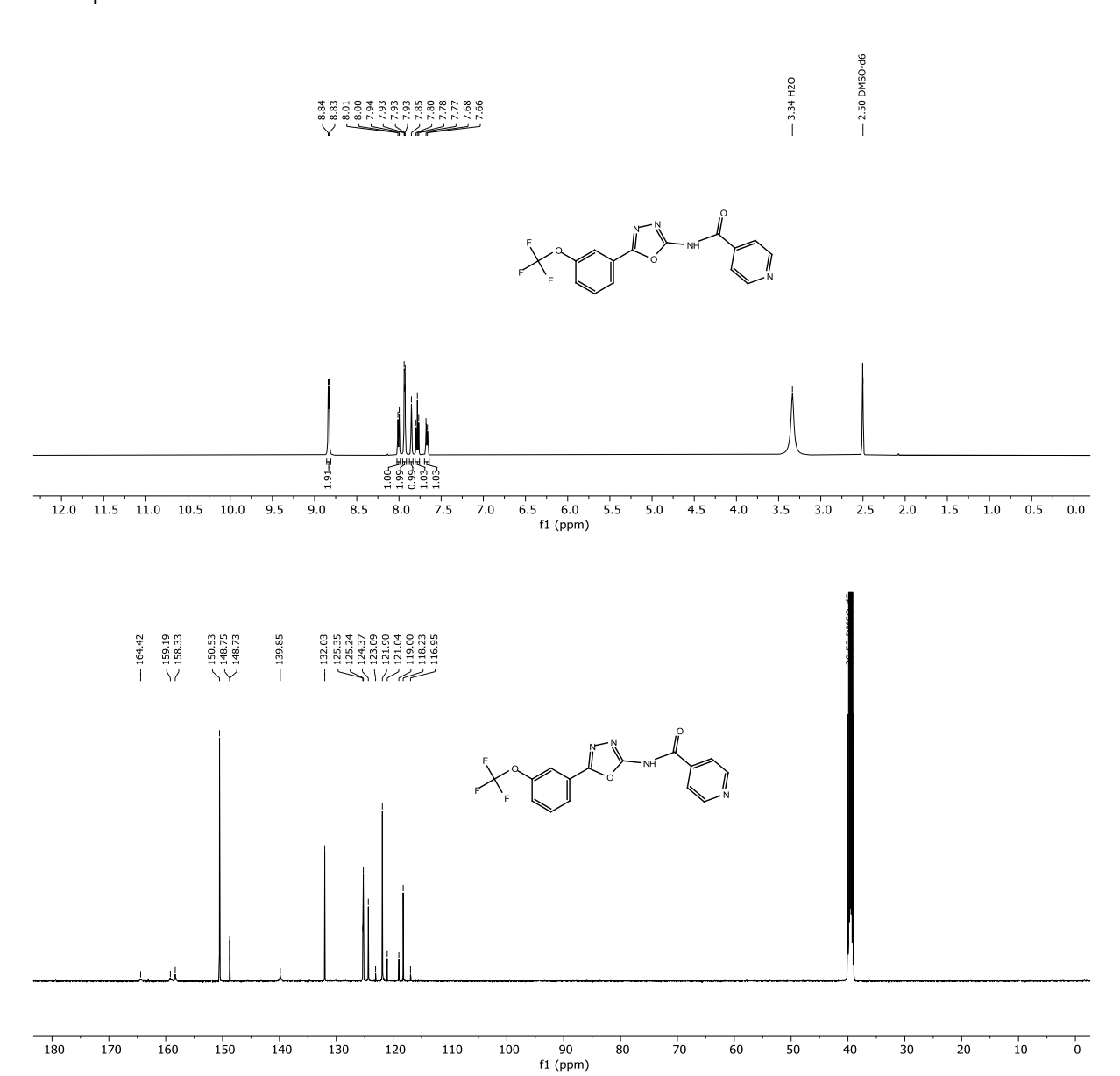


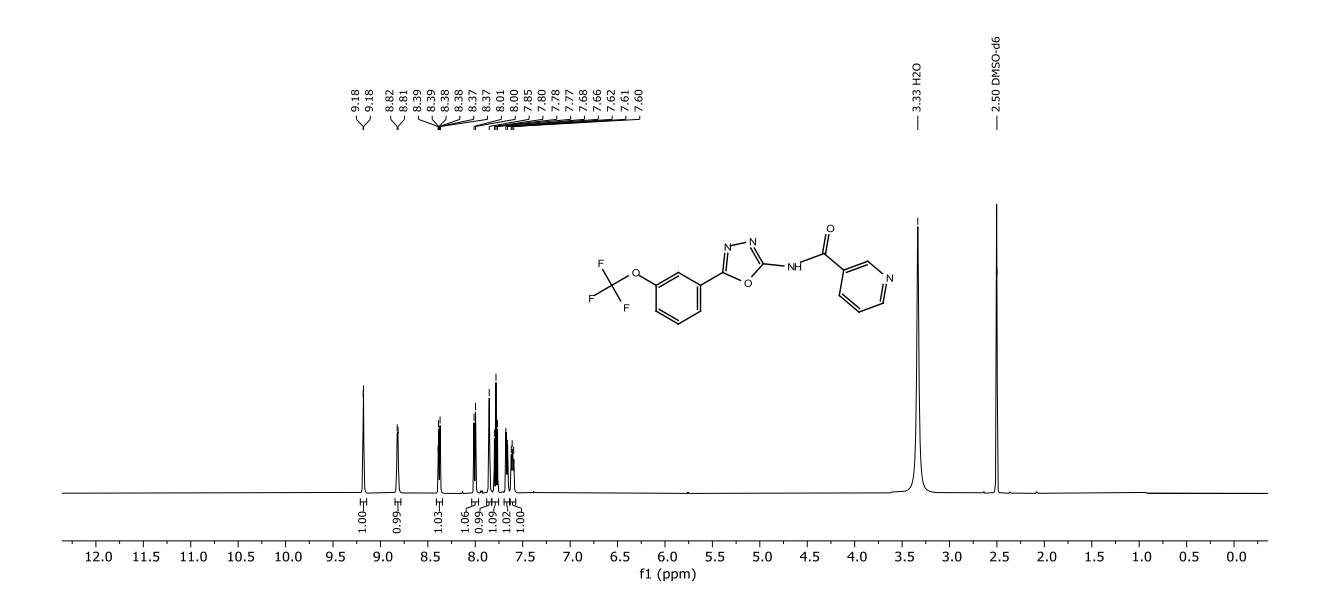


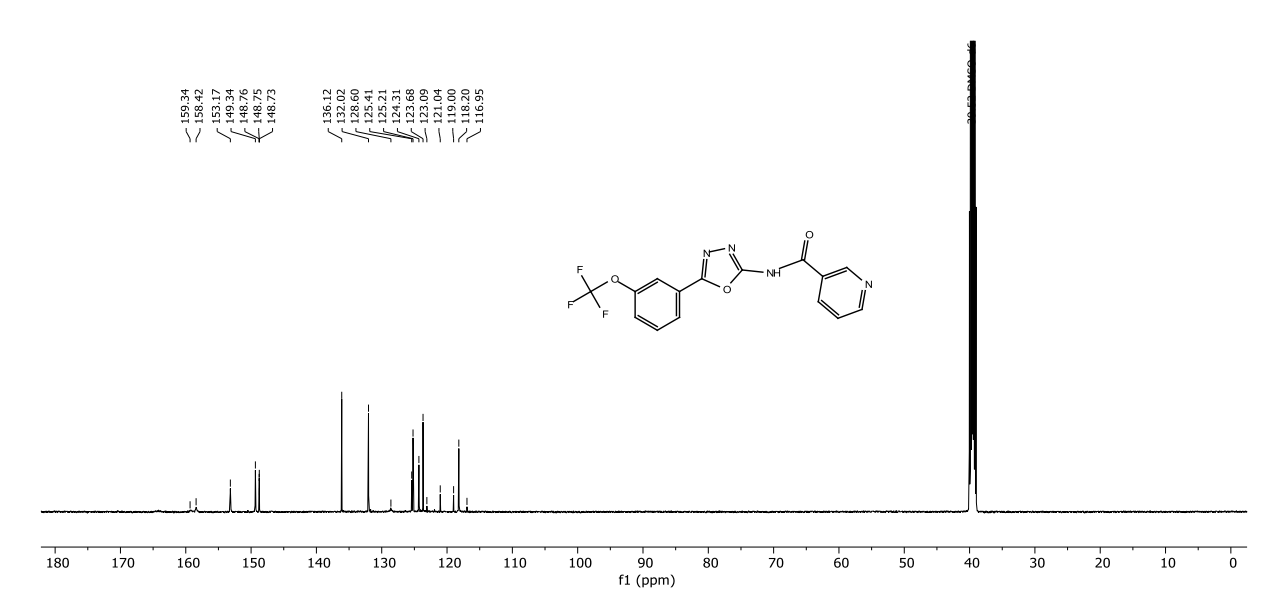


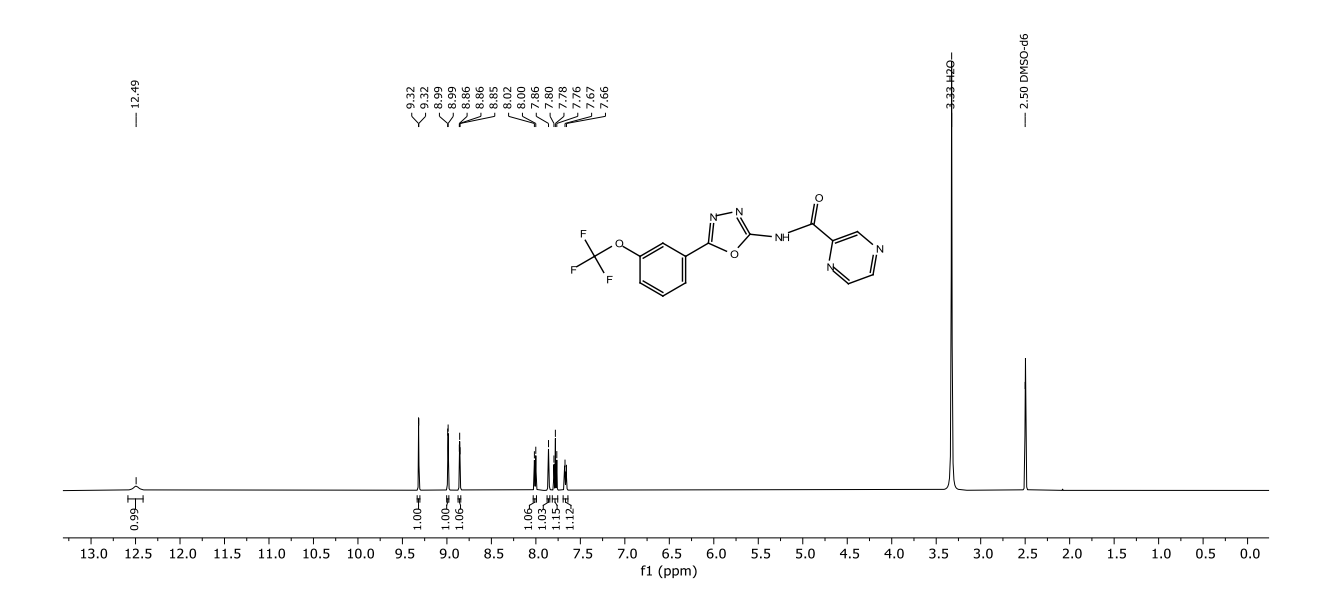


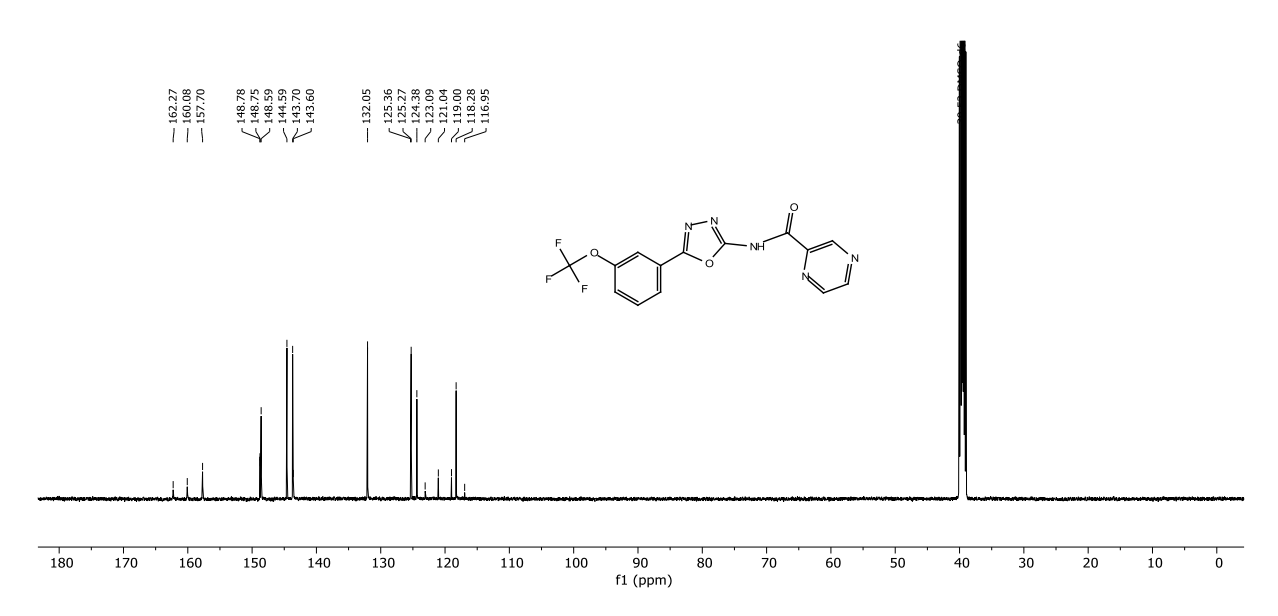


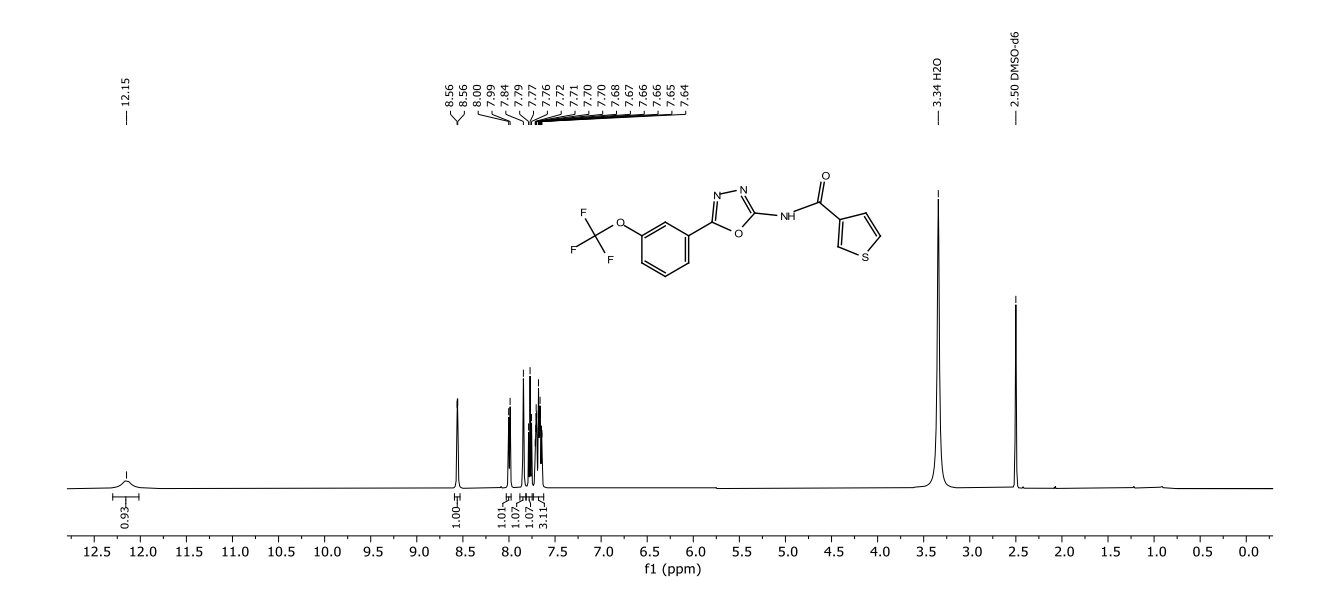


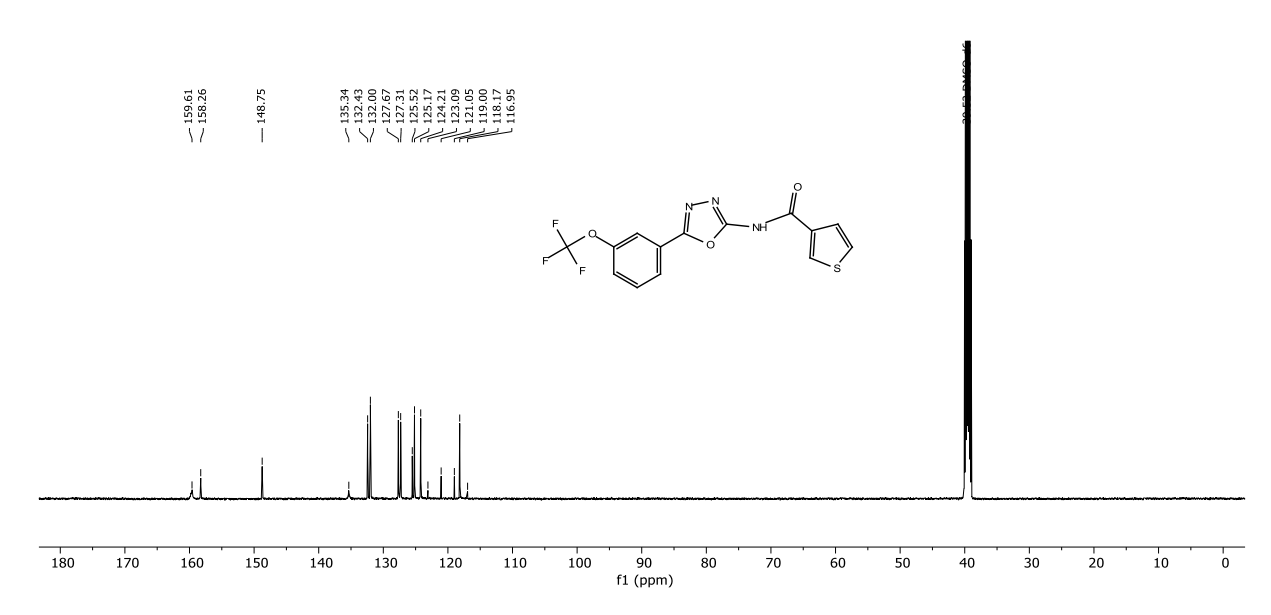


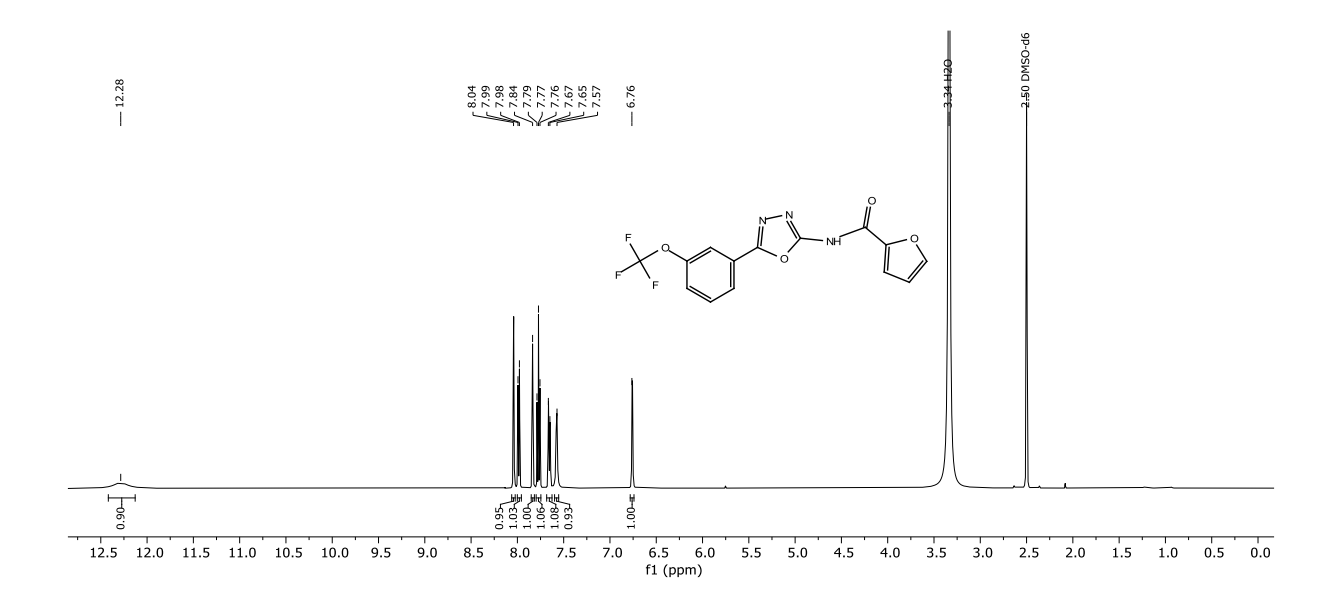


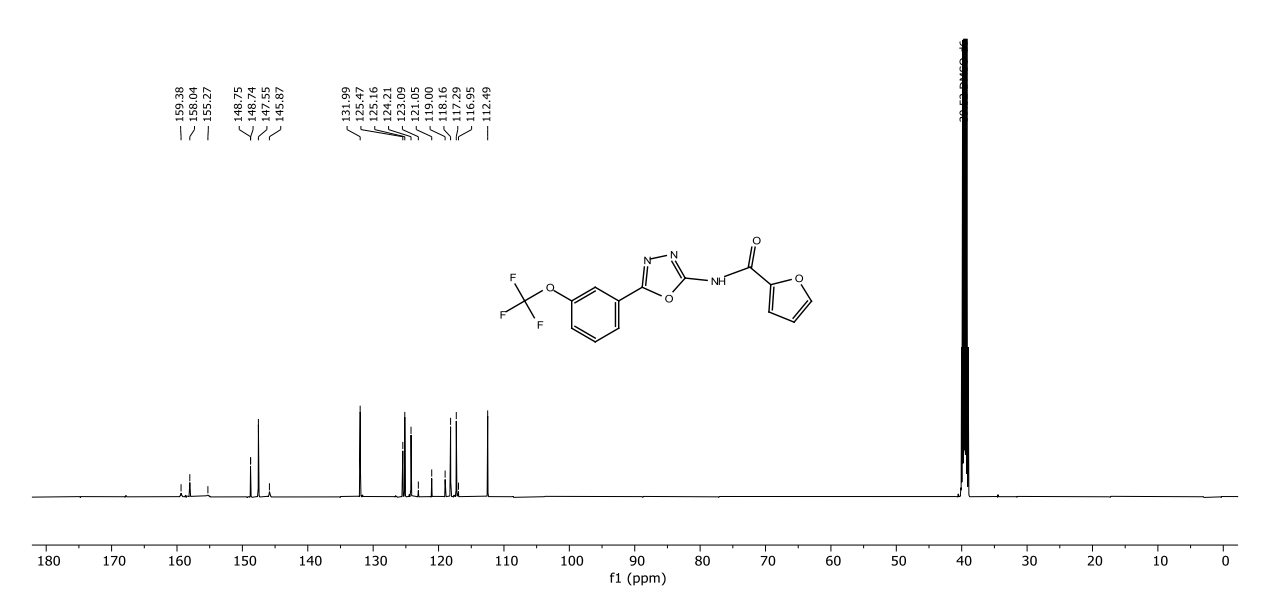












2.3 Chapter C

Direct Monitoring of Intracellular Polymer Degradation via BODIPY Dynamic Dequenching

Justine Bassil^{a,b}, Mohamed A. M. Kamal^{a,b}, Aljoscha Gabelmann^{a,b}, Anastasia Christoulaki^c, Marcus Koch^d, Mostafa Hamed^a, Brigitta Loretz^a, Markus Gallei^{e,f}, Eric Buhler^c, Claus-Michael Lehr^{a,b}, Anna K. H. Hirsch*^{a,b}, and Sangeun Lee*^{a,b}

^aHelmholtz Institute of Pharmaceutical Research Saarland (HIPS) – Helmholtz Centre for Infection Research (HZI), Campus E 8.1, 66123 Saarbrücken, Germany

^bDepartment of Pharmacy, PharmaScienceHub, Saarland University, Campus C4. 1, 66123 Saarbrücken, Germany

^cLaboratoire Matière et Systèmes Complexes (MSC), UMR 7057, Université Paris Cité, Physics Department, Bâtiment Condorcet, 75013 Paris, France

^dINM-Leibniz Institute for New Materials, Campus D2 2, 66123 Saarbrücken, Germany

^ePolymer Chemistry, Campus C4 2, 66123 Saarbrücken, Germany

^fSaarene, Saarland Center for Energy Materials and Sustainability, Campus C4 2, 66123 Saarbrücken, Germany

This manuscript is submitted and currently under review at Materials & Design

Contribution to the presented work

Author's Contribution:

The author contributed to the conception of this project. She was responsible for designing and conducting the experiments, collecting, analyzing, and interpreting the resulting data. She synthesized the monomer and polymer and carried out biological evaluations such as pH-responsive degradation and fluorescent experiments. Additionally, she conceived the project and wrote the manuscript.

Contribution by others:

Mohamed A. M. Kamal performed the cellular uptake and cytotoxicity assay and the degradation rate of the polymer. Aljoscha Gabelmann carried out the *in vitro* polymer degradation assay. Marcus Koch conducted the cryo-TEM measurements. Anastasia Christoulaki and Eric Buhler performed and interpreted the SAXS and SANS measurement for polymer characterization. Markus Gallei performed the SEC measurement. Mostafa Hamed and Brigitta Loretz were involved in the conception, coordination and supervision of the project. Claus-Michael Lehr, Anna K. H. Hirsch, and Sangeun Lee were responsible for the overall conception, conceiving, design and supervision of the project.

All authors contributed to writing, editing and approving of the submitted manuscript.

Abstract

Biodegradable polymers play a crucial role in biomedical applications, particularly as nanocarriers in drug delivery. While labeling the polymers with fluorescent dyes facilitates monitoring their biodistribution and post cellular uptake, tracking polymer degradation within biological systems remains a challenge. This raises important unanswered questions regarding the fate of the polymers, their degradation products, and the degree of their degradation within biological systems. In this study, we developed a novel dynamic biodynamer (BDP-Lys) composed of BODIPY and lysine-hydrazide monomers linked by reversible dynamic covalent bonds, designed to control the fluorescence of BODIPY by degradation. The BDP-Lys undergoes pHresponsive degradation, leading to recovery of quenched BODIPY and enhanced fluorescence emissions, thereby enabling direct monitoring of intracellular polymer degradation. Physicochemical characterization revealed its molecular weight, filament-like morphology, and a notable 12-fold increase in fluorescence intensity at acid-induced degradation. In vitro studies demonstrated excellent biocompatibility, efficient cellular uptake and a threefold increase in fluorescence due to polymer degradation in mammalian cells, resulting in a maximum of 17.07% monomer release in the first 24 h. Thus, BDP-Lys emerges as a promising tool for exploring polymer behavior in biological systems, providing real-time insights into degradation and offering new opportunities to address unresolved questions in the field.

Keywords: biodegradable polymer; biodynamers; fluorescent labeling; BODIPY

Introduction

Biodegradable and biocompatible polymers have attracted significant attention, emerging as a prominent area of research in drug delivery and biomedical applications, due to their adaptable functional properties in biological environments. Such polymers often serve as nanocarriers capable of encapsulating, protecting, delivering, and releasing various therapeutic agents in a controlled and targeted manner [1–4]. Labeling of these nanocarriers using imaging agents like fluorescent dyes enables the monitoring of their biodistribution and cellular uptake within the tissues, making them available in biological studies and diagnostics [5,6].

Most current fluorescent labeling techniques are achieved through chemical dye conjugation to polymeric carriers or direct encapsulation of dyes in nanocarriers during particle formation [7–10]. However, it is important to note the limitations of both labeling approaches. For instance, while encapsulation of fluorescent dyes allows monitoring of dye release, it also poses risks of uncontrollable leakage and quenching, potentially affecting biodistribution and altering the interpretation of polymer breakdown [11]. More importantly, the release of encapsulated dye is often associated with dissociation or disassembly of the polymeric nanocarriers as a consequence of polymer degradation. Thus, the real-time tracking of the degradation process with this approach is highly challenging or most likely impossible, as it is difficult to distinguish between polymer breakdown and nanocarrier disassembly [9,12,13], and few study [14] effectively monitor and track polymer breakdown in situ within biological systems.

Covalent dye conjugation offers theoretically the most stable labeling, provided that the dye remains attached during polymer degradation. Nonetheless, fluorescence imaging or measurements primarily tracks the fluorescence signal of the dye, making it difficult to distinguish whether the signal originates from the nanoparticle, the polymer itself, or the released dye, which complicates the interpretation of such data [15]. Typically, it is recommended to keep fluorescent labels within a weight percentage of 0.1-5% of the polymer in order to minimize structural changes and effects of polymer degradation. Another argument is to avoid changes in Corona formation and nano-bio interactions of such drug carriers [16,17]. Regardless of molecular weight of dye covalent labeling there are still challenges in accurately assessing polymer breakdown and accumulation, especially after exposure to biological systems, as various degradation pathways can occur without affecting any of the labeled units – whether it is through breaking bonds along the polymer chain or removing monomers from ends. Moreover, the presence of the conjugated dye can alter the degradation of the polymer, potentially affecting both in-chain and endchain degradation mechanisms such as hydrolysis, oxidation, or enzymatic cleavage [15,18–20].

Concerns regarding the biocompatibility and potential toxicity of the dyes or the degraded polymers before or after degradation might arise and further complicate their interaction and application in vivo [21,22]. Although the stability, toxicity, and leakage issues of the labeling methods are frequently evaluated [23–26], each study employs different nanoparticles and techniques for individual dyes, making it challenging to identify the best strategy for particle labeling preparation with the desired fluorescent properties. Thus, while fluorescent labeling of polymeric carriers or its encapsulated cargo is convenient for initial biodistribution studies, it does not provide insight into polymer degradation, accumulation, and fate following cellular uptake. This highlights the need for new approaches to effectively monitor these processes.

Biodynamers have emerged from the application of constitutionally dynamic chemistry to polymer science, with their polymerization occurring through reversible dynamic covalent bonds (DCB), most often imines and acylhydrazone bonds [27,28]. They undergo spontaneous physical and chemical modification via bond forming, bond breaking, and exchange of biologically inspired monomers under specific conditions. As a result, the inherent properties of biomolecular monomers and reversible DCB equip biodynamers with numerous advantages such as biocompatibility, biodegradability, biofunctionality, tuneability, and self-healing capabilities, making them the ideal stimuli-responsive materials for versatile applications in the biomedical field, particularly as polymers for nanocarriers [29,30]. In our previous studies, we reported a carbazole-based biodynamer (CA-Lys) composed of water-soluble carbazole dicarboxaldehyde (CA) and lysine hydrazide, which exhibits significant pH-dependent changes in both morphology and fluorescence properties [31]. Upon polymerization, the spherical micelles of the CA monomer transformed into rigid nanorods, accompanied by a pronounced redshift in fluorescence emission as the pH increases from pH 3 to pH 13. This shift is attributed to the protonation effects on the carbazole fluorophores, which alter their conjugated systems and optical properties [31]. Consequently, both polymerization and pH changes impact fluorescence intensity and spectral characteristics, highlighting the complex interplay between pH, morphology, and optical behavior in biodynamers.

In this context, the controlled integration of fluorescent dyes into the biodynamers offers a promising approach to gain insight into the degradation and fate of polymers. Herein, we present a novel biodynamer (BDP-Lys) capable of monitoring intracellular polymer degradation. The BDP-Lys was designed to dynamically reactivate and enhance fluorescence emission upon degradation under acidic environments within cells (Figure 1). It is composed of two key monomers: on one hand, BODIPYdialdehydes (BDP), consisting of a hydrophobic and fluorescent aromatic core and a hydrophilic hexaethylene glycol (HG) chain on its meso-position, and on the other hand, lysine hydrazides (Lys). BODIPY, known for their fluorescence properties, offers a high fluorescence quantum yield, sharp emission/absorption in UV-visible range that is barely affected by pH environment [32], low toxicity, and is widely used in bioimaging and sensors applications [33,34]. Conversely, lysine hydrazide, a derivative of an amino acid, serves as a versatile building block with pharmaceutical applications [35]. First, we report the design and synthesis of BDP-Lys, followed by investigating its characteristics in terms of size, morphology, optical, and pHresponsive behavior using several physical methods. Next, we evaluated its compatibility with mammalian cells and performed the first studies for cellular uptake, and in situ degradation within the cells.

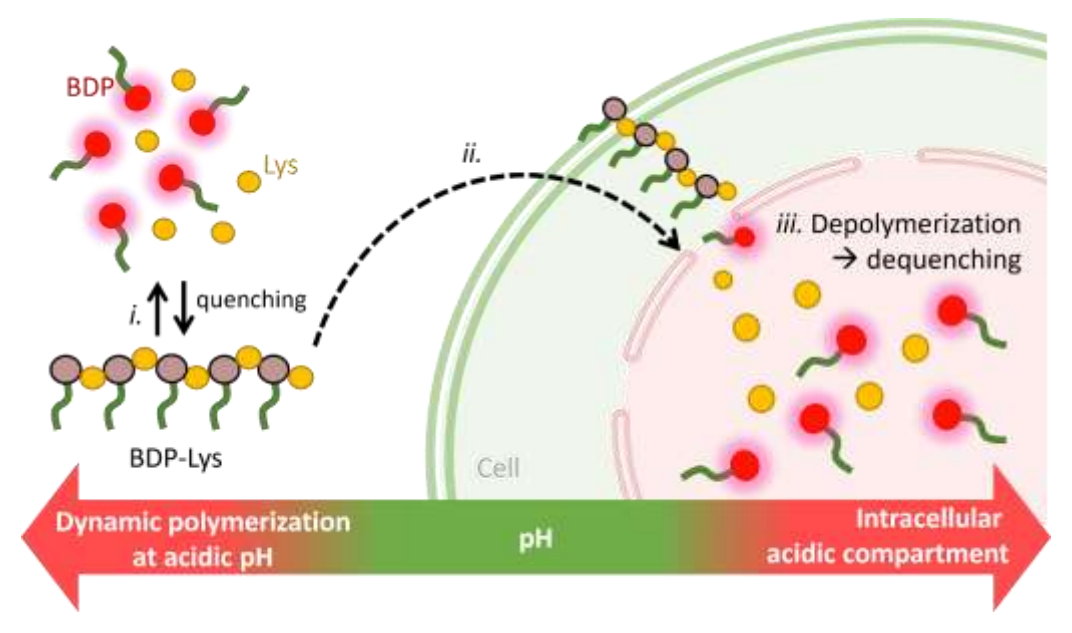


Figure 1. Schematic illustration of BDP-Lys dynamer, highlighting *i*) its polymerization under acidic pH in cuvette and *ii*) its fluorescence quenching, followed by cellular-uptake, and *iii*) its fluorescence activation upon degradation *in situ* within the biological system under acidic pH.

Materials and methods

General information

Reagents and dry solvents like dimethylformamide (DMF), dichloromethane (DCM) and dichloroethane (DCE) were purchased from the highest commercial sources and used as received, unless otherwise stated. Normal solvents were purchased as technical grade and used as received. Lysine methyl ester (H-Lys-OMe.2HCl) was purchased from Fluorochem Ltd. (Karlsruhe, Germany). All air- or moisture-sensitive reactions were carried out in dried solvents and in oven-dried glassware (>100 °C) under an atmosphere of nitrogen or argon. Thin layer chromatography (TLC) was performed with 0.25 mm E. Merck silica plates (60F-254), with a suitable solvent system and was visualized using UV fluorescence (254 & 366 nm).

Purification of the products was done via Column chromatography using either the automated flash chromatography system (normal phase) CombiFlash Rf+ (Teledyne Isco, Lincoln, NE, USA) equipped with RediSepRf silica columns (Axel Semrau, Sprockhövel Germany), or the automated flash chromatography system (reversed phase) Pure C-850 Flashprep (BUCHI, Switzerland) equipped with TELOS C18 flash columns.

Product purity was determined by a 1) Liquid chromatography-mass spectrometry (LC-MS) system, featuring a Dionex UltiMate 3000 pump, autosampler, column compartment and MWD or DAD detector (Thermo Fisher Scientific, Dreieich, Germany) and ESI quadrupole MS (MSQ Plus or ISQ EC, Thermo Fisher Scientific, Dreieich, Germany). Columns used: a) Hypersil Gold column, 100×2.1 mm, $3 \mu m$. At a flow rate of 700 μ L/min, the gradient of water (H₂O) + 0.1% formic acid (FA) and acetonitrile (ACN) + 0.1% FA starting from 5% ACN and then increased to 100% over 7 min. b) Hypersil Gold column, 100×1.9 mm, $2.1 \mu m$. At a flow rate of 600μ L/min, the gradient of H₂O + 0.1% FA and ACN + 0.1% FA started from 5% ACN and then increased to 100% over 5.5 min. The mass spectrum was measured in positive and negative mode in a range from 100–1000 m/z. 2) High-resolution mass spectra (HR-MS) were recorded with a ThermoScientific system where a Dionex Ultimate 3000 RSLC was coupled to a Q Exactive Focus mass spectrometer with an electrospray ion (ESI) source. An Acquity UPLC® BEH C8, 150×2.1 mm, $1.7 \mu m$ column equipped with

a VanGuard Pre-Column BEH C8, 5×2.1 mm, $1.7 \,\mu\text{m}$ (Waters, Germany) was used for separation. At a flow rate of 250 μ L/min, the gradient of (A) H₂O + 0.1% FA and (B) ACN + 0.1% FA was held at 10% B for 1 min and then increased to 95% B over 4 min. The mass spectrum was measured in positive mode in a range from 120–1000 m/z. Proton (1 H) and carbon (13 C) nuclear magnetic resonance (NMR) spectra were recorded on a Bruker Avance Neo 500 MHz spectrometer (1 H at 500.0 MHz; 13 C at 126.0 MHz) using deuterated solvents as an internal reference (Chloroform (CDCl₃): 7.26 ppm 1 H NMR, 77.2 ppm 13 C NMR; Dimethyl sulfoxide (DMSO– d_6): 2.50 ppm 1H NMR, 39.5 ppm 13 C NMR). The chemical shifts are recorded in parts per million (ppm) and the coupling constants (J) in Hertz (Hz). The following abbreviations were used for NMR peaks multiplicities (s: singlet, br s: broad singlet, d: doublet, dd: doublet of doublets, t: triplet, q: quartet, m: multiplet).

Synthesis of monomers and polymer BDP-Lys

2,5,8,11,14,17-hexaoxanonadecan-19-yl 4-methylbenzenesulfonate (1)

A solution of hexaethyleneglycolmonomethylether (2.5 g, 8.44 mmol) and trimethylamine (TEA) (1.35 mL, 9.7 mmol) in dry DCM (10 mL) was set stirring in an ice bath, and a solution of tosyl chloride (1.69 g, 8.86 mmol) in dry DCM (20 mL) was added dropwise over a period of 20 minutes (min). The ice bath was then removed, and the reaction was stirred at room temperature (r.t.) for 14 hours (h) followed by the addition of a 1M hydrochloric acid solution (20 mL) and H_2O (30 mL). The resulting mixture was extracted with DCM. The organic phase was washed with brine (50 mL), dried over sodium sulfate (Na₂SO₄), filtered and concentrated to a yellow oil, which was subject to automated flash chromatography (DCM/methanol (MeOH), 100/0 \rightarrow 95/5), yielding as a product a colorless oil (3 g, 79%). ¹H NMR (500 MHz, CDCl₃) δ 7.78 (d, J = 8.2 Hz, 2H), 7.33 (d, J = 8.4 Hz, 2H), 4.14 (t, J = 9.7 Hz, 2H), 3.68 – 3.53 (m, 22H), 3.36 (s, 3H), 2.43 (s, 3H). ¹³C NMR (126 MHz, CDCl₃) δ 144.89, 133.11, 129.92, 128.08, 72.03 - 68.77, 59.13, 21.74. LC-MS calculated (calcd) for $C_{20}H_{34}O_9S$ [M+H]⁺: 451.20, found 451.30.

4-((2,5,8,11,14,17-hexaoxanonadecan-19-yl)oxy)benzaldehyde (**2**)

To a solution of 4-hydroxybenzylaldehyde (500 mg, 4.09 mmol) and tosyl group $\mathbf{1}$ (1.84 g, 4.09 mmol) in 20 mL dry DMF were added caesium carbonate (Cs₂CO₃) (4.34 g,

13.31 mmol) and sodium iodide (NaI) (6.14 mg, 40.94 μmol). The reaction mixture was stirred at r.t. overnight. Then, H_2O was added, and the resulting mixture was extracted with EtOAc. The organic layer was dried over Na_2SO_4 , filtered and concentrated under reduced pressure. The crude product was purified via automated flash chromatography (DCM/MeOH, $100/O \rightarrow 90/10$) affording of the desired product **2** (1.4 g 85 %) as a yellow oil. ¹**H NMR** (500 MHz, CDCl₃) δ 9.88 (s, 1H), 7.82 (d, J = 6.8 Hz, 2H), 7.02 (d, J = 8.7 Hz, 2H), 4.23 – 4.19 (m, 2H), 3.90 – 3.87 (m, 2H), 3.73 – 3.53 (m, 20H), 3.37 (s, 3H). ¹³**C NMR** (126 MHz, CDCl₃) δ 190.66, 163.71, 131.80, 129.89, 114.73, 71.78, 70.76, 70.48 – 70.36, 69.32. **LC-MS** calcd for $C_{20}H_{32}O_8$ [M+H]⁺: 401.22, found 401.43.

10-(4-((2,5,8,11,14,17-hexaoxanonadecan-19-yl)oxy)phenyl)-5,5-difluoro-1,3,7,9-tetramethyl-5H-4l4,5l4-dipyrrolo[1,2-c:2',1'-f][1,3,2]diazaborinine (**3**)

To a heat dried Schlenk tube equipped with a magnetic stirring bar, the corresponding aldehyde 2 (850.0 mg, 2.12 mmol) and 2,4-dimethyl-1H-pyrrole (444.3 mg, 4.67 mmol) were dissolved in 60 mL dry DCM under nitrogen atmosphere. Trifluoroacetic acid (TFA) (185.2 µL, 2.42 mmol) was added and the resulting mixture was stirred overnight at r.t. in the dark. After complete consumption of the aldehyde, which was monitored on LC-MS, Dichloro-5,6-dicyano-1,4-benzoquinone (DDQ) (578.2 mg, 2.55 mmol) was added, and the reaction was stirred for an additional 1 h. Then, TEA (2.2 mL, 12.74 mmol) and boron trifluoride etherate (BF₃·Et₂O) (2.2 mL, 17.91 mmol) were added and mixture left to stir at r.t. for another 1 h. The resulting crude was concentrated in vacuum and purified via automated flash chromatography (DCM/MeOH, $100/0 \rightarrow 90/10$) affording a reddish fluorescent solid (500 mg, 38 %). ¹H **NMR** (500 MHz, CDCl₃) δ 7.15 (d, J = 8.5 Hz, 2H), 7.02 (d, J = 8.5 Hz, 2H), 5.97 (s, 2H), 4.18 (t, J = 4.7 Hz, 2H), 3.90 (t, J = 4.7 Hz, 2H), 3.75 - 3.56 (m, 20H), 3.37 (s, 3H), 2.54(s, 6H), 1.42 (s, 6H). ¹³**C NMR** (126 MHz, CDCl₃) δ 159.75, 155.64, 143.55, 142.21, 132.22, 129.55, 127.60, 121.49, 115.57, 72.33, 71.30, 70.98 (m), 70.13, 67.88, 59.44, 14.99. **LC-MS** calcd for $C_{32}H_{45}BF_2N_2O_7[M-H]^-$: 617.32, found 617.66.

10-(4-((2,5,8,11,14,17-hexaoxanonadecan-19-yl)oxy)phenyl)-5,5-difluoro-1,3,7,9-tetramethyl-5H-5l4,6l4-dipyrrolo[1,2-c:2',1'-f][1,3,2]diazaborinine-2-carbaldehyde (4)

Under nitrogen atmosphere, phosphoryl chloride (POCl₃) (11.4 mL, 122.80 mmol) was added dropwise to dry DMF (11.3 mL, 146.56 mmol) while maintaining the temperature below 25 °C (cooling in an ice bath). After complete addition, the mixture was stirred for 30 min at r.t. Compound 3 (490 mg, 0.792 mmol) was dissolved in 60 mL dry DCE, and carefully added. The temperature was raised to 50 °C and the reaction mixture was stirred for 2 h. After cooling to r.t., the mixture was slowly poured into a cooled sat. aq. solution of sodium bicarbonate (NaHCO₃) (100 mL) and further stirred for 60 min. Then, H₂O (20 mL) was added, and the resulting mixture was extracted with DCM (3 x 50 mL). The combined organic phases were dried over Na₂SO₄, filtered and solvents were removed under vacuum. The crude product was subject to an automated flash chromatography (DCM/MeOH, $100/0 \rightarrow 90/10$) yielding **4** (410 mg, 80%) as a red fluorescent solid. ¹**H NMR** (500 MHz, CDCl₃) δ 10.00 (s, 1H), 7.15 (d, J = 8.5 Hz, 2H), 7.05 (d, J = 8.5 Hz, 2H), 6.13 (s, 1H), 4.19 (t, J = 4.7, 2H), 3.91 (t, J = 4.7 Hz, 2H), 3.75 - 3.62 (m, 20H), 3.36 (s, 3H), 2.80 (s, 3H), 2.60 (s, 3H), 1.70 (s, 3H),1.46 (s, 3H). ¹³C NMR (126 MHz, CDCl₃) δ 185.95, 161.42, 159.81, 156.38, 147.35, 143.74, 142.89, 134.49, 130.18, 128.98, 126.26, 123.90, 115.53, 71.92, 70.65 – 70.53, 69.69, 67.58, 59.05, 15.10, 13.02, 11.81. **LC-MS** calcd for $C_{33}H_{45}BF_2N_2O_8$ [M+H]⁺: 647.33, found 647.67.

10-(4-((2,5,8,11,14,17-hexaoxanonadecan-19-yl)oxy)phenyl)-5,5-difluoro-1,3,7,9-tetramethyl-5H-4l4,5l4-dipyrrolo[1,2-c:2',1'-f][1,3,2]diazaborinine-2,8-dicarbaldehyde (**BDP**)

Under nitrogen atmosphere, POCl₃ (8.9 mL, 95.9 mmol) was added dropwise to dry DMF (8.8 mL, 114.5 mmol) while maintaining the temperature below 25 °C using an ice bath. After complete addition, the mixture was stirred for 30 min at r.t. To this mixture was added **4** (400 mg, 0.618 mmol) in 80 mL dry DCE and the reaction was stirred for additional 5 h at 60 °C. After cooling to r.t., the mixture was slowly poured into a sat. aq. solution of NaHCO₃ (100 mL) under ice conditions, and further stirred for 60 min. Then, H_2O (20 mL) was added, and the resulting mixture was extracted with

DCM (3 x 50 mL). The combined organic phases were dried over Na₂SO4, filtered and solvents were concentrated under vacuum. The crude product was purified using automated flash chromatography reversed phase (H_2O :ACN + 0.05% FA, gradient flow 5% to 100% ACN for 30 min) to afford the respective product **BDP** (110 mg, 26 %) as red-green, fluorescent solid. ¹H NMR (500 MHz, CDCl₃) δ 10.05 (s, 2H), 7.16 (d, J = 8.5 Hz, 2H), 7.10 (d, J = 8.5 Hz, 2H), 4.22 – 4.19 (m, 2H), 3.94 – 3.90 (m, 2H), 3.77 – 3.57 (m, 20H), 3.36 (s, 3H), 2.86 (s, 6H), 1.76 (s, 6H). ¹³C NMR (126 MHz, CDCl₃) δ 185.54, 160.42, 160.14, 148.24, 147.41, 132.14, 128.59, 127.87, 125.40, 115.79, 71.81, 70.81, 70.48, 70.40, 69.51, 67.54, 58.92, 13.64, 12.21. HRMS calcd for $C_{34}H_{45}BF_2N_2O_9$ [M+H]⁺: 675.32598, found 675.32837.

Lysine Hydrazide (**Lys**)

To a solution of L-Lysine methyl ester dihydrochloride (200 mg, 0.86 mmol) in anhydrous MeOH (4 mL) was added hydrazine hydrate (w% of N_2H_4 64-65%) (0.25 mL, 6.86 mmol) and the reaction was stirred at r.t. for 24 h. After the completion of the synthesis, MeOH was removed under vacuum (60°C, 20 mPa). Finally, 4 mL distilled H_2O is added to the product and freeze dried overnight to remove excess hydrazine hydrate. The product **Lys** (80 mg, 80%) was obtained as a transparent oil. Care was taken to avoid exposure to moisture. ¹H NMR (500 MHz, D_2O) δ 3.49 (t, J = 6.6 Hz, 1H), 3.03 - 2.97 (m, 2H), 1.74 - 1.65 (m, 4H), 1.44 - 1.32 (m, 2H).

Synthesis of BDP-Lys

BODIPY-dialdehydes (BDP) and lysine hydrazide (Lys) monomers were dissolved in deuterated DMSO with 10 mM deuterated acetic acid (pH 3.0) to achieve 20 mM concentration. Then, they were mixed at 1:1 molar ratio to yield a final concentration of 10 mM. The mixture was left reacting for 48 h at r.t. and excluded from light. The polymerization completion was monitored by ¹H NMR at different time points, showing depletion of the aldehyde peak and successful polymerization (Figure S7). The formed BDP-Lys were lyophilized without any washing step assuming complete consumption of the BDP monomers as indicated by the absence of aldehyde peaks. Another indication of successful polymerization is the change in color from light-red fluorescent to dark purple color with time.

Structure characterization of BDP-Lys

Size Exclusion Chromatography (SEC)

SEC was carried out determining the molar mass distributions (\mathcal{D}), weight average molecular weight (M_n) number average molecular weight (M_n) employing a setup consisting of a 515 HPLC pump by Waters, a RI Waters 2410 and an UV Waters 2487 as the detectors and a PSS Gram column setup (30 Å, 2x 1000 Å) at 60 °C. DMF with 1 g L⁻¹ LiBr was used as the eluent with a flow rate of 1 mL min⁻¹ and calibration were carried out using PEG standards from PSS.

Cryogenic Transmission Electron Microscopy (cryo-TEM)

Cryo-TEM images of the biodynamer were obtained using a JEM-2100 LaB $_6$ (JEOL, Akishima, Japan) microscope. A droplet (3 μ L) of the molecular biodynamer solution (1 mg/ml, in a mixture of 10 % DMSO in H $_2$ O) was placed on a S147-4 holey carbon film (Plano, Germany) and blotted to a thin liquid film for 2 s. Afterward the sample was plunged at T= 108 K into liquid ethane using a Gatan (Pleasanton, USA) CP3 cryo plunge system and transferred under liquid nitrogen to a Gatan 914 cryo-TEM holder operating at T= 100 K. Then cryo-TEM measurements were performed at an accelerating voltage of 200 kV at low-dose conditions.

Small-Angle Neutron Scattering (SANS)

Characterization of the BDP-Lys was carried out with SANS on D11 beamline at the Institut Laue-Langevin at Grenoble (ILL, France). By varying the wavelength of the incident beam and the sample to detector distance one can access the scattering vector $q = \frac{4\pi}{\lambda} sin \frac{\theta}{2}$ where θ is the angle between the direct and the scattered beam. Three sets of wavelength λ and sample to detector distance D were used (λ =11.5 (Å), D=17.6 (m); λ =6 (Å), D=17.6 (m) allowing to measurement with scattering wavevectors q of $4.7 \times 10^{-4} \le q$ (Å-1) $\le 1.4 \times 10^{-2}$, $3.7 \times 10^{-3} \le q$ (Å-1) ≤ 0.6 , $1.1 \times 10^{-2} \le q$ (Å-1) ≤ 0.7 . Conversion to absolute intensity units (cm-1) followed classical data reduction procedures that are correct for empty cell, electronic background, detector response and normalization by the attenuated beam. The incoherent scattering leading to a plateau at the high q region of the scattering curve of the sample is due to hydrogen atoms coming from the macromolecule and the solvent. Incoherent

scattering masks structural correlations therefore it has been substracted from the data. The high q data can be fitted by a Guinier expression for the form factor of the cross-section:

$$I(q) = \frac{A}{q}e^{-\frac{R_C^2q^2}{2}}$$
 Equation (1)

Where $A=\varphi\Delta\rho^2\pi a_c$, a_c is the section area of the filaments, R_c the radius of gyration of the cross section, φ the volume fraction of monomers and $\Delta\rho$ the difference in the scattering length density between the solvent and the scattering object.

The scattering intensity for a centosymmetric object is given by

$$I = \varphi V \Delta \rho^2 P(q) S(q)$$
 Equation (2)

Where

 φ : volume fraction of repeating units

 ${\it V}\,$ the volume of the scattering object, i.e. of the N repeating units (monomers) in a chain

P(q): the form factor

S(q): the structure factor

Small-Angle X-Ray Scattering (SAXS)

SAXS measurements with the Xeuss 2.0 diffractometer were performed at CEA-Saclay, at a wavelength λ of 1.54 Å. For low scattering vectors range a sample-to-detector distance of 2500 (mm) was used with a collimation slit of 0.6 x 0.6 (mm) and 0.5 x 0.5 (mm), at the collimation distance of 1200 (mm). For the high q range the sample to detector distance was set at 540 (mm), the collimation slits dimensions were 1.2 x 1.2 and 0.8 x 0.8 (mm) with a collimation distance at 1200 (mm).

The scattering wavevectors investigated were in the range of 4.4×10^{-2} (Å⁻¹) $\leq q \leq 1.1$ (Å⁻¹) and standard procedures were employed for reducing the data to absolute units (cm¹).

For SANS the scattering length density is determined by $\rho = \frac{\Sigma n_i b_i}{m \times v/N_A}$ where n_i is number of atoms of the monomer or solvent, b_i the scattering length, N_A is the Avogadro's number, m is the molar mass of monomer or solvent, and v is the specific volume of the repeating unit (or solvent molecule).

The scattering length b_i is for neutrons depends on the isotope as neutrons interact with the nucleus of the atom. Unlike, for SAXS the electron cloud of the atom determines the propability for the scattering and so b_i is replaced by the $Z_i \times r_e$ where Z_i is the atomic number of the ith atom and r_e =2.81×10⁻¹³ (cm) is the electron radius. In Table 2. the scattering length densities ρ , the contrast term $\Delta \rho$ have been calculated for the whole BDP-Lys monomer unit, for the different parts of the dynamer as well as the solvent.

Quenching of BDP-Lys fluorescence and absorbance

BDP and BDP-Lys were diluted in a solvent mixture of 1% DMSO in H_2O containing 1% polyvinyl alcohol (PVA) to achieve a final concentration of 25 μ M. The fluorescence emission and absorbance scan before and after polymerization was measured using microplate reader (Infinite 200 PRO, Tecan Instruments, Männedorf, Switzerland), by taking 180 μ L of the final solution into a black-96 well plate. For emission scan, the samples were excited at λ = 470 nm and highest emission for monomer/polymer was λ = 520 nm/550 nm (broad) respectively.

Based on preliminary experiments, we selected a 470 nm excitation wavelength for effective BDP monomer excitation and used it consistently to compare monomeric and polymeric BDP-Lys, highlighting its degradation and fluorescence enhancement.

Dequenching of BDP-Lys by pH-responsive degradation

To analyze pH-responsive fluorescence emission, BDP-Lys and BDP monomer were each diluted in a mixture of 1% DMSO in the corresponding buffer solutions (10 mM containing 1% PVA) to achieve a final concentration of 25 μ M. The buffer solutions used included phosphate buffers at pH 3, 7.4, and 11, acetate buffer at pH 5, and carbonate buffer at pH 9. Fluorescence intensity was measured using the microplate reader, by taking 180 μ L of the final solution into a black-96 well plate, with excitation at λ = 470 nm and emission at λ = 520 nm at various time intervals (0, 1, 3, 6, 9, 24, 48, 72, and 94 h) in each pH media.

The effect of pH on the absorbance of BDP-Lys and BDP monomer was carried out following the same procedure as the fluorescence measurements, with absorbance

specifically measured at 502 nm. The experiment was independently performed twice, with triplicates.

Fluorescence monitoring of BDP with sodium ascorbate in pH 3

BDP monomer were diluted in a mixture of 1% DMSO in the respective phosphate buffer (pH 3, 10 mM with 1% PVA) with or without sodium ascorbate (E301), to achieve a final concentration of 25 μ M. The first sample contained BDP diluted solely in the pH 3 buffer. The second sample included BDP diluted in pH 3 buffer containing 250 μ M E301 (prepared by dissolving 0.5 mg of E301 in a 10 mL pH 3 buffer). In the final sample BDP was diluted in pH 3 buffer containing 20 mM E301 (prepared by dissolving 40 mg of E301 in a 10 mL pH 3 buffer). Fluorescence intensity was measured at various time intervals (0, 1, 3, 6, 9, 24, 48, 72, and 94 h) using a microplate reader. 180 μ L of each solution was transferred into a black 96-well plate for measurements. The excitation and emission wavelengths were set at λ = 470 nm and λ = 520 nm, respectively. These measurements were used to observe the fluorescence behavior of the monomer in the presence and absence of E301. The experiment was performed twice, each with duplicates samples.

pH-responsive degradation of BDP-Lys

Dialysis was performed using a membrane with a molecular cut-off of 6 kDa. BDP-Lys was dissolved in DMSO: H_2O (1:1) at a concentration of 300 µg/mL and loaded into the membrane. The sealed dialysis membrane was then immersed in a beaker containing 100 mL of each respective buffer solutions (10 mM containing 1% PVA of each phosphate buffer pH 3, pH 7.4 and acetate buffer pH 5). The dialysis was carried out at 37 °C with gentle stirring for 3 days. At various time points (0, 3, 6, 9, 24, 48, 72 h), 180 µL aliquots were withdrawn from the dialysate. The degraded amount of BDP-Lys was determined by measuring the absorbance at λ = 502 nm using the microplate reader. Calibration curves were done using BDP monomer. Dialysis experiments were conducted twice in triplicates.

Cytotoxicity assay

A549 cells were seeded into 96 well plates with 20 000 cells/well in RPMI medium supplemented with 10% FCS. The plate was incubated until cells reached 95%

confluency with fresh medium added every 2 days. On the day of the experiment, the medium was removed. Then, the cells were washed twice with HBSS buffer and treated with the desired concentration of BDP-Lys (25, 50, 100, 200 and 400 μ g/mL) and BDP monomer (31, 63, 125, 250 and 500 μ g/mL) in HBSS. The dead control was 2% TritonX-100 in HBSS, and the live control was HBSS. The cells were incubated at 150 rpm shaking at 37° C with 5% CO₂. After 4 h, the treatment was removed, and the cells were washed once with HBSS. 100 μ L HBSS + 10 μ L PrestoBlueTM Cell Viability Reagent were added on the cells for 4 h while shaking. Fluorescence was measured by the plate reader at an excitation of 570 nm and an emission of 610 nm. % Viability was calculated as follows:

$$\%\ viability = \frac{Fl.\,of\ sample - Fl.\,of\ dead\ control}{Fl.\,of\ live\ control - Fl.\,of\ dead\ control}*100\%$$

Cellular uptake assay

To prepare our labeled BDP-Lys for cellular uptake studies, we began by preparing BDP-Lys as a 40 mM solution and Alexa Fluor 594 (AF594) as a 2 mM solution in DMSO. Subsequently, equal volumes of the two solutions were mixed to achieve the desired molar ratio: 20 mM product with 5% dye incorporation. The mixture was allowed to stir for 24 h at r.t., shielded from light. Subsequent purification was performed by washing the sample with 0.01% TEA using an Amicon Ultra filter, employing a centrifugation step at 5000 g for 10 minutes and repeating this wash process three times to eliminate all unbound AF594. Finally, the purified product was lyophilized and used as-is for further experiments.

A549 cells were seeded on a black 24-well plate with transparent bottom at a density of 100 000 cells/well for CLSM imaging. After 48 h incubation, cell medium was exchanged and further incubated until cells reached 90–95% confluency. The cells were washed with HBSS buffer (x2) and then the desired labelled BDP-Lys-594 (500, 100, 50 and 10 μ g/mL) in HBSS (500 μ L) was added. After 4 h incubation at 37 °C, cells were washed again with HBSS (x2) and fixed using 4% paraformaldehyde (PFA) (500 μ L) for 30 min at r.t. After rinsing with HBSS (x2), cells nuclei were stained for 20 min with DAPI (Sigma; 0.5 μ g/mL in HBSS). Cells were washed with HBSS and membrane

was stained using Concanavlin A Alexa Fluor 633 Conjugate (Fisher Scientific; 5 µg/mL). After rinsing with HBSS, cells were analyzed by CLSM.

Confocal Laser Scanning Microscopy (CLSM): Images acquisition was performed using Fluotar VISIR 25x/0.95 water and the following settings were used: BD-Lys-594 fluorescent (excited at 561 nm, 2% laser intensity) was detected between 590–610 nm. For DAPI and Concanavlin A, the emission filters were set between 410–466 nm (excited at 405 nm, 10% laser intensity) and 650–776 nm (excited at 633 nm, 1% laser intensity), respectively. Confocal z-stacks were recorded in a range of 50 μ m and images were processed with the Leica Application Suite (LAS) X Software.

In vitro BDP-Lys degradation

50,000 A549 cells were seeded in 250 μ l RPMI medium supplemented with 10% FCS in half of the wells of a 48-well plate (Ref 677180, Greiner Bio-One GmbH, Frickenhausen, Germany) and incubated for 24 h. Then, cells were washed twice with HBSS and 250 μ l PBS was added to three wells containing cells and three empty wells. To these 6 wells, BDP-Lys was added at a concentration of 20 μ g/well and cells were incubated at 37 °C in a 5% CO₂ atmosphere. After 4 h, wells containing cells were washed twice with PBS and 250 μ l PBS was added again. The 48-well plate was put inside a standard humidity cassette (large, Tecan Trading AG, Switzerland) containing 6 mL deionized H₂O in each reservoir and the cells were incubated at 37 °C and 5% CO₂ in the Tecan SparkCyto (Tecan Trading AG, Switzerland) for 48 h. Cells were imaged at baseline (t=0 h) and after 48 h using both brightfield and green fluorescence channels. Fluorescence images were captured with an LED intensity set to 80% and an exposure time of 70 ms. Additionally, fluorescence intensity of all wells containing BDP-Lys was measured every 6 h using an excitation wavelength of 470± 15 nm and an emission wavelength of 520± 10 nm with 4×4 reads taken per well.

Estimating the degradation of polymer intracellularly vs time

20,000 A549 cells were seeded into 48-well plate. Cells were left to grow until 90% confluency. Before t0 by 4 h, 20 μ g/well of BDP and BDP-Lys were added into separate wells. Cell control wells were included for the background subtraction later and cells were incubated in a 37 °C with 5% CO₂. At 0 h (after 4 h incubation), cells were washed and PBS was added, then fluorescence emission scan was measured between 500 and 700 nm, by

exciting the samples at 470 nm using the microplate reader, with a manual gain of 80 at 0 h and 24 h.

The fluorescence signal (Fl_{total}) was subtracted from the average cell fluorescence (Fl_{cell}) to get the pure polymer or monomer fluorescence (pFl)

$$pFl = Fl_{total} - Fl_{cell}$$

Then the degree of polymerization or monomer portion (M Index) was estimated for the monomer and polymer at 0 h and 24 h via the ratio between fluorescence at 518 and 578 nm, using the following equation:

$$M index = \frac{pFl_{518nm}}{pFl_{578nm}}$$

Finally, degree of degradation was estimated via the following equation:

$$Degradation \ (\%) = \frac{M \ index_{polymer \ at \ 24h} - M \ index_{polymer \ at \ 0h}}{M \ index_{Monomer \ at \ 24h} - M \ index_{polymer \ at \ oh}}$$

Two replicates were conducted, and standard deviation was calculated.

Results & discussion

Synthesis of Monomers

The corresponding monomers BDP and Lys were prepared as illustrated in Scheme 1A (detailed in Scheme S1). The synthesis began with 4-hydroxybenzaldehyde, which was converted to substituted aryl aldehyde **2**. BODIPY cores are usually constructed by the condensation reaction between a carbonyl group and a pyrrole followed by in situ complexation with boron trifluoride etherate (BF₃·Et₂O) in the presence of a base [36]. Compound **3**, therefore, was obtained from reacting 2,4 dimethylpyrrole with aryl aldehyde **2**, followed by treatment of the reaction mixture with each BF₃·OEt₂ and TEA. Subsequently, both formyl groups were introduced via a Vilsmeier-Haack reaction, in a two-step process, yielding the corresponding monomer BDP as a red fluorescent compound. The synthesis of the Lys monomer was achieved by treating L-Lysine methyl ester dihydrochloride with hydrazine hydrate in MeOH. The chemical structures of each monomer were characterized by ¹H NMR and ¹³C NMR spectrometry (Figures S1–S6).

Scheme 1. (A) Synthesis of monomers BODIPY-dialdehydes (BDP) and lysine hydrazide (Lys). Reagents and conditions: i. 1, Cs_2CO_3 , NaI, DMF, 12 h; ii. TFA, DDQ, TEA, BF $_3$ ·OEt $_2$, DCM, 18 h; iii. (4) DMF, POCl $_3$, DCE, 50 °C 2–5 h, reaction repeated twice to generate the di-aldehyde structure; iv. N_2H_4 , MeOH, 24 h. HG = (CH $_2$ CH $_2$) $_6$ OMe. (B) Hexaethylene glycol conjugated BDP and Lys polymerized reversibly into biodynamers by acylhydrazone and imine bond formation in acidic medium (pH 3.0).

Synthesis of BDP-Lys

We generated BDP-Lys biodynamer (BDP-Lys) using reversible C=N bond formation. It is a condensation reaction between aldehydes and primary amines or hydrazides, known as the Schiff-base reaction. Formed imines and acylhydrazones often exhibit rapid interconversion rates between formation and hydrolysis, particularly under acidic conditions [37]. The polycondensation of BDP and Lys monomers (Scheme 1B) was carried out at a 1:1 molar ratio with a final concentration of 10 mM in a solvent mixture of DMSO and acetic acid. After 48 h at r.t., BDP-Lys polymerization was

monitored by ¹H NMR spectroscopy (Figure S7). Notably, during the reaction, the aldehyde C-H resonance at δ = 10.0 ppm was completely depleted after 48 h, indicating the consumption of BDP monomers through imine and acylhydrazone bond formation. These bond formations are evident around δ = 12.0 ppm. Extreme peak broadening in the aliphatic region is a typical feature of polymers, mainly caused by intramolecular interactions.

In the context of polymerization selectivity, α -position amines are known to be more reactive than ϵ -position amines and predominantly participate in biodynamer polymerization. This higher reactivity of α -amines is attributed to their greater nucleophilicity, as the adjacent carbonyl group enhances electron density and stabilizes the developing positive charge. Furthermore, cation— π and electrostatic interactions restrict the accessibility of ϵ -amines, which are more susceptible to be protonated than α -amines, thereby favoring α -amines as the preferred sites for imine bond formation [38,39].

Molecular weight estimation of BDP-Lys

The resulting polymers were injected into SEC to confirm the polymerization. The measurements of BDP-Lys were carried out in DMF with PEG standard at a concentration of 0.6 g/L. A molar mass of approximately M_w = 10 000 g/mol, with a dispersity (θ) value of 10.4 has been observed after the polymerization (Figures S8), suggesting a broad molecular-weight distribution.

This broad dispersity can be attributed to the specific polymerization conditions, the underlying mechanisms and the fact that the polymer was analyzed without purification to allow a direct comparison with the previously reported biodynamer. In the case of the previously CA-based biodynamer, the hydrophobic CA core gained water solubility due to the attached hydrophilic HG chains, allowing polymerization in an aqueous environment following a nucleation-elongation (N-E) mechanism [38–40]. A key feature of N-E polymerization is the formation of a critical polymer chain length, after which elongation becomes more favorable than initiating new chains. This process was driven by the enhanced stability of CA-based biodynamer, resulting from hydrophobic interactions and π - π stacking, and folding of CA core units.

Meanwhile, the hydrophilic HG chains extended into the solvent, promoting a more stable and controlled nucleation-elongation process [38]. In contrast, BDP-Lys polymerization was conducted in DMSO due to the poor BDP solubility in water, even in the presence of the hydrophilic HG chain. DMSO, being a polar aprotic solvent, ensured the solubility of both monomers, facilitating polymerization. However, these conditions weaken the N-E mechanism by decreased hydrophobic interaction between the monomers, and accelerate the reaction kinetics, which was observed by the immediate color change from red to purple upon lysine addition. This fast reaction rate likely caused uncontrolled nucleation events and a broad distribution of chain lengths, reflected in the wide dispersity observed in SEC measurements. To obtain a refined BDP-Lys biodynamer, further optimization of polymerization conditions or modification of monomer structures to enhance their water solubility may be necessary.

Structure analysis of BDP-Lys

To provide complementary information on the structure of the BDP-Lys, a certain set of experimental techniques has been found to be useful in the context of biodynamers, including cryogenic transmission electron microscopy (cryo-TEM) [41], small-angle neutron (SANS) [42], and X-ray (SAXS) scattering [43]. Figure 2A shows a micrograph of a vitrified solution about 200-300 nm thick at c= 1 g/L (in a mixture of 10% DMSO in H2O). The image shows polydisperse rod-like filaments of various lengths (8–100 nm) with random orientations relative to the plane of observation and with a high optical density cross-section suggesting a local molecular packing [39]. The inset displays a magnified image of a long filament larger than 60 nm. A common feature is that filaments are rigid over long lengths. They also appear to exhibit regular sequences of alternating gray and black regions of higher electronic contrast along the main axis of the filaments. The inset of Figure 2A allows for the measurement of a cross-sectional diameter of Dc-TEM= 4 nm. This dimension is larger than the monomer unit diameter (Dmon<11 Å (calculated by Avogadro excluding HG)), indicating a well-defined local organization and molecular packing inside the assemblies, as previously observed for similar biodynamers [31].

To obtain more precise insights on the local structure and conformation of the assemblies, we employed SANS and SAXS, complementary techniques well-suited for probing structural parameters and molecular organization over the range of 1–30 nm.

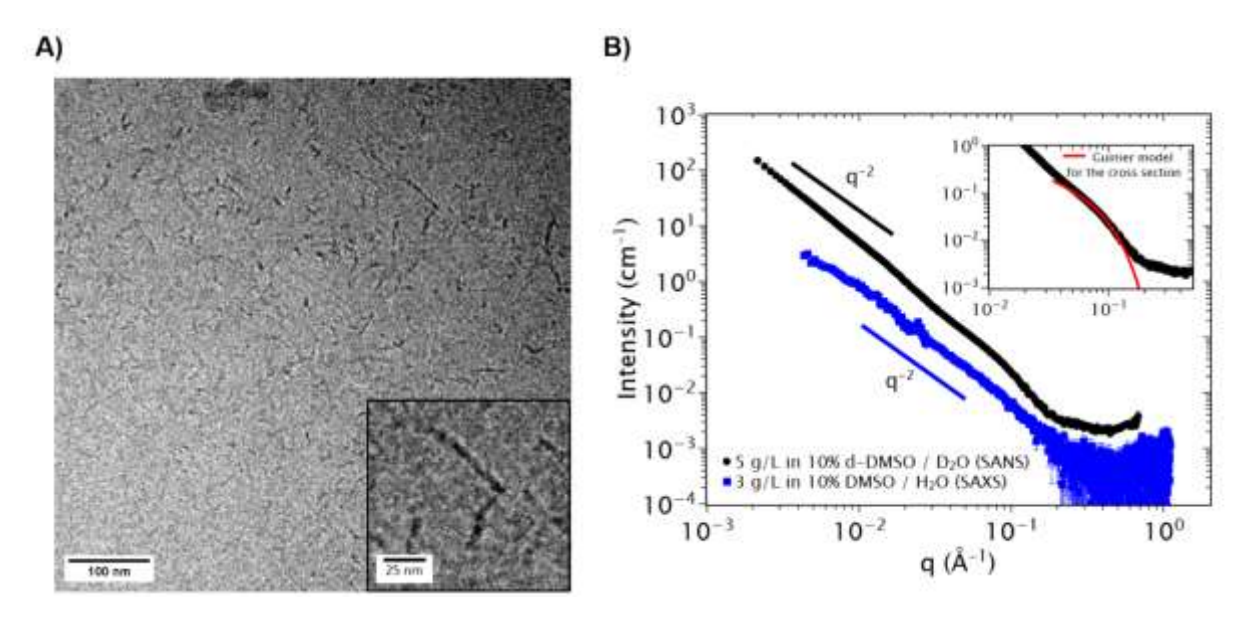


Figure 2. (A) Cryo-TEM image of BDP-Lys at a concentration of 1 g/L in a mixture of 10% DMSO in H₂O. (B) Scattering patterns for BDP-Lys: SANS measurements of solution of BDP-Lys at a concentration of 5 g/L in a mixture of 10% d-DMSO in D₂O (black squares) and SAXS measurements at a concentration of 3 g/L in a mixture of 10% DMSO in H₂O (blue squares). The scattering intensity of the sample was measured at three different configurations of wavelength λ and sample to detector distance D (11.5 (Å) – 17.6 (m), 6 (Å) – 17.6 (m), 6 (Å) – 5.6 (m)). Inset: The high q data were fitted using a Guinier model for the cross section (red line) giving a characteristic radius of gyration R_c of 15Å for the cross section.

A typical SANS scattering pattern representing the variation of the scattered intensity with the magnitude of the scattering wave-vector q can be visualized in Figure 2B for BDP-Lys at the concentration c=5 g/L. The absence of a Guinier plateau, associated with objects of finite mass and size, in the low q region indicates that the size of the self-assemblies is larger than 30 nm. Instead, we observe an extended regime which can be described by a power law with characteristic exponent equal to -2, as for Gaussian chains or for a planar 2D local organization or stacking. This q^{-2} regime is followed at higher q, i.e., larger than 0.06 Å $^{-1}$, by an exponential decay associated with the cross-sectional dimension of the filaments.

The high q data can be fitted by a Guinier expression for the form factor of the cross-section (Equation (1), see materials and methods), and the obtained parameters are collected in Table S1.

We found a value of 1.5 nm for the cross-sectional radius of gyration, R_c , corresponding to a diameter of about D_{c-SANS} = 3 nm, a value in good agreement with the section found from the cryo-TEM analysis (D_{c-TEM} = 4 nm). The value of R_c is greater than $R_c > \sqrt{\frac{a_c}{\pi}}$, which suggests that the section of the filaments assumed to be circular is not full.

At first sight, the q^{-2} regime could be associated with the random distribution of monomers as in a Gaussian wormlike chain. However, in this case, we would expect to observe a q^{-1} regime at larger q scattering wavevectors, associated with the rigid behavior of the chain or filaments for distances smaller than the persistence length L_p which is not the case. Another possibility is that the local organization of the filaments is planar, as is the case for helical or twisted ribbons. This could explain the rather large cross-sectional dimensions combined with a relatively small value of the cross-sectional area a_c . This also explains the regular alternations of contrast along the filaments observed in the cryo-TEM images. It should be noted that the small deviation from the observed q^2 behavior in the very low q range could arise from the roughness of the 2D interface related to the hydrophilic side chains of the monomers or from the branching and/or aggregation of the filaments at larger scales, as observed by cryo-TEM.

More insight into the molecular packing and the hypothetical local 2D organization can be obtained using SAXS, a technique much more sensitive to the electronically dense parts of molecules, such as the aromatic groups of the hydrophobic core of the BDP. As a result, the contrast term Δp for the hydrophobic aromatic core of the dynamer is much larger than that of the hexaethylene glycol chains (Table S2) and the SAXS signal will be dominated by the aromatic core, while the side chains and lysine will be invisible. By contrast, SANS is sensitive to the overall scattering objects. The scattering profile of SAXS displayed in Figure 2B exhibits a clear extended q^{-2} power law, suggesting that the 2D local organization arises from the packing of the aromatic

components. A rather weak bending is observed at small q, which, if real, could be associated with objects of finite size and mass. In this case, one could envisage a structure that would result from the self-association of small ellipsoids in the form of filaments. This model would explain why the SEC measurement gives such small masses (mass of elementary ellipsoids) and why the filaments are so polydisperse.

Quenching of BDP-Lys fluorescence and absorbance

After confirming the structure of the prepared BDP-Lys through various characterization techniques, its fluorescence properties, arising from these structural features, were subsequently investigated. As previously discussed, BODIPY is a well-known fluorescent dye used in biological applications due to its high fluorescence quantum yield, independence of pH, and excellent photostability. However, it is also well known for aggregation-induced quenching (AIQ) by H-type (face-to-face) aggregation [44,45], which can occur during the polymerization, and can be strategically leveraged in biomedical applications [46]. Given the molecular packing of the hydrophobic core observed in SANS and SAXS, we expected that polymerization of BPD-Lys would lead to fluorescence quenching.

At a concentration of 25 μ M, BDP monomer exhibited sharp fluorescence emission and absorbance at λ_{em} = 520 nm and λ_{abs} = 502 nm, respectively. In contrast, the polymeric form BPD-Lys showed complete fluorescence quenching, as expected, along with a broadened absorbance band and lower intensity compared to the monomer (Figure 3). In addition to the AIQ of BODIPY, another possible explanation for these changes is the introduction of a C=N bond to the BODIPY core, which facilitates photoinduced electron transfer (PET) processes. The acylhydrazone and imine bonds formed act as an electron-withdrawing group (EWG), promoting PET from the BODIPY core to the C=N moiety and leading to fluorescence and absorbance depletion. These observations align with previous reports [47,48], where C=N bonds caused a fluorescence turn-off of the BODIPY probe with the potential of re-inducing a turn-on by the removal of the reversible C=N moiety. Therefore, the formation of C=N bonds and polymerization-induced aggregation have a big influence on the photophysical properties of BODIPY, in particular leading to quenching of both fluorescence and absorbance.

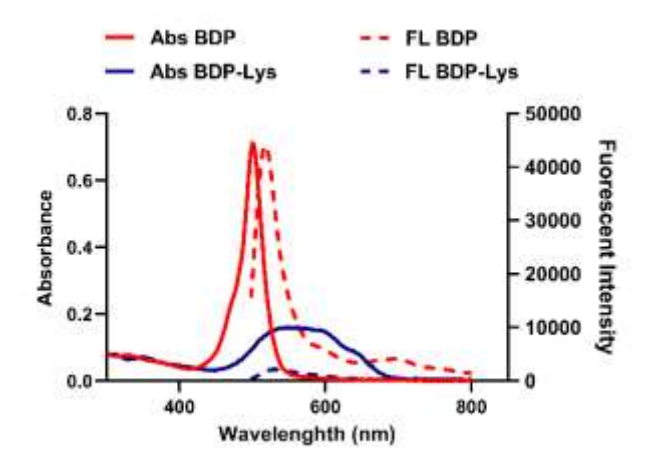


Figure 3. Optical changes by molecular biodynamer formation showing absorbance (straight line) and fluorescence (dotted line) at a concentration of 25 μ M in a mixture of 1% DMSO in H₂O, when excited at λ = 470 nm. Fluorescent quenching of BDP monomer and the peak shifted from λ = 520 nm (dotted red line) to a broad signal of λ = 530–560 nm (dotted blue line). Absorbance broadness and shift of BDP monomer peak after polymerization (blue line).

Dequenching of BDP-Lys by pH

We anticipated that the polymerization-induced quenching of BODIPY could be reversed through acid-triggered degradation of the biodynamer, as BDP-Lys exhibits dynamic reversible behavior under acidic conditions due to the acylhydrazone and imine bonds in the backbone. Therefore, we evaluated the pH effect on the optical properties of the biodynamer. BDP-Lys was incubated in different buffer solutions (10 mM, pH 3-11) for 96 h at r.t., and the emissions were measured at different time intervals. As shown in Figure 4A, the fluorescence emission remained stable in neutral (pH 7.4) and basic environments (pH 9 and 11) throughout the entire incubation period. However, a significant increase in fluorescence was observed at pH 3, with a 14-fold increase after 72 h, compared to the other pH conditions. Additionally, within the first hour of incubation at pH 3, the emission spectrum of BDP-Lys was broadened. Over the next 6 h, the broad peak gradually shifted to a single narrow emission at λ = 520 nm, corresponding to λ_{max} of the BDP monomer (Figure 4B). Only protonation by acid alone is unlikely to counteract the AIQ effect and restore fluorescence. We, thus, believe that this emission increase and shift under acidic conditions result from the reversal of the previously described quenching effect, driven by the pH-responsive DCB in BDP-Lys and their subsequent

hydrolysis into monomers e.g., degradation, indicating that BDP-Lys might be a useful tool for tracking polymer degradation under acidic conditions.

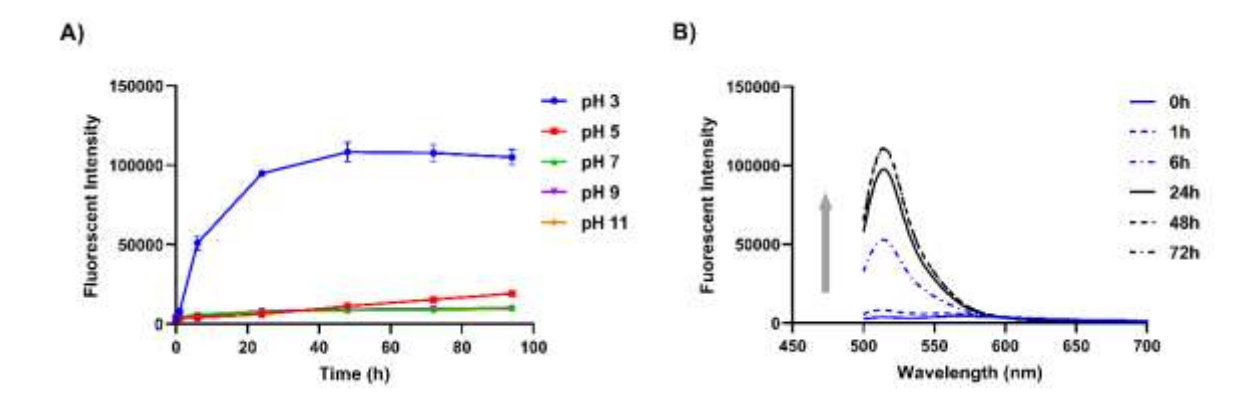


Figure 4. pH-responsive optical changes of BDP-Lys: (A) Fluorescence emission recovery of BDP monomer at λ_{em} = 520 nm in different pH at different time points. Errors bars were obtained from duplicated experiments (N= 2 and n= 6) (B) Emission shifts at pH 3 as a function of time. Broad peak shift from around λ_{em} = 550–580 nm to a sharp peak at λ_{em} = 520 nm. The concentration of BDP-Lys is set to 25 μ M and 10 mM buffer solutions (pH 3–11) were used.

pH-Dependent fluorescence of BDP

Assuming that monomer release is responsible for the increase in fluorescence intensity, we also evaluated the possibility of acid-dependent fluorescence changes of the released monomer before investigating relation of fluorescence increase and polymer degradation. While investigating the pH effect on BDP, a significant fluorescence emission increase was observed. The fluorescence emission of the BDP monomer increased over time after incubation at pH 3 but remained stable in other media (pH 5–11, Figure 5A).

This fluorescence change is attributed to the presence of the aldehyde groups, which are prone to protonation and oxidation to carboxylic acid in acidic pH conditions [49,50]. As EWG, aldehydes can increase the electron deficiency of the BODIPY core, facilitating intramolecular charge transfer and PET, both critical for changing fluorescence. Therefore, the oxidation of the aldehyde group has a possibility of an enhancement in fluorescence. Additionally, the oxidation to carboxylic acid group may improve the solubility of BDP, as the hydroxyl and carbonyl group increase polarity, which can further contribute to fluorescence enhancement [49]. Similar

behavior has been reported in various studies, where certain BODIPY derivatives show marked fluorescence enhancement at acidic pH due to the protonation of respective EWG moieties [51–53] or cleavage of ester group to carboxylic acid [54]. Given that the fluorescence of BDP increase at pH 3 required almost 24 h, we speculate here that protonation followed by oxidation restored fluorescence intensity.

To further support this hypothesis, we incubated BDP at pH 3 with the presence of antioxidant, sodium ascorbate (E301), and analyzed the effect in fluorescence under conditions that restrict oxidation at low pH. As shown in Figure 5B, the addition of 20 mM E301 suppressed the increase in fluorescence emission, supporting that the oxidation was involved in the fluorescence enhancement under acidic conditions. Therefore, not only low pH conditions, such as pH 3, but also reactive oxygen species (ROS)- and enzyme-mediated oxidation, could potentially enhance the fluorescence intensity of the monomeric BDP. For example, aldehyde dehydrogenases (ALDH) [55] are responsible for the oxidation of aldehydes to carboxylic acids and protect living organisms against oxidative stress [56]. Thus, we expect that the fluorescence increase of the released monomers after BDP-Lys degradation will be advantageous feature of the system. Although investigation into enzymatic oxidation of the monomer in biological systems was not feasible with the current monomer due to the limited solubility, additional investigations with modified versions of the BDP, and their pathways will further prove this hypothesis.

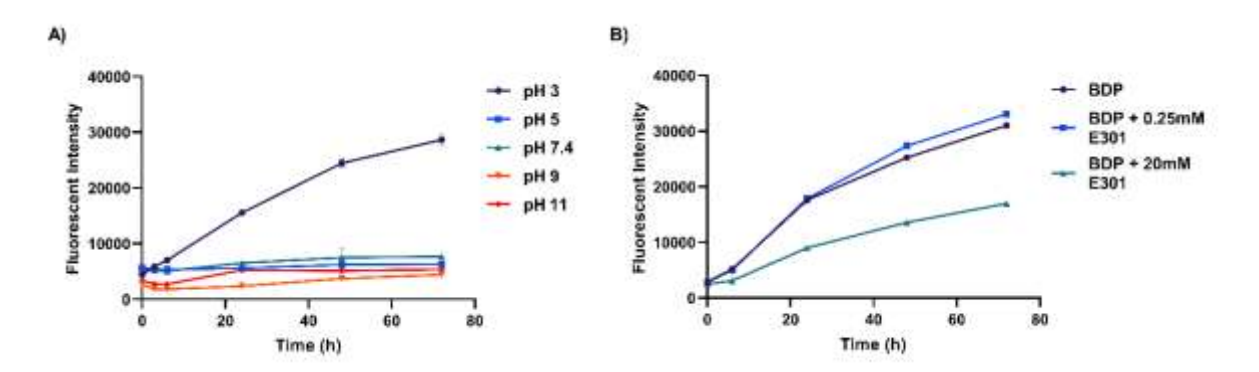


Figure 5. Fluorescent emission spectra of (A) BDP monomer in different pH medium and various time points. (B) BDP monomer incubated at pH 3 in the presence of E301 (0.25 and 20 mM), highlighting the impact of the antioxidant on the stability and emission properties of the monomer under acidic pH.

pH-responsive degradation of BDP-Lys

Next, we monitored BDP-Lys degradation, which might be associated with the fluorescence increase. Given that the fluorescence of BDP monomer is pH-dependent, we first confirmed its absorbance stability across different pH levels (pH 3, 5 and 7.4) to ensure accurate data. The absorbance of the BDP monomer remained stable and independent of pH changes (Figure S9). Therefore, the degradation degree of BDP-Lys was determined by measuring the absorbance at 502 nm. Approximately 37% of BDP-Lys degraded into monomers and oligomers smaller than 6 kDa at pH 3 within 72 h. In contrast, about 15% of BDP-Lys degraded in a buffer at pH 7.4 due to the limited dynamicity of the DCB (Figure 6). This degradation under acidic conditions (phosphate buffer, pH 3), recovered BODIPY fluorescence by 14-fold during a 72-h incubation at 37 °C. Considering the correlation between its degradation and the fluorescence increase, we can conclude that, at acidic pH, biodynamers start to shorten and fluorescence increases over time due to the polymer degradation with dynamic nature, followed by oxidation of the BDP.

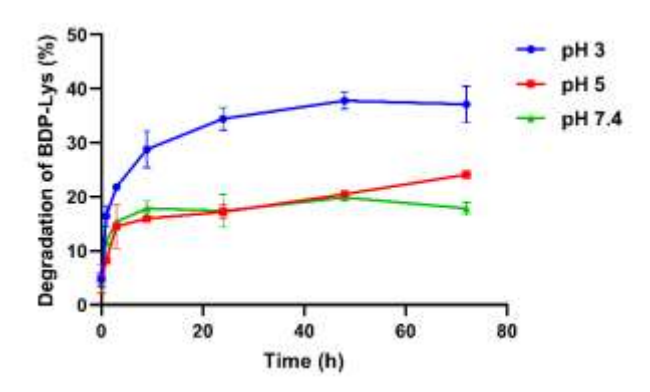


Figure 6. Acid-responsive degradation of BDP-Lys at 37 °C (300 μ g/mL) in phosphate buffer (pH 3 and pH 7.4, 10 mM) acetate buffer (pH 5, 10 mM). Errors bars were obtained from duplicated experiments (N= 2 and n= 3).

The high stability of BDP-Lys under acidic conditions, along with its limited degradation, is surprising given the inherent reactivity of imine and acylhydrazone bonds in the polymer backbone. The DCB, which was used in this polymerization process, is known to be unstable in aqueous media, and its application in polymer backbones has been very limited [57,58]. However, our previous work demonstrated that non-covalent bonds within the polymer, hydrophobic interactions and π - π

stacking, stabilize DCB, leading to enhanced polymerization efficiency and stability in aqueous media. For example, the CA-Lys biodynamer benefits from π - π stacking and hydrophobic interactions from the CA group along with cation- π stacking from the Lys residue [28,31,38]. This resulted in significantly higher polymerization efficiency, with a degree of polymerization (DP) reaching 100, compared to biodynamers without the CA group [31,40]. Moreover, in the case of CA-Lys, 60% degradation was observed over 72 h at pH 5.0 [59].

For BDP-Lys, these stabilizing effects by non-covalent bonds were further enhanced, requiring additional conditions to make the DCB irreversible. In fact, BODIPY has a strong tendency for stacking, resulting in strengthening non-covalent bonds and significant quenching. Additionally, its limited solubility in aqueous solutions necessitated the use of DMSO as a solvent for polymerization, unlike CA-Lys. The increased hydrophobicity and enhanced π - π stacking likely shifted the equilibrium of DCB further toward bonding, making the polymer more stable to degradation in aqueous media. Consequently, although a mild acidic condition may be sufficient to trigger the cleavage of DCB within BDP-Lys, the bond can be later reversibly recovered under the mild acidic conditions. Thus, higher acidity concentration was necessary to promote the gradual oxidation of BDP's aldehyde groups, which caused DCB cleavage and irreversible polymer degradation (Scheme 2). This oxidation can occur not only at low pH but also by oxidants or intracellular oxidases such as ALDH as mentioned earlier. Therefore, we hypothesized that the increase in fluorescence intensity due to polymer degradation, similar to that observed at pH 3, could be achieved through the induction of degradation under intracellular mild acidic conditions and the inhibition of reversible reactions by intracellular oxidases.

Scheme 2. Mechanism of both biodynamers CA-Lys and BDP-Lys: In CA-Lys, pH 5 with low concentration promotes degradation to monomers and irreversible DCB cleavage. In BDP-Lys, mild acidic conditions initiate DCB cleavage and degradation, while higher acidity (*e.g.*, pH 3) triggers oxidation of BDP aldehyde to BDP*, making the DCB irreversible and enhancing fluorescence.

Cell Viability of BDP-Lys and their degradation products

Therefore, to examine the degradation of BDP-Lys within cells, its cytotoxicity was first confirmed. Cell viability of our biodynamer was conducted in the mammalian cell line A549, using Presto Blue as an indicator. The results in Figure 7A show no significant toxicity of BDP-Lys across the tested concentration range, confirming its biocompatibility and safety for potential biomedical applications. In contrast, the BDP monomer (Figure 7B) lowered cell viability to <80% at higher concentrations than 500 µg/mL. This toxicity may be attributed to the presence of dialdehyde groups within the molecule, which aligns with the results of previously investigated CA-Lys.

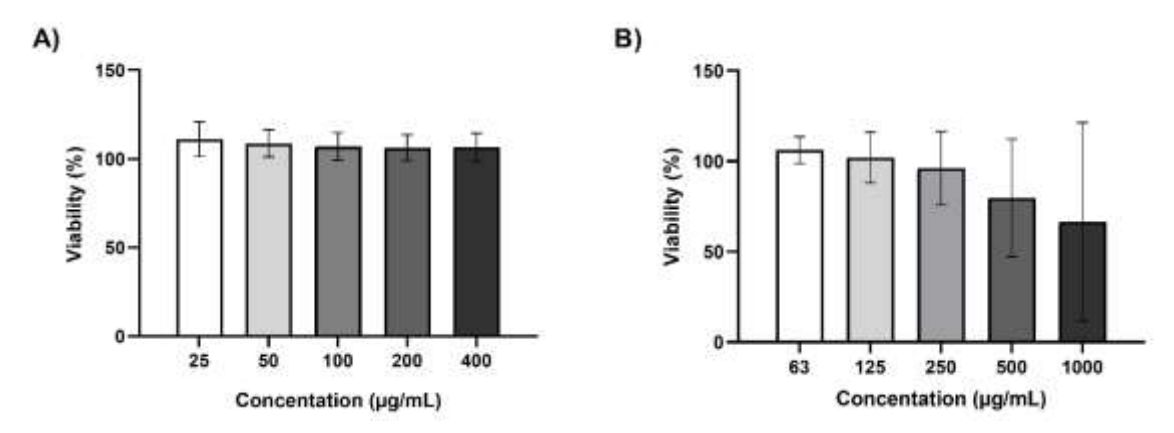


Figure 7. Cell (A549) viability of BDP-Lys biodynamer (A) and BDP monomer (B). Viability was determined by Presto blue assay using Triton-X (2%) as a positive control, after 4 h incubation with the respective samples at 37 °C. Errors bars were obtained from duplicate experiments (N= 2 and n= 3).

Intracellular degradation of BDP-Lys

Before monitoring polymer intracellular degradation, we first assessed whether BDP-Lys could be efficiently taken up by cells. Due to the quenching of BODIPY intrinsic fluorescence in BDP-Lys, Alexa Fluor 594 dye was conjugated on the Lys side chain via amine-NHS ester reaction to monitor its cellular uptake. BDP-Lys-Alexa was incubated with A549 cells for 4 h at 37 °C. After incubation, cells were washed and stained with DAPI for the nucleus (blue) and Concanavalin Alexa Fluor 633 for the membrane (purple) to visualize intracellular structures using the confocal microscope. As shown in Figure 8, there was a strong overlap between BDP-Lys-Alexa and the cytoplasmic region of the cells, confirming their high possibility of cellular uptake.

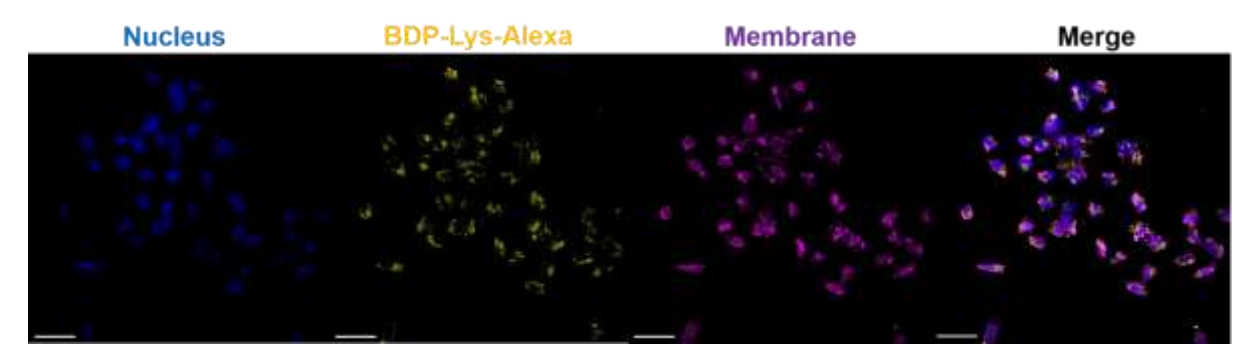


Figure 8. Confocal laser scanning microscopy visualization of the A549 cellular uptake after incubation with BDP-Lys-Alexa for 4 h. DAPI-stained cell nuclei (blue), Concanavlin A Alexa Fluor™633 stained cytoskeleton (purple), and dynamer labeled BDP-Lys-Alexa (yellow). Scale bar is 50 μm.

Following the confirmation of efficient cellular uptake, we aimed to evaluate polymer degradation and determine whether fluorescence recovery could be observed upon degradation of BDP-Lys within the cells. Thus, we incubated the BDP-Lys (20 µg/well) with A549 cells. After 4 h, cells were washed to remove any BDP-Lys that had not been taken up by the cells and then further incubated for 24 h. Although one would not expect to reach pH as low as 3 within cells, as in those cuvette experiments, our results in Figure 9 show that the fluorescence intensity of BDP-Lys increases significantly within the cells after 24 h, with approximately a threefold increase. This indicates degradation of the polymer and subsequent recovery of BDP fluorescence, due to the presence of oxidating agents like ROS and ALDH in cells, which supports oxidation and contributes to the observed increase in fluorescence. In contrast, the control sample without cells showed no changes in fluorescence, which is expected, since as previously demonstrated, biodynamers are stable in neutral conditions. This confirms that the fluorescence increase observed in the presence of cells is due to polymer degradation and subsequent BDP oxidation.

Moreover, this fluorescence increases within the cells allowed us to estimate the degradation rate of the BDP-Lys. The intracellular degradation kinetics was estimated using the characteristic fluorescence emission scan pattern, which was found to be different for BDP-Lys and its monomer, BDP (Figure 3). The amount of released monomers from the BDP incubated in the cells was determined using fluorescence pattern of degrading BDP-Lys relative to the pure monomer pattern which was considered as standard. Resultingly, BDP-Lys was degraded by about $17.07 \pm 2.23\%$ in the first 24 h, reflecting specific rate constant (k) of $0.007 \, h^{-1}$, assuming first-order

degradation kinetics (see materials and methods for further details). Note that this is the maximum degradation rate, considering that fluorescence intensity also increases by the hour in cells.

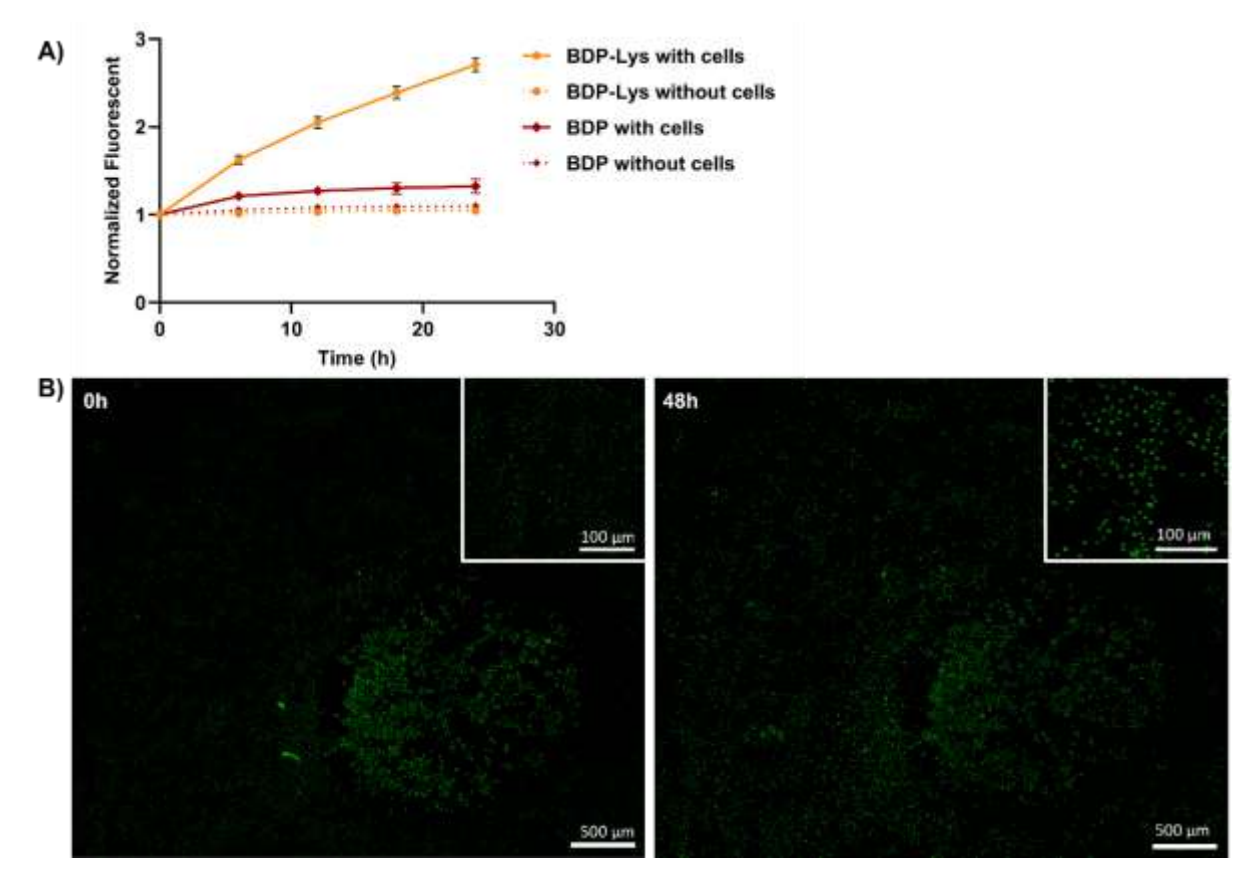


Figure 9. Fluorescence intensity of BDP and BDP-Lys with and without A549 cells for 24 h. A) Normalized fluorescence intensity over time for BDP-Lys incubated with A549 cells and BDP-Lys without cells as control. B) Fluorescence plate-reader images of BDP-Lys incubated with A549 cells at 0 h (left) and 48 h (right).

Conclusions

In summary, our study detailed the design and synthesis of a novel biodynamer composed of BODIPY-dialdehyde (BDP) and lysine hydrazide (Lys), highlighting its dynamic nature in response to pH changes. By using ¹H NMR spectroscopy, cryo-TEM, SEC, SANS and SAXS, we characterized the polymerization and structure of the resulting BDP-Lys. We evaluated its optical properties, noting that fluorescence is quenched in polymeric form which is the case in neutral conditions. Under acidic conditions, however, as in certain intracellular compartments (e.g., lysosome), biodynamer fluorescence is de-quenched as a consequence of polymer degradation and subsequent oxidation of the released monomer. The *in vitro* studies highlight the

cellular internalization of BDP-Lys leading to polymer degradation and successful fluorescence recovery within mammalian cells. Overall, BDP-Lys biodynamer provides a promising starting point for further investigation of polymer degradation and fate within biological systems. Considering the possibility to modify the amino acid monomer composition, BDP-based biodynamers offer great potential for both biomedical and drug delivery applications.

Conflicts of interest

There are no conflicts to declare.

Acknowledgments

The authors would like to thank, Blandine Boßmann for help with SEC measurements.

Supplementary Data

The data supporting this study are provided in supplementary information, which includes scheme, NMR spectra, and supplementary figures.

Corresponding authors

Sangeun Lee Helmholtz Institute for Pharmaceutical Research Saarland (HIPS), Helmholtz Centre for Infection Research (HZI), Saarland University, 66123 Saarbrücken, Germany; Department of Pharmacy, Saarland University, 66123 Saarbrücken, Germany. E-mail: sangeun.lee@uni-saarland.de

Anna K. H. Hirsch Helmholtz Institute for Pharmaceutical Research (HIPS) – Helmholtz Centre for Infection Research (HZI), Saarland University, Campus Building E8.1, 66123 Saarbrücken, Germany; Department of Pharmacy, Saarland University, 66123 Saarbrücken, Germany. E-mail: anna.hirsch@helmholtz-hips.de

Author Contributions

Justine Bassil: Writing – review & editing, Writing – original draft, Visualization, Validation, Investigation, Methodology, Formal analysis, Data curation, Conceptualization. Mohamed A.M. Kamal: Writing – review & editing, Validation, Methodology. Aljoscha Gabelmann: Writing – review & editing, Validation, Methodology. Anastasia Christoulakie: Writing – review & editing, Validation,

Methodology, formal analysis. **Eric Buhler:** Writing – review & editing, Validation, Methodology, formal analysis. **Marcus Koch:** Validation, Methodology. **Markus Gallei:** Writing – review & editing, Validation, Methodology. **Brigitta Loretz:** Writing – review & editing, Supervision, Project administration, Conceptualization. **Mostafa M. Hamed:** Writing – review & editing, Supervision, Project administration, Conceptualization. **Claus-Michael Lehr:** Writing – review & editing, Supervision, Project administration, Funding acquisition, Conceptualization. **Anna K.H. Hirsch:** Writing – review & editing, Supervision, Project administration, Funding acquisition, Conceptualization. **Sangeun Lee:** Writing – review & editing, Visualization, Supervision, Project administration, Investigation, Data curation, Conceptualization.

References

- [1] R. De, M.K. Mahata, K.-T. Kim, 2022. Structure-Based Varieties of Polymeric Nanocarriers and Influences of Their Physicochemical Properties on Drug Delivery Profiles. Adv. Sci. 9, 2105373. https://doi.org/10.1002/advs.202105373.
- [2] A. Zielińska, F. Carreiró, A.M. Oliveira, A. Neves, B. Pires, D.N. Venkatesh, A. Durazzo, M. Lucarini, P. Eder, A.M. Silva, A. Santini, E.B. Souto, Polymeric Nanoparticles: Production, Characterization, Toxicology and Ecotoxicology, Molecules 25 (2020). https://doi.org/10.3390/molecules25163731.
- [3] N. Kamaly, B. Yameen, J. Wu, O.C. Farokhzad, Degradable Controlled-Release Polymers and Polymeric Nanoparticles: Mechanisms of Controlling Drug Release, Chem. Rev. 116 (2016) 2602–2663. https://doi.org/10.1021/acs.chemrev.5b00346.
- [4] S. Shehata, C.J. Serpell, S.C. Biagini, Architecture-controlled release of ibuprofen from polymeric nanoparticles, Materials Today Communications 25 (2020) 101562. https://doi.org/10.1016/j.mtcomm.2020.101562.
- [5] R. Duncan, M.J. Vicent, Polymer therapeutics-prospects for 21st century: the end of the beginning, Adv. Drug Deliv. Rev. 65 (2013) 60–70. https://doi.org/10.1016/j.addr.2012.08.012.
- [6] S. Parveen, R. Misra, S.K. Sahoo, Nanoparticles: a boon to drug delivery, therapeutics, diagnostics and imaging, Nanomedicine 8 (2012) 147–166. https://doi.org/10.1016/j.nano.2011.05.016.

- [7] A.M. Breul, M.D. Hager, U.S. Schubert, Fluorescent monomers as building blocks for dye labeled polymers: synthesis and application in energy conversion, biolabeling and sensors, Chem. Soc. Rev. 42 (2013) 5366–5407. https://doi.org/10.1039/c3cs35478d.
- [8] S. Bou, A.S. Klymchenko, M. Collot, Fluorescent labeling of biocompatible block copolymers: synthetic strategies and applications in bioimaging, Mater. Adv. 2 (2021) 3213–3233. https://doi.org/10.1039/d1ma00110h.
- [9] V. Zhukova, N. Osipova, A. Semyonkin, J. Malinovskaya, P. Melnikov, M. Valikhov, Y. Porozov, Y. Solovev, P. Kuliaev, E. Zhang, B.A. Sabel, V. Chekhonin, M. Abakumov, A. Majouga, J. Kreuter, P. Henrich-Noack, S. Gelperina, O. Maksimenko, Fluorescently Labeled PLGA Nanoparticles for Visualization In Vitro and In Vivo: The Importance of Dye Properties, Pharmaceutics 13 (2021). https://doi.org/10.3390/pharmaceutics13081145.
- [10] A.S. Klymchenko, F. Liu, M. Collot, N. Anton, Dye-Loaded Nanoemulsions: Biomimetic Fluorescent Nanocarriers for Bioimaging and Nanomedicine, Adv. Healthcare Mater. 10 (2021) e2001289. https://doi.org/10.1002/adhm.202001289.
- [11] S. Snipstad, S. Hak, H. Baghirov, E. Sulheim, Ý. Mørch, S. Lélu, E. von Haartman, M. Bäck, K.P.R. Nilsson, A.S. Klymchenko, C. de Lange Davies, A.K.O. Åslund, Labeling nanoparticles: Dye leakage and altered cellular uptake, Cytometry, Part A 91 (2017) 760–766. https://doi.org/10.1002/cyto.a.22853.
- [12] A. Reisch, A.S. Klymchenko, Fluorescent Polymer Nanoparticles Based on Dyes: Seeking Brighter Tools for Bioimaging, Small 12 (2016) 1968–1992. https://doi.org/10.1002/smll.201503396.
- [13] P. Álamo, V. Pallarès, M.V. Céspedes, A. Falgàs, J.M. Sanchez, N. Serna, L. Sánchez-García, E. Voltà-Duràn, G.A. Morris, A. Sánchez-Chardi, I. Casanova, R. Mangues, E. Vazquez, A. Villaverde, U. Unzueta, Fluorescent Dye Labeling Changes the Biodistribution of Tumor-Targeted Nanoparticles, Pharmaceutics 12 (2020). https://doi.org/10.3390/pharmaceutics12111004.
- [14] S. Bou, F. Ng, E. Guegain, C. Peloso, A. Lopez-Noriega, M. Collot, Evaluating the in vivo stability of water-soluble PEG-PLA copolymers using FRET imaging, Reactive and Functional Polymers 187 (2023) 105579. https://doi.org/10.1016/j.reactfunctpolym.2023.105579.

- [15] T.P. Gustafson, Y.H. Lim, J.A. Flores, G.S. Heo, F. Zhang, S. Zhang, S. Samarajeewa, J.E. Raymond, K.L. Wooley, Holistic assessment of covalently labeled core-shell polymeric nanoparticles with fluorescent contrast agents for theranostic applications, Langmuir 30 (2014) 631–641. https://doi.org/10.1021/la403943w.
- [16] M.P. Monopoli, D. Walczyk, A. Campbell, G. Elia, I. Lynch, F.B. Bombelli, K.A. Dawson, Physical-chemical aspects of protein corona: relevance to in vitro and in vivo biological impacts of nanoparticles, J. Am. Chem. Soc. 133 (2011) 2525–2534. https://doi.org/10.1021/ja107583h.
- [17] F. Bertoli, D. Garry, M.P. Monopoli, A. Salvati, K.A. Dawson, The Intracellular Destiny of the Protein Corona: A Study on its Cellular Internalization and Evolution, ACS Nano 10 (2016) 10471–10479. https://doi.org/10.1021/acsnano.6b06411.
- [18] J. Vohlídal, Polymer degradation: a short review, Chemistry Teacher International 3 (2021) 213–220. https://doi.org/10.1515/cti-2020-0015.
- [19] M.M. Perfilov, A.S. Gavrikov, K.A. Lukyanov, A.S. Mishin, Transient Fluorescence Labeling: Low Affinity-High Benefits, Int. J. Mol. Sci. 22 (2021). https://doi.org/10.3390/ijms222111799.
- [20] D. Shrestha, A. Bagosi, J. Szöllősi, A. Jenei, Comparative study of the three different fluorophore antibody conjugation strategies, Anal. Bioanal. Chem. 404 (2012) 1449–1463. https://doi.org/10.1007/s00216-012-6232-z.
- [21] L. Arms, D.W. Smith, J. Flynn, W. Palmer, A. Martin, A. Woldu, S. Hua, 2018. Advantages and Limitations of Current Techniques for Analyzing the Biodistribution of Nanoparticles. Front. Pharmacol. 9, 802. https://doi.org/10.3389/fphar.2018.00802.
- [22] T. Thomsen, A.B. Ayoub, D. Psaltis, H.-A. Klok, Fluorescence-Based and Fluorescent Label-Free Characterization of Polymer Nanoparticle Decorated T Cells, Biomacromolecules 22 (2021) 190–200. https://doi.org/10.1021/acs.biomac.0c00969.
- [23] M.M.A. Abdel-Mottaleb, A. Beduneau, Y. Pellequer, A. Lamprecht, Stability of fluorescent labels in PLGA polymeric nanoparticles: Quantum dots versus organic dyes, Int. J. Pharm. 494 (2015) 471–478. https://doi.org/10.1016/j.ijpharm.2015.08.050.

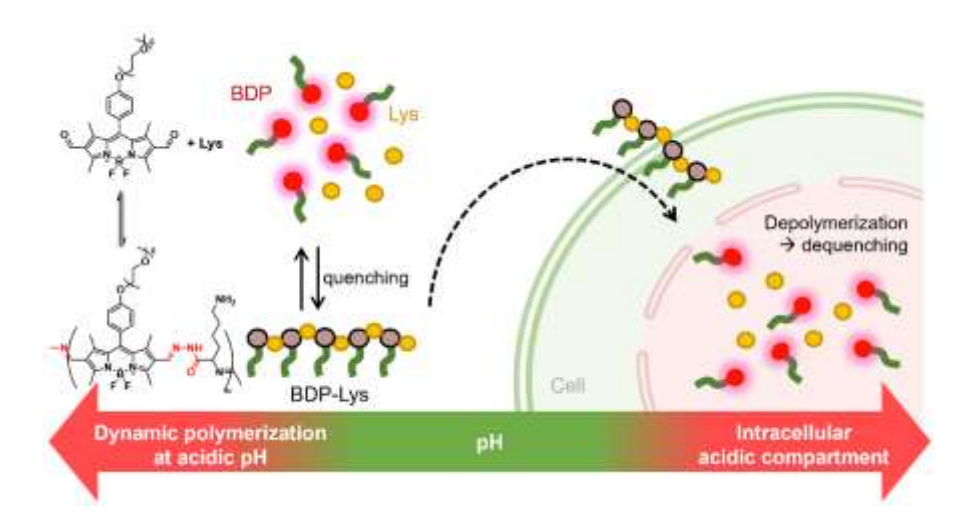
- [24] S. Behzadi, M. Gallei, J. Elbert, M. Appold, G. Glasser, K. Landfester, D. Crespy, A triblock terpolymer vs. blends of diblock copolymers for nanocapsules addressed by three independent stimuli, Polym. Chem. 7 (2016) 3434–3443. https://doi.org/10.1039/c6py00344c.
- [25] C. Simonsson, G. Bastiat, M. Pitorre, A.S. Klymchenko, J. Béjaud, Y. Mély, J.-P. Benoit, Inter-nanocarrier and nanocarrier-to-cell transfer assays demonstrate the risk of an immediate unloading of dye from labeled lipid nanocapsules, Eur. J. Pharm. Biopharm. 98 (2016) 47–56. https://doi.org/10.1016/j.ejpb.2015.10.011.
- [26] B.J. Marquis, S.A. Love, K.L. Braun, C.L. Haynes, Analytical methods to assess nanoparticle toxicity, Analyst 134 (2009) 425–439. https://doi.org/10.1039/B818082B.
- [27] E. Kolomiets, J.-M. Lehn, Double dynamers: molecular and supramolecular double dynamic polymers, Chem. Commun. (Camb) (2005) 1519–1521. https://doi.org/10.1039/B418899C.
- [28] Y. Liu, J.-M. Lehn, A.K.H. Hirsch, Molecular Biodynamers: Dynamic Covalent Analogues of Biopolymers, Acc. Chem. Res. 50 (2017) 376–386. https://doi.org/10.1021/acs.accounts.6b00594.
- [29] Y. Liu, M.C.A. Stuart, E. Buhler, A.K.H. Hirsch, Dynamic Proteoids Generated From Dipeptide-Based Monomers, Macromol. Rapid Commun. 39 (2018) e1800099. https://doi.org/10.1002/marc.201800099.
- [30] Y. Liu, M.C.A. Stuart, M.D. Witte, E. Buhler, A.K.H. Hirsch, Saccharide-Containing Dynamic Proteoids, Chemistry 23 (2017) 16162–16166. https://doi.org/10.1002/chem.201703584.
- [31] S. Lee, C. Kaya, H. Jang, M. Koch, B. Loretz, E. Buhler, C.-M. Lehr, A.K.H. Hirsch, pH-Dependent morphology and optical properties of lysine-derived molecular biodynamers, Mater. Chem. Front. 4 (2020) 905–909. https://doi.org/10.1039/c9qm00651f.
- [32] A. Loudet, K. Burgess, BODIPY dyes and their derivatives: syntheses and spectroscopic properties, Chem. Rev. 107 (2007) 4891–4932. https://doi.org/10.1021/cr078381n.

- [33] A. Loudet, K. Burgess, BODIPY Dyes and Their Derivatives: Syntheses and Spectroscopic Properties, Chem. Rev. 107 (2007) 4891–4932. https://doi.org/10.1021/cr078381n.
- [34] S. Das, S. Dey, S. Patra, A. Bera, T. Ghosh, B. Prasad, K.D. Sayala, K. Maji, A. Bedi, S. Debnath, BODIPY-Based Molecules for Biomedical Applications, Biomolecules 13 (2023) 1723. https://doi.org/10.3390/biom13121723.
- [35] I. Shih, Y. Van, M. Shen, Biomedical Applications of Chemically and Microbiologically Synthesized Poly(Glutamic Acid) and Poly(Lysine), Mini-Rev. Med. Chem. 4 (2004) 179–188. https://doi.org/10.2174/1389557043487420.
- [36] T. Ozdemir, J.L. Bila, F. Sozmen, L.T. Yildirim, E.U. Akkaya, Orthogonal Bodipy Trimers as Photosensitizers for Photodynamic Action, Org. Lett. 18 (2016) 4821–4823. https://doi.org/10.1021/acs.orglett.6b02418.
- [37] S. Zheng, G. Liu, Polymeric Emissive Materials Based on Dynamic Covalent Bonds, Molecules 27 (2022) 6635.
- [38] Y. Liu, M.C.A. Stuart, E. Buhler, J.-M. Lehn, A.K.H. Hirsch, Proteoid Dynamers with Tunable Properties, Adv. Funct. Mater. 26 (2016) 6297–6305. https://doi.org/10.1002/adfm.201601612.
- [39] A.K.H. Hirsch, E. Buhler, J.-M. Lehn, Biodynamers: self-organization-driven formation of doubly dynamic proteoids, J. Am. Chem. Soc. 134 (2012) 4177–4183. https://doi.org/10.1021/ja2099134.
- [40] J.F. Folmer-Andersen, E. Buhler, S.-J. Candau, S. Joulie, M. Schmutz, J.-M. Lehn, Cooperative, bottom-up generation of rigid-rod nanostructures through dynamic polymer chemistry, Polym. Int. 59 (2010) 1477–1491. https://doi.org/10.1002/pi.2864.
- [41] A.L. Parry, P.H.H. Bomans, S.J. Holder, N.A.J.M. Sommerdijk, S.C.G. Biagini, Cryo electron tomography reveals confined complex morphologies of tripeptide-containing amphiphilic double-comb diblock copolymers, Angew. Chem. Int. Ed Engl. 47 (2008) 8859–8862. https://doi.org/10.1002/anie.200802834.
- [42] Y. Wei, M.J.A. Hore, 2021. Characterizing polymer structure with small-angle neutron scattering: A Tutorial. Journal of Applied Physics 129, 171101. https://doi.org/10.1063/5.0045841.

- [43] R. Ishige, Precise structural analysis of polymer materials using synchrotron X-ray scattering and spectroscopic methods, Polym J 52 (2020) 1013–1026. https://doi.org/10.1038/s41428-020-0357-2.
- [44] L. Wang, L. Li, D. Cao, A BODIPY-based dye with red fluorescence in solid state and used as a fluorescent and colorimetric probe for highly selective detection of cyanide, Sensors and Actuators B: Chemical 239 (2017) 1307–1317. https://doi.org/10.1016/j.snb.2016.09.112.
- [45] T. He, D. Tang, C. Lin, X. Shen, C. Lu, L. Xu, Z. Gu, Z. Xu, H. Qiu, Q. Zhang, S. Yin, Conjugated Polymers Containing BODIPY and Fluorene Units for Sensitive Detection of CN-Ions: Site-Selective Synthesis, Photo-Physical and Electrochemical Properties, Polymers 9 (2017) 512. https://doi.org/10.3390/polym9100512.
- [46] Z. Chen, Z. Chen, Functional supramolecular aggregates based on BODIPY and aza-BODIPY dyes: control over the pathway complexity, Org. Chem. Front. 10 (2023) 2581–2602. https://doi.org/10.1039/D3QO00148B.
- [47] X. Song, X. Han, F. Yu, J. Zhang, L. Chen, C. Lv, A reversible fluorescent probe based on C²N isomerization for the selective detection of formaldehyde in living cells and in vivo, Analyst 143 (2018) 429–439. https://doi.org/10.1039/c7an01488k.
- [48] W.-C. Chen, P. Venkatesan, S.-P. Wu, A turn-on fluorescent probe for hypochlorous acid based on HOCl-promoted removal of the C²N bond in BODIPY-hydrazone, New J. Chem. 39 (2015) 6892–6898. https://doi.org/10.1039/c5nj01083g.
- [49] Francis A. Carey, Richard J. Sundberg, Advanced Organic Chemistry Part A: Structure and Mechanisms (5th ed.): Part A: Structure and Mechanisms (5th ed.), Springer (2007). https://doi.org/10.1007/978-0-387-44899-2.
- [50] Y. Liao, A. Aspin, Z. Yang, Anaerobic oxidation of aldehydes to carboxylic acids under hydrothermal conditions, RSC Adv. 12 (2022) 1738–1741. https://doi.org/10.1039/d1ra08444e.
- [51] E. Teknikel, C. Unaleroglu, Colorimetric and fluorometric pH sensor based on bis(methoxycarbonyl)ethenyl functionalized BODIPY, Dyes Pigm. 120 (2015) 239–244. https://doi.org/10.1016/j.dyepig.2015.04.021.
- [52] H. Liu, W. Song, D. Gröninger, L. Zhang, Y. Lu, K.S. Chan, Z. Zhou, K. Rurack, Z. Shen, Real-time monitoring of newly acidified organelles during autophagy enabled

- by reaction-based BODIPY dyes, Commun. Biol. 2 (2019) 442. https://doi.org/10.1038/s42003-019-0682-1.
- [53] R.C.R. Gonçalves, E. Belmonte-Reche, J. Pina, M. Da Costa Silva, S.C.S. Pinto, J. Gallo, S.P.G. Costa, M.M.M. Raposo, Bioimaging of Lysosomes with a BODIPY pH-Dependent Fluorescent Probe, Molecules 27 (2022). https://doi.org/10.3390/molecules27228065.
- T. Komatsu, Y. Urano, Y. Fujikawa, T. Kobayashi, H. Kojima, T. Terai, K. Development 2,6-carboxy-substituted Hanaoka, Τ. Nagano, of boron dipyrromethene (BODIPY) as a novel scaffold of ratiometric fluorescent probes for live cell imaging, Chem. Commun. (Camb) (2009)7015–7017. https://doi.org/10.1039/b917209b.
- [55] T. Knaus, V. Tseliou, L.D. Humphreys, N.S. Scrutton, F.G. Mutti, A biocatalytic method for the chemoselective aerobic oxidation of aldehydes to carboxylic acids, Green Chem. 20 (2018) 3931–3943. https://doi.org/10.1039/c8gc01381k.
- [56] K. Shortall, A. Djeghader, E. Magner, T. Soulimane, Insights into Aldehyde Dehydrogenase Enzymes: A Structural Perspective, Front. Mol. Biosci. 8 (2021) 659550. https://doi.org/10.3389/fmolb.2021.659550.
- [57] C. Godoy-Alcántar, A.K. Yatsimirsky, J.-M. Lehn, Structure-stability correlations for imine formation in aqueous solution, J. Phys. Org. Chem 18 (2005) 979–985. https://doi.org/10.1002/poc.941.
- [58] M.E. Belowich, J.F. Stoddart, Dynamic imine chemistry, Chem. Soc. Rev. 41 (2012) 2003–2024. https://doi.org/10.1039/c2cs15305j.
- [59] Y. Liu, S. Ashmawy, L. Latta, A.-V. Weiss, A.F. Kiefer, S. Nasr, B. Loretz, A.K.H. Hirsch, S. Lee, C.-M. Lehr, pH-Responsive Dynaplexes as Potent Apoptosis Inductors by Intracellular Delivery of Survivin siRNA, Biomacromolecules 24 (2023) 3742–3754. https://doi.org/10.1021/acs.biomac.3c00424.

Graphical abstract



Dynamic polymerization of a red-fluorescent BODIPY (BDP) and lysine hydrazide (Lys) under acidic pH conditions in a cuvette, leads to the formation of a quenched fluorescent biodynamer (BDP-Lys). Upon cellular uptake, BDP-Lys undergoes depolymerization, restoring fluorescence and enabling polymer visualization within the intracellular system.

2.3.1 Supplementary information

Direct Monitoring of Intracellular Polymer Degradation via BODIPY Dynamic Dequenching

Justine Bassil^{a,b}, Mohamed A. M. Kamal^{a,b}, Aljoscha Gabelmann^{a,b}, Anastasia Christoulaki^c, Marcus Koch^d, Mostafa Hamed^a, Brigitta Loretz^a, Markus Gallei^{e,f}, Eric Buhler^c, Claus-Michael Lehr^{a,b}, Anna K. H. Hirsch^{*a,b}, and Sangeun Lee^{*a,b}

^aHelmholtz Institute of Pharmaceutical Research Saarland (HIPS) – Helmholtz Centre for Infection Research (HZI), Campus E 8.1, 66123 Saarbrücken, Germany

^bDepartment of Pharmacy, PharmaScienceHub, Saarland University, Campus C4. 1, 66123 Saarbrücken, Germany

^cLaboratoire Matière et Systèmes Complexes (MSC), UMR 7057, Université Paris Cité, Physics Department, Bâtiment Condorcet, 75013 Paris, France

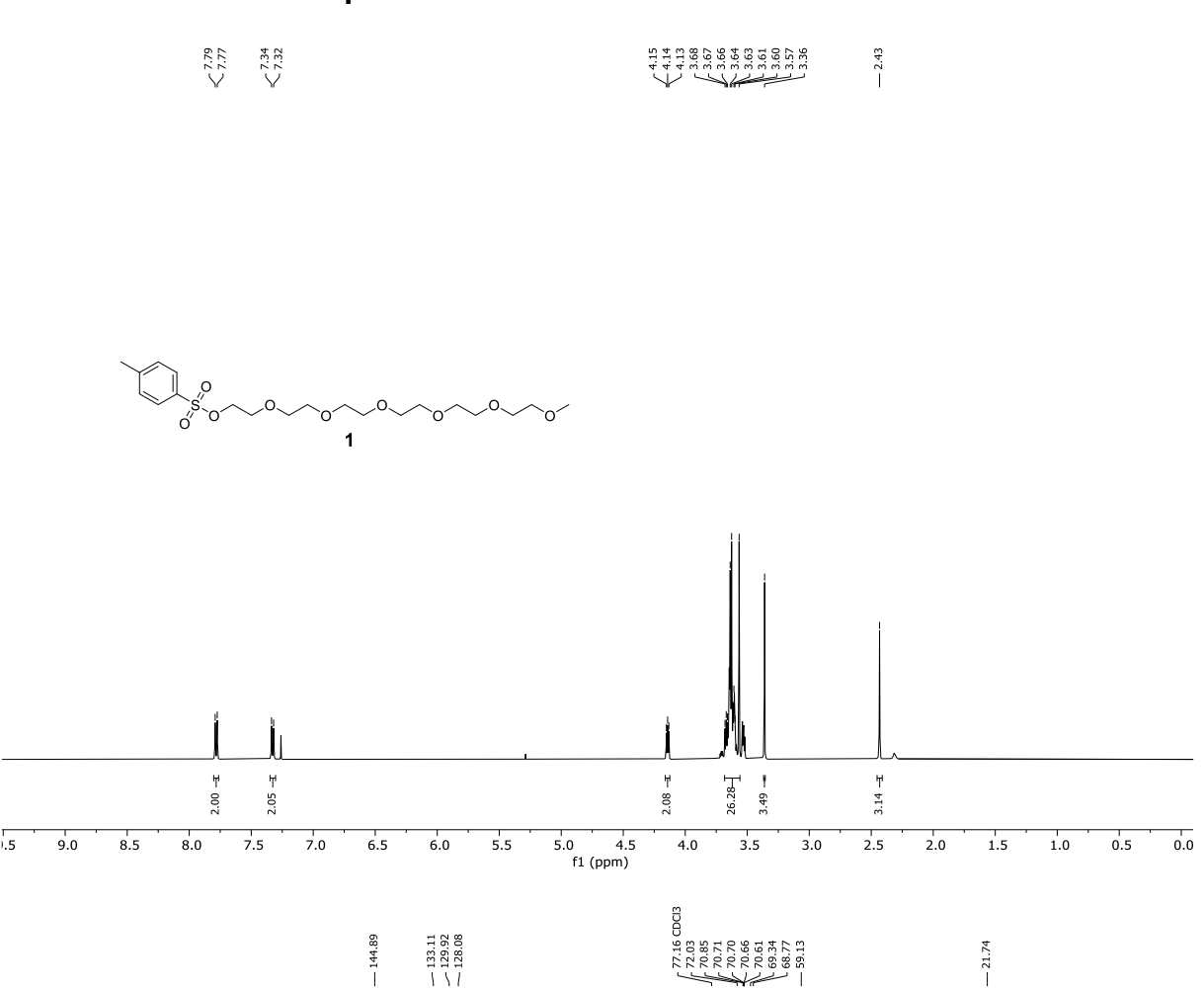
^dINM-Leibniz Institute for New Materials, Campus D2 2, 66123 Saarbrücken, Germany

^ePolymer Chemistry, Campus C4 2, 66123 Saarbrücken, Germany

^fSaarene, Saarland Center for Energy Materials and Sustainability, Campus C4 2, 66123 Saarbrücken, Germany

Scheme S1. General scheme of the synthetic route of BODIPY-dialdehyde monomer BDP

¹H NMR and ¹³C NMR spectra



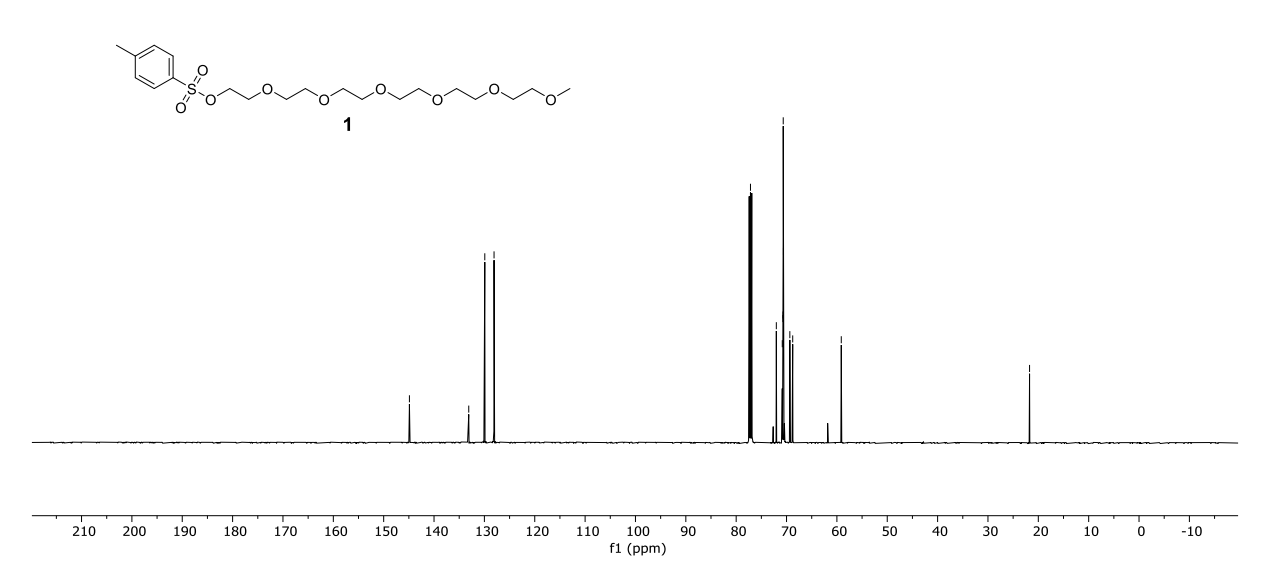
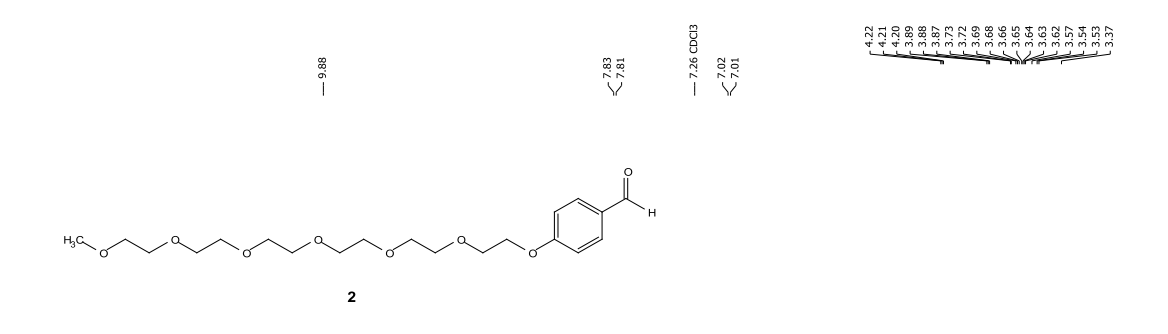
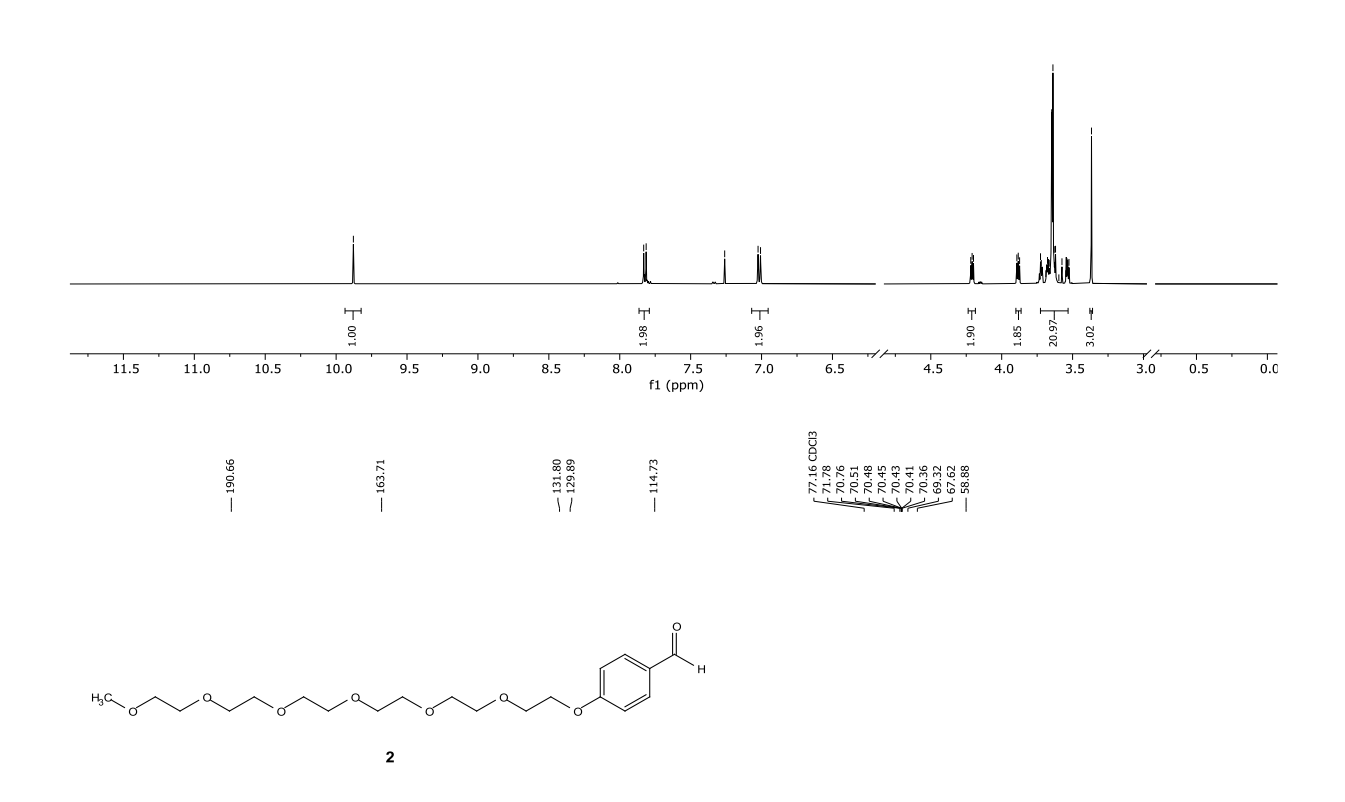


Figure S1. Proton NMR (top) and carbon NMR (bottom) spectra of compound 1 in CDC l_3 .





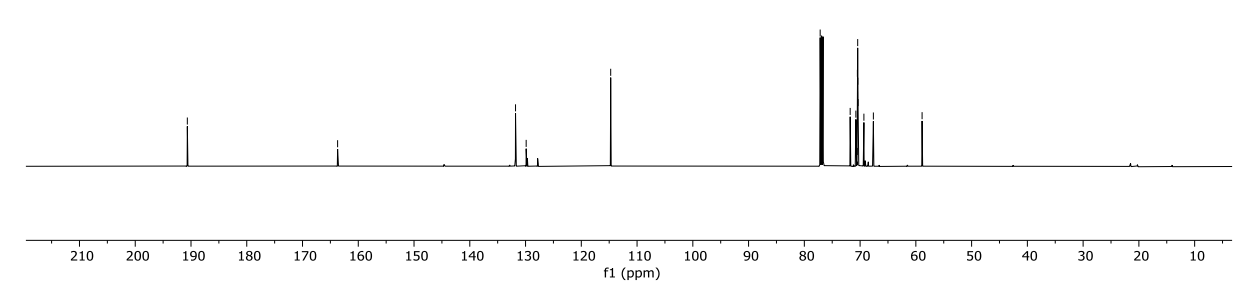


Figure S2. Proton NMR (top) and carbon NMR (bottom) spectra of compound 2 in CDCl₃.

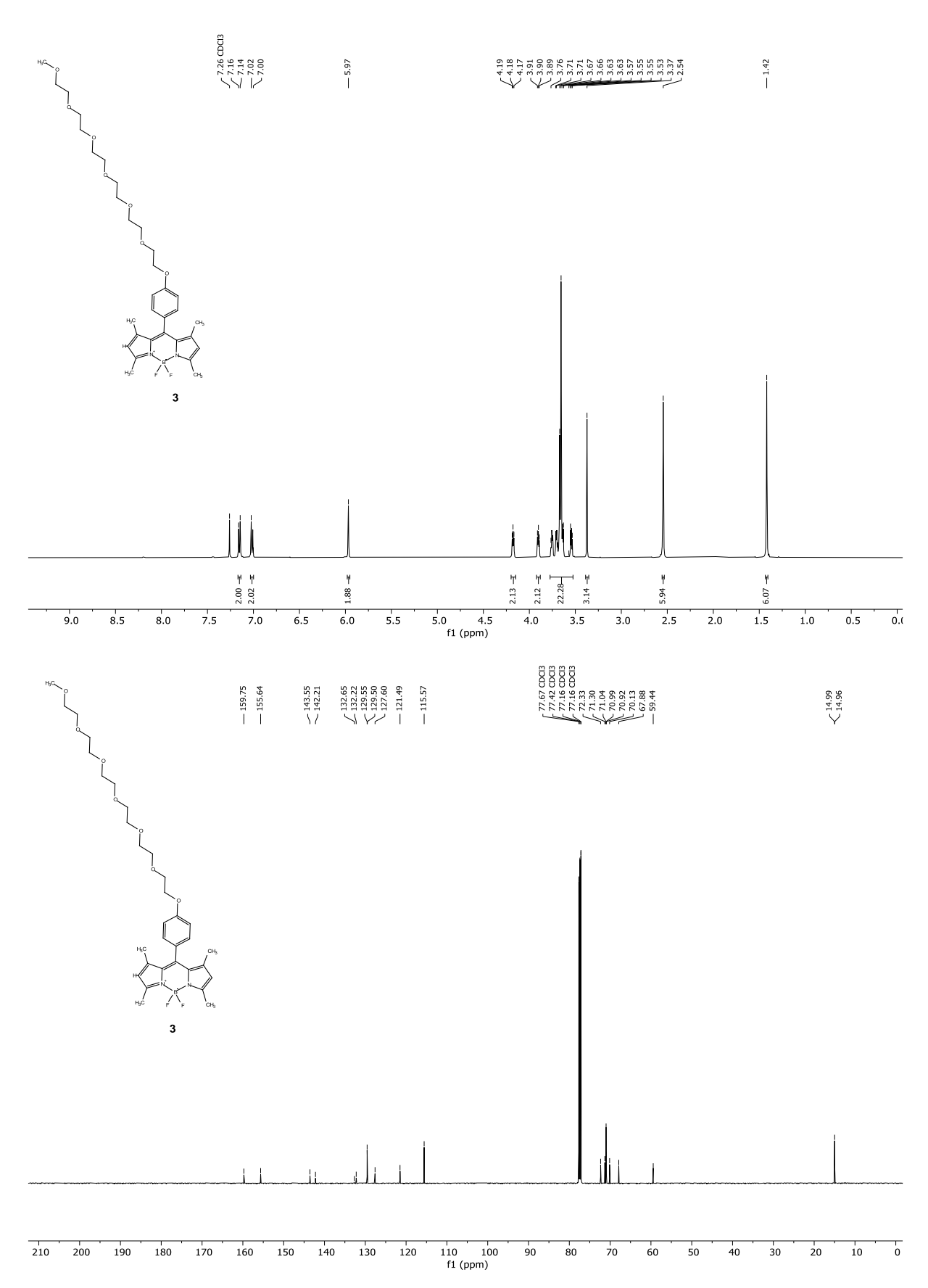


Figure S3. Proton NMR (top) and carbon NMR (bottom) spectra of compound 3 in CDCl₃.

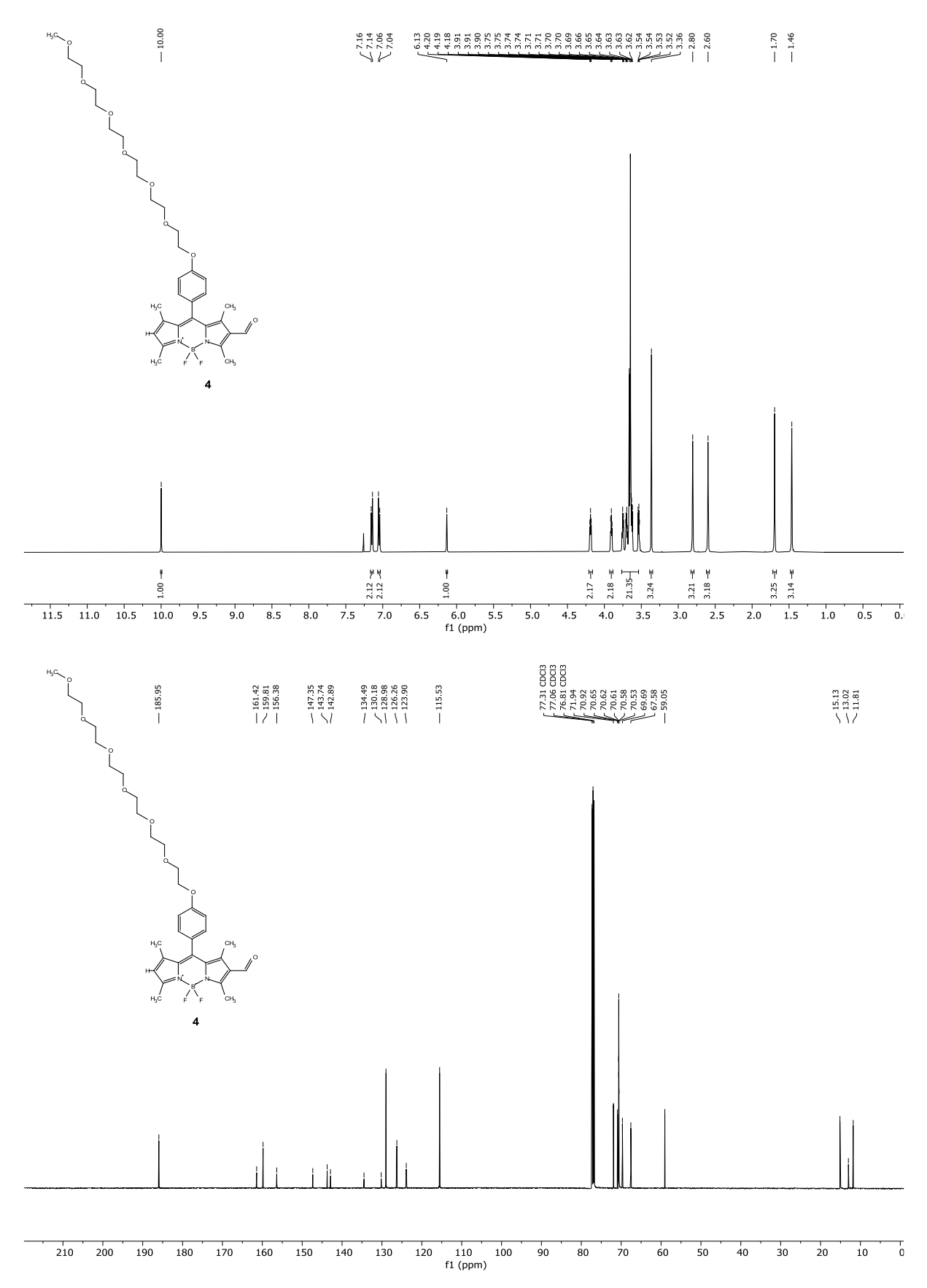
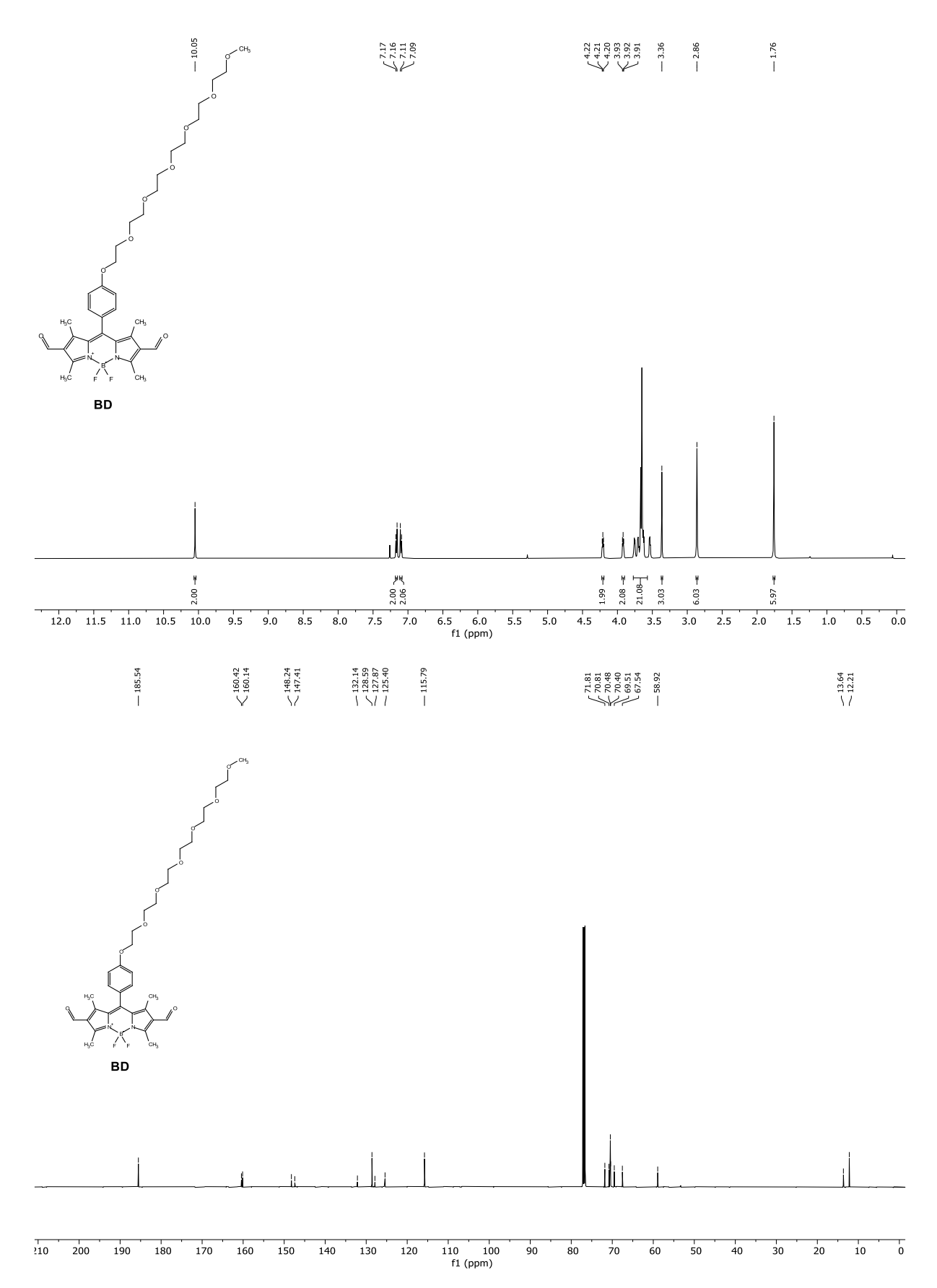


Figure S4. Proton NMR (top) and carbon NMR (bottom) spectra of compound 4 in CDCl₃.



 $\textbf{Figure S5.} \ Proton \ NMR \ (top) \ and \ carbon \ NMR \ (bottom) \ spectra \ of \ compound \ \textbf{BDP} \ in \ CDCl_3.$

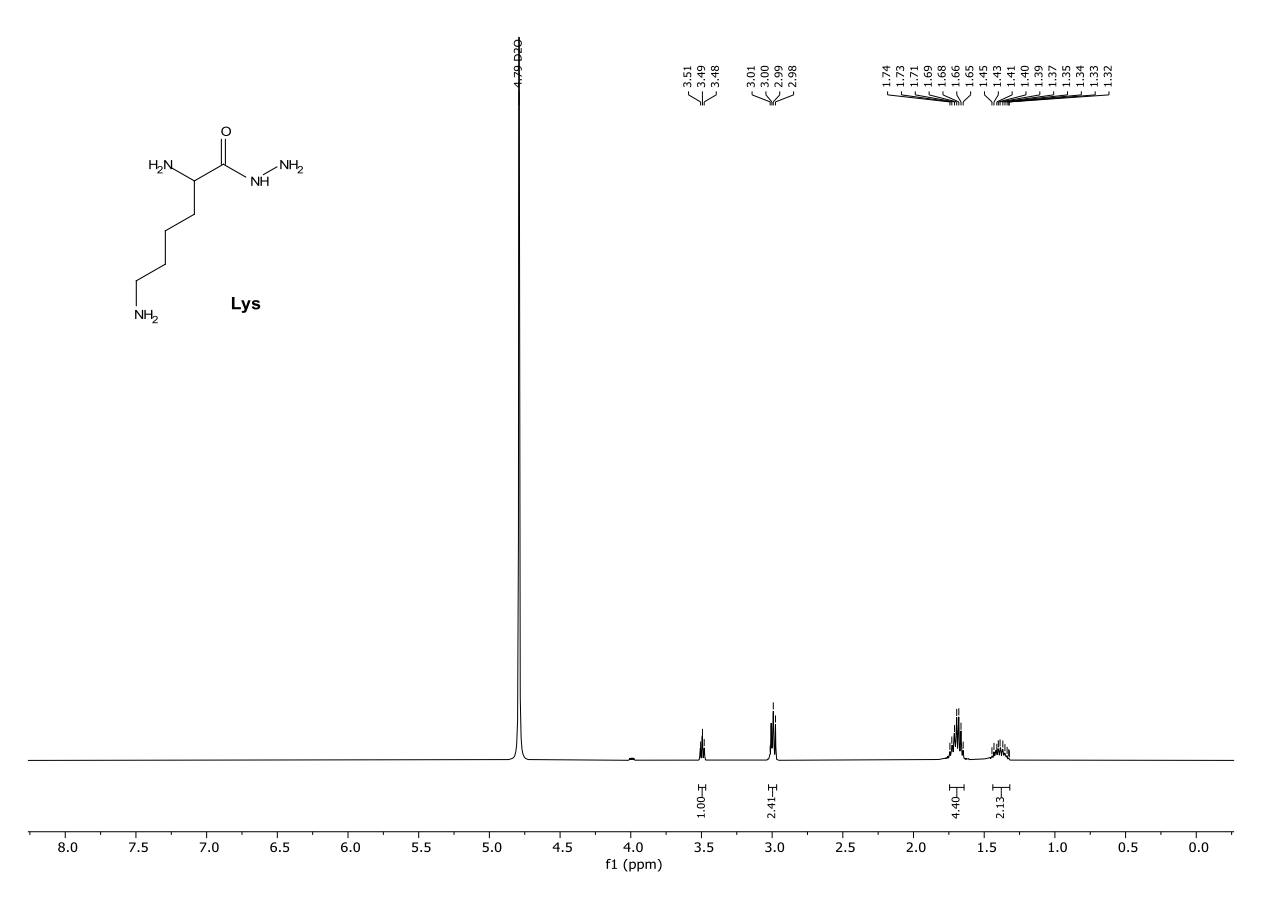


Figure S6. Proton NMR spectra of compound Lys in D₂O.

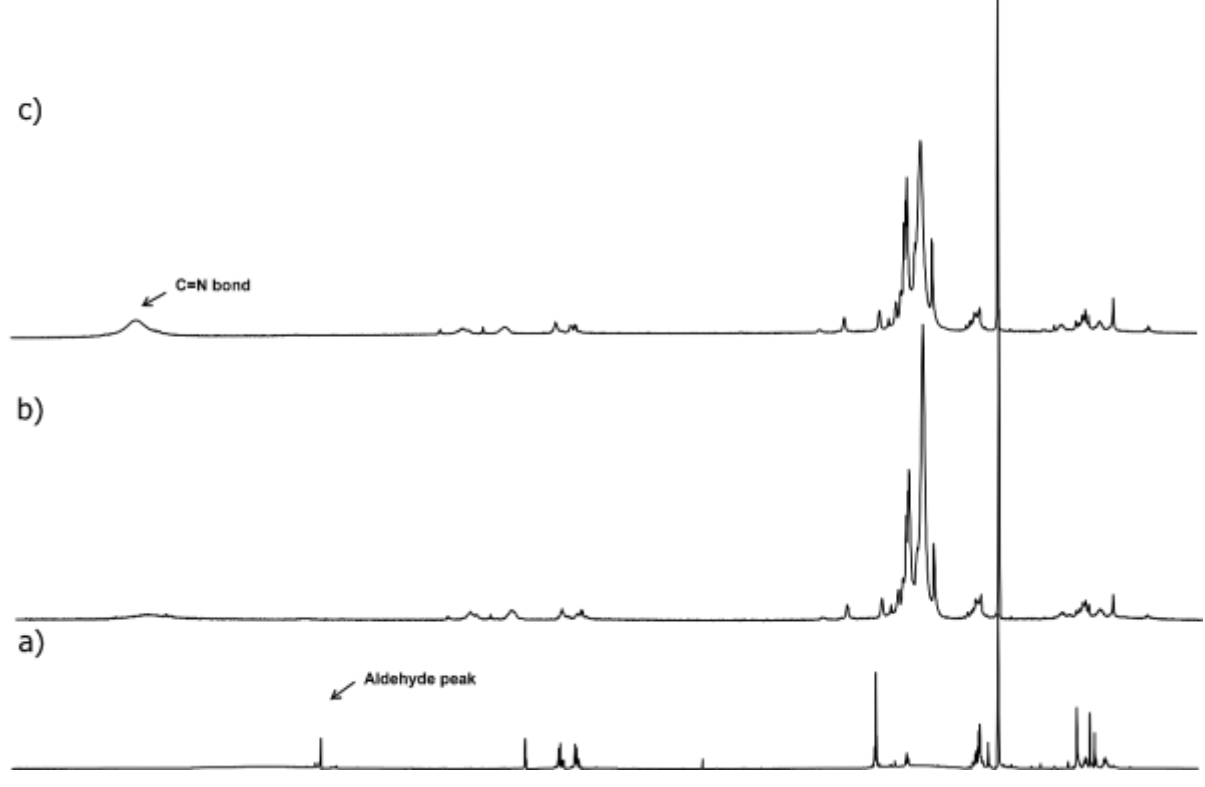


Figure S7. Parts of 1 HNMR spectrum of BDP-Lys polymerization (10 mM, DMSO-d₆, pH 3.0, 500 MHz) at different time points a) 1h b) 24 h and c) 48 h.

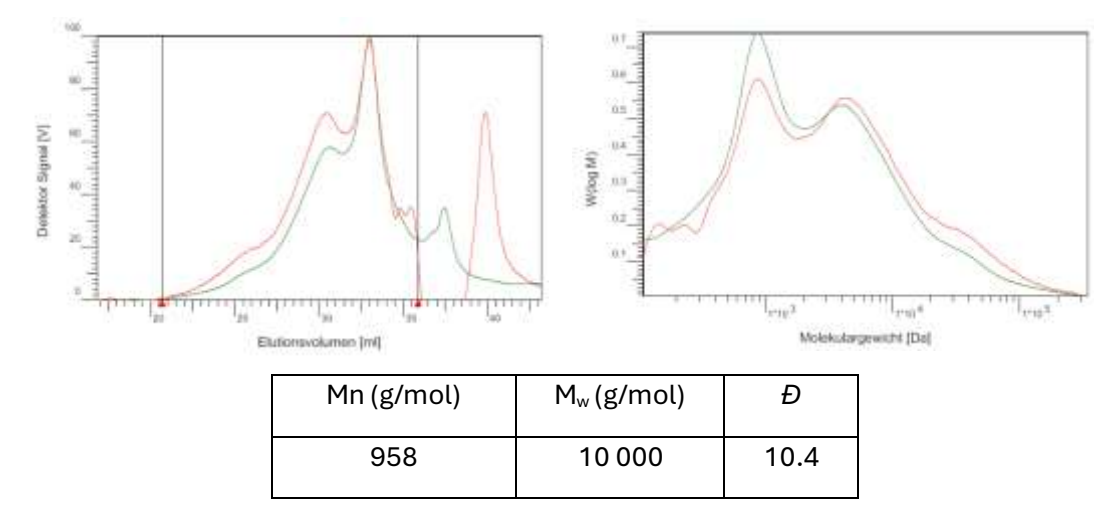


Figure S8. SEC measurements of BDP-Lys in DMF at a concentration of 0.6 g/L using PEG as standard. The molar mass distributions (\mathcal{D}), weight average molecular weight (M_w), number average molecular weight (M_n) were determined by employing HPLC pump by Waters. Detection was carried out with a refractive index (RI) Waters 2410 (red line) and an UV Waters 2487 (green line). Values are shown in the attached table.

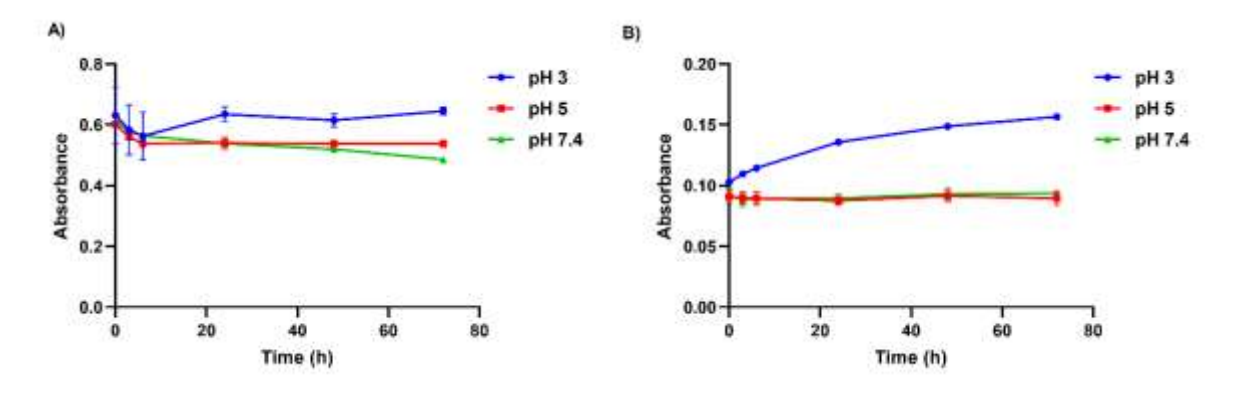


Figure S9. Optical density at λ = 502 nm in different pH and time of A) BDP monomer and B) BDP-Lys at a concentration of 25 μ M. Solvent mixture used is 1% DMSO in the corresponding buffer solutions containing 1% PVA (phosphate buffer (pH 3 and pH 7.4, 10 mM) or acetate buffer (pH 5, 10 mM)). Errors bars were obtained from duplicated experiments (N= 2 and n= 3).

Table S1. Parameters obtained by the fit of the SANS data in the high q regime using a Guinier model for the cross-section

SANS	
Imposed parameters	
φ	0.0034
$ ho_{monomer}$	1.89×10 ¹⁰ cm ⁻²
$ ho_{solvent}$	6.2×10 ¹⁰ cm ⁻²

d (monomer density)	1.46 g /cm ³
Derived	
parameters	
Α	0.00724 cm ⁻¹ .Å ⁻
	1
R_c	15.1 Å
a_c	365 Ų

Table S2. Calculated scattering length densities of the different components for the SANS and SAXS.

BDP- Lysizine hydrazide	Density	ρ	Δho^2	ρ	$\Delta \rho^2$	Chemical
(whole monomer)		SANS	SANS	SAXS	SAXS	composition
		*10 ⁻¹⁰	*10 ⁻²⁰	*10 ⁻¹⁰	*10 ⁻²⁰	
	(g/cm³)	(cm ⁻²)	(cm ⁻⁴)	(cm ⁻²)	(cm ⁻⁴)	
Polymer system	1.46	2.2	16	13.1	13.3	C ₄₀ H ₅₇ BF ₂ N ₆ O ₈
Solvent	1.10	6.2		9.5		C ₂ D ₆ OS / C ₂ H ₆ OS
10% d-DMSO / 90% D ₂ O			-		-	
BDP core	1.46	2.6	13.2	12.8	11.8	C ₂₂ H ₂₁ BF ₂ N ₂ O ₃
Hexathylene glycole	1.10	0.6	31.0	10.1	0.4	C ₁₂ H ₂₄ O ₆
Lysizine hydrazide	1.13	1.5	22.1	10.9	2.0	C ₆ H ₁₄ BFN ₄ O ₃
BDP core- Lysizine	1.46	3.8	14.4	13.0	12.3	C ₂₈ H ₃₃ BF ₂ N ₄ O ₃
hydrazide (hydrophilic						
chains excluded)						

3 Conclusions & Future Perspectives

The escalating threat of antimicrobial resistance (AMR) requires urgent efforts to expand the anti-infective arsenal with novel agents targeting: i) underexplored drug targets such as ECF transporters and ii) major pathogenic organisms such as *Mtb*. Additionally, the development of smart biodynamers that hold potential for tracking degradation and further enhancing drug-delivery systems.

Our search for inhibitors targeting the underexploited ECF transporters (Chapter A) led to the identification of picolinic acid derivatives through experimental screening of internal and external compound libraries. We conducted an SAR study to optimize the hit compound considering all parts of its structure. These modifications, however, did not improve the solubility of the synthesized derivatives, with our initial hit remaining among the most soluble. Nevertheless, our three frontrunners showed superior activity in the whole-cell based assay and favorable ADMET properties including high metabolic and plasma stability with no cytotoxic effects. The proteoliposome-based assay confirmed their strong selectivity for bacterial ECF transporters, with no cross-reactivity against human ABC transporters. Further screening against a panel of bacterial pathogens revealed low micromolar antibacterial activity against S. pneumoniae, particularly its penicillin-resistant strains, highlighting their potential for further development. While promising results were obtained, further research is necessary to advance these inhibitors to lead compounds. Next steps include obtaining co-crystal or cryo-TEM structures to define the binding pocket, further optimizing structural features for improved potency, solubility, and conducting in vivo zebrafish and PK/PD studies in mice. Similarly in Chapter B, screening of our compound library against Mtb revealed a promising hit bearing a 1,3,4-oxadiazole scaffold. We initiated an SAR study to explore structural modifications of the hit compound, resulting in two derivatives with enhanced MIC values, and no significant toxicity against HepG2. When screened against a range of GPB, our frontrunners demonstrated strong antibacterial activity against S. pneumoniae, S. aureus, and B. subtilis. In this study, we managed to obtain inhibitors with antituberculosis activity, but additional studies are required to elucidate the mode of action, evaluate the in vitro ADMET profiling, and explore possible synergistic effects with firstline anti-tuberculosis drugs.

In Chapter C, we successfully developed a novel dynamic polymer BDP-Lys, composed of BODIPY-dialdehyde (BDP) and lysine-hydrazide monomer (Lys) linked by reversible imine and acylhydrazones bonds. Comprehensive physicochemical characterization using various techniques (e.g., ¹H-NMR, GPC, cryo-TEM, SAXS, and SANS) provided us with insights into the structure and properties of BDP-Lys. We analyzed the polymer optical properties, finding that its fluorescence was quenched in polymeric form but is recovered and enhanced in acidic environments, particularly at pH 3, due to pHresponsive degradation. Moreover, with the fluorescence enhancement of BDP monomer in acidic pH, we further hypothesized a subsequent oxidation of BDP monomer from aldehyde to carboxylic acid a process that could be facilitated by enzymes in biological systems and improve our polymer-fate tracking. However, this hypothesis remains elusive during the scope of this PhD project. Despite this, we further conducted in vitro studies in mammalian cells, which revealed excellent biocompatibility, efficient cellular uptake by endocytosis, and a threefold increase in BDP-Lys fluorescence, indicating polymer degradation and recovery of monomer fluorescence. Overall, in this study we were able to prove that BDP-Lys holds significant potential for providing realtime tracking of polymer degradation within biological systems, marking it as a promising starting point for future investigations into the fate and degradation of pH-responsive biodynamers. Several next steps are required for advancing this study including confirming the hypothesized intracellular oxidation of BODIPY-(dialdehyde) to -(dicarboxylic acid) groups. Synthesizing and comparing the behavior of both BODIPY groups, particularly their fluorescence properties in both cellular and extracellular environments will provide valuable insights. Long-term degradation studies and better visualization techniques will be essential for fully understanding the extended fate of BDP-Lys and its degradation products. Additionally, optimizing the biodynamer composition by modifying the amino acid monomer could enhance its properties, and offer great potential for biopharmaceutical and drug-delivery applications. Lastly, taking advantage of its pH-responsive and fluorescent properties, we can explore its potential as a nanocarrier for targeted drug-delivery and overcoming biological barriers (such as dynaplexes or potentiators). This area holds great promise for future research in tackling AMR.

4 Appendix

Abbreviations

AMR Antimicrobial resistance

MDR Multidrug resistance

XDR Extensive drug resistance

WHO World health organization

GNB Gram-negative bacteria

GPB Gram-positive bacteria

SAR Structure—activity relationship

DNA Deoxyribonucleic acid

RNA Ribonucleic acid

mRNA Messenger ribonucleic acid

LPS Lipopolysaccharide

ATP Adenosine 5'-triphosphate

ADP Adenosine 5'-diphosphate

ABC ATP-binding cassette

TMD Transmembrane domain

NBD Nucleotide-binding domain

SBP Substrate binding protein

ECF Energy coupling factor

L. casei Lacticaseibacillus casei

L. delbrueckii Lactobacillus delbrueckii

FolT Folic acid ot folate

PanT Pantothenic acid or panthothenate

ECF-FolT2 Folate transporter

ECF-PanT Pantothenate transporter

S. aureus Staphylococcus aureus

S. pneumoniae Streptococcus pneumoniae

SBVS Structure-based virtual screening

IC₅₀ Half-maximal inhibitory concentration

Appendix

MIC Minimum inhibitory concentration

TB Tuberculosis

Mtb Mycobacterium tuberculosis

INH Isoniazid

RIF Rifampcin

CDC Constitutional dynamic chemistry

DCC Dynamic covalent chemistry

DCBs Dynamic covalent bonds

DyNas Dynamic analogues of nucleic acids

Lys Lysine

Arg Arginine

His Histidine

CA Carbazole-dialdehyde

HG Hexaethylene glycol chain

Publications included in this thesis and contribution declaration

Bassil, J. †; Exapicheidou, A. I.†; Stefan, K.; Tsarenko, A.; Zulu, A. I.; Kany, A. M.; Haupenthal, J.; Stefan, S. M.; Slotboom, D. J.; Hamed, M. M.; Hirsch, A. K. H. Discovery of picolinic acid derivatives as a new class of energy-coupling factor transporters (ECF-T) inhibitors. (Manuscript will be submitted to European Journal of Medicinal Chemistry) †Authors contributed equally to the work

<u>Contribution:</u> The author contributed to the conception and design of this study. She was responsible for the synthesis and characterization of the compounds analyzing and interpreting the resulting data. She contributed to conceiving and writing the manuscript.

Bassil, J.; Kamal, M. A. M.; Gabelmann, A.; Christoulakic. A.; Koch, M.; Hameda, M. M.; Loretza, B.; Gallei, M.; Buhler, E.; Lehr, C.-M.; Hirsch, A. K. H.; Lee, S.

Direct Monitoring of Intracellular Polymer Degradation via BODIPY Dynamic Dequenching. (Manuscript submitted and under revision at Materials & design Journal)

<u>Contribution:</u> The author Justine Bassil contributed to the conception of this project. She was responsible for designing and conducting the experiments, collecting, analyzing, and interpreting the resulting data. She synthesized the monomer and polymer and carried out biological evaluations such as pH-responsive degradation and fluorescent experiments. Additionally, she wrote the manuscript.

Bassil, **J.** *et al*. Discovery of a New Oxadiazole Derivative as Antitubercular Agents: Structure—Activity Relationship and Mode-of-Action Studies. (Manuscript in preparation)

Contribution: The author contributed to the conception and design of this study. She performed all the synthesis and characterization of the compounds. She analyzed and interpreted the resulting data. She contributed to writing the manuscript.

Publications not included in this thesis and contribution declaration

Kamal, M. A. M.; **Bassil, J.**; Loretz, B.; Hirsch, A. K. H.; Lee, S.; Lehr, C.-M. Ar-Biodynamers as Antibiotic Potentiators through Interacting with Gram-Negative Outer Membrane Lipopolysaccharides. *Eur. J. Pharm. Biopharm.* **2024,** 200, 114336. https://doi.org/10.1016/j.ejpb.2024.114336.

<u>Contribution:</u> Writing – review & editing, Validation, Methodology. The author has synthesized the carbazole-dialdehyde monomer. She described the method and results for the all the synthesis and reviewed the manuscript.

Zeroug-Metz, L.; Kamal, M. A. M.; **Bassil, J.**; Elamaldeniya, K.; Ryu, B. H.; Buhler, E.; Lee, S. Fluorescent Histidine-Derived Biodynamers as Biocompatible and Highly Water-Soluble Copper(II)-Sensors. *RSC Appl. Polym.* **2024**, *1* (9), 1234-1245. https://doi.org/10.1039/D4LP00126E

<u>Contribution:</u> The author has synthesized the carbazole-dialdehyde monomer necessary for the study.